



**This electronic thesis or dissertation has been
downloaded from Explore Bristol Research,
<http://research-information.bristol.ac.uk>**

Author:

Lalemi, Lara

Title:

**Measurements of Microscopic Droplet Surface Tensions and Investigations of the
Potential Impacts of Aerosol Science and Decolonial Work on Wider Society**

General rights

Access to the thesis is subject to the Creative Commons Attribution - NonCommercial-No Derivatives 4.0 International Public License. A copy of this may be found at <https://creativecommons.org/licenses/by-nc-nd/4.0/legalcode> This license sets out your rights and the restrictions that apply to your access to the thesis so it is important you read this before proceeding.

Take down policy

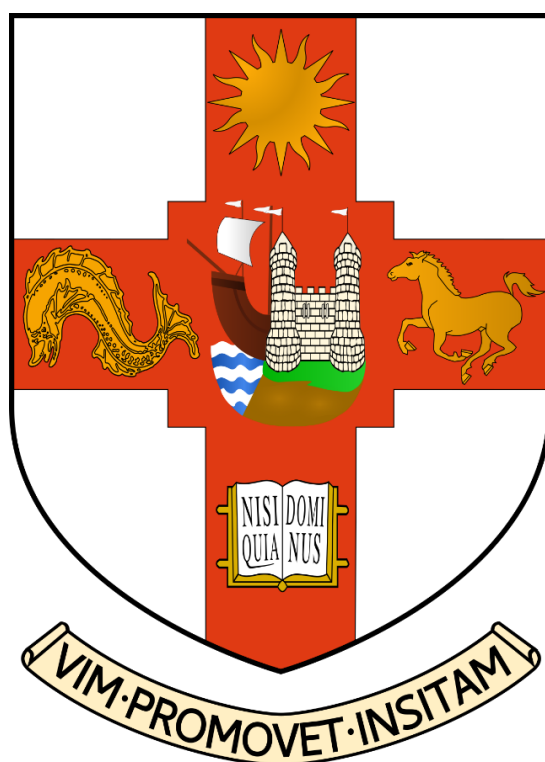
Some pages of this thesis may have been removed for copyright restrictions prior to having it been deposited in Explore Bristol Research. However, if you have discovered material within the thesis that you consider to be unlawful e.g. breaches of copyright (either yours or that of a third party) or any other law, including but not limited to those relating to patent, trademark, confidentiality, data protection, obscenity, defamation, libel, then please contact collections-metadata@bristol.ac.uk and include the following information in your message:

- Your contact details
- Bibliographic details for the item, including a URL
- An outline nature of the complaint

Your claim will be investigated and, where appropriate, the item in question will be removed from public view as soon as possible.

Measurements of Microscopic Droplet Surface Tensions and Investigations of the Potential Impacts of Aerosol Science and Decolonial Work on Wider Society

By Lara Lalemi



A dissertation submitted to the University of Bristol in accordance with the requirements of
the degree of Doctor of Philosophy in the School of Chemistry, Faculty of Science

March 2023

75,632 words

Abstract

Atmospheric aerosols play a pivotal role in the global radiative balance yet represent one of the largest uncertainties in radiative forcing. This work investigates essential microphysical characteristics of aerosols, such as surface tension, which influences both the direct and indirect impacts of aerosols on the atmosphere. Additionally, it explores viscosity, a factor capable of modifying mass and chemical reactivity through its influence on gas-particle partitioning.

The characterisation of these properties was conducted using various experimental techniques to analyse both aerosol droplets and bulk-phase solutions. The technique of the droplet oscillation method employed a microdispenser to eject particles of 30 – 50 μm diameter and capture their oscillation trajectory using precisely timed stroboscopic imaging. The surface tension was retrieved from the frequency of droplet oscillations at specific delay times. The validity of this technique was assessed with a non-dynamic system where the droplet and bulk data should be similar to one another. Following the validation of the method, more complex, dynamic systems were investigated. Notably, a novel data analysis method was employed to determine the dynamic surface tension of a surfactant droplet. These measurements can be used to provide early time points (within microseconds) of the dynamic surface tension profile before equilibrium is reached. The dynamic surface tension remains a crucial factor in exploring aerosol chemistry, surfactant dynamics and cloud droplet activation.

Additionally, this thesis reports the study of aerosol viscosity using the holographic optical tweezers for the trapping and manipulation of the levitated particles under different ambient conditions. Following on from previous studies, this work examined the effect of relative humidity on droplet viscosity and diffusion which are vital to understanding the kinetic limitations to particle growth. The principal components employed in this study were highly viscous organic proxies, organic acids, and inorganic salts, which were selected to mimic the mixtures present in the atmosphere. While real systems are more complex, this work forms part of a fundamental understanding from which complexity of the system can be increased.

The irradiation of a photoactive aerosol droplet was studied using the Electrodynamic Balance (EDB) and a broad wavelength UV light source. These preliminary experiments were conducted as part of the investigation into the properties that inhibit aerosol photochemistry, specifically, the effects of viscosity and the presence of surface-active molecules.

Research in aerosol science, as explored in this thesis, operates within a complex landscape shaped by social, economic, political, and cultural factors, all of which bear the historical imprint of colonialism in various forms. Since 2020, knowledge of colonialism's effects on wealth distribution, resources, and

research funding have prompted universities to integrate decolonisation into their strategies to increase inclusivity and belonging. However, within STEM fields, there has been a lack of comprehensive frameworks to guide individuals towards achieving these goals. This thesis aimed to address this gap by pioneering a novel decolonial framework, developed by the Decolonising the Science Working Group from 2018 to 2022. The framework empowers universities to identify and confront colonial legacies within their scientific disciplines and research environments, thereby identifying meaningful steps towards decolonisation. Using this framework to analyse of the EPSRC Centre for Doctoral Training in Aerosol Science curriculum, revealed areas for enhancing diversity and adopting decolonial thinking within the field of aerosol science education. Herein, it is proposed that such efforts can increase social, cultural and self-awareness as well as foster a heightened global consciousness among university students, qualities highly valued by employers.

Acknowledgements

Firstly, I would like to thank Dr. Bryan Bzdek for all his guidance and advice over the course of my PhD. I would also like to thank my co-supervisor Professor Andrew Orr-Ewing for the support and advice.

I am privileged to reflect on an academic journey that has been significantly enriched by the unwavering support and a nurturing environment provided by the Bristol Aerosol Research group. The completion of my PhD is owed, in part, to the guidance and encouragement I have received within this group. It would be impossible to name everyone whom I have come to value and see as incredible people so I would like to say thank you to you all. A special thanks goes out to Dr. Dan Hardy, Dr. Alison Bain and Dr. Florence Gregson for your support and being the light that I needed some days. I am deeply grateful for Dr. Allen Haddrell and Dr. Jim Walker without whom this thesis would not be here. To Dr. Kerry Knox and Dr. Josie Gill, thank you for your belief in my work beyond the scientific aerosol research. Your support was instrumental to completing Chapter 2 and starting my journey into science education.

To my friends, I would like to thank all of you but a special thank you is held for Helen Gaden, Isabel Quant, and Hilary McCarthy. You have all been there when I have needed it the most and so I want to say thank you for putting up with me over the last few years, making me laugh, food and holding space for me, it was what I needed to stay the course.

To my family, without whom I would not be doing a PhD **at all**. The enormous support for my educational progress is only matched by the immense amount of love that you all have given to me. To my brother, Dr. Christopher Lalemi, thank you for forming the blueprint to success and achievement. And finally, to my parents who have sacrificed so much for me to be here today, thank you for your belief, stability, and delicious food during what has been a turbulent time in my life, **this is for you**.

They say it takes a village to raise a child, but I also believe it takes a village, full of mentors, supporters and cheerleaders to create a successful PhD student. So, all in all, I have been very lucky to have the people around me.

Author's Declaration

I declare that the work in this dissertation was carried out in accordance with the requirements of the University's Regulations and Code of Practice for Research Degree Programmes and that it has not been submitted for any other academic award. Except where indicated by specific reference in the text, the work is the candidate's own work. Work done in collaboration with, or with the assistance of, others, is indicated as such. Any views expressed in the dissertation are those of the author.

Signature.....

Date.....

Table of Contents

Abstract.....	i
Chapter 1 Introduction.....	1
1.1 Overview of Aerosol	1
1.2 Atmospheric Aerosols: Size, Lifetime and Distribution.....	2
1.3 Atmospheric Aerosols: Composition	4
1.3.1 Organic Aerosols.....	4
1.3.2 Inorganic Salt and Organic Acid Mixtures	6
1.3.3 Atmospheric Surfactants.....	7
1.4 Influence of Aerosols on the Climate	8
1.4.1 Radiative forcing of the Earth’s Atmosphere.....	9
1.4.1 Cloud-Light Interactions.....	10
1.4.1.1 Cloud Albedo	10
1.4.1.2 Cloud Radiative Effect.....	10
1.4.1.3 The Direct Effect.....	11
1.4.1.4 The Indirect Effect	11
1.5 Nucleation and Particle growth.....	12
1.5.1 Partitioning of Water onto an Aerosol Droplet.....	12
1.5.2 Köhler Theory	14
1.5.3 Hygroscopicity and Growth Factor.....	16
1.5.4 Surface Tension and surface concentration.....	18
1.5.4.1 Defining Gibbs Dividing Surface.....	18
1.5.4.2 Gibbs Isotherm.....	19
1.5.4.3 Theoretical Adsorption Isotherms.....	22
1.5.4.4 Surface Activity	25
1.5.4.5 The Influence of Aerosol Surface Tension on CCN Activation	26
1.6 The Kinetics of Aerosol Processes	26

1.7 Aerosol-Light Interactions	29
1.7.1 Aerosol Optical Properties and Refractive Index	29
1.7.1.1 The Three Size Regimes for the Interaction of Light with a Particle	30
1.7.2 Aerosol Photochemical Reactions	31
1.7.3 Optical Tweezing of Aerosol Droplets	33
1.8 Aerosol Measurement Techniques	35
1.8.1 Techniques for Measuring Surface Tension	35
1.8.1.1 Bulk-Phase Measurements	36
1.8.1.2 Droplet-phase Measurements.....	36
1.8.1.3 Dynamic Bulk Measurements	36
1.8.2 Techniques for Measuring Viscosity	37
1.8.2.1 Determining Viscosity by Applied Force	37
1.8.2.2 Determining Viscosity by Relaxation Techniques.....	38
1.8.2.3 Determining Viscosity by Fluorescence Imaging	38
1.9 Thesis Aims	38
1.10 Thesis Summary	39
Chapter 2 Preparing researchers in aerosol science to be inclusive, self-aware and globally conscious: A decolonial approach	41
2.1 Overview	41
2.1.1 Contextualising this chapter	41
2.1.2 Awareness in Academia	42
2.1.2.1 Self Awareness.....	43
2.1.2.2 Global Awareness	43
2.2 Decolonising and Contextualising the Curriculum	45
2.2.1 Decolonising the curriculum and the five dimensions.	48
2.2.1.1 Decolonising the Dentistry Curriculum	48
2.2.1.2 Decolonising the Biomedical Science Curriculum	50
2.2.1.3 Decolonising the Science Curriculum in a UK School	51

2.2.1.4 Decolonising the SPAIS Curriculum	52
2.2.1.5 Decolonising International Social Work.....	53
2.2.2 Decolonising and Diversifying the Science Working Environment.....	53
2.2.2.1 Being BME in STEM Half-Day Conference	53
2.2.2.2 The Inclusive Research Collective Training Programme	54
2.2.2.3 Inspirational Bristol Scientists Board.....	55
2.3 Decolonising Aerosol Science Curriculum and Teaching Activities	56
2.3.1 Methodology of Delivering the Framework.....	58
2.3.2 The Decolonising Aerosol Science Workshop.....	59
2.3.3 Adaption of the Aerosol Science Program Content	62
2.3.3.1 Knowledge Production and Dissemination in Aerosol Science.....	63
2.3.3.2 The Economy and Access to Funding in Aerosol Science.....	64
2.3.3.3 Policies and Aerosol Science	67
2.3.3.4 Language, Culture and Aerosol Science	68
2.4 Conclusion	70
2.5 Final Remarks.....	72
Chapter 3 Experimental Techniques and Methodology	73
3.1 Overview	73
3.2 Droplet Oscillatory Method	73
3.2.1 Droplet Oscillatory Method Setup.....	75
3.2.2 Droplet identification and Image Analysis	76
3.2.3 Determining Error in Calculations	78
3.3 Holographic Optical Tweezers	79
3.3.1 Components of the Holographic optical tweezers	79
3.3.2 Aerosol Delivery and Trapping Cell Design	81
3.3.3 Trapping Chamber Design.....	82
3.3.5 Environmental Control of Gas Phase Conditions	83
3.3.6 Brightfield Imaging and Droplet Illumination	85

3.3.7 SLM and Hologram Generation	86
3.3.8 Raman Spectroscopy.....	87
3.3.8.1 Spectrograph and CCD Detector.....	87
3.3.8.2 Acquisition of Spectra (LARA)	88
3.3.8.3 Analysis of Raman Spectra	88
3.3.9 Calculating Viscosity.....	91
3.3.9.1 Raman Spectrum of Coalescing Droplets	92
3.4 Electrodynamic Balance.....	96
3.4.1 The Experimental EDB Set-up	96
3.4.2 Droplet Delivery and Generation	98
3.4.3 Droplet Confinement	98
3.4.4 Environmental Control.....	99
3.4.5 Estimating Droplet Size	100
3.4.6 UV-Vis Droplet Illumination.....	101
3.5 Bulk Phase Measurements	102
3.5.1 Maximum Bubble Pressure Tensiometer.....	102
3.5.2 Determining the Surface Tension	102
3.5.2.1 Hydrostatic pressure, p_0	104
3.5.3 Measuring Surface Tension.....	104
3.6 Wilhelmy Plate Method.....	105
3.6.1 Determining the Critical Micelle Concentration.....	106
3.6.2 A Standard Measurement.....	106
3.7 Conclusion and Future Work	107
Chapter 4 The Surface Tension of Organic Acids, Inorganic Salts, and Their	
Mixtures	109
4.1 Overview.....	109
4.1.1 The Surface Activity and Tension of Organic Acids.....	109
4.1.2 The Surface Activity and Tension of Inorganic Salts	111

4.1.3 Surface Tension of Inorganic and Organic Mixtures	112
4.1.3.1 The Salting Effects.....	113
4.1.4 Modelling Surface Tension of Inorganic and Organic Mixtures.....	114
4.1.4.1 Origin and Derivation of Binary System Models	115
4.1.4.2 Derivation of Multicomponent System Models	116
4.1.4.3 Boyer et al. Model.....	117
4.2 Measurement Techniques	118
4.2.1 Droplet Oscillatory Method	118
4.2.2 Maximum Bubble Pressure Tensiometer	119
4.3 Results and Discussion	119
4.3.1 Summary of study	119
4.3.2 Surface Tension of Binary System.....	121
4.3.2.1 Surface Tension of Organic Acids	121
4.3.2.2. Surface Tension of Monovalent Inorganic Salts	127
4.3.3 Surface Tension of Ternary Systems.....	129
4.3.3.1 Setschenow Coefficients	130
4.3.3.2 Ammonium Sulfate: Oxalic Acid	131
4.3.3.3 Ammonium Sulfate:Malonic Acid.....	132
4.3.3.4 Ammonium Sulfate:Pyruvic Acid.....	134
4.3.3.5 Ammonium Sulfate:Levulinic Acid.....	135
4.4 Conclusion and Future Work.....	137
 Chapter 5 Explorations of Surfactant Partitioning in Microscopic Droplets and Bulk Solutions	 140
5.1 Overview	140
5.1.1 Modelling surfactant dynamics and behaviour	141
5.1.1.1 Diffusion-Controlled Adsorption Model.....	142
5.1.1.2 Kinetic-Controlled Adsorption Model	144
5.1.1.3 The Presence of Micelles and Their Impact on Adsorption.....	144
5.1.1.4 Adsorption Energy Barrier.....	146

5.1.2 Bulk surfactant depletion within a droplet	146
5.1.2.1 Comparing Droplet Size and Curvature.....	148
5.1.2.2 Bulk Surfactant Depletion Within a Droplet.....	150
5.1.2.3 Comparing Surfactant Properties and Structure.....	152
5.2 Experimental	155
5.2.1 Droplet Dynamic Surface Tension Measurements	155
5.2.2 Bulk Dynamic and Static Surface Tension Measurements	155
5.3 Results and Discussion	155
5.3.1 Bulk Surface Tension Measurements	155
5.3.1.1 Dynamic Bulk Surface Tension Measurements.....	155
5.3.1.2 Equilibrium Bulk Surface Tension Measurements	160
5.3.2. Droplet Dynamic Surface Tension Measurements	165
5.3.2.1 Characterization of Surface Tension in Relation to Surfactant Concentration and Type	170
5.3.2.2 Characterization of Surface Tension in Relation to Droplet Size and Dispensing Frequency.....	176
5.3.2.3 Combining Droplet and Bulk Data using the Hua-Rosen Equation.....	181
5.4 Conclusion	183
5.5 Future Work	184
Chapter 6 The Measurement of Viscosity and Photoinduced Size Change in Aerosol Droplets Under Different Humidity Conditions	185
6.1 Overview	185
6.1.1 The Impact of Particle Composition on the Viscosity of Aerosol Particles.....	188
6.1.2 Predicting Viscosity Using Mixing Models	189
6.1.2.1 AIOMFAC Viscosity Model.....	190
6.1.2.2 Mixing Binary Model.....	190
6.1.3 Aerosol Droplet Photochemical Reactions	191
6.2 Experimental	192
6.2.1 Holographic Optical tweezers (HOT)	192

6.2.2 Electrodynamic Balance	194
6.3 Results and Discussion	196
6.3.1 Measurement of Viscosity Under Different Environmental Conditions and Mass Ratios.....	196
6.3.1.1 Comparison of inorganic-organic mixtures at different wt% ratios.....	196
6.3.1.2 Organic acid-organic compounds mixtures.	198
6.3.2 Observations of Levitated Sodium Nitrate Droplet Size Changes Upon UV Illumination	200
6.4 Conclusion and Future Work	202
Chapter 7 Summary, Conclusions, and Future work	204
7.1 Summary of Findings	204
7.2 Conclusions.....	204
7.2.1 Addressing Aerosol Science research, Curriculum, and Culture.....	204
7.2.1.1 The Creative Tuition Collective Initiative	205
7.2.2 Surface tension measurements.....	205
7.2.3 Viscosity and Photochemistry Related measurements	206
7.3 Future Directions.....	207
7.3.1 CTC Aerosol Project Proposal with a Decolonial Approach	207
7.4 Final Remarks.....	209
References	210

List of Figures

Figure 1-1: Schematic of the size distribution, with the sources, removal mechanisms and particle lifetimes indicated for each size mode. Based on the image from Seinfeld and Pandis 3

Figure 1-2: An illustrative map displaying the total mass concentration and mass fractions of nonrefractory inorganic species along with organic components in submicrometre aerosols 4

Figure 1-3: The Global mean radiative forcings (RF) from 2019 compared to 1750 from the IPCC 6th Assessment Report Technical Summary..... 9

Figure 1-4: The processes which influence the scattering or absorption of light radiation by aerosols or clouds adapted from the IPCC’s fourth assessment report. 10

Figure 1-5: Illustration of the hygroscopic response of a sodium chloride droplet to a decrease in relative humidity. 13

Figure 1-6: A picture of the global relative humidity distribution..... 13

Figure 1-7: The Köhler curve shown to be a product of Raoult’s Law and the Kelvin effect..... 14
..... 17

Figure 1-8: The hygroscopic behaviour of a sodium chloride aerosol..... 17

Figure 1-9: Modelled aerosol hygroscopic curves calculated by E-AIM. 18

Figure 1-10: Concentration profile of a solution at a surface boundary 19

Figure 1-11: An image to depict a surfactant monomer, the transfer of surfactant monomers in the bulk to the surface and the desorption of a monomer away from the surface..... 22

Figure 1-12: Illustration of the three kinetic regimes that limits to mass transport to or within a droplet 27

Figure 1-13: A graph to show how the Knudsen number varies with particle diameter..... 28

Figure 1-14: A schematic of the interaction of light radiation with a particle..... 30

Figure 1-15: An illustration of the three size regimes for the treatment of light interacting with a particle. accounting for the size and wavelength es..... 31

Figure 1-16: Illustration showing the sources of terrestrial and arial sources of the reactants which contribute to the production of ozone	32
Figure 1-17: Distribution of light intensity around droplets of different radii.....	33
Figure 1-18: The lateral recentring a trapped and displaced aerosol droplet using a Guassian propagating beam.....	34
Figure 1-19: A method of recentring a droplet falling out of the beam along the direction os the propagated light.	35
Figure 2-1: The distribution of scientific published papers in 2016 according to world mapper	47
Figure 2-2: Images of the 2019 eight inspirational Bristol scientists and the awarding ceremony for the inspirational Bristol scientists in 2023	56
Figure 2-3: A structural overview of the ESPRC Aerosol CDT training program.....	57
Figure 2-4: Simplified depiction of the elements upholding coloniality for academics, non-academics, and students.....	59
Figure 2-5: The wheel of privilege showing the twenty identity types across seven categories	60
Figure 2-6: Three discussion scenarios for aerosol science-related decolonial workshop	61
Figure 2-7: The simplified decolonial framework to provoke critical reflection of the self and one’s course.	62
Figure 2-8: A lecture on the ‘Introduction to measuring aerosol particle distributions’ delivered by Dr. Ben Murray	64
Figure 2-9: Lecture from the CAS 2.6 module on the ‘Introduction to bioaerosols’ delivered by Ian Colbeck	65
Figure 2-10: The ILO 6 lecture on the Interactions of particles with the respiratory epithelium delivered by Terry Tetley	67
Figure 3-1: T Three modes of oscillation in a spherical droplet. Each mode, l, represents the lth spherical harmonic.	74
Figure 3-2: A top and side view schematic of the Droplet Oscillatory Method Instrument.	76

Figure 3-3: A top and side view schematic of the Droplet Oscillatory Method Instrument	77
Figure 3-4: The method of using droplet oscillatory method to determine surface tension.	79
Figure 3-5: A schematic of Holographic optical tweezers.....	80
Figure 3-6: The imaginary part of the refractive index for water against wavelength.....	81
Figure 3-7: Medical Nebuliser, NE-U22-E MicroAir Omron	82
Figure 3-8: Trapping cell showing the three separate components of the cell and the fully assembled trapping cell	83
Figure 3-9: Environmental control system. RH is achieved using the Mass Flow Controllers which enable the wet and dry flow ratios to be adjusted	84
Figure 3-10: A typical HOT experimental profile, showing how changing the RH impacts the droplet radius and refractive index.....	85
Figure 3-11: Example of brightfield imaging of a coalescing droplet imaged during an experiment.	86
Figure 3-12: Schematic of the trap position as a function of the kinoform pattern and droplet position	87
Figure 3-13: An example of a Raman spectrum of a levitated sucrose droplet.	89
Figure 3-14: An optically levitated sucrose droplet spectrum showing the spontaneous band and stimulated peaks indicated as either transverse electric or transverse magnetic	90
Figure 3-15: An illustration of the anti-Stokes, Raleigh, and Stokes scattering that occurs when an incoming light interacts or with a droplet..	91
Figure 3-16: The methods used to calculate aerosol droplet viscosity.....	93
Figure 3-17: The characteristic damping time for relaxation in the particle shape against viscosity ..	95
Figure 3-18: A picture to show the oscilloscope used to determine the damping time in the underdamped regime.....	95
Figure 3-19: An image of the top-view of the open Electrodynamic Balance (EDB).	96
Figure 3-20: An image of the side-view the open single particle electrodynamic balance (EDB)	97

Figure 3-21: Illustration of the calculated absolute value of the electric field in the cross-section of the modified electrodynamic trap	99
Figure 3-22: The EDB sizing system showing the reflected and refracted light from the illuminated droplet. In-phase interferences lead to the phase function pattern.	100
Figure 3-23: Primary photoinitiated processes and subsequent reactions during NO_3^- photolysis ...	101
Figure 3-24: Photographic pictures of the BP100 maximum bubble pressure tensiometer taken in the KRÜSS lab.....	103
Figure 3-26: An illustration of the Wilhelmy plate method.....	106
Figure 3-27: A method of determining the CMC by plotting the surfactant concentration against the equilibrium surface tension.....	107
Figure 4-1: The structures of the organic compounds used in this work	111
Figure 4-2: A snapshot of 1.2 M aqueous solution of ammonium chloride, sodium sulfate, and ammonium sulfate MD simulations along with their density profiles	112
Figure 4-3: A depiction of how the model treats the separate components in a multi-component solution.	117
Figure 4-4: Comparing the dynamic behaviour of water droplet with a binary solution of aqueous levulinic acid.....	120
Figure 4-5: The surface tension of the aqueous binary solutions of oxalic acid, malonic acid, pyruvic acid and levulinic acid.	122
Figure 4-6: Maximum surface concentration of oxalic acid, malonic acid, pyruvic acid and levulinic acid.....	123
Figure 4-7: Surface tension of ammonium sulfate measured using the droplet oscillatory method..	128
Figure 4-8: Surface tension of ammonium sulfate measurement compared to the surface tension given by E-AIM model at different temperatures ranging from 278.5-303.15 K.....	129
Figure 4-9: Surface tension of ammonium sulfate, oxalic acid, and the mixed aqueous ammonium sulfate:oxalic acid	1322

Figure 4-10: Surface tension of ammonium sulfate, malonic acid, and the mixed aqueous ammonium sulfate:malonic acid.	1333
Figure 4-11: Surface tension of ammonium sulfate, pyruvic acid, and the mixed aqueous ammonium sulfate:pyruvic acid.....	1344
Figure 4-12: Surface tension of ammonium sulfate, levulinic acid, and the mixed aqueous ammonium sulfate:levulinic acid.	1366
Figure 4-13: Surface tension as a function of the organic mole fraction for the systems oxalic acid, malonic acid, pyruvic acid and levulinic acid.....	1367
Figure 5-1: A schematic representing the sources of surfactant and the change in surface tension as the droplet grows and become an activated particle.	141
Figure 5-2: Short and long-time approximation fits to the DST collected data of Triton X-100	144
Figure 5-3: A An illustrative graph showing how the critical micelle concentration can be determined from fitting two regions on a surface tension against concentration plot	145
Figure 5-4: A depiction of the diffusion-controlled adsorption mechanism and the kinetic controlled mechanism.	146
Figure 5-5: A A depiction of a defined volume planar interface and a spherical droplet interface... ..	147
Figure 5-6: To show the different characteristic timescale regimes for planar diffusion, diffusion from inside the confined volume	149
Figure 5-7: The spherical characteristic timescale decreases with a decrease in droplet radius as diffusion becomes faster due to more surfactant molecules being near the surface of the droplet.....	150
Figure 5-8: The normalised depletion bulk effective concentration as a function of C_i	152
..... Error! Bookmark not defined.	
Figure 5-9: The macroscopic dynamic surface tension plotted against time collected using the MBT of SDS, Tween 20 and TX-100	157
Figure 5-10: Diffusion coefficient plotted against the diffusion coefficient type.....	158
Figure 5-11: The effective long time diffusion coefficient as a function of bulk concentration	159

Figure 5-12: The surface coverage as a function of the log C for the surfactants TX-100, SDS and Tween 20.....	161
Figure 5-13: Comparison of the Frumkin model and Langmuir-Szyskowski equation with experimental data taken using the Wilhelmy Plate for SDS, TX-100 and Tween-20	162
Figure 5-14: The log concentration of surfactants plotted against the equilibrium surface tension and the surfactant surface activity at the air water interface.....	164
Figure 5-15: The normalised effective bulk depletion concentration as a function of the initial bulk concentration.....	165
Figure 5-16: Characteristic timescale for diffusion of the surfactants to a spherical surface as a function of the normalised droplet radius.....	168
Figure 5-17: Droplet aspect ratio plotted against delay time and associated Lorentzian line fit. The data to the right of each vertical dotted line underwent a separate FFT and plotted with a Lorentzian fit	170
Figure 5-18: he droplet surface tension plotted against the delay time for SDS surfactant concentrations and the CMC of sodium dodecyl sulfate in aqueous solution.....	172
Figure 5-19: The droplet surface tension plotted against the time for TX-100 surfactant concentrations below and above CMC of Triton X-100 in aqueous solution..	173
Figure 5-20: The rate of surface tension change over given time duration plotted against surfactant concentration.....	174
Figure 5-21: The droplet surface tension plotted against the time for Tween 20 surfactant concentrations below and above the CMC of Tween 20 in aqueous solution.....	175
Figure 5-22: The normalised characteristic timescale for diffusion as a function of the droplet radius at a constant concentration of 20 mM.....	176
Figure 5-23: The rate of surface tension decay in a 150 μ s time duration plotted against droplet radius for each surfactant type at the concentration of 20 mM.....	177
Figure 5-24: The surface tension plotted against time for SDS, TX-100, and Tween 20 at a concentration of 20 mM between 30-55 μ m	178
Figure 5-25: A schematic to demonstrate the population of surfactant monomers at the droplet meniscus before dispensing from the microdispenser tip at difference frequencies.....	179

Figure 5-26: Surface tension plotted against delay time, at dispensing frequencies.....	180
Figure 5-27: Dynamic surface tension of droplet and bulk measurements plotted against time and fitted to the Hua-Rosen model.....	182
Figure 6-1: Impacts of particle viscosity on the time taken to achieve equilibration through gas-particle partitioning of water and the ability to form ice nucleating particles	186
Figure 6-2: The characteristic time of mass-transport and mixing by molecular diffusion in particles	188
Figure 6-3: The characteristic time of mass-transport and mixing by molecular diffusion in particles	191
Figure 6-4: alculuation of viscosity using aspect ratios corresponding to brightfield imaging of two coalescing droplets and the elastically backscattered light collected during the coalescence event...	194
Figure 6-5: Measured and modelled relative humidity dependent viscosity of sucrose/sodium nitrate mixture ⁶	197
Figure 6-6: The log(viscosity) plotted against the mass fraction of water and water activity for the ternary sucrose/sodium nitrate mixtures	198
Figure 6-7: Measured and modelled relative humidity dependent viscosity of sucrose/citric acid mixtures for binary sucrose and citric acid	199
Figure 6-8: The evaporation of a droplet under the RH 80 %, 60 %, 30 % with the UV-VIS light on and off	202

List of Tables

- Table 1-1:** Common adsorption isotherms and corresponding surface concentration equations. 24
- Table 2-1:** The nine postgraduate research competencies set 58
- Table 3-1:** Spectrograph diffraction gratings and the associated CCD spectral range and resolution. 88
- Table 4-1:** The chemical information of each compound used in this experiment..118
- Table 4-2:** The number of adsorbed molecules at the surface calculated alongside the parameter a and b from the experimental data using the Langmuir-Szyszkowski equation. 124
- Table 4-3:** The fitted parameters a and b from the Langmuir-Szyszkowski equation. 125
- Table 4-4:** The inverse activity coefficient β of various organic species and area per molecule, calculated from the Langmuir-Szyszkowski equation. 127
- Table 4-5:** The chemical composition of mixtures which have been used in the experiments. 130
- Table 4-6:** Setschenow constants calculated from AIOMFAC model with the salt concentrations used in this study. 131
- Table 5-2:** The chemical structures and details of the surfactants used in this study. 154
- Table 5-3:** The literature data of the effective diffusion coefficients of SDS, TX-100 and Tween 20. 159
- Table 5-4:** To show the calculated CMC, the maximum surface tension excess, area per molecule and KL, the ratio between k_{ads} and k_{des} 161
- Table 5-5** The spherical depletion length scale h_s in comparison to the droplet radii for each type of surfactant used in this study. 167
- Table 5-6:** The equilibrium surface tension of SDS, TX-100 and Tween 20. 171
- Table 5-7:** A table for the constants calculated from the fitting of the Hua-Rosen Approach to the experimental droplet and bulk dynamic surface tension data. 181

Chapter 1

Introduction

1.1 Overview of Aerosol

Aerosols ubiquitous in nature exist as colloidal dispersions of liquid or solid particles in the gaseous phase.² Aerosols arise from both naturally occurring sources such as sea spray, volcanoes, mineral dust, and anthropogenic sources which include combustion of fuels, industrial pollution, and human activities. Over the last century, growth in the study of aerosols has revealed their application in fields ranging from medicine delivery to the engineering of nanomaterials.^{3,4} Their considerable effect on air quality, climate and human health, for example increasing the prevalence of respiratory problems, has made their characterisation fundamental in the future of scientific research.

Aerosols, like many colloidal systems, are thermodynamically unstable due to their dispersed nature and high surface area-to-volume ratio when compared to their equivalent bulk phase. It is in fact more favourable for aerosols to sediment out of the air, aggregate or coagulate with other aerosols, however, these processes are counteracted by air currents, and the probability and success of collisions. They are therefore kinetically stabilised remaining in the atmosphere from anywhere between a few hours to a few days see Figure 1-1.

Primary and secondary are two classifications of atmospheric aerosol denoting their origin and formation processes. Primary aerosols are directly emitted from a source. Examples include emissions from biological materials, plants fragments, pollen and microorganisms, biomass burning, combustion of fuels and volcanic eruptions. Conversely, secondary aerosols are derived from *in situ* partitioning of low volatility gaseous compounds into particles often involving homogenous nucleation of gaseous pollutants and organic material. For example, secondary organic aerosols (SOAs) are formulated from transformation of volatile organic compounds (VOCs) such as monoterpenes and aromatic compounds by oxidation. The nucleation and growth of aerosols is affected by atmospheric conditions and particle properties such as surface tension and viscosity, both of which are important to understanding the environmental impact of aerosols.^{5,6}

The focus of this thesis is to conduct laboratory measurements on proxy atmospheric aerosols to deduce their properties which govern their growth into cloud condensation nuclei and to inform climate models

used to predict their behaviour. In this chapter, the motivation for investigating these properties and their impact on the Earth's climate will be described.

1.2 Atmospheric Aerosols: Size, Lifetime and Distribution

Atmospheric aerosols exist over a wide range of sizes from a few nanometres for newly formed particles to several hundred micrometres. Airborne particles are defined in three different size distributions corresponding to their diameter: *nucleation*, *accumulation* and *coarse* mode.⁷ Each mode has different lifetimes and removal processes within the atmosphere that dictate their impact on the climate. The nucleation mode accounts for newly formed particles produced from the nucleation of VOCs into the condensed droplet phase, covering diameters up to 0.1 μm . Though nucleation mode particles are the most prevalent in the atmosphere, they only make up a small percentage of the total mass and surface area due to their small size. Coagulation with larger particles and vapour condensation account for their short lifetimes < 1 hour, causing the particles to grow into the *accumulation mode*, see Figure 1-1.

Accumulation mode particles account for sizes between 0.1 to 1 μm and are generated from either nucleation mode particles or the emission of particles directly into the atmosphere due to combustion processes. Accumulation mode particles are slowly removed from the atmosphere due to their size and rate of particle diffusion resulting in long lifetimes when compared with the other two modes. This coupled with the fact that these particles constitute a large portion of the total aerosol mass and surface area, make this mode significant in atmospheric aerosol research. Both the nucleation mode and accumulation mode particles are defined as fine aerosols and account for the largest number of particle types in the atmosphere. Particles larger than approximately 1 μm fall into the coarse mode and are typically generated by mechanical processes, such as wave breaking that produces sea spray or quarrying activities. These particles are quickly removed from the atmosphere by sedimentation leading to their relatively short lifetimes.

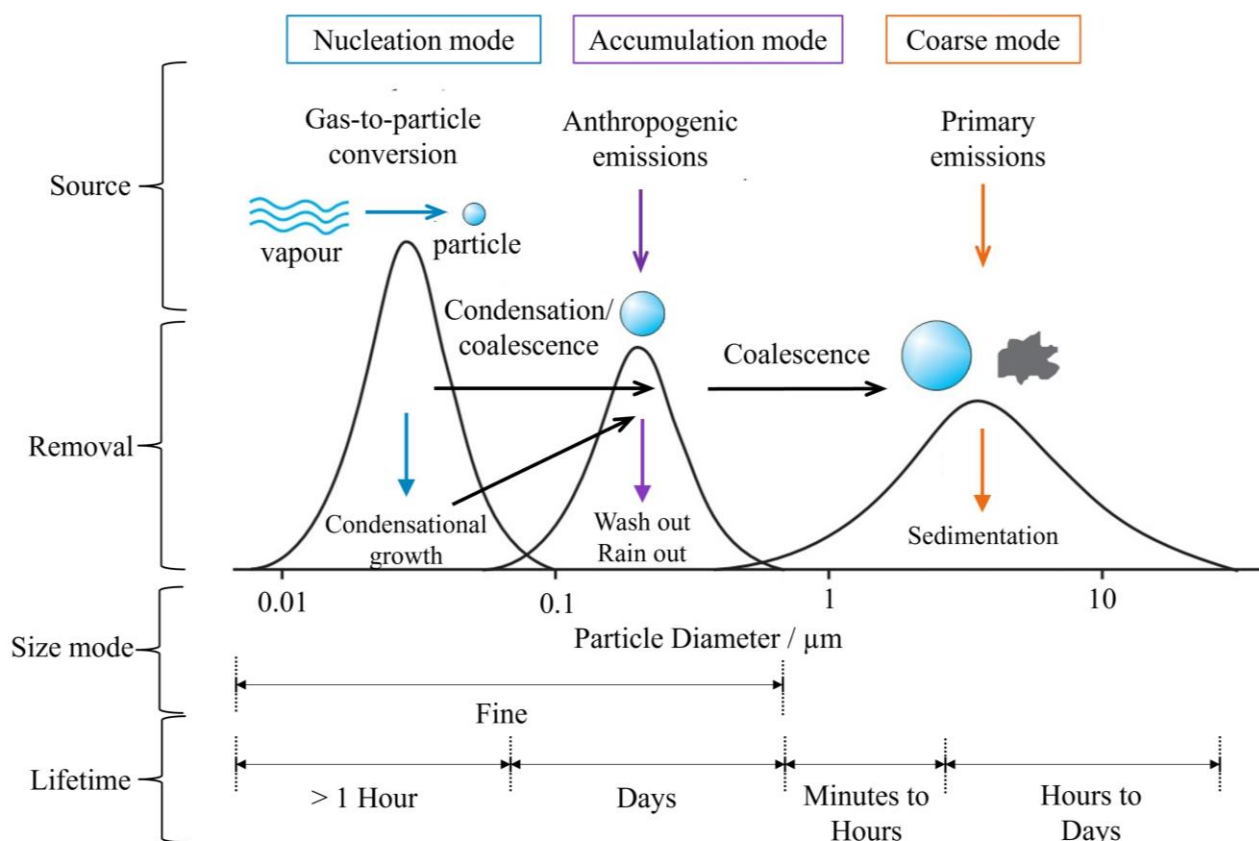


Figure 1-1: Schematic of the size distribution, with the sources, removal mechanisms and particle lifetimes indicated for each size mode. Based on the image from Seinfeld and Pandis.⁸

Particulate matter (PM) is often classified under the terms PM_{10} , $\text{PM}_{2.5}$, and PM_1 which relates to the particulate mass concentration of particles with diameters $< 10 \mu\text{m}$, $< 2.5 \mu\text{m}$, and $< 1 \mu\text{m}$, respectively. Aerosols that fall within the category of PM_1 are best described as ultra-fine particles. The size of these particles allows them to penetrate deep into the human respiratory system resulting in cardiovascular exposure and therefore the whole body becomes exposed rendering them a human health hazard.⁹

The source of aerosol emissions can lead to their different typologies, morphologies, and compositions varying between urban and rural sources within a country as well as a globally. For example, Africa is one of the world's largest sources of dust particles from the Sahara Desert and due to industrial regional growth produces approximately a third of global biomass burning particulates. Air quality-related fatalities are among the highest ranked causes of death in Africa, accounting for approximately 780,000 premature deaths a year.¹⁰ Understanding particle source and composition is therefore pertinent to mitigating the effects of aerosols on local communities.

1.3 Atmospheric Aerosols: Composition

Atmospheric aerosols are typically comprised of a complex mixture of compounds. A single population of aerosols can contain inorganic components including salts, trace metals, crustal materials, and organic species. A substantial fraction of the atmospheric fine particulate matter is composed of organic compounds, constituting approximately 20 – 90 % of aerosol mass in the lower troposphere.^{11,12} In the troposphere, single particle composition measurements have shown organic material to be internally mixed with inorganic species. Recordings at several sites reveal urban fine particle are composed of 28 % sulfate, 31 % organic carbon, 8 % ammonium, 9 % elemental carbon, and 6 % nitrate by weight.^{13,14} Figure 1-2 shows the global distributions of these components.

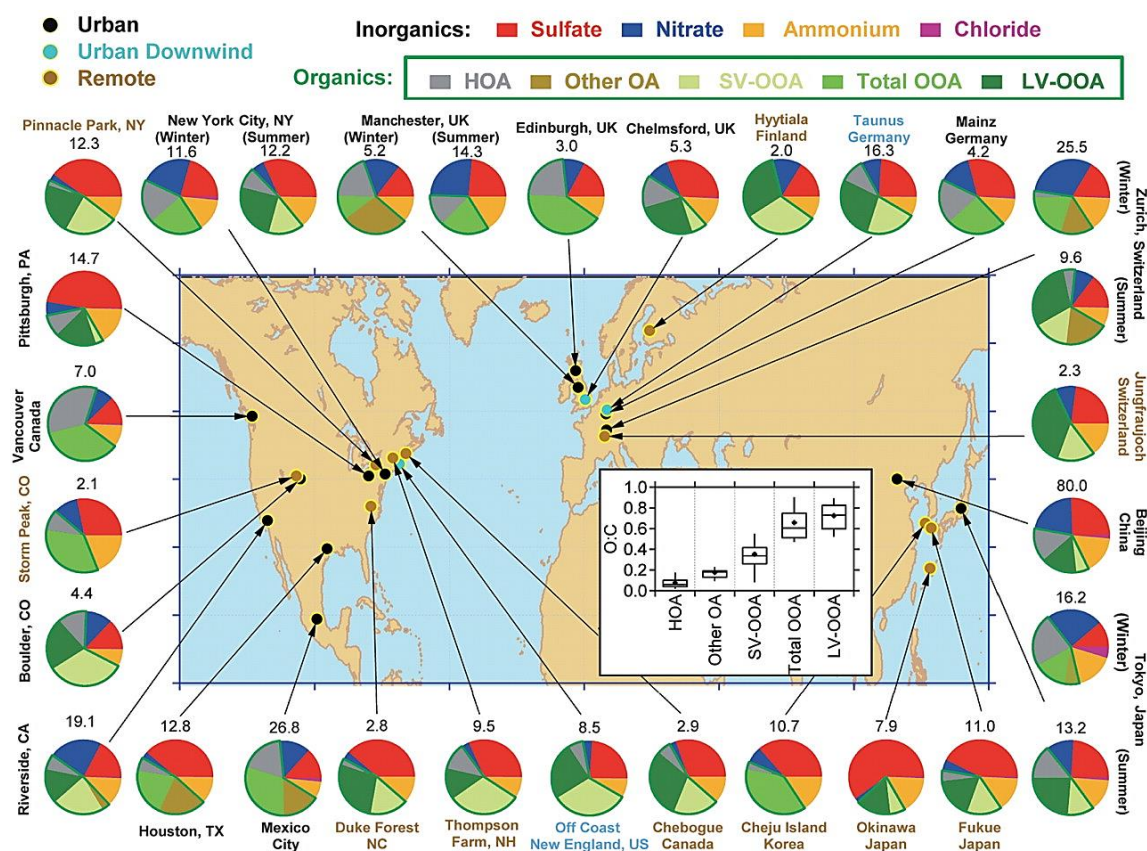


Figure 1-2: An illustrative map displaying the total mass concentration (in micrograms per cubic meter) and mass fractions of nonrefractory inorganic species along with organic components in submicrometre aerosols. These measurements were conducted with the AMS at multiple surface locations in the Northern Hemisphere. Image acquired from Jimenez et al.¹⁵

1.3.1 Organic Aerosols

The prevalence of aliphatic and aromatic organic acids both in the biosphere and troposphere renders them essential when climate modelling and in simulating the surface tension of real cloud and fog droplets.¹⁶ High solubility, small dicarboxylic acids and low volatility, long-chain fatty acids, are formed from chemical processes which include the reaction of ozone with olefinic organics and direct injection into the atmosphere by processes such as the breaking of air bubbles containing organic-rich coated particles at the surface of a natural body of water, respectively.¹⁷ According to Hsieh et al. the

Chapter 1- Introduction

most abundant of these acids is oxalic acid ($\sim 449.3 \text{ ng m}^{-3}$), followed by malic acid ($\sim 53 \text{ ng m}^{-3}$), maleic acid ($\sim 45.5 \text{ ng m}^{-3}$), succinic acid ($\sim 29.6 \text{ ng m}^{-3}$) and malonic acid (20.8 ng m^{-3}).¹⁸

Primary Organic Aerosol

The source of primary organic aerosol emissions, as discussed in Section 1.1, include fossil fuel burning, cooking and biomass burning, estimated to be ~ 10 to 30 TgC yr^{-1} . Between 1870 to 2000, Ito and Penner estimated the global emissions of fossil fuel and biofuel organic carbon has risen by a factor of 3, leading to changes in air quality, the chemical processing of oxidants and radiative forcing.^{19,20}

Secondary Organic Aerosol

Precursors to SOAs are both anthropogenic and biogenic compounds, whereby SOA growth has been observed from the oxidation of biogenic terpenoid compounds and anthropogenic aromatics such as toluene and xylene. SOA accounts for 70 percent of the organic carbon (OC) aerosol mass in the troposphere²¹ and therefore have a large impact on human health and climate.²² Isoprene, largely emitted from trees, is one of the most abundantly emitted VOC at $\sim 600 \text{ Tg yr}^{-1}$ and the largest contributor to the global secondary organic aerosol budget.²¹ As a precursor to SOA, isoprene derived products such as glycolaldehyde, glyoxal and methyglyoxal account for ~ 70 percent of the total global SOA. These substances exhibit a strong solubility in water and partition into cloud droplets. Within these droplets, they undergo additional oxidation by $\cdot\text{OH}$, forming low volatility organic acids such as glyoxylic, pyruvic acid and oxalic acids.²³ Since modelling frameworks, such as the Community Atmosphere Model (CAM3), have incorporated isoprene photooxidation and the subsequent production of stabilised Criegee intermediates, a significant step has been towards characterising the processes that impact SOA formation.^{12,24} This serves an example of the importance in characterising the properties and processes within atmospheric organic compounds.

The organic compounds that will be investigated in this thesis are sucrose, citric acid, malonic acid, oxalic acid, pyruvic acid and levulinic acid, all used as atmospheric proxy organic systems. Owing to their relatively low vapour pressures, carboxylic acids are expected to participate in nucleation of particles in the atmosphere. Their relevance will be discussed here briefly. Mkoma et al.²⁵ using ion chromatography, found samples collected in Tanzania contained a high abundance of oxalate and malonate ions in $\text{PM}_{2.5}$ measured aerosols along with pyruvate which was also present in high concentrations.²⁵ Research findings indicate that the particulate mass concentration of dicarboxylic acids tends to rise as the carbon number decreases, as observed in various studies.^{26,27,28,29} Consequently, oxalic acid emerges as the predominant dicarboxylic acid in particulate form composing around 50 % of the total atmospheric dicarboxylic acid compounds.^{30,31} Despite oxalic acid being found in higher abundance, malonic acid has been shown, in both experiment and theoretical results, to be a much more important and stronger acid at reducing the barrier to activation.³² Kawamura et al. found there was a

presence of water-soluble dicarboxylic acids (diacids) such as malonic (concentrations between $7.4 - 475 \text{ ng cm}^{-3}$) during the wheat burning season over the mountains tops in North China Plain.³³ Additionally, Zhang et al. reported how malonic acid plays a role in enhancing the intermolecular forces between sulfuric acid and ammonia at 218 K, promoting aerosol clustering, a step in the process of cloud formation.³⁴ Pyruvic acid (PA) commonly found in the atmosphere is an oxidative product of isoprene used in models as a proxy for alpha dicarbonyls.³⁵ The photodegradation of aqueous PA along the photodecarboxylation pathway was shown by Leemakers and Vesley to lead to the significant production of CO_2 which has a positive radiative forcing effect with acetoin being the major product of the reaction.³⁶ Kappes et al. observed the production of oligomers and additional surface active molecules during the actinic radiation of the aqueous PA droplets showing the acid's environmental importance.³⁷ Though not atmospherically significant, levulinic acid and its derivatives are highly useful as they are an easy and efficient alternative to the use of fossil fuel-based chemicals, helping to reduce the carbon foot of consumer products.³⁸ In this work citric acid (CA) and sucrose are used as proxies for atmospheric aerosol. CA serves as an established proxy for oxygenated organic material in the atmosphere, given its extensively researched thermodynamic characteristics, water diffusivity, and viscosity.³⁹ Sucrose is used as a proxy SOA compound and has been proven to be an effective means of modifying droplet viscosity.^{40,41} Both compounds are important for investigating the impact of relative humidity on viscosity and the subsequent dynamic behaviour within a droplet in this thesis.

1.3.2 Inorganic Salt and Organic Acid Mixtures

In varying proportions, mixtures of inorganic and organic compounds exist in tropospheric aerosols affecting the activation and growth into cloud condensation nuclei.⁴² Secondary inorganic aerosols (SIA) formed through the oxidation of sulfur dioxide and NO_x dominate the high particulate matter levels and haze events, strongly affecting hygroscopicity and aerosol acidity.⁶ Water soluble inorganic components such as ammonium sulfate and sodium chloride are the most common salts in the atmosphere and have been well characterised in their ability to affect the uptake of water. However, organic molecules and their mixtures with inorganic salts are less well understood due to the large array of organics that exist in the atmosphere.⁴³ Species within the organic fraction have either a high-water solubility and/or low volatility making them favourable for absorption by inorganic salts.⁴⁴

Commonly, organic solutes lower surface tension below that of pure water by adsorbing at the surface whereas inorganic salts remain within the interior of the particle due to attractive ion-water interactions which destabilise the water-water interactions leading to an increase in surface tension.⁴⁵ Mixed inorganic and organic aerosols influence particle growth in two main ways: the surface tension of the solution is higher than that of the pure organic compound or the presence of the inorganic salt enhances surface activity of the organic molecules furthering the surface tension depression.^{46,47} Cruz and Pandis found the water absorption of ammonium sulfate-organic and sodium chloride-organic particles to be enhanced in most systems studied by a factor of 2 to 3 with a high organic volume.⁴⁸ Conversely, despite

the film of organic surfactant decreasing the deliquescence point of the inorganic salt, Andrews and Larson observed that the hygroscopic behaviour of the salt was reduced along with the ability to adsorb water and subsequently grow into CCN.⁴⁹ In this regard, understanding the addition of the organic compounds previously outlined in Section 1.3.1 to the inorganic salt, ammonium sulfate, and the impact on surface tension and the activation barrier will be the focus of Chapter 4.

1.3.3 Atmospheric Surfactants

Through impacting the climate directly by the scattering of solar radiation and indirectly by serving as cloud condensation nuclei, aerosols have an effect on the Earth's hydrological systems and cloud radiative forcing.⁵⁰ The aerosol indirect effect, a theme that will be re-visited in Section 1.4, has one of the largest uncertainties in the terrestrial radiative forcing due to a lack of understanding in the aerosol-cloud interactions, aerosol populations, particle transport and water availability at a given supersaturation.^{50,51} The formation and growth of cloud droplets from the condensation of water onto particles is quantified by the Köhler equation, in which the surface tension of the particle is one of the key parameters in determining the critical activation point. A lower surface tension than that of pure water (72.8 mN m^{-1}) results in a decrease of the critical supersaturation activation barrier, S_c , where γ_w is the water activity coefficient, x_w denotes the mole fraction of water, M_w is the molar weight of water, σ_w is the surface tension of water, T is the temperature, ρ_w is the density of water and R is the gas constant, and r_c which describes the critical droplet radius. The barrier refers to the level of supersaturation required for a cloud condensation nucleus to initiate growth into a cloud droplet.

$$S_c = \gamma_w x_w \times \exp\left(\frac{2M_w \sigma_w}{RT \rho_w r_c}\right) \quad (1.01)$$

Surface-active agents (surfactants) alter surface tension. Surfactants are surface dwelling molecules commonly made up of a hydrophilic 'head' and a hydrophobic 'tail' though these can be interchangeable. In previous studies of surfactants in rainwater and atmospheric aerosols, it has been suggested their effect on cloud processes is negligible, too low in concentration to have an impact or assumed to be the surface tension of water, particularly in climate models. However, more recent research has found higher concentrations of surfactant may exist in smaller growing droplets, lowering the surface tension and increasing the number of cloud condensation nuclei by up to 30-50 %.^{52,53} Facchini et al. estimated a 30 % decrease in surface tension due to the presence of realistic concentrations of surfactants, leading to a 20 % increase in droplet number concentration.⁵⁴ This may lead to a prolonging of the cloud lifetime and enhancement of cloud albedo. Gerard et al. found surfactants in samples taken of $\text{PM}_{2.5}$ at the Baltic station in Sweden. Using the colorimetric technique, Gerard et al.⁵³ was able to identify surfactant concentrations of up to $27 \pm 6 \text{ mM}$ reducing the surface tension to $32 - 40 \text{ mN m}^{-1}$. When a surface tension depression due to the addition of surfactants is included in calculations of the indirect radiative effect, changes of up to 1 W m^{-2} are observed bringing

estimations closer to the predictions of aerosol cloud interaction radiative forcing.⁵⁵ Despite this evidence, it is important to not omit the effect of bulk-to-surface partitioning and the subsequent reduction in the hygroscopic water uptake when characterising the effect of surfactants on the growth of cloud droplets.

Not only do surfactants impact climate, but they can also cause damage to human health. Surfactants that have contaminated respirable particles have been found to destabilise the mucus membrane in the respiratory system leading to allergies and asthma.⁵⁶ Vejrurp and Wolkoff found surfactants can also reduce the surface tension in tear film leading to irritation of the eye.⁵⁷

There are a wide range of surfactants that exist in the atmosphere from a number of different sources. Biosurfactants derived from the secretion of bacteria from the aquatic systems are some of the strongest naturally occurring surfactants known. Surface active organics such as aromatic dicarboxylic and tricarboxylic acids have been detected in ambient aerosols along with humic-like substances (HULIS).⁵⁸ Samples of oxidised soot, biomass burning aerosol, and photochemically aged secondary aerosol have all shown the presence of HULIS, defined as surface active oxygenated oligomers or polycarboxylic acids, shown to reduce surface tension. Often Triton X-100, sodium dodecyl sulfate (SDS) and dimethyldioctadecylammonium bromide (DTAB) are used as proxy systems in laboratory studies of surfactants as they closely mimic the behaviour of biosurfactants, fatty acid sodium salts and ambient aerosol samples, respectively.⁵¹

1.4 Influence of Aerosols on the Climate

The chemical composition of the atmosphere determines the incident solar radiation that is reflected back into space, absorbed by solid, condensed, and gaseous phases, and propagates to the Earth's surface. The radiation that reaches the Earth's surface falls within the visible light region and is re-emitted in the form of blackbody radiation at the infra-red wavelengths. The first IPCC report in 1990 established the presence of agents such as greenhouse gases, tropospheric and stratospheric aerosols and volcanic eruptions which have led to the additional absorption of the infra-red radiation and global temperature increases.^{59,60} Subsequent reports have continued to present a comprehensive assessment of the climate system.⁶¹

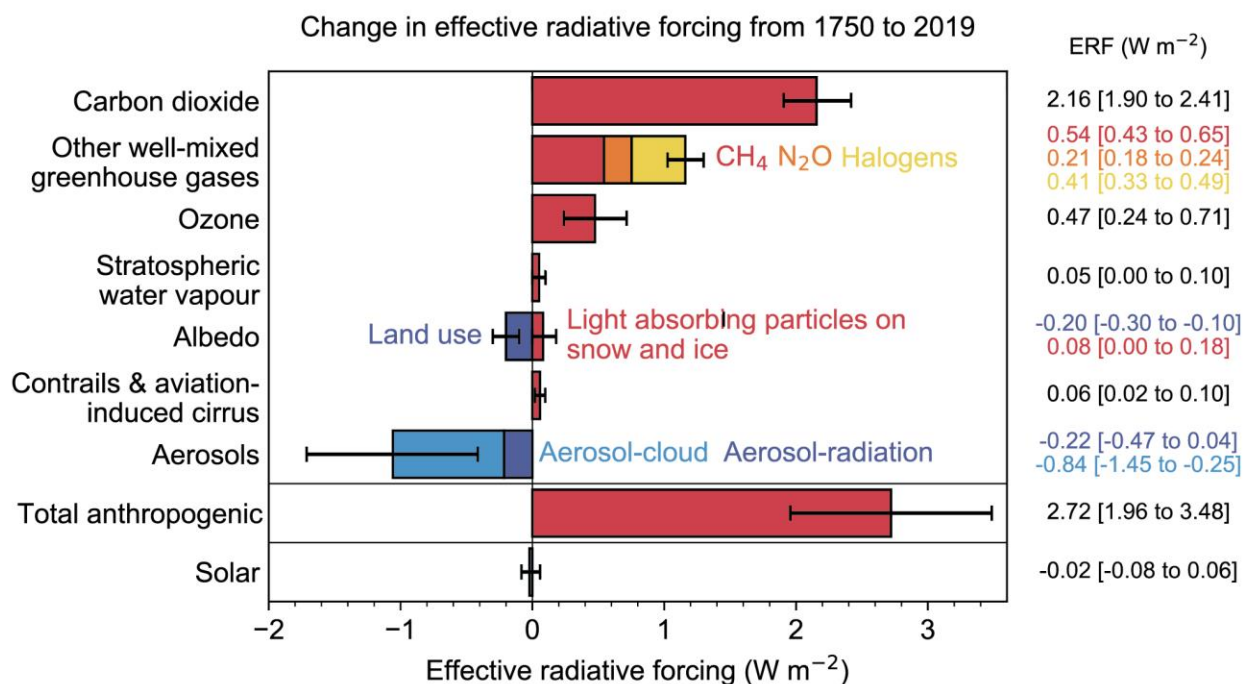


Figure 1-3: The Global mean radiative forcings (RF) for different atmospheric components that contribute to climate change in 2019 compared to 1750 from the IPCC 6th Assessment Report Technical Summary.⁶² The horizontal error bars represent the uncertainty in each RF. The effective relative humidity includes all tropospheric and land surface adjustments compared to RF which only includes an adjustment for stratospheric temperature change. **This image has been taken from the IPCC report of 2019⁶³**

1.4.1 Radiative forcing of the Earth's Atmosphere

Radiative forcing (RF) describes the net change in the Earth's energy balance due to external factors which alter the incoming solar radiation or outgoing planetary infrared radiation. It is typically expressed in $W m^{-2}$ averaged over a particular period of time.⁶⁴ The global RF in the context of climate change is often compared to pre-industrial atmospheric conditions when the atmosphere was unperturbed by human activity.

Anthropogenic aerosols are a major component in atmospheric radiative forcing due to their ability to scatter and absorb short as well as long wave radiation via either the direct or indirect effect. In comparison with the well-known effects of greenhouse gases such as CO₂ that have a net positive radiative forcing (warming) and a relatively small uncertainty, the uncertainty in the net cooling effect of aerosols remains rather large. Figure 1-3 shows the extent of this uncertainty, attributed to the high degree of non-uniformity of atmospheric aerosols and numerous ways they perturb incoming light radiation demonstrated in Figure 1-4.

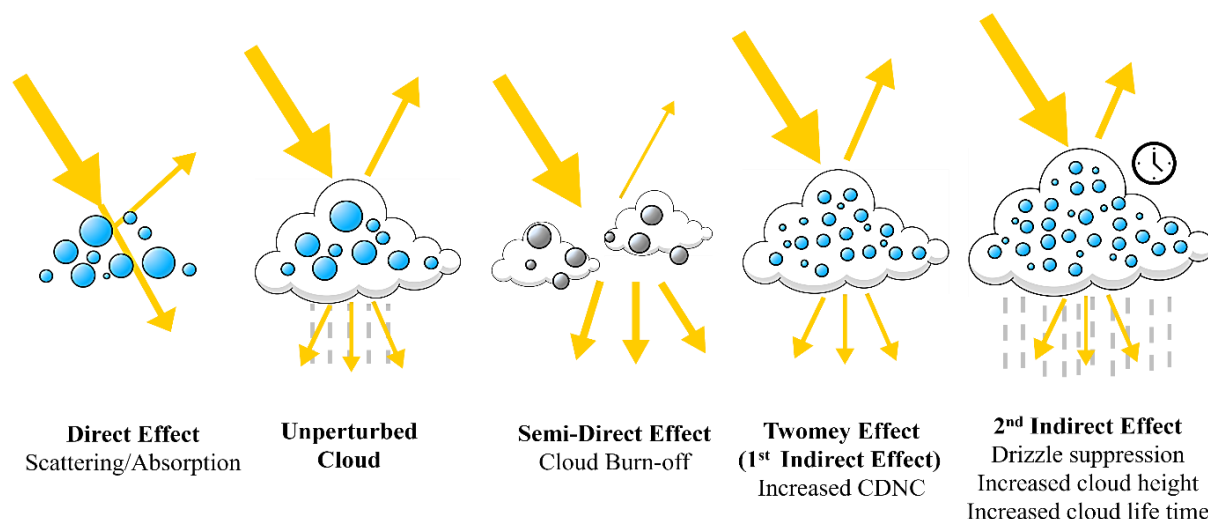


Figure 1-4: The processes which influence the scattering or absorption of light radiation by aerosols or clouds adapted from the IPCC's fourth assessment report. The yellow arrows represent the incident and reflected back solar radiation. The grey lines represent rainfall.

1.4.1 Cloud-Light Interactions

1.4.1.1 Cloud Albedo

The cloud albedo is a measure of the light radiation that is scattered back into space by a cloud. To understand, analyse and interpret the Earth's radiation budget, it is paramount to determine albedo. Albedo can vary over different parts of the Earth. For example, ocean surfaces and rain forests have low albedos, they reflect a small fraction of incoming solar light, whereas deserts, ice and clouds have higher albedos due to reflecting a greater portion of the sun's energy. Over the surface of the Earth approximately 30 % of the incoming solar radiation is reflected back into space as ice and clouds tend to be white, they are highly reflective whereas the sea is dark therefore highly absorbing of incoming solar radiation. Without clouds the Earth's albedo would drop from ~ 100 to $\sim 50 \text{ W/m}^2$ and the absorbed solar energy would increase from ~ 240 to $\sim 290 \text{ W/m}^2$ causing greater warming of the planet.⁶⁵ Clouds reflect more shortwave radiation than the surface beneath them therefore the higher the cloud albedo, the greater attenuation of solar radiation reaching the Earth's surface.

1.4.1.2 Cloud Radiative Effect

Clouds can also have a warming greenhouse effect on the planet by trapping longwave infra-red radiation at the top of the atmosphere. The effect is measured using satellite data to compare the upwelling radiation in cloudy and non-cloudy regions. In general the short wave radiative flux (-50 W/m^2) tends to be larger than the long wave radiative flux (30 W/m^2) and so clouds are said to have a net cooling effect on the planet.⁶⁶

1.4.1.3 The Direct Effect

Aerosol particles can either directly scatter or absorb electromagnetic radiation thereby perturbing the Earth's energy budget.^{67,68} The optical properties of an aerosol and the underlying surface of the Earth governs the extent at which these processes take place and negatively or positively exert on the radiative forcing. Scattering of radiation back into space results in a cooling effect while absorption leads to a warming effect.⁶⁹ Quantifying the relative magnitudes of these effect is important to determining the impact of aerosols on climate change. The normal and Bond albedo are useful metrics when assessing scattering potential of objects. Normal albedo is a measure of a surface's reflectivity when illuminated relative to its brightness. Typically, snow has an albedo of approximately 1. Bond albedo is a measure of the total radiation reflected from a planet when compared to the total incident radiation from the Sun. The Earth's bond albedo is estimated to be 0.301 ± 0.002 .⁷⁰ To counteract the impact of the doubling in global carbon dioxide levels due to industrialisation, a projected increase of 0.018 in the Bond albedo would be needed.⁷¹

An example of a direct effect can be observed by examining the sulfate aerosol which has been calculated to have a global mean radiative forcing in the range of -0.81 to -0.56 W m^{-2} .⁷² Depending on the region over which these measurements are taken, calculations of sulfate aerosol annual radiative forcing vary between over land compared to over sea (ratios varying between 1.25 to 3.54) as well as between hemispheres.^{73,74} This is attributed to the degree of reflectivity of the underlying surface decreasing planetary albedo and increasing net radiative forcing. A negative radiative is also exhibited in both mineral dust and nitrate aerosols due to their ability to scatter solar wavelengths.^{61,75} Absorbing aerosol, notably black carbon from biomass burning, have a global mean radiative forcing of $+0.2 \text{ W m}^{-2}$ estimated by Penner et al. for an external mixture.⁷² Studies have suggested higher global mean radiative forcing over July to August owing to higher concentrations of fossil black carbon from the Northern Hemisphere coupled with larger insolation leading to localised warming.

1.4.1.4 The Indirect Effect

Aerosols serve as the seeds of cloud droplets thus modifying the microphysical and radiative properties as well as the lifetime of the clouds. This is known as the indirect effect. At a particular liquid water content, an increase in the aerosol number concentration can either: increase the number of CCN activating into cloud droplets resulting in a decrease cloud droplet radii due to competition for water vapour and increase in cloud albedo or may cause a decrease in precipitation, increasing the water content of the cloud, cloud lifetime and cloud thickness.^{76,77,78} The former indirect effect or Twomey effect, leads to an increase in the droplet surface area which in turn increases the albedo of the cloud and its scattering of light rays.⁷⁹ The latter effect is described as the second indirect effect. The semi-indirect effect in clouds derives from localised heating from black carbon causing a decrease in water content resulting in cloud burn-off.^{80,81} Not all clouds have a net cooling effect. Measurements have shown in areas with high air traffic, soot deposits from aircrafts increase ice nucleation and the cloud

crystal number concentrations. These particles have a smaller mean crystal size which result in a net warming effect compared to liquid water droplet which have a net cooling effect. The model estimations have shown the increase in the radiative forcing to be of the order 0.3 W m^{-2} , under the assumption that there is a 20 % decrease in the mean crystal size in regions of dense air traffic.^{82,83}

Better quantification of the indirect effect will help to reduce the uncertainty found in the radiative forcing with improved understanding of the activation of aerosol droplets into cloud droplets. The activation of growing droplets is governed by the particle composition, hygroscopicity, surrounding atmospheric conditions and equilibrium droplet size.

1.5 Nucleation and Particle growth

Equilibrium droplet size is a key physical parameter in determining the CCN potential of an atmospheric aerosol droplet. The interplay between the partitioning of water and the concomitant droplet size adopted under certain atmospheric conditions such as the relative humidity (RH) is important to predicting their subsequent impact on climate. Herein, the role of aerosol thermodynamics in regulating the uptake of water will be discussed with the kinetics of droplet growth addressed in Chapter 3.

1.5.1 Partitioning of Water onto an Aerosol Droplet

As a major component of the atmosphere, water exists in both the gaseous and liquid phase. Atmospheric water content and particle composition determine the uptake of water as well as the particle phase behaviour, depending on the mixture of soluble and insoluble species in the aerosol particle. The RH (expressed as a percentage) is an appropriate metric to describe the amount of water vapour in parcel of air compared to the total amount of water vapour that can exist in the air at a given temperature, Eq. 1.2:

$$RH (\%) = \frac{p_w}{p_0} \times 100 \quad (1.02)$$

Where p_w describes the partial pressure of water vapour in the gas phase and p_0 denotes the saturation vapour pressure of water at any specified temperature. Fluctuations in ambient RH dictate the take up or loss of water by the particle in order to remain at thermodynamic equilibrium with the surroundings, illustrated in Figure 1-5. Typically, the global RH lies between 20 – 80 %, however Figure 1-6 shows regions around the equator that can reach $RH < 10 \%$ in regions within the Southern Hemisphere and more than 90 % in the upper regions of the Northern Hemisphere. Although RH denotes the water content of the surroundings, the extent at which water can be adsorbed onto a particle is governed by the hygroscopicity of the aerosol.

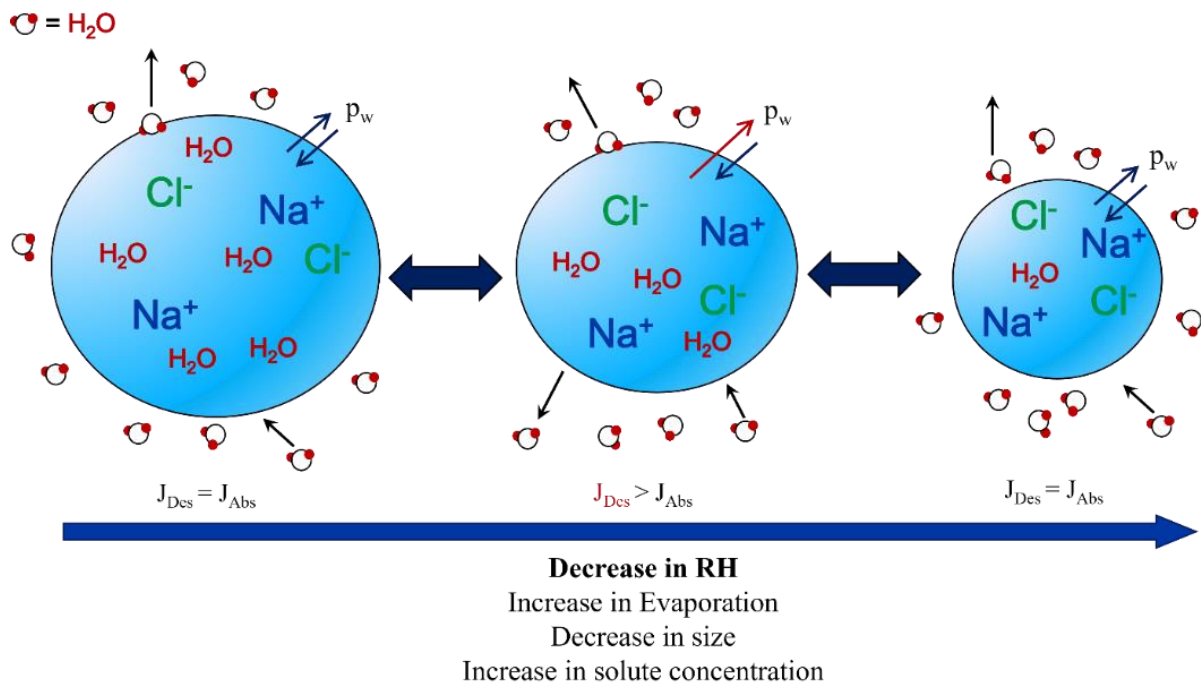


Figure 1-5: Illustration of the hygroscopic response of a sodium chloride droplet to a decrease in relative humidity. As the RH decreases, the mass flux of water (J) from the droplet increases such that equilibrium is re-established. The loss of water results in a decrease in droplet size and an increase in solute concentration. The process occurs in reverse when the RH is increased.

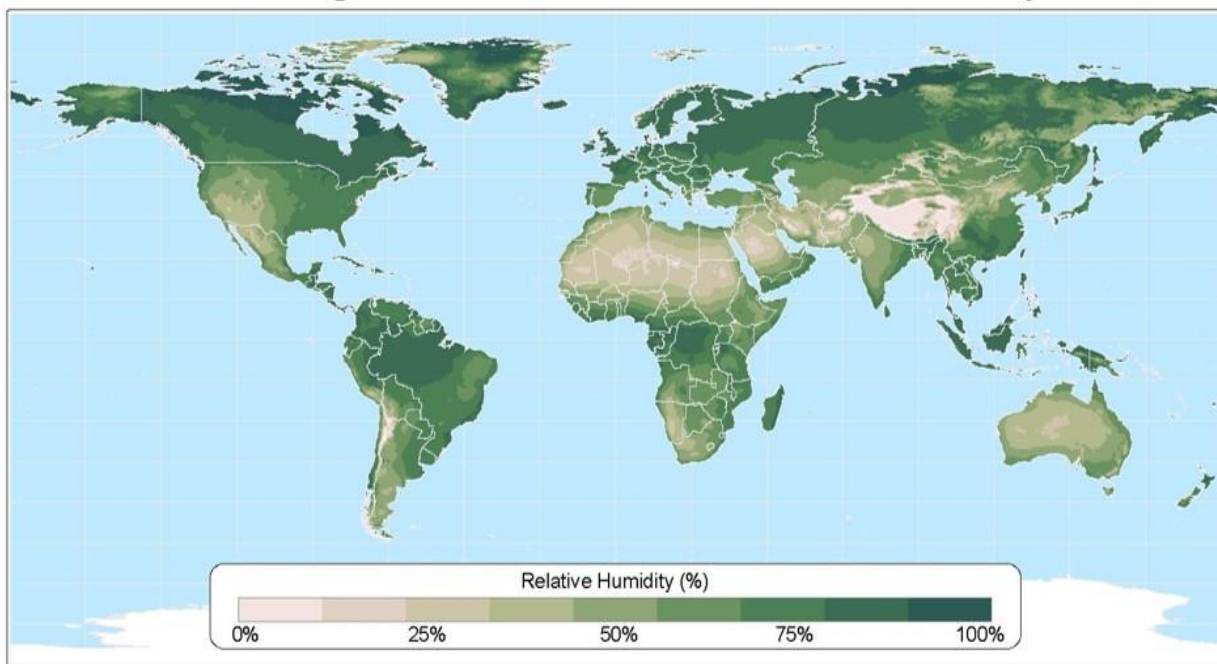


Figure 1-6: A picture of the global relative humidity distribution. This image was taken from the Climate Research Unit, Univ. of East Anglia.⁸⁴

1.5.2 Köhler Theory

By considering the vapour pressure above a particle surface, it is possible to understand the partitioning of water between the condensed and gaseous phase and hence the critical size of activation of the particle into a cloud droplet when $RH > 100\%$. It is important to characterise the equilibrium size, as at this point the partial pressure of water (p_w) for the particle must be equal to the partial pressure of water in the vapour phase, as described by Eq. 1.01.

Köhler theory is used to describe the interplay between the surface curvature of a droplet and the solute effect and shown in Figure 1-7. Within the equation there are two terms: the Kelvin effect, denoted the curvature term as it describes the vapour pressure relative to a flat surface, and the Raoult's term, denoted the solute effect as it describes the water activity of a solution relative to that of pure water.

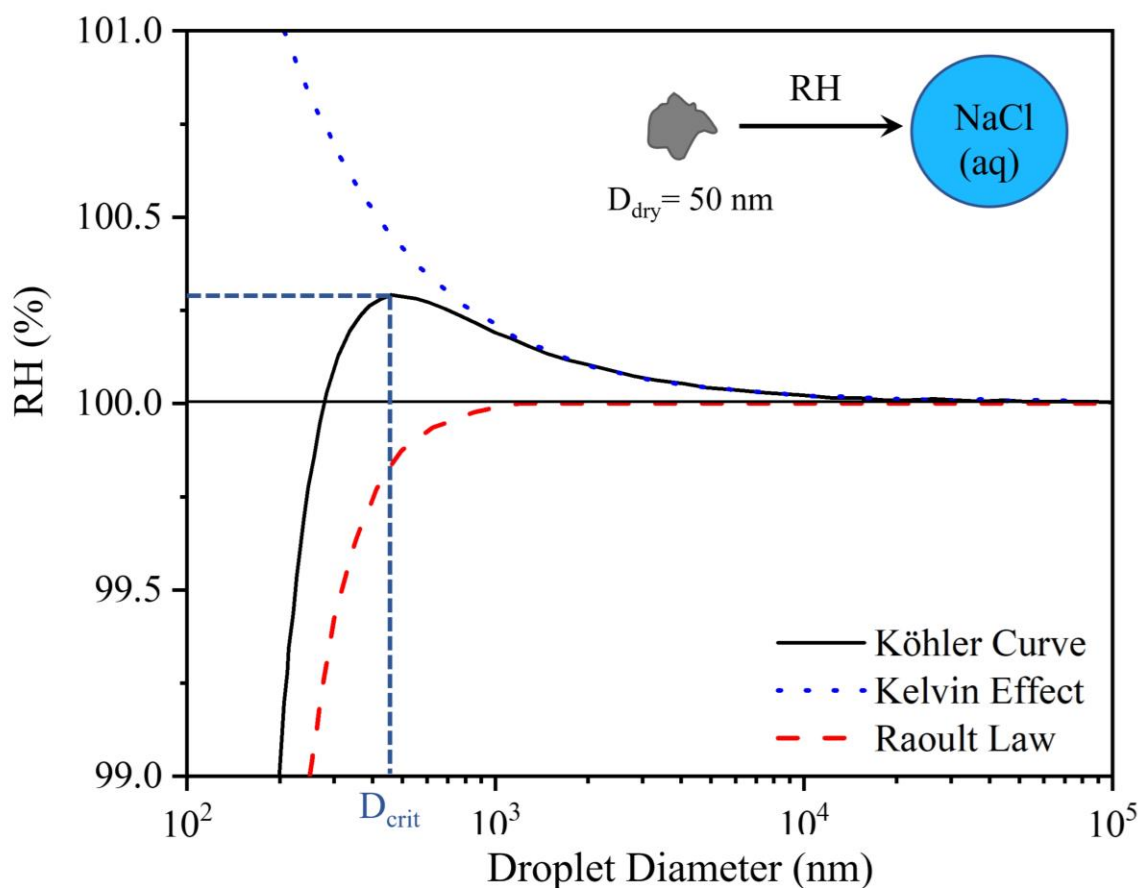


Figure 1-7: The Köhler curve (black line) shown here is the product of Raoult's Law (red, dashed line) and the Kelvin effect (blue, dotted line). The curve illustrates an aqueous sodium chloride droplet with a dry diameter of 50 nm. D_{crit} denotes the diameter of the droplet at activation at approximately 100.3 % RH.

To examine the Kelvin effect, it is appropriate to depict the effect on a single droplet of pure water and the interactions of the water molecules at the surface. A water molecule has fewer neighbouring water molecules on a curved surface and therefore has fewer stabilising intermolecular forces when compared to a flat surface. Due to fewer intermolecular forces, less energy is needed for a water molecule to

partition into the gas phase from the condensed phase. For this reason, a curved surface of a droplet has a higher vapour pressure above the surface than above a flat surface. This effect is represented by Eq. 1.3, where p_c represents the partial pressure of water above a curved surface, p_0 is the vapour pressure above a flat surface of pure water, M_w is the molar weight of water, σ_w is the surface tension of water, T is the temperature, ρ_w is the density of water and R is the gas constant. As the droplet radius decreases and the surface curvature correspondingly increases, the vapour pressure increases non-linearly as per Eq. 1.02, becoming particularly significant for $r < 50$ nm.

$$p_c = p_0 \times \exp\left(\frac{2M_w\sigma_w}{RT\rho_w r}\right) \quad (1.03)$$

Conversely, the presence of inorganic or organic solute acts to decrease the vapour pressure compared to a pure water droplet opposing the Kelvin effect. By introducing the solute particles, the mole fraction of water is reduced along with the vapour pressure of solvent (i.e., water) at the surface. First approximated by Raoult's Law, the solute effect is represented by Eq. 1.04 and 1.05.

$$p_w = a_w \times p_0 \quad (1.04)$$

$$a_w = \gamma_w x_w \quad (1.05)$$

With this in mind, Eq. 1.3 must be modified to encompass the presence of the solute within the droplet and solute-solvent interactions by considering water activity (a_w), water activity coefficient (γ_w) and the mole fraction of water (x_w). An aqueous aerosol particle is considered to be in a state of thermodynamic equilibrium with its surrounding environment when the water vapour pressure at the particle surface is in a state of equilibrium with the ambient relative humidity (RH) of the surrounding atmosphere. This state of equilibrium is achieved when the particle's radius remains constant over time, indicating that the particle is neither gaining nor losing mass.

The Köhler equation (Eq. 1.6) is a combination of these two effects:

$$\frac{RH}{100} = \frac{p}{p_0} = a_w \times \exp\left(\frac{2M_w\sigma_w}{RT\rho_w r}\right) \quad (1.6)$$

At low solute concentrations the water activity tends to one i.e., the water activity of pure water and the Köhler equation is dominated by the Kelvin effect. In the context of a large droplet radii where the surface curvature is significantly reduced, the exponential term tends to one and Eq. 1.6 is governed by the solute effect. At RH levels below 100 % and before the point of activated growth, an aqueous particle will assume a particular size corresponding to each specific RH value. When RH increases, more water partitions into the condensed phase, causing the particle's radius to increase. Upon reaching

a certain level of supersaturation ($RH > 100\%$), known as the critical supersaturation (S_c), the particle will continuously absorb water as long as the RH remains supersaturated. This process leads to the activation of the aerosol particle, transforming it into a cloud droplet. The radius of the particle at the critical supersaturation is referred to as the critical radius. Figure 1-7 shows at the critical radius, the Kelvin effect requires the RH to be supersaturated before the particle can activate. In accordance with Kohler theory, at activation, particles of smaller dry particle size (less solute mass) have a higher Kelvin effect and require an increased relative humidity in the surroundings in order to activate.

The hygroscopic nature of an aerosol particle impacts the critical supersaturation needed for activation. The greater the hygroscopicity of a droplet, the lower the critical supersaturation necessary for that droplet to activate.

1.5.3 Hygroscopicity and Growth Factor

Hygroscopicity is a measure of the capacity of a particle to take up water from the surrounding gas phase. The impact of aerosol hygroscopicity on public health is profound; once inhaled, aerosol droplets growth within the respiratory system affects the penetration depth within the lung.⁸⁵ Additionally, hygroscopicity influences the climate by directly impacting the radiative balance of the atmosphere. By controlling droplet size, hygroscopic growth along with refractive index affects the aerosol absorption cross-section and the ability to scatter light radiation.⁸⁶ In the literature, the hygroscopicity of an aerosol has been represented in terms of radial growth factor (GF_r) which is a ratio between the wet particle radius (r_{wet}) and the dry particle radius (r_{dry}), shown in Eq. 1.07.

$$GF_r = \frac{r_{wet}}{r_{dry}} \quad (1.07)$$

Figure 1-8 shows how the size and the physical state of a sodium chloride particle changes as a function of RH. At a low RH, the sodium chloride exists as a crystal. As the ambient RH increases, the radial growth factor remains at 1 which means the droplet size is equal to that of a dry droplet, until the deliquescence RH (DRH) is reached. In this instance, the solid particle begins to spontaneously take up water inducing a phase change from a solid to a dissolved particle, forming an aqueous droplet. Further increase in RH results in an increase in droplet size and a decrease in solute concentration. Conversely, lowering the RH causes a loss of water from the droplet, a decrease in size and an increase in droplet solute concentration as it equilibrates with the surrounding RH. At this point, the droplet becomes supersaturated with respect to the solute reaching a metastable state that cannot be achieved in the bulk due to the lack of nucleation sites within the liquid particle. The droplet will continue to lose water until a critical supersaturation point called the efflorescence RH (ERH) where the remaining water is lost, and the droplet becomes a solid. This cycle is known as a hysteresis and is indicated in Figure 1-8 by the red lines. Within this region highlighted in red, the particle can exist as a solid, semi-solid (inclusions, core shell) or a liquid.

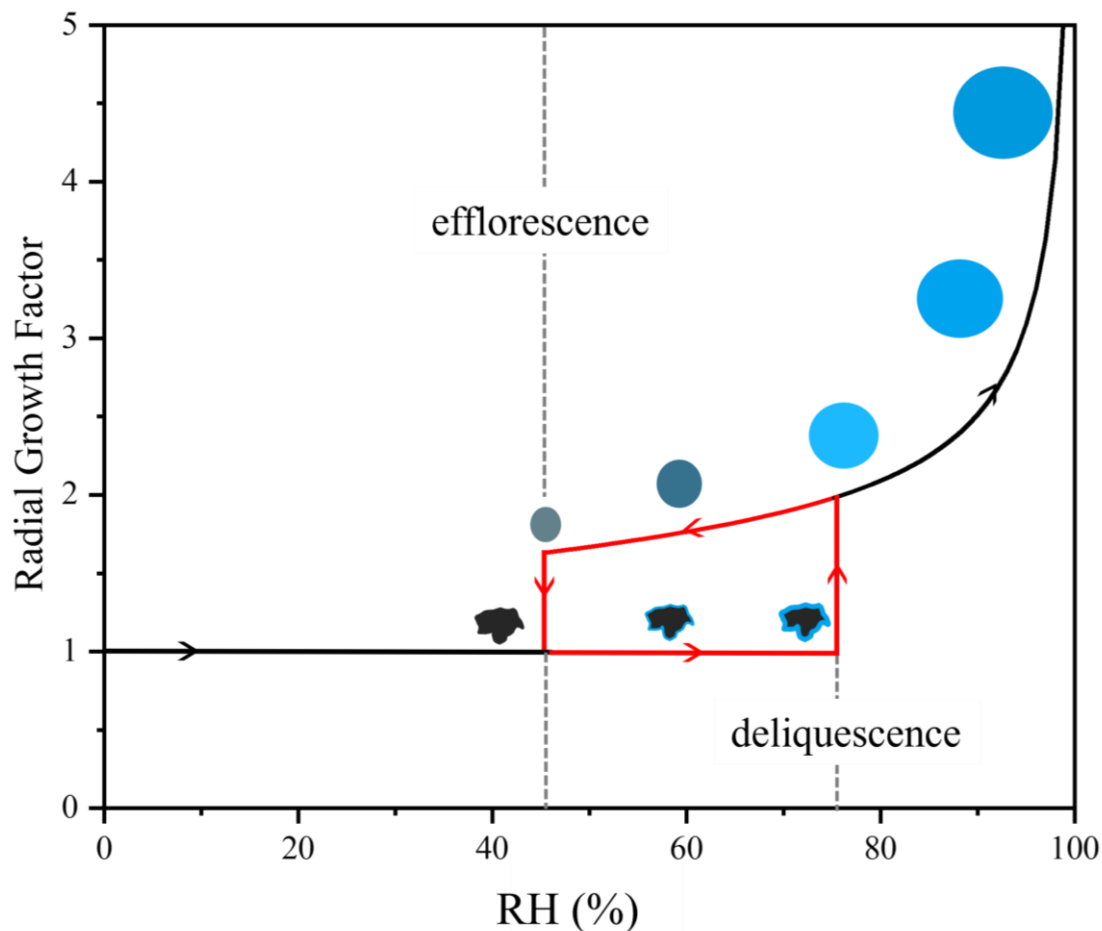


Figure 1-8: The hygroscopic behaviour of a sodium chloride particles as the RH increases and decreases. The extended aerosol inorganics model (E-AIM) was used to predict the variation of the radial growth factor as a function of RH (%).

The hysteresis cycle in Figure 1-8 is common for most inorganic aerosol single component particles. Figure 1-9 shows models for three different single component inorganic aerosols, sodium chloride, ammonium sulfate and sodium nitrate. As the RH increases, the size of the droplet increases along with the sensitivity to a small change in RH. Sodium chloride is the most hygroscopic of the three compounds adopting the larger of the equilibrium sizes. The partitioning of water between the gas and condensed droplet phase is best described by Köhler theory which considers the importance of solution thermodynamics and surface curvature when calculating the equilibrium droplet size.

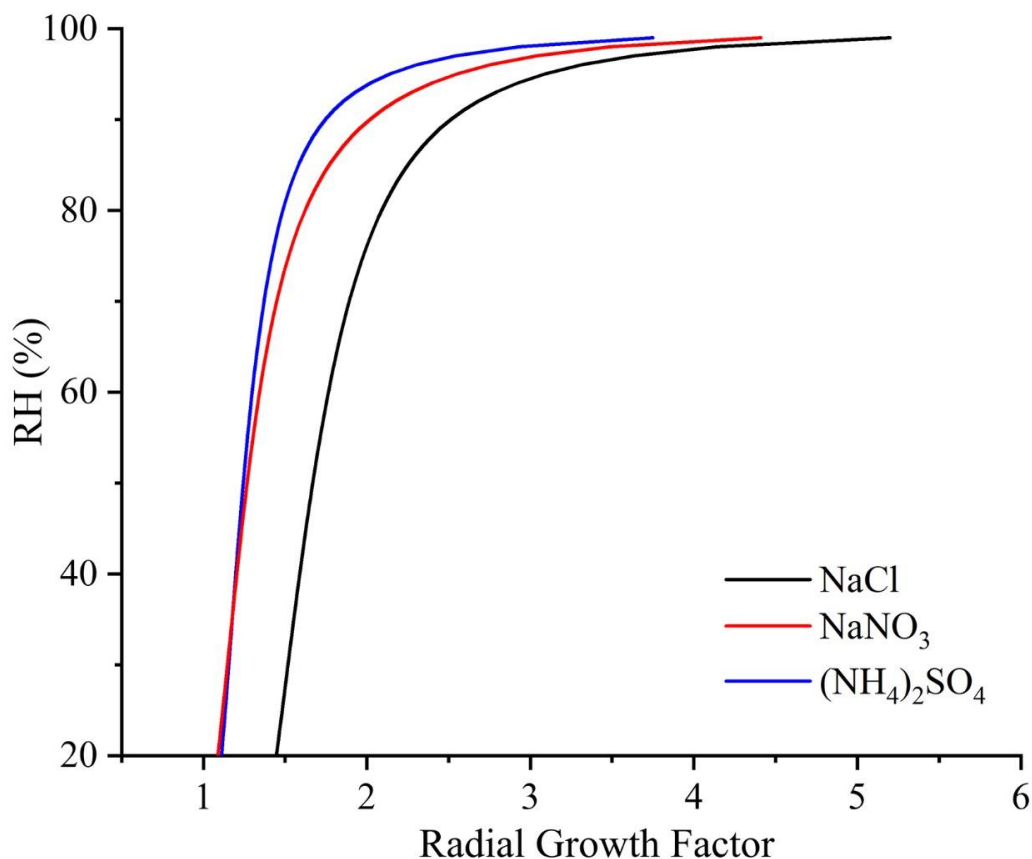


Figure 1-9: Modelled aerosol hygroscopic curves from E-AIM. The black line is sodium chloride the most hygroscopic; red is sodium nitrate and blue is ammonium sulfate.

1.5.4 Surface Tension and surface concentration

Surface tension, a property describing the behaviour of fluids at interfaces such as the surface of a liquid in contact with air, can be derived from the Young-Laplace equation. The equation, $\Delta E = \sigma \Delta A$, relates the change in surface energy (ΔE) and area ΔA to the surface tension (σ). Using this, surface tension is defined as the ratio of the change in the surface energy of a liquid to the surface area of the liquid that resulted in the change in energy.

1.5.4.1 Defining Gibbs Dividing Surface

In a real system as shown in Figure 1-10, the surface is defined as the phase between two continuous phases α and β . For the purposes of this explanation, α is the gaseous phase and β is the liquid water phase (solvent). The concentration of liquid water changes as a function of distance from the bulk of the β phase to the α phase and the surface phase as indicated in Figure 1-10 will have a given thickness. In the Gibbs dividing surface model, the surface phase is defined as a plane such that the properties of the β and α phase stay constant up until the plane is reached. The Gibbs dividing surface is treated as infinitely thin and therefore has no volume.

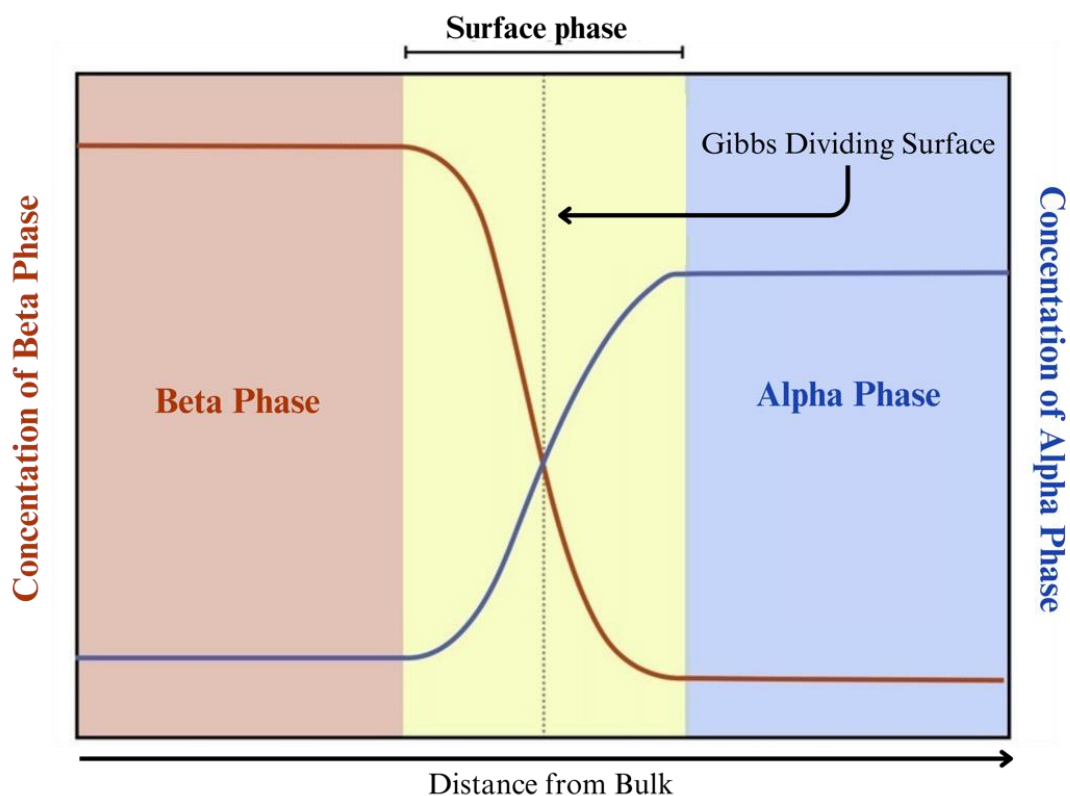


Figure 1-10: Concentration profile of solution denoted beta phase, the surface phase and the vapour (air) denoted alpha phase. The point at which the concentration of the beta phase rapidly decreases as the alpha increases indicates the surface layer.

1.5.4.2 Gibbs Isotherm

The Gibbs Isotherm is a crucial method for modelling surface tension and excess, especially when introducing organic or inorganic compounds into a solvent such as water. Eq. 1.09 shows the differentiated Gibbs energy equation for a system, where S is the entropy, T is the temperature, V is the volume, p denotes the pressure, n_i is the excess number of moles at the surface, μ_i is the chemical potential of component i , A is the area and σ describes the surface tension:

$$G = \sum \mu_i n_i + \sigma A \quad (1.08)$$

$$dG = -SdT + Vdp + \sum \mu_i dn_i + \sigma dA \quad (1.09)$$

Note, the term $+\sigma dA$ shows that when the surface area is increased, for example when creating a droplet surface, the Gibbs free energy of the surface increases illustrating how it costs the system energy to create the surface.

Defining surface concentration

In this section, the part of the Gibbs energy equation due to the Gibbs dividing surface will be discussed and the term γ used as reference to the surface. As mentioned in Section 1.5.4.1. the dividing surface has no volume therefore the Vdp tends to zero and can be removed from Eq. 1.09 when characterising the surface boundary and written as Eq. 1.10. Taking the differential of Eq. 1.08 gives the Eq. 1.11:

$$dG^\gamma = -S^\gamma dT + \sum \mu_i dn_i^\gamma + \sigma dA \quad (1.10)$$

$$dG^\gamma = \sum \mu_i dn_i^\gamma + \sum n_i^\gamma d\mu_i + \sigma dA + Ad\sigma \quad (1.11)$$

Both Eq. 1.10 and 1.11 describe the change in the Gibbs energy of the Gibbs dividing surface at the interface therefore Eq. 1.10 is equal to Eq. 1.11. A new equation can be subsequently written:

$$-S^\gamma dT + \sum n_i^\gamma d\mu_i + Ad\sigma \quad (1.12)$$

Rearrange Eq. 1.12:

$$-Ad\sigma = S^\gamma dT + \sum n_i^\gamma d\mu_i \quad (1.13)$$

As the system is isothermal, the $S^\gamma dT$ becomes zero and the equation is written as Eq 1.14 solving for the change in surface:

$$d\sigma = - \frac{\sum n_i^\gamma d\mu_i}{A} \quad (1.14)$$

Within a system with two chemical components such as water (component 1) and an organic compound (component 2), hence the equation becomes:

$$d\sigma = - \left(\frac{n_1^\gamma d\mu_1}{A} + \frac{n_2^\gamma d\mu_2}{A} \right) \quad (1.15)$$

The surface concentration is described by Γ_i and relates to n_i^γ/A . To note, the maximum surface excess concentration is defined as Γ_{max} , and the surface excess concentration of surfactant at equilibrium is

defined as Γ_{eq} . Equ.1.15 can therefore be written as Eq. 1.16, if the convention of the solvent surface concentration is zero at the surface:

$$d\sigma = -\Gamma_2 d\mu_2 \quad (1.16)$$

If:

$$\mu_2 = \mu_2^\circ + RT \ln a_2 \quad (1.17)$$

Where a_2 is the activity of component 2 at the surface, where for an ideal solution activity is equal to the unitless concentration (C_i) of component 2, R is the gas constant and μ_2° is the standard state chemical potential of component 2. By differentiating Eq.1.17 and inserting into Eq. 1.16, the following equations is derived:

$$d\sigma = -\Gamma_2 RT d(\ln C) \quad (1.18)$$

$$\frac{d\sigma}{d(\ln C)} = -\Gamma_2 RT \quad (1.19)$$

Eq. 1.19 is the mathematical expression for the Gibbs adsorption isotherm.

In the presence of a surfactant, upon stretching the surface by creating a new drop or by the formation of an air bubble in a liquid, there is a reduction in the amount of surfactant at the surface ($\Gamma < \Gamma_{eq}$) where Γ is defined at the surface excess concentration, which results in an increase in adsorption to re-establish the equilibrium between the bulk concentration, C_{bulk} , and surface excess concentration, Γ ($j_{ads} > j_{des}$).⁸⁷ This equilibrium state, where $j_{ads} = j_{des}$, reflects the balance between the unfavourable entropic cost of adsorbing to the surface and the favourable enthalpy change. The change in surface excess concentration over time is described by Eq. 1.20.⁸⁸

$$\frac{d\Gamma}{dt} = j_{ads} - j_{des} \quad (1.20)$$

Where Γ_{eq} is the surface excess concentration of a surfactant at equilibrium, j_{ads} describes the adsorbing flux and j_{des} denotes the desorbing flux. Due to the presence of a hydrophobic surfactant tail, increasing the bulk concentration leads to an increase in unfavourable interactions between the solvent and the surfactant 'tails' such that adsorption is favoured, thus a monolayer of surface is formed.

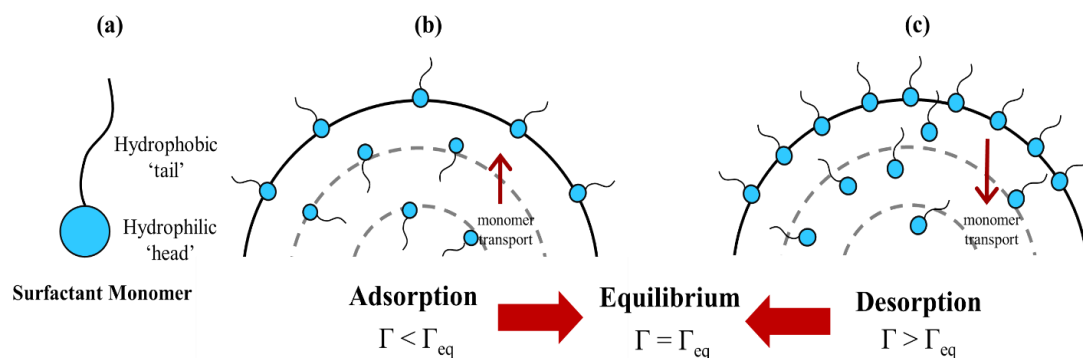


Figure 1-11: An image to depict (a) a surfactant monomer (b) the transfer of surfactant monomers in the bulk to the surface for adsorption to re-establish the equilibrium and (c) the desorption of a monomer away from the surface to re-establish equilibrium.

1.5.4.3 Theoretical Adsorption Isotherms

An adsorption isotherm is the graphical representation of the relationship between bulk and adsorbed surface excess concentration of surfactant monomers. The isotherm describes the equilibrium distribution of the adsorbing molecule on the liquid surface at a given temperature and can be used to predict key surface properties such as the surface excess concentration, the surface area occupied per molecule and the rate of adsorption and desorption on the surface.

Henry Isotherm

The Henry isotherm is the simplest isotherm (Eq. 1.21) where K_H is the equilibrium constant that reflects the surface activity of the surfactant. This isotherm remains valid at low surfactant concentrations, i.e., when $C_{bulk} \rightarrow 0$, as it operates on the assumption that no interactions occur between the adsorbed monomers and that there is no defined limit of Γ .

$$\Gamma = K_H C \quad (1.21)$$

Langmuir Isotherm

The Langmuir isotherm is a model comprises of four assumptions:

1. each adsorption site on the lattice is equal.
2. the likelihood for a molecule to be able to adsorb at an empty site is not dependent on the vacancy of a neighbouring site.
3. there is no presence of interactions between monomers within the lattice or intermolecular forces between monomers at the surface.
4. adsorption is limited to a monolayer.

The rate at which surfactant molecules occupy the surface is dependent on the bulk surfactant concentration and the number of available sites to occupy at the interface (Eq. 1.22). Eastoe et al.

suggests that as the surface excess concentration increases, the adsorption enthalpy becomes more positive implying that the more energetically favourable sites are occupied first.⁸⁷

$$\frac{d\Gamma}{dt} = k_a C \Gamma_{max} \left(1 - \frac{\Gamma}{\Gamma_{max}}\right) \quad (1.22)$$

In Eq. 1.22, k_a is the rate of adsorption, C denotes the surfactant concentration and Γ_{max} is the maximum surface excess concentration. The change in Γ is dependent on both adsorption and desorption of monomers from the interface (see Eq. 1.23), with the number of molecules desorbing proportional to the number of molecules adsorbing. The ratio of the adsorption and desorption rates is denoted in the Langmuir equilibrium adsorption constant $K_L = k_a/k_d$ used in the Langmuir isotherm Eq. 1.23.

$$\frac{d\Gamma}{dt} = k_d \Gamma \quad (1.23)$$

The Langmuir isotherm, Eq. 1.24, has a good fitting quality when compared to alternative two-parameter, monolayer adsorption isotherm models such as Freundlich, Dubinin-Radushkevich and Temkin which are beyond the scope of this work:

$$\Gamma = \Gamma_{eq} \left(\frac{K_L \cdot C}{1 + K_L \cdot C} \right) \quad (1.24)$$

Frumkin Isotherm

The Frumkin isotherm follows on from the Langmuir isotherm with the inclusion of non-ideal solute-solvent interactions and adsorbed monomer interactions at the surface. It allows time-dependent coverage of the surface, $\Gamma_i(t)$, to be related to the sub-surface concentration $C_i(t)$, and therefore has been used to study many systems. Of note, the Frumkin isotherm best describes non-ionic surfactants and surfactants at an oil-water interface well and is given by⁸⁹:

$$C(t) = A_{L,i} \frac{\theta_i}{1 - \theta_i(t)} \exp[K_i \theta_i(t)] \quad (1.25)$$

Where i denotes the adsorbed species, $\theta_i(t) = \Gamma_i(t)/\Gamma_{i,max}$ is the fraction of surface coverage of the surface-active species, i at a given interface time, t , and $\Gamma_{i,max}$ represents the maximum surface excess concentration of substance i . The dissociation constant, $A_{L,i}$ captures the propensity of the surface-active species to adhere to the interface, while the parameter, K_i which depends on the non-ideality of the surface layer accounts for the interactions between the surface molecules within the interface relative to the thermal energy, $k_B T$.⁸⁹ In this work, Eq. 1.27 is used to calculate K_L and the maximum surface excess concentration using a non-linear regression process.

$$\Pi = \sigma^0 - \sigma \quad (1.26)$$

$$\Pi = -nRT\Gamma_{max} \ln \left(1 + \left(\frac{K_L \cdot C}{1 + K_L \cdot C} \right) \right) \quad (1.27)$$

where $n=1$ for non-ionic surfactants, neutral molecules or ionic surfactants in the presence of excess electrolyte and $n=2$ for 1:1 ionic surfactants assuming electrical neutrality of the surface.⁸⁷ Here, R is the gas constant ($\text{J K}^{-1} \text{mol}^{-1}$) and T is the temperature in Kelvin. Table 1-1 presents a summary of other surface isotherms used in the study of surfactant dynamics depending on their assumptions and parameters. The Langmuir isotherm is chosen due to its ability to accurately describe the behaviour of surfactants up to a well-defined monolayer on the surface often at low solute concentrations. When a multilayer occurs, the surface excess concentration data begins to exceed values predicted by the Langmuir isotherm and deviates from the linear relationship between the surfactant concentration and surface excess concentration. Another model is therefore required to represent data more accurately. The Frumkin model can be used to describe the multilayer the aggregation of surfactant molecules at the surface. Both describe the equilibrium surface tension well over the range of surfactant concentrations used in this study (10^{-4} to 10^2 mM). The Volmer model is described for completeness as it is not typically used according to Eastoe et al.⁸⁷

Table 1-1: Common adsorption isotherms and corresponding surface concentration equations. In the Freundlich isotherm both k and n are constants. In the Volmer isotherm K is a constant with units of concentration, Γ_{max} is defined at the maximum surface excess concentration and Γ the surface excess concentration.

Isotherm	Description	Γ
Henry	Based on ideal solution	$K_H C$
Freundlich	Empirically derived	$kC^{1/n}$
Volmer	Accounts for non-ideal, non-localised adsorptions for a finite molecule size	$\frac{\Gamma_{max} K C}{\exp \left[\frac{\Gamma}{\Gamma_{max} - \Gamma} \right] + K C}$

The formation of a surfactant monolayer at a surface can be characterised by ideal behaviour isotherms akin to the Langmuir equation. However, surfactants can often display non-ideal behaviour such as aggregation, competitive adsorption at the surface or electrostatic interactions. Competitive adsorption occurs in complex systems containing different surfactants or other active interfacial species (e.g., organic acids, polymers). Where surfactants can carry charges that interact with ions at the surface, electrostatic charges may affect the adsorption deviating from ideal behaviour. The surface activity of a component model can provide another method of characterising the surfactant behaviour against concentration for non-ideal behaviour.⁹⁰ The surface activity is important to describe due its role in

defining the chemical potential of surfactants at a surface. The chemical potential is a measure of energy required to add one additional surfactant molecule to a system⁹¹. The surfactant composition, bulk phase, molar surface area and surface tension of any given component are the determining factors for the chemical potential within the surface layer. The well-known relation in Eq. 1.28 defines the dependence chemical potential, μ_i^s , on these factors:

$$\mu_i^s = \mu_i^{0,s}(T, P, \sigma) + RT \ln(a_i^s x_i^s) \quad (1.28)$$

the superscript 's' denotes the surface, x_i^s refers to the mole fraction of component i , and a_i^s is the surface activity coefficient of component i .⁹¹ The T, P, σ are defined as the temperature, pressure and surface tension respectively. Defining the surface activity of the surfactant remains important to determining the chemical potential of a surfactant, which is information used in the manufacture of foams, emulsions, and detergents.

1.5.4.4 Surface Activity

Sprow and Prausnitz⁹² devised an equation which describes the dependence between the surface tension of an aqueous surfactant solution and the activity of water (Eq. 1.29) as well as surfactants (Eq. 1.30) in the surface layer and bulk phase.⁹² These equations can be expressed as follows

$$\sigma = \sigma^0 + \frac{RT}{\omega_w} \ln \frac{a_w^s}{a_w^B} \quad (1.29)$$

$$\sigma = \sigma^0 + \frac{RT}{\omega_w} \ln \frac{a_s^S}{a_s^B} \quad (1.30)$$

Where σ^0 denotes the surface tension of water, ω_w is the molar area of water equal to $0.6 \times 10^5 \text{ m}^2 \text{ mol}^{-1}$, a_w^s and a_w^B are the activity of water in the surface layer and bulk phase, respectively, and a_s^S and a_s^B are the activity of surfactant in the surface layer and bulk phase, respectively. In dilute solutions, it is assumed the bulk phase surfactant activity is negligible hence Eq. 1.30 can be reduced to:

$$\sigma = \sigma^0 + \frac{RT}{\omega_w} \ln a_w^s \quad (1.31)$$

Subsequently, the activity of surfactants at the surface can be determined from $a_s^S = 1 - a_w^s$. Here this will be used for solutions above and below the critical micelle concentration (CMC) for each surfactant and compared with other environmental and synthetic surfactant systems.

1.5.4.5 The Influence of Aerosol Surface Tension on CCN Activation

Water has a high surface tension due to the strong hydrogen bonding among water molecules. However, solvation of organic species can disrupt these hydrogen bonds along with the ordered structure of the water molecules in the bulk.⁹³ The addition of organic molecules results in a decrease in surface tension as these components are surface dwelling, thus the energy at the surface is decreased in comparison to the bulk. Additionally, the favourable partitioning of these species to the surface of the droplet leads to a lowering in the S_c and the droplet activation barrier.⁹⁴ When ions such as in an inorganic salt are added to a solvent (water), they are expelled from the interface and associated with a negative surface excess concentration leading to an increase in surface tension according to the Gibbs adsorption isotherm. Onsager and Samaras were the first to depict this surface depletion in a molecular interpretation modelling the surface as a sharp boundary between two dielectric media and representing the ions as point charges repelled from the surface.⁹⁵ In the presence of inorganic salts, some organic species are impacted by the ‘salting-out’ effect which causes a decrease in their solubility and a further decrease in the surface tension of the droplet. However previous studies have also highlighted that bulk depletion must be accounted for when examining the impact of surface-active compound on surface tension depression and particle activation.^{96,97}

The impact of surfactants on the droplet surface tension remains ambiguous therefore it is necessary to conduct further studies to resolve this. Chapter 5 will explore the impacts of different surfactant types on the surface tension of aerosol droplets and bulk solutions.

While it is important to characterise the thermodynamic barriers to the activation of cloud condensation nuclei, the kinetic limitations to particle growth must also be considered and discussed.

1.6 The Kinetics of Aerosol Processes

In non-equilibrium conditions, microphysical kinetic processes that control the rate of evaporation and condensation of volatile and semi-volatile species dictates the dynamic behaviour of aerosols. There are three limiting cases where the kinetic limitation plays a key role in mass transfer processes of a species into and from a particle as shown in Figure 1-11.

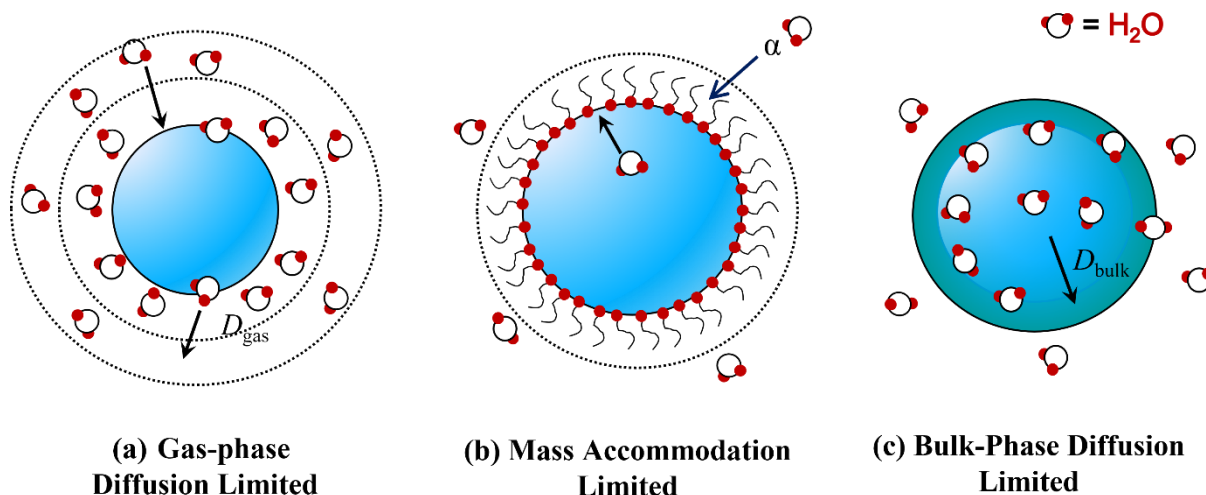


Figure 1-12: Illustration of the three kinetic regimes that limits to mass transport to or within a droplet. (a) The diffusion of water toward and from the droplet surface dictates the evaporation and condensation of water with the surrounding gas-phase. (b) Mass accommodation, α , of water through a restrictive surfactant layer. (c) Diffusion of the water through the bulk of a semi-viscous droplet leading to compositional gradients. **This image is derived from the thesis of R. Power.⁹⁸**

Figure 1-12(a) illustrates the gas-phase process of condensation and evaporation to and from the droplet. The rate at which molecules are transported to and from the gas phase determines the rate of evaporation or condensation of volatile compounds. By defining the Knudsen number, the kinetic regime used to correctly treat the evaporation kinetics can be determined. The Knudsen number, defined in Eq.1.32, characterises the boundary conditions of a fluid flow.⁹⁹ It is the ratio between the mean free path, λ , and the particle radius, r .

$$Kn = \frac{\lambda}{r} \quad (1.32)$$

$$\lambda = \frac{k_B T}{\sqrt{2}\sigma p} \quad (1.33)$$

where k_B is the Boltzmann constant, T is the temperature (K), σ is the surface tension and p denotes pressure. When $Kn \gg 1$, particles are able to ‘slip’ between the gas phase molecules in between collision. When $Kn \ll 1$, the surroundings behave as a continuum dominated by viscous forces and thermal diffusion.⁹⁹ In this regime, if the particle size is large in a high-pressured gas, evaporation and condensation are limited by gas phase diffusion.¹⁰⁰

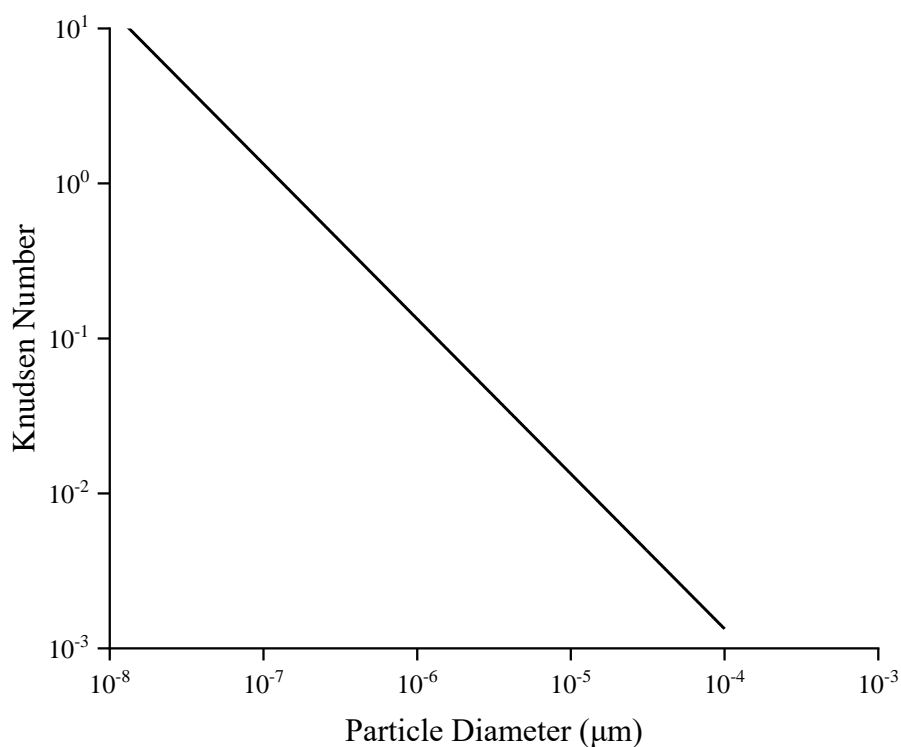


Figure 1-13: A graph to show how the Knudsen number varies with particle diameter. As the particle size increases the Knudsen number decreases as expected from the inverse relationship. The data was collected at 298K in this graph was collected by Dr. Daniel Hardy.¹⁰¹

Once a molecule diffuses through the gas phase close to the particle, it must be accommodated onto the surface and transferred into the bulk. The mass accommodation coefficient, α , denotes the proportion of colliding gas molecules that will be incorporated onto the surface and into the particle phase. Surface adsorbed molecules such as an organic or surfactant film as depicted in Figure 1-12(b), can influence the surface accommodation of molecules onto a droplet. Davies et al. found evidence for the influence of adsorbed molecules when investigating the evaporation coefficient.¹⁰⁰ The work showed the coefficient was reduced by two orders of magnitude in the presence of condensed monolayer films at the surface of the droplet. Conversely, the study reported no limitation to condensation of water molecules onto the droplet surface in the presence of condensed films showing condensation is not limited by surface active molecules.¹⁰⁰

Mass transport within a droplet can be kinetically arrested by the property viscosity. Viscosity is a measure of the resistance of a fluid to flow. The higher the viscosity the slower bulk diffusion inside the droplet to the surface. This can inhibit chemical reaction rates, evaporation of water from the particle, and the absorption of gaseous molecules into the droplet.¹⁰² Kuwata et al. showed the uptake of ammonia into aerosol particles and the particle-phase reactions were limited by the solid and semisolid adipic acid particles which in turn has implications on the droplet composition.¹⁰³

1.7 Aerosol-Light Interactions

1.7.1 Aerosol Optical Properties and Refractive Index

An aerosol can interact with light in various ways highlighted in Figure 1-13. Direct interaction with the electromagnetic radiation can result in scattering which includes processes such as diffraction, refraction and reflection or absorption. The light can be either elastically scattered whereby the scattered light has the same frequency as the incident light and therefore the photon of energy is conserved or inelastically scattered, whereby there is a shift in the frequency and the energy of scattered light compared to the incident light. The refractive index, size, and shape of the droplet influence how intensely the light is scattered and the amount that is absorbed by the droplet. The refractive index (n) describes the perturbation of light through a material or medium. It is comprised of a real (m) and imaginary part (k), see Eq. 1.34.

$$n = m + ik \quad (1.34)$$

The real part of the equation is a ratio that describes the speed of light as it passes through a medium (q) compared to the speed of light through a vacuum (c) as shown in Eq. 1.35; it determines the amplitude of scattering by atoms or molecules within a medium.

$$m = \frac{c}{q} \quad (1.35)$$

The imaginary part of the refractive index describes how the light through the medium is attenuated by absorption by the medium. The real part of Eq. 1.34 is a bulk property and thus affected by the molecular polarizability of the substance. Both components are dependent on the incident wavelength of light, temperature, and density. Refractive index is therefore an important metric to define when analysing the scattering and absorption abilities of a compound.

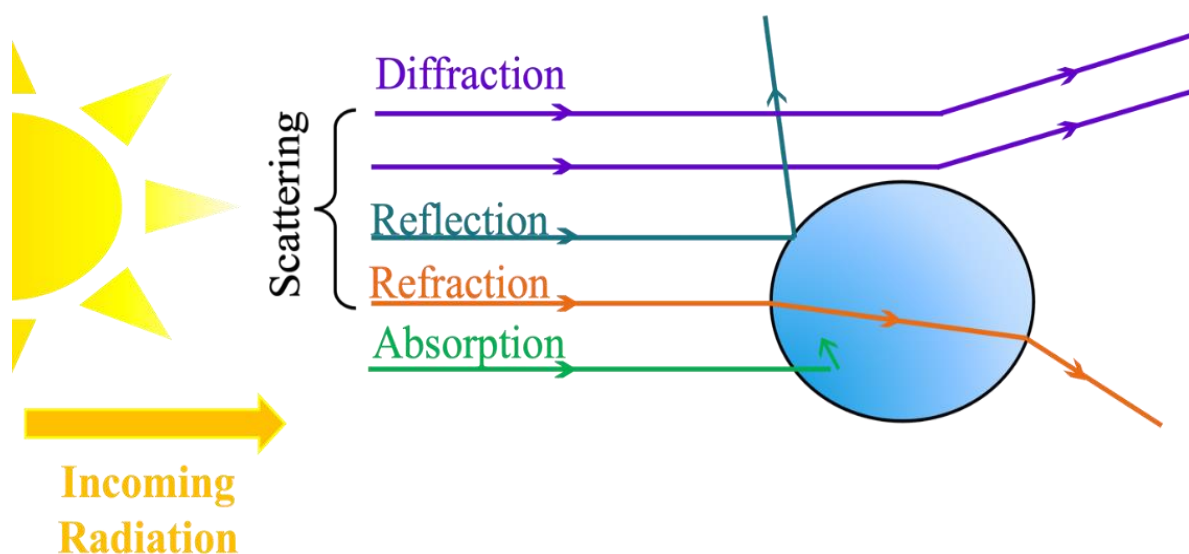


Figure 1-14: Schematic of the interaction of light radiation with a particle. Light can diffract around the droplet, reflected from the droplet surface, refracted through the droplet, or absorbed by the droplet. Adapted from Seinfeld and Pandis, 2016¹⁰⁴

1.7.1.1 The Three Size Regimes for the Interaction of Light with a Particle

The treatment of light interacting with a particle is separated into three regimes dependent on the size of the particle relative to the wavelength of the incident light illuminating the particle. A relationship between radius (r) and wavelength (λ) is provided by the size parameter (x_p):

$$x_p = \frac{2\pi r n_0}{\lambda} \quad (1.36)$$

where n_0 is the refractive index of the surrounding medium in Eq. 1.36.

In the Rayleigh regime, the radius of the particle is much smaller than the incoming wavelength of light ($r < \lambda/20$) and therefore the particles are treated as point dipoles, an example of this is air molecules. The scattering of light occurs isotropically, meaning it is symmetrically scattered forward and backward independent of the particle size or shape. Within this size range, the scattering of light has a strong dependence on wavelength ($I_{sca} \propto \lambda^{-1}$) with shorter wavelength being scattered with greater efficiency. Light at wavelengths $\lambda = 400 - 490$ nm, are among the shortest wavelengths in the visible spectrum and so the most efficiently scattered by air molecules when compared to any other longer wavelengths in the visible region. For this reason, on Earth, the sky is blue ($\lambda = 450$ nm).

Where particle sizes become large ($r > 20\lambda$), Mie theory calculations are too computationally expensive to use and therefore ray optics approximations are used as an alternative. At this limit, particles act like lenses and the approximation through geometrical considerations is used for the treatment of scattering. Diffraction and interference effects are not accounted for here.

Within this work, Mie theory is used in the treatment of light scattering of a particle as the size of the particle is comparable to the wavelength of the incident light. Treatment using Mie theory allows for the analytical description of light interacting with a spherical particle as a plane wave. In small and large size regimes, the calculation using Mie theory is applicable and less cumbersome.

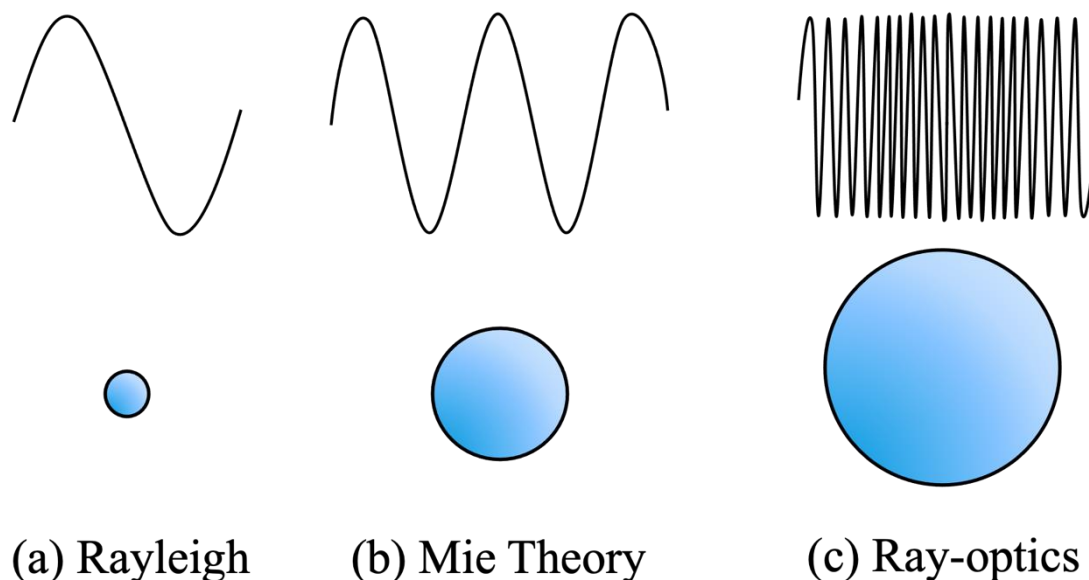


Figure 1-15: An illustration of the three size regimes for the treatment of light interacting with a particle. (a) Rayleigh scattering where the particle is smaller than the wavelength of light (b) Mie theory accounting for the size and wavelength being of comparable sizes and (c) ray optics where particles act more like the bulk phase and are treated as lenses.

1.7.2 Aerosol Photochemical Reactions

Sunlight drives much of the atmospheric chemistry hence understanding gas, condensed and cloud processes that govern these reactions remains fundamental to the improvement of atmospheric global models. Photochemical reactions where aerosol droplets function as active reaction sites remain challenging to characterise due to transport processes, surface effects and optical phenomena. In the past, atmospheric photolytic studies have predominantly focused on gaseous phase reactions; however, recent research has shed a light on the importance of incorporating condensed-phase photochemistry into the processes that influence global organic and inorganic budget predictions. Examples of atmospherically relevant particle-phase, photochemical reactions include the photolysis of iron carboxylate complexes, energy or charge-transfer reactions and photolysis of nitrate and nitrite in aqueous aerosols.¹⁰⁵ Typical timescales of these reactions range from seconds to hours at various layers of the atmosphere.¹⁰⁶ The reaction rates are influenced by several factors, namely the particle size, composition, viscosity and charge and the concentration of the photoactive component. In this thesis, the effect of concentration, droplet composition and viscosity on irradiated photoactive droplets will be outlined in Chapter 6.

Photolytic gas phases processes can be either categorised as direct or indirect, whereby direct photochemical ageing refers to the absorption of solar radiation within a particle in the tropospheric actinic window. Indirect photolysis occurs when reactions with sunlight result in reactive species such as a singlet oxygen ($^1\text{O}_2$), hydroxyl radicals (HO^\bullet) or triplet excited states which go on to react with aerosol droplets as shown in Figure 1-16.¹⁰⁷ When predicting global organic aerosol production and lifetime, Nizkorodov et al. demonstrated the importance of including the direct photochemical aging of secondary organic aerosols to account for the discrepancies observed between field, laboratory and model data.¹⁰⁸

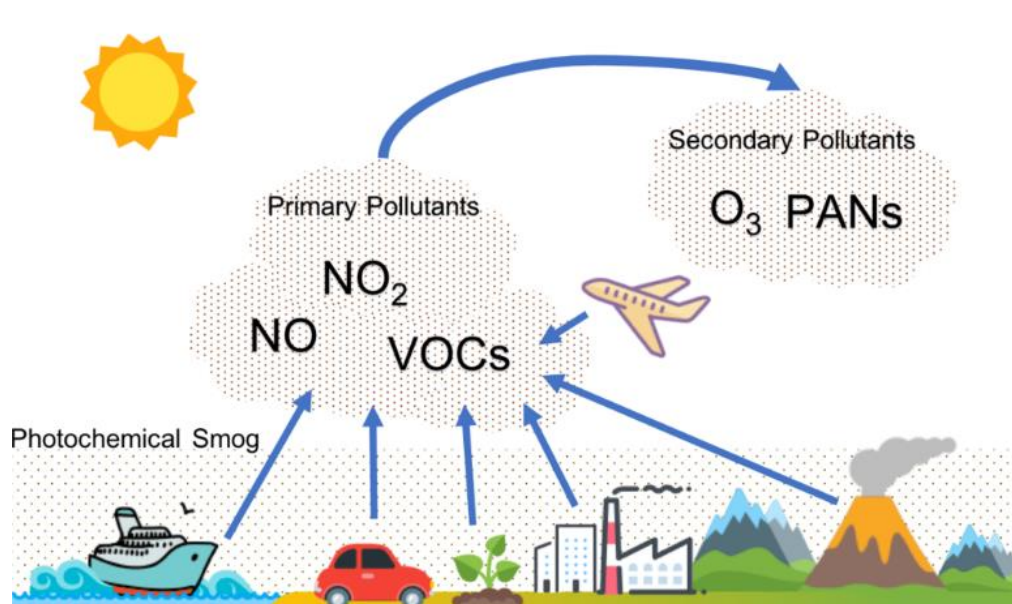


Figure 1-16: Illustration showing the sources of terrestrial and aerial sources of the reactants which contribute to the production of ozone. **Image by Liweichao.Vivian and licensed under their own work, CC BY-SA 4.0.**¹⁰⁹

The composition of the photolyzed aerosol droplet is crucial to the scattering and absorption of the incoming UV light radiation and the subsequent reduction in air quality seen within cities in Northern America and Europe. One of the products from the photoageing of ozone is photochemical smog which has a substantial impact on air quality in cities such as Los Angeles. Dickerson et al. found within the terrestrial boundary layer, particles that were UV-scattering accelerate gas-phase photochemical reactions and smog production. Conversely, UV-absorbing aerosols such as mineral dust and soot were shown to inhibit smog production from ozone.^{110,111}

While some atmospheric inorganic, organic and mixed aerosol particles scatter light radiation resulting in a net cooling effect, others absorb UV radiation and undergo photochemical reactions that result in volatile photoproducts. Klodt et al. showed the inorganic salts, sodium nitrate and ammonium nitrate accelerated the loss of high-molecular-weight compounds of the secondary organic aerosol proxies, α -

Pinene and α -Humulene under irradiation and in dark conditions, resulting in dissolved SOA becoming smaller and more volatile.¹⁰⁸

The work of Signorell et al.¹¹² highlights the size-dependent nanofocusing effects in small climate relevant droplets and the subsequent effect on the photokinetics of the particle. The nanofocusing of electromagnetic radiation inside small VIS441/TEG solution droplets (< 100 nm) shown in Figure 1-16, leads to variation of light intensity within a droplet and plays a key role in compositional inhomogeneity. The nanofocusing of light occurs in the position opposite to the incident light resulting in spatial variations of photoactivity within the droplet.¹¹² Further work by Arroyo et al. on sub-micron particles confirms this resonance phenomenon showing pronounced photoreduction rates in hotspot regions within iron citrate droplets.¹⁰⁵ The study found particle rotation and intra-particle molecular transport additionally accelerated the photochemistry.¹¹³ Transport via diffusion continually replenishes the area of highest light intensity with more reactant and removes the products from the reaction site. As droplet viscosity can inhibit diffusion and reaction rates it is an important area of study when observing photoinitiated reactions, and a focus of the work discussed in Chapter 6.¹¹³

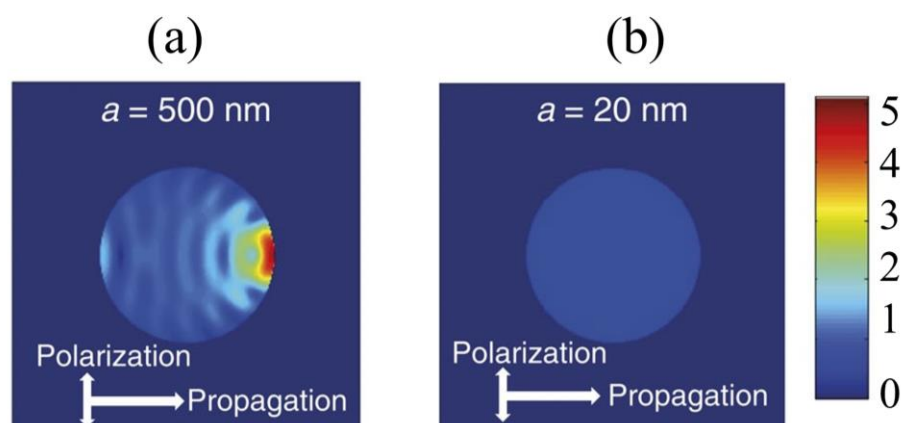


Figure 1-17: Distribution of light intensity within a) 500 nm and b) 20 nm droplet. Level 1 denoted blue on the scale signals intensity of the incident light. **Image taken from journal paper by J. Cremer licensed under a Creative Commons Attribution 4.0 International License.**¹¹²

1.7.3 Optical Tweezing of Aerosol Droplets

The way in which nanosized particles interact with light can be observed using optical trapping and laboratory aerosol measurements. Optical trapping refers to the phenomenon of trapping and manipulating particles with light and optical tweezers apply the use of optical trapping to grip, move and manipulate trapped particles like a ‘tweezer’ moving a physical object. In this thesis the two terms are used interchangeably.

The formation of an optical trap arises when a laser beam is tightly focused by a high numerical aperture (NA) lens. When near the focus of the beam, a particle experiences a force due to the transfer of momentum from the scattering of the incident light.¹¹⁴ This interplay between the Gaussian beam and

dielectric particle gives rise to two optical forces: a scattering and a gradient force.¹¹⁵ The interaction between these two forces is fundamental to understanding how a particle is trapped.

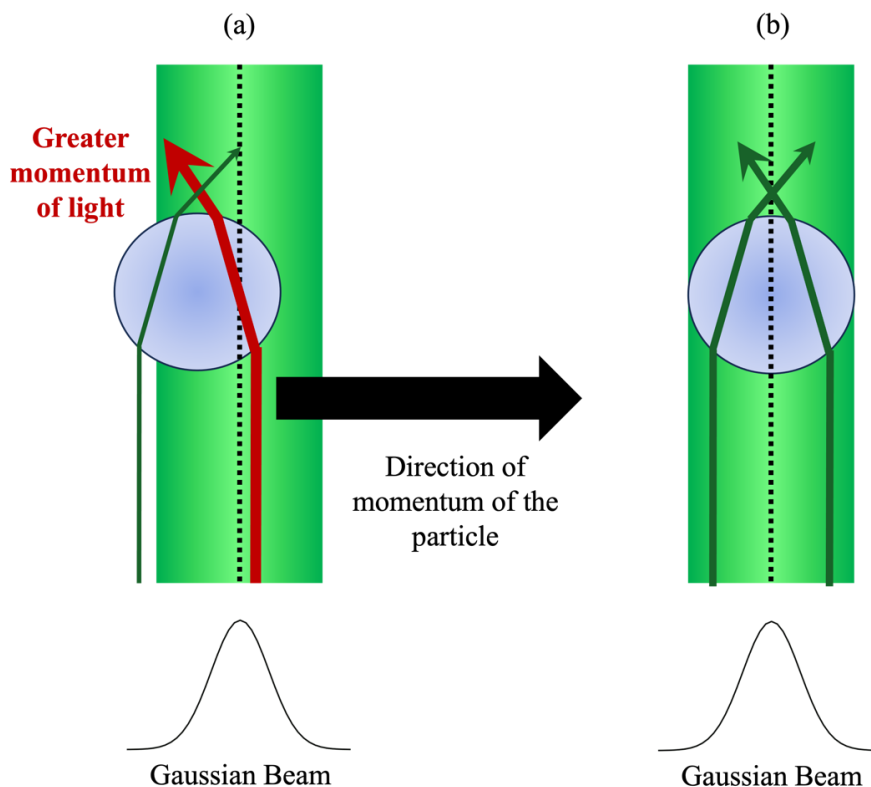


Figure 1-18: Diagram illustrating the (a) off centre droplet which causes the propagating light to bend towards the left, as momentum must be conserved. Restorative forces push the droplet towards the centre of the Gaussian beam as shown in (b). Images were replicated from work conducted by J.E. Molloy et al.¹¹⁶

The gradient force acts as a net restoring force should a particle laterally move away from the centre. When the particle is laterally displaced, the incoming beam is refracted by the particle in a particular direction along with the momentum of photons to conserve Newton's third law, subsequently the particle experiences an equal change in the opposite direction forcing it towards the centre of the Gaussian beam. The higher the intensity of the incoming beam the greater the force that recentres the particle hence high intensity lasers are used during optical tweezing shown in Figure 1-18 (a) and (b).

In the event of the particle being displaced in the direction of the beam, the light that is absorbed transfers momentum to the particle moving it in the direction of the beam and away from the centre. By focusing the light through a microscope objective, the beam converges at a focal point on the particle which increases the momentum of light travelling along the direction of the beam. The momentum must be conserved; therefore, the net transfer of momentum pushes the particle in the opposite direction towards the objective as shown in Figure 1-19.^{117,114} By acting in three dimensions, i.e., in the axial plane and lateral planes, the particle is moved towards the position of maximum light intensity of the Gaussian beam.^{118,119,120} Trapping efficiency can be increased by slightly overfilling the back aperture

of the inverted microscope objective such that the ratio of trapping to scattering force is increased and the trapping efficiency improved.¹²¹

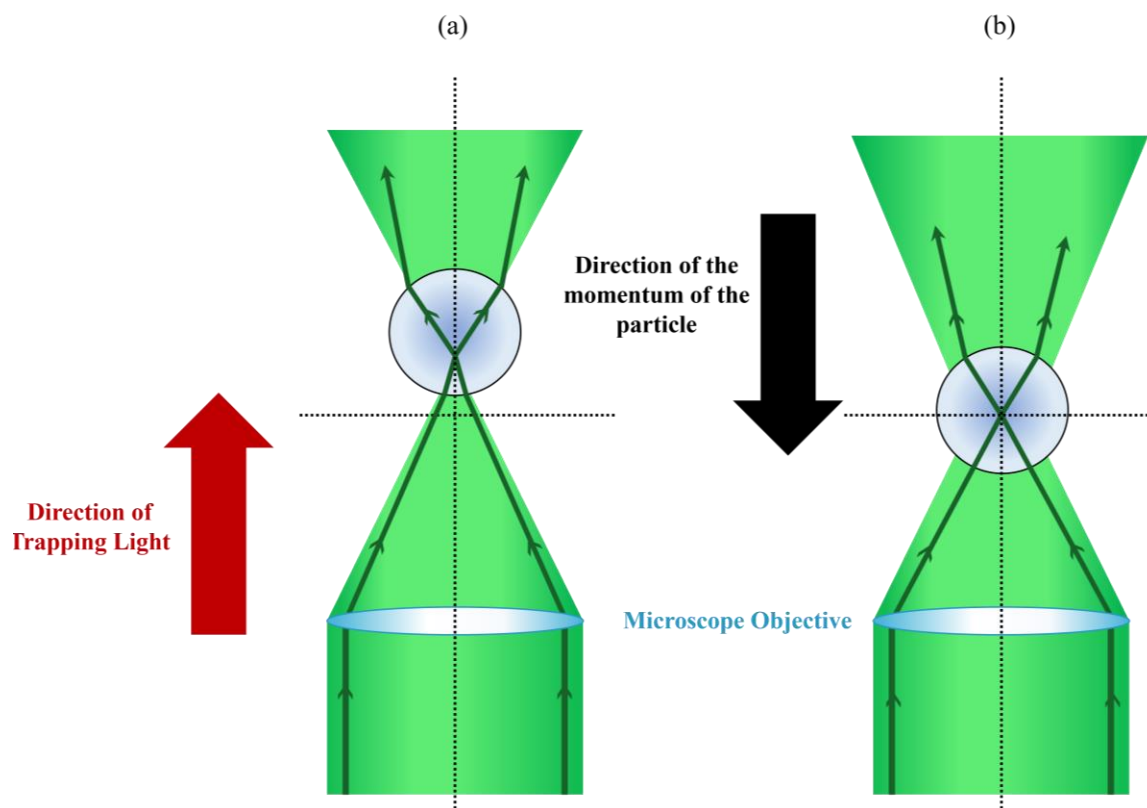


Figure 1-19: The displaced particle in (a) is forced into the centre shown in (b). By focusing of the trapping light onto the particle via the microscope objective the momentum of light is increased in the direction of the trapping light and the momentum of the particle is pushed in the opposite direction.

1.8 Aerosol Measurement Techniques

As previously discussed, a number of properties can inhibit the growth of droplet into a CCN, namely, surface tension, relative humidity and viscosity. Where bulk methods are able to provide determination of aerosol physical properties and their parameters, unlike single particle techniques, they are unable to provide contactless aerosol measurements, as closely replicate droplet conditions, or measure droplet behaviour at supersaturated solute states. A more comprehensive description of the techniques used to measure these in thesis will be given in Chapter 3.

1.8.1 Techniques for Measuring Surface Tension

Surface tension measurement techniques are classified into two modes: static and dynamic. Static measurements include Wilhelmy Plate, pendant drop, the droplet oscillatory method and the holographic optical tweezer technique while dynamic measurements include bubble pressure tensiometry and the drop volume technique.

1.8.1.1 Bulk-Phase Measurements

Wilhelmy plate is a frequently used method to measure static surface tension. A vertical plate with a well-defined geometry, attached to a balance is submerged into a solution. The force required to pull the plate out of the solution is subsequently measured and from this the surface tension can be calculated. Similarly, the du Nouy Ring enables the measurement of surface tension by the same means of force but without the influence of the wetting properties of the liquid.¹²² Rather than using force to derive surface tension, the pendant droplet method uses the relationship between the surface tension of a droplet and gravity. To minimise the surface area, surface tension seeks to form a spherical droplet, whereas gravitation distorts the spherical shape by elongation into a pear-like shape. The technique uses a dosing needle to hang liquid droplet which is captured using a camera and analysed using bespoke software. By combining Pascal's Law (hydrostatic pressure) and Young-Laplace equations a numerical fit of the theoretical drop shape and the shape captured by the camera yield the surface tension.¹²³

1.8.1.2 Droplet-phase Measurements

Holographic optical tweezing has emerged as a contactless, non-invasive technique that enables the measurement of surface tension of aqueous solutions with volumes of 1 – 4 pL. The method enables the characterisation and manipulation of droplets between 1 μm to 10 μm . Optical, three-dimensional trapping is achieved by focussing a laser beam into the back aperture of a microscope which tightly focuses the light. Coupled with Raman spectroscopy and Mie theory simulations, this technique is able to extrapolate the surface tension from the coalescence of two levitated droplets under specified RH conditions using radius, refractive index, and droplet oscillations. This techniques has been shown to determine surface tension to accuracies better than $\pm 1 \text{ mN m}^{-1}$ as a consequence of the high accuracy in droplet size and refractive index.¹²⁴

The droplet oscillatory method is a technique developed to calculate surface tension from the serial oscillation of an ejected droplet. Using a droplet-on-demand dispenser, this method tracks the trajectory of the oscillating droplets using stroboscopic imaging timed with the dispenser pulses. From this the aspect ratio (a_x/a_y) is collected and converted to a frequency using a fast Fourier transform which can used to calculate the surface tension of the solution. Droplet formation and oscillation typically occurs over less than 1 ms which is shorter than the evaporation time scale of several seconds and the droplet flight path around 100 μs .¹²⁵ This technique is particularly useful for measuring the surface tension of surfactant solutions as the average adsorption of a surfactant molecule occurs on the order of milliseconds.

1.8.1.3 Dynamic Bulk Measurements

Bubble pressure tensiometer is a favourable method for determining the dynamic surface tension over a maximum surface age of 2×10^5 ms. The Young-Laplace equation dictates that the internal pressure of a spherical gas bubble depends on the radius of curvature and the surface tension. From this equation,

the bubble pressure method is able to calculate the surface tension of droplet by producing a series of bubbles and measuring the time from the start of the bubble formation to the occurrence of the pressure maximum, known as the surface age. By varying the speed at which the bubbles are produced, surface tension can be measure against surface age. This technique remains crucial to measuring the dynamic surface tension of surfactant solutions, enabling the calculation of both the diffusion and adsorption rates associated with surfactant used in this work.

Growing droplet technique is another method used for measuring the dynamic interfacial tension whereby a drop is grown at the end of a capillary tube into another immiscible fluid. With the ability to measure both liquid-gas and liquid-liquid tensions over a range of timescales (10 ms to several hours), the method captures the actual transient tension evolution of the interface rather than interval times as with the bubble pressure method. The drop Bond number is utilised to quantify the interfacial tension and gravity of the growing droplet along with two measures of the drop size, the horizontal drop radius at the equator and the vertical distance from the drop apex to the equator.¹²⁶

1.8.2 Techniques for Measuring Viscosity

The rate of droplet growth and evaporation, photochemical reactions, and absorption of gaseous compounds are all dependent on droplet viscosity which varies with relative humidity in the atmosphere.¹²⁷ For example, viscosity dictates the rate of droplet growth and evaporation of organic hence characterising their viscosity is central to predicting their behaviour in the atmosphere.¹²⁸ Measuring viscosity is important in determining droplet dynamics and cloud formation. Many techniques have been created to measure viscosity and here lies a description of some these methods.

1.8.2.1 Determining Viscosity by Applied Force

Different rheometer designs measure over varying viscosities and require large sample sizes. Rotational rheometry encourages mechanical distortion by applying weak levels of torque to a liquid sample and measuring the amount of torque required to cause rotation. Measured across a horizontal plane, the varying levels of shear force relate to the sample viscosity. In contrast the vibrating viscometer technique measures viscosity by applying oscillating vibrations to a sample and measuring the damping of the oscillations over a given time. Viscosity can be inferred by monitoring the decay time of oscillations, changes in resonated frequency or analysis of the power input.¹²⁹ Additionally, atomic force microscopy has been used to determine viscosity by force, however, is restricted to low viscosities ($\leq 5 \times 10^{-2}$ Pa s) due to dissipative effect experienced at higher viscosities.

The bead-mobility technique is capable of measuring viscosity over a wider range ($10^{-3} < \eta < 10^3$ Pa s) due to the real-time control of the RH conditions. A sample is sprayed onto a slide, collecting droplets with diameters (D) between 20 – 50 μm . A dilute solution of hydrophilic melamine beads is sprayed and left to settle onto the sample on the slide and placed in a controlled flow cell. The gas flow over the sample generates shear stress at the surface of the droplet stipulating circular fluid movement.

The displacement of beads within the droplet is monitored using optical microscopy from which the average bead velocity is calculated. Using a calibration curve the bead velocity can be converted into viscosity of the sample solution.¹³⁰

1.8.2.2 Determining Viscosity by Relaxation Techniques

Poke and flow technique first proposed by Murray *et al.*¹³¹ and later developed by Renbaum-Wolff *et al.*¹³², deposits droplets ($25 \leq D \leq 70 \mu\text{m}$) onto a hydrophobic substrate within a flow cell in controlled RH conditions. Using a needle attached to a micromanipulator, the droplet is poked which distorts the droplet from its equilibrium geometry. Optical microscopy monitors the droplet relaxation to minimise the increase in surface energy of the system, an experimental flow time can be determined (time it takes for relaxation back to equilibrium droplet state). Viscosity is inferred when comparing the determined flow rate with simulated flow times.¹³³

Aerosol Optical tweezers capture two aerosol droplets ($6 \leq D \leq 20 \mu\text{m}$) in optical traps and by bringing the traps together the droplets undergo a coalescence event. The oscillation relaxation of the coalesced droplet over a characteristic dampening time determines the viscosity of the droplet at a controlled environmental condition. In the same vein as when determining the surface tension, capillary driven relaxation to the spherical shape is observed by optical microscopy (overdamped region, typically $< 50\%$ RH) and a photodetector (underdamped region, typically $> 60\%$ RH), while the final particle size and refractive index are determined by the whispering gallery modes on the spontaneous bands within the Raman spectrum. The technique enables viscosities between $10^{-3} - 10^9 \text{ Pa s}$ to be extracted.

1.8.2.3 Determining Viscosity by Fluorescence Imaging

Within biosystems, viscosity is an important parameter to determine, as any perturbations have been linked to diseases and malfunction at the cellular level. As the spatial resolution of this technique is $\sim 250 \text{ nm}$, objects at the submicron size can be observed. Fluorescence lifetime imaging coupled with molecular rotors is a highly sought after method to establish the local microscopic viscosity for a single cell. The non-radiative decay of the molecular rotor is influenced by the cellular viscosity which affects the fluorescence quantum yield.¹³⁴ The probed viscosity range is dependent on the choice of molecular rotor and the hydrophilic or lipophilic system in which they are in. Viscosity can be measured in real time either by use of sessile droplets with the molecular rotor incorporated in micromolar concentrations or in levitated aerosol particles, both non-destructive in their approach.¹³⁵

1.9 Thesis Aims

This chapter has presented atmospheric aerosols and their importance in climate as well as to our human health. Whilst highlighting their importance, this chapter has presented properties that can impede or accelerate droplet growth into a CCN. Understanding of this process is integral to characterising the influence of these properties on the aerosol indirect effect on radiative forcing which remains the largest

uncertainty in radiative forcing. In terms of quantifying surface tension, many previous studies have focused on bulk phase dynamic and equilibrium behaviour of surfactants, organics, and inorganic-organic mixtures. The main aim of this thesis is to introduce a technique for measuring the equilibrium surface tension of binary and ternary inorganic and organic aqueous mixtures; the dynamic surface tension of a surfactant laden solutions in the aerosol and bulk phase; and the measurement of droplet viscosity and photochemistry using established techniques of HOT and EDB. Development and implementation of techniques such as these will prove vital in our understanding of droplet dynamics which in turn influence the growth of aerosol droplets into CCN.

1.10 Thesis Summary

Chapter 2. The following chapter addresses the various ways to decolonise and contextualise aerosol science within and for the aerosol science community. The discussion centres around the benefits of using a decolonial approach to identify global issues and address the historical impacts of colonialism and coloniality on aerosol science research and aerosol science education. This chapter provides a framework that can be adopted within the ESPRC aerosol CDT program to promote critical analysis and reflection on the curriculum and learning environment.

Chapter 3. The chapter herein discusses the experimental techniques used to collect measurements of the droplet and bulk surface tension, droplet viscosity and the photo-driven droplet size change. The theoretical and physical aspects of each technique will be discussed and related to their use and function within this work. For the first time the droplet oscillation method has been used to calculate the dynamic surface tension of surfactant droplets which is new in its approach.

Chapter 4. This chapter evaluates the surface tension measurements conducted in the droplet and bulk phase to ensure the droplet oscillation technique is a valid method in calculating surface tension. These measurements are compared to various models to observe their ability to account for the change in surface tension with an increase in solution concentration in binary and ternary inorganic and organic mixtures.

Chapter 5. Following on from the previous chapter, the dynamic and bulk surface tension of surfactant solutions were investigated using the same techniques as previously mentioned. This chapter discusses the equilibrium surface tension of SDS, TX-100 and Tween-20 using various models to derive key elements such as the CMC and surface excess concentration. The droplet-phase measurements delivered a novel method of calculating the dynamic nature of surfactants within a particle and the ability to compare the data with bulk phase measurements.

Chapter 6. The final results chapter discusses the measurement of droplet viscosity of ternary mixtures using the HOT technique at various ambient conditions. Additionally, an EDB was used to levitate a

Chapter 1- Introduction

sodium nitrate aerosol droplet irradiated by a UV light source to examine photochemically driven effect radii change.

Chapter 7. A summary of the experimental findings and details of the future progression of the work conducted in this thesis.

Chapter 2

Preparing Researchers in Aerosol Science to be Inclusive, Self-Aware and Globally Conscious: A Decolonial Approach

2.1 Overview

2.1.1 Contextualising this Chapter

In this thesis, the surface tension and viscosity of different atmospherically relevant aerosols is detailed with the primary objective of enhancing existing surface tensions models and advancing our comprehension and predictive capabilities concerning the surface tension of aerosols found in the atmosphere.^{1,2} Upon initial observation, the fundamental aerosol science research presented may not seem directly related to social science concepts such as decolonisation or diversification. However, upon deeper examination, it becomes evident that aerosol science is embedded within a societal context influenced by colonial legacies. For example, disparities persist in the accessibility of aerosol science research, with a notable skew towards institutions in the global North compared to those in the global South. As humanity faces unprecedented global challenges, notably climate change, famine, and widespread viral diseases, there is a danger that these events will continue to disproportionately effect those within the global South. Addressing these challenges demands unparalleled levels of interdisciplinary collaboration³, global awareness, and cross-cultural communication fostered across universities and continents.

This chapter focuses on a decolonial framework that could be used to teach and enhance university students' self and global awareness equipping them with the ability to discuss global issues related to colonialism and equitable research practices. This includes exploring the intersecting socioeconomic, political, and cultural inequitable barriers that exists for marginalised groups as well as foster international equitable collaborations. Here, a decolonial approach is delineated as acknowledging where shared scientific and historical processes and exchanges have been shaped by colonialism, coupled with the dismantling of collaborative and exploitative systems inherent in developing scientific and technological knowledge. Decolonial efforts have demonstrated their capacity to foster a globally relevant curriculum and aware student body across academia⁶, as evidenced by case studies from the UK and beyond in this chapter. Global awareness will be defined and subdivided into five dimensions as proposed by Hanvey in 1976. The dimensions include 'perspective consciousness, state-of-the-planet awareness, cross-cultural awareness, knowledge of global dynamics, and awareness of human choices.^{4,5} Specifically, this chapter will showcase how initiatives aimed at decolonising aerosol science

teaching materials can stimulate critical thinking and self-awareness, enrich understanding of aerosol science and its context, and illuminate the role and influence of researchers within the global aerosol science community.

Having the Decolonising and Contextualising the Science Curriculum (DCSC) framework and awareness of the five dimensions as a point of departure, this study will highlight social, political, economic, and cultural barriers within aerosol science and the broader scientific community. The framework, developed by the Decolonising the Science Curriculum working group, is rooted in recognising political and economic influences, understanding the impact of language and culture, and exposing hidden knowledge and barriers to dissemination—all shaped by coloniality. It has been tested in workshops in various universities as a method to introduce participants, including university staff and students, to fundamental decolonial concepts. Here, it is crucial to acknowledge that what constitutes ‘decolonising’ or ‘a decolonial approach’ within its origin of the Global South (GS) will differ from that in the Global North (GN).¹ Therefore, this thesis in the Global North can only approach the topic from this perspective and nuanced understanding.

2.1.2 Awareness in Academia

Self and global awareness are fundamental to transcribing the information gained from the world around us into knowledge that breeds cultural compassion, understanding and action. In a paper reflecting on lessons from Ghana in 2000, Wilson articulates that “we may be conscious of our perspective but often are not aware how strongly our nationality, our culture, and our experiences inform that perspective.”⁷ Building on this insight, Burnouf emphasises the value of cross-cultural experiences, such as “watching videos and reading online newspapers from other countries,” as practical means of fostering a global perspective.⁴ By organising activities within the aerosol science curriculum, around principles of “free expression, respect for diverse viewpoints, active participation, and a genuine desire to communicate,” it is proposed that individuals can broaden their understanding of the world they inhabit and thereby improve the solutions to worldwide issues..

Furthermore, Merryfield drawing from Edward Said's seminal work "Orientalism," underpins the significance of self-awareness and global consciousness within Western contexts to counteract misrepresentations. Merryfield reveals how European scholars historically misrepresented non-Western cultures by interpreting them through their own cultural lenses.⁶ This orientalist scholarship, spanning five centuries, not only served political agendas but also reinforced the belief in European superiority and “affirmed the European right to rule and "civilise" Africans, Asians, Arabs, Indians.” In response

¹ Global North represent the economically developed societies of Europe, North America, Australia, Israel, South Africa, amongst others, the Global South represents the economically backward countries of Africa, India, China, Brazil, Mexico amongst others. (L. E. Odeh, A comparative analysis of global north and global south economies, *J. Sustain. Dev.*, 2010, 12, 1-11).
<https://worldpopulationreview.com/country-rankings/global-north-countries>

to this historical context, it becomes crucial to create spaces within universities for students to explore self-awareness and global consciousness to stop the past from repeating itself within academia. This chapter contends that adopting a decolonial approach in education enables students to critically reflect on their positionality and significance within the global context, thereby expanding and enriching their knowledge beyond Western perspectives. Additionally, this approach equips university students with the tools necessary to apply critical thinking and decolonial perspectives to their own scientific research. By doing so, research can be established on a foundation aimed at rectifying imbalances, contextualising knowledge, and breaking down barriers to inclusion.

2.1.2.1 Self Awareness

According to Goleman, self-awareness refers to a deep understanding of one's emotions, strengths, weaknesses, needs, and drives.⁸ This ability to choose action imbues humans with the power to shape their futures. Consequently, as individuals enhance their awareness of the choices at their disposal, they also heighten their sense of personal responsibility for the outcomes of these choices. Lio et al. argue that students who develop self-awareness can advance their “self-regulation and build healthy interpersonal relationships with others.”⁹ Similarly, Eurich states that upon developing our self-awareness, ‘we make sounder decisions, build stronger relationships, and communicate more effectively.’¹⁰ This work intends to demonstrate how decolonising the curriculum and research environment represents a powerful method for enhancing students' self-awareness.

Decolonising the curriculum entails more than just critically assessing teaching materials and content; it also involves reflecting on one's identity and positionality within the global context, known as 'reflexive thinking.'¹¹ Through this process, individuals can engage in an exploration of identity and challenge assumptions, key components of self-awareness. Such efforts help students develop the capacity to make informed decisions that consider different perspectives, experiences, and narratives. In the context of science and science students, this holds particular importance as students represent the potential future generation of scientists. They wield the power to determine the direction of scientific research and its impact on both the Global North and South communities.¹²

2.1.2.2 Global Awareness

The integration of global awareness into teaching materials is imperative in our ever-evolving society.¹³ With the growing internationalisation of universities, aerosol science students now have significant opportunities to collaborate extensively with peers from diverse cultural and national backgrounds and engage with stakeholders worldwide.^{4,14} Consequently, university students today are immersed in an environment rich with diversity, encountering individuals from various ethnicities, genders, languages, races, and socioeconomic backgrounds.⁵ With access to a wealth of knowledge, news, and social media platforms, they are constantly confronted with global issues such as significant health disparities, inequalities between less developed and more developed nations, environmental degradation,

overpopulation, transnational migrations, and ethnic nationalism¹³⁶ — all of which are deeply rooted in Western colonial history. This exposure underscores the importance of fostering global awareness among students, as it equips them with the understanding and empathy needed to navigate and address the complex challenges facing our interconnected world. According to Kirkwood, Hanvey proposed definitions of the five global awareness dimensions as follows:

1. Perspective consciousness: Students need a grasp of the diverse perspectives among people and nations worldwide. These viewpoints, influenced by unconscious factors, shape individuals, groups, and nations' deeply held beliefs and assumptions, regardless of time or space. Such perspectives, not universally shared, significantly impact human actions. The work of Merryfield and Subedi expands on Hanvey's concept by recognising that perspective consciousness must include an understanding of 'the power one holds either locally or globally', which will be considered in this work.
2. State-of-the-planet awareness: Students must understand current world conditions, developments, trends, and challenges facing the global community. This necessitates understanding the causes and effects of events on nations and people, addressing issues like population growth, migrations, economic disparities, resource depletion, and both inter- and intra-national conflicts. Global learners must be attuned to the world's complexities and dynamics.
3. Cross-cultural awareness: Students are shaped by the variety of ideas and practices across human societies and by understanding how their own culture is viewed from different perspectives. This necessitates a high level of global awareness and empathy.
4. Knowledge of global dynamics: Understanding the world as an interconnected system of complex traits and mechanisms and unforeseen consequences that arise. Adopting a systems approach aids students in comprehending the processes of growth and the dynamics of change at local, national, and international levels.
5. Awareness of human choices: to be global thinkers, students must be aware of human decisions and consequences. They must realise the problems of choice confronting individuals and nations as the world expands.

Understanding multiple different perspectives and dynamics regarding growth and development around science can increase critical thinking skills, understanding of cultural diversity and awareness of global scientific issues, as found in a study by Tata Mbugua.¹⁵ Research by Maani and Maharaj builds on this idea, suggesting that individuals who comprehensively understand a system's structure and composition before devising strategies and taking action are more adept at problem-solving and performing more effectively. By connecting global awareness with an understanding of decolonial concepts, students will be able to understand the positionality of their research fully.

2.2 Decolonising and Contextualising the Curriculum

European colonial endeavours, dating back to the 15th century, have profoundly shaped social, political, and cultural inequities within the scientific academic community and curricula.¹⁶ With Western scientists using enslaved people and slave ships to collect and collate specimens and knowledge from the colonised world, science and scientific institutions were instrumental motivators for the continued extraction and exploitation of Indigenous peoples and lands. This exploitation fuelled the West's economic expansion and pedagogical hegemony, establishing a 'universal monopoly on the truth and sound knowledge'.^{16,17} This significance on our modern-day curricula and worldview is underscored by Wane's observation that those who 'produce knowledge wield significant power' over how we perceive and interact with the world around us. Through colonialism, Western imperial powers imposed a Eurocentric worldview on its colonies, spreading a mainstream curriculum as part of an elitist project to advance religious education (led by Christianity) in the colonies¹⁸, justified as a "civilising mission".¹⁹ Hence, European colonial narratives have erected enduring barriers to progress and the equitable distribution of the benefits of scientific research, impacting individuals across various identities including race, geography, class, gender, and sexuality. UK universities home to world-leading science centres were built on the 'spoils' of slavery and colonialism.²⁰ Methods of exclusion include segregating scientific knowledge into specific topics and occluding Indigenous ways of knowing and being as part of the dominating agenda. This narrowing perspective has contributed to what Vandana Shiva describes as the "monoculture of the mind."¹⁸ Decoloniality allows the scientific community to reflect on this and deconstruct barriers to science built in the colonial era, paving the way for a more holistic and multi-dimensional understanding of the world around us across intersecting levels.

The decolonisation movement originated as a post-modernism approach in the Global South, beginning in Asia and spreading northward. Initially, it aimed to liberate and repatriate the colonised lands and people from imperial dominance and control, gifting back 'power' to the colonised. However, as noted by the renowned writer Ngũgĩ wa Thiong'o in his seminal work "Decolonising the Mind," decolonisation must extend beyond the repatriation of land, speaking of the importance of addressing the cultural and psychological consequences of colonialism alongside its economic, political, and military dimensions.²¹ wa Thiong'o viewed decolonisation as a way to liberate people from the imposed worldview towards seeing themselves to themselves and other selves in the universe.²² Hence, the concept of decolonisation evolved, giving rise to decoloniality, which provides a broader understanding of the widespread impact of colonialism on both the colonised, the diaspora and the modern-day matrix of power.

In 2015, the term decolonisation entered the mainstream media when students at the University of Cape Town drew attention to colonial and imperialist legacies in higher education curricula in the Global South via the #Rhodesmustfall movement.^{23,24} The initiative stemmed from students' disillusionment

with colonial figures and cultures prevalent in university life at certain higher education institutions. The movement gained momentum with students demanding the removal of statues depicting Cecil John Rhodes and other colonial figures from universities and public spaces, marking a significant turning point. As Mbembe 2016²⁵ argues

there is something not only wrong, but profoundly demeaning, when we are asked to bow in deference before the statues of those who did not consider us as human and who deployed every single mean in their power to remind us of our supposed worthlessness.

This movement resonated globally, prompting universities in the UK and USA to acknowledge the need for decolonial work. The conversation gained renewed momentum during the 2020 'Black Lives Matter' movement²⁶, prompting universities to confront inequities and concerted efforts to decolonise their systems and curricula. Central to this effort is "rediscovering knowledge and practices relegated to inferior positions by colonial/imperialist structure" and incorporating such knowledge alongside western narratives.²³ For instance, in learning a module like Inclusive Education, students can explore Western theories, such as Bronfenbrenner's (1979) ecological systems theory, alongside the African philosophy of ubuntu, to comprehensively understand the concept. In science, Neil Williams used this understanding to develop an inclusive curriculum that allowed students to explore atmospheric chemistry in countries or areas personal to them, resulting in students researching countries such as Nigeria and Bangladesh.²⁷ This comprehensive approach can extend across curricula, practices, and research, urging both staff and students to learn the history of their subjects, critically assess their research methodologies, and evaluate the inclusivity of the working environment.

There is no universally agreed-upon framework for conceptualising the decolonisation of science curricula. This complex matter does not offer a singular approach or solution, so it is crucial to establish its definition here. In this chapter, decolonising can firstly be understood as a tool to actively dismantle social, structural, and institutional barriers to higher education that intersect with race, gender, sexuality, and class prejudice inherited from colonialism. These barriers can exclude and marginalise voices, people, and knowledge systems within the scientific community, perpetuating the concentration of knowledge and power within the GN. For instance, a study published in 2016 found that over 50 % of research articles were authored by GN countries see Figure 2-1, with 75 % of them written in English.²⁸ However, only 20 % of the global population can understand English.²⁹ The decolonial approach adopted here promotes critical inquiry and a willingness to challenge established Westernised norms while serving as a means to delink the academe from Eurocentrism. Such reflection is crucial to avoid repeating historical errors, as exemplified by the pseudoscientific Eugenics movement and its tragic consequences, including widespread sterilisation programs. A decolonised and diversified curriculum has highlighted the need for a broader range of ethnic patient images to be included in educational materials. This ensures that students are exposed to a more diverse skin rashes and diseases, improving

their diagnostic skills and enhancing patient safety. In this case, a decolonised, diversified curriculum could be lifesaving.

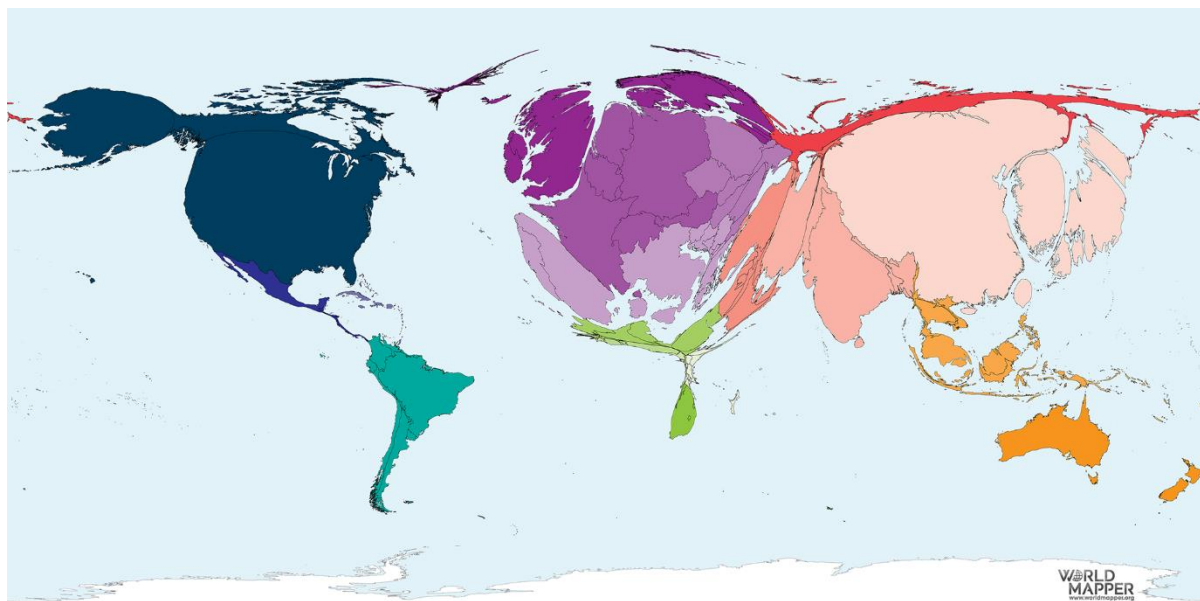


Figure 2-1: The distribution of scientific published papers in 2016. The map shows a significant skew in science papers towards the Global North/Western countries compared to the Global South which correlates to the world variation in GDP and scientific research output. **This image was taken from World mapper under the published under a Creative Commons Attribution – Non-Commercial – ShareAlike 4.0 International License**

Secondly, the decolonial work involves challenging the hegemony of Western scientific science culture, which impacts knowledge production and dissemination. This hegemony, described by the Portuguese scholar de Sousa Santos as 'cognitive injustice,' perpetuates societal narratives prioritising Western perspectives.³⁰ Economou-Garcia goes on to detail that even in the instance where GN researchers conduct research in the GS, it often fails to collaborate with local scientists or to build local scientific capacity, this is known as 'parachute science'.³¹ Additionally, the less economically developed a country is (based on the Human Development Index), the less likely that country is to have local authors involved in ecological research on that country. In adopting a decolonial approach, what has been denied or hidden in the periphery of subjects or fields, known as the null curriculum, can be made visible and when conducted appropriately, without being 'tokenistic' or 'exclusionary'.²³ Decolonisation seeks to decentre the Global North while embracing and exploring local and global knowledge beyond the Western canon.

Lastly, drawing on Gandolfi and influenced by Barton³² and Ideland³³, it is highlighted that many curricula promote 'utilitarian and triumphalist perspectives on science and technology without critically examining their limitations,' cultural relevance or connections to colonialism. Ladson-Billings proposes that to create a more culturally relevant pedagogy, educators need to demonstrate a commitment to fostering cultural competence within home and school environments, recognising, and leveraging

students' skills from their cultural backgrounds.¹⁵ Educators should strive to 'cultivate sociopolitical or critical consciousness in students, guiding them to identify, critique, and address social injustices.'¹⁵ Decoloniality serves as a catalyst for not only reframing and reconstructing pedagogy but also university systems and practices to be grounded in principles of equity, inclusion, justice and belonging, which also entails socioeconomic, political, and cultural reflections. Examining the research presented in this thesis through a decolonial lens has sparked innovative approaches to aerosol research, including the incorporation of diverse perspectives and knowledge systems in data collection. Additionally, it has led to investments in educational initiatives like the Creative Tuition Collective (CTC), aimed at dismantling colonial educational barriers. CTC seeks to tackle social, political, and economic inequity in the STEM environment by providing STEM upskilling programs for marginalised students and encouraging scientific research projects that involve the public and school stakeholders. Further details on these initiatives will be discussed in Chapter 7.

2.2.1 Decolonising the curriculum and the five dimensions.

Since the 1970s, scholars have aimed to deconstruct the idealised view of science, advocating for acknowledgement of the "socially contingent nature of scientific knowledge."³⁴ This perspective includes reliability, replication, socio-cultural influences, and non-human elements. A decolonial approach within the curriculum addresses these factors by promoting critical inquiry and a willingness to challenge established Westernised norms, fostering ongoing innovation and reflection in the scientific academe. This section will provide examples of initiatives aimed at decolonising the curriculum and illustrate how these endeavours are linked to raising both self- and global awareness.

decolonising pedagogy . . . must be guided by a conceptually dynamic worldview; strategically utilize theorizations and understandings from various fields and conceptual frameworks to unmask the logics, workings and effects of internal colonial domination, oppression and exploitation (Tejada et al., 2003)³⁵

2.2.1.1 Decolonising the Dentistry Curriculum

R. Lala highlights how diversity initiatives alone are insufficient in addressing the colonial power dynamics that have contributed to racial and class disparities within dentistry.²⁰ Historical commodities like sugar, tobacco, and rum played pivotal roles in the slave trade and are linked to oral health issues among low-income and marginalised communities in Britain. The lack of understanding of diverse dental practices perpetuates misinformation and inadequate dental care for marginalised ethnic groups in Western societies.³⁶ These historical contexts and health disparities are often overlooked in dental curricula, leading to the underrepresentation of minority ethnic groups. This underrepresentation can result in disparities in patient care and have significant implications for the health and well-being of minority communities.³⁷ Decolonizing dental curricula is essential to enhance the cultural competence of dental graduates and requires a reevaluation of curriculum content, delivery methods, community-based dental care, and the promotion of reflective practices.³⁸

The journey towards decolonising Bristol Dental School began with the release of National Student Survey findings in 2019, which revealed instances of everyday racism experienced by some students from staff members.³⁹ Subsequently, two independent reviews were conducted, leading to the implementation of anti-discrimination training for all staff. In the academic year 2021-22, Dr. Nilu Ahmed conducted a comprehensive study using surveys and focus group interviews to explore student and staff perceptions of decolonising the curriculum. Her findings, agreeing with the work of R. Lala²⁰ indicated ongoing experiences of everyday racism among minority staff and students, the prevalence of a 'white' curriculum, and a desire among both staff and students for further education on decolonisation. Bristol Dental School acknowledged the significance of these findings and committed to developing a school strategy prioritising the ongoing decolonisation of the dental curriculum.

In 2023, during a 6-month timeframe, two dental educators (Konrad Spiteri Staines, specialising in oral medicine, and Patricia Neville, a sociologist) collaborated with a learning technologist (Chrysanthi Tseloudi) to develop an educational e-resource tailored for advanced dental undergraduates, specifically those in their fourth year of a five-year dental surgery degree program. The purpose of this resource was to decolonise and refocus oral medicine instruction to centre on ethnically diverse patients. Its objective was to enhance students' understanding and diagnostic confidence in recognising the clinical presentation of oral diseases among ethnically diverse patient populations. Staines sourced material from clinical images of racially minoritised patients with dark(er) skins from his and his team's archives, writing a series of case notes with the images.⁴⁰ The initiative also integrated the oral disease experiences of racially minoritised groups into dental curricula to offer context for the students. It is crucial to acknowledge that this initiative contributes to diversification efforts within the broader framework of curriculum decolonisation, although it does not constitute decolonial work on its own.

The initiative enhances students' perspective consciousness by broadening their exposure to diverse perspectives and experiences nationally and globally. By diversifying the patients they encounter, students gain insight into the varied backgrounds and cultural contexts shaping dental care worldwide. This culturally relevant approach fosters cross-cultural awareness, enabling students to develop a deeper understanding of how individuals' backgrounds and experiences influence their engagement with dentistry. As Ladson-Billings suggests, this knowledge empowers students intellectually, socially, emotionally, and politically, utilising cultural references to impart knowledge, skills, and attitudes. The overwhelmingly positive response from the sample, with ninety per cent expressing strong agreement, underscores the effectiveness of the e-resource in meeting its learning objectives. The utilisation of an interactive, case-based teaching method was deemed particularly suitable for this topic by the respondents.

2.2.1.2 Decolonising the Biomedical Science Curriculum

Adopting a decolonial approach, undergraduate and postgraduate biomedical students were trained and enlisted to evaluate specific modules within the biomedical curriculum, identifying areas for decolonisation, diversification, and enhanced contextualisation. The students compiled the assessment results, reflecting on their experiences through video diaries, providing valuable insight into the project's impact. This innovative method empowered students to contribute to knowledge production within the curriculum actively. Their feedback was shared with unit directors, who had the opportunity to engage and adjust their lecture materials to incorporate decolonisation and diversification. For instance, one lecturer described incorporating discussions on biopiracy into relevant lectures due to this feedback.

In addition to this student-led initiative, T. Lue et al. explored staff and student perspectives on decolonising the biomedical science curriculum. The findings underpinned a gap in awareness between students and staff regarding ongoing decolonisation efforts. Minority ethnic students expressed a sense of underrepresentation in the curriculum compared to their white counterparts. Thematic analysis of qualitative data identified three key themes for a decolonised curriculum: rediscovery, representation, and readiness. It is worth noting that funding from the Bristol Institute for Learning and Teaching (BILT) supported this work and ensured ongoing resources for its development.⁴¹

In 2023, the 3R framework guided additional workshops integrated into an optional unit for second-year biomedical students. These workshops aimed to educate students on decolonisation and how to address social and scientific issues within their disciplines that colonialism's historical impacts have influenced. These issues included discussion about race, gender, and sexuality for students to debate in a constructive space alongside trained facilitators. Feedback from a post-workshop survey was overwhelmingly positive, with 84 % of students expressing enjoyment and a similar percentage recommending the workshop to their peers. A sample of the student feedback revealed that students enjoyed:

“The discussions around science and the impact certain studies and viewpoints and realising how so many studies and theories have a controversial background to them.”

“Bringing awareness to these issues and to the forefront of our minds. It is important to realise our privilege and recognise its impacts on others.”

Through this work, students could engage with all five dimensions of global awareness. Notably, they delved into the 'state-of-the-planet,' as the session shed light on ‘current world conditions, developments, trends, and challenges facing the global community.’ Moreover, through an initial exercise titled “Walking the wheel of privilege,” students, especially those from intersectional backgrounds, had the opportunity to delve into the concept of “double consciousness.” This approach encouraged them to relate the discussed biomedical science issues to their lived experiences, fostering more profound

understanding and engagement. Given the close connection between biomedical science curricula and societal issues, the session effectively tackled significant disparities in representation and economic inequalities between the Global North and South within the curriculum and research. This prompted students to examine their existing knowledge critically and consider what additional information they should be acquiring.

2.2.1.3 Decolonising the Science Curriculum in a UK School

Gandolfi, in 2021 worked collaboratively with a schoolteacher to deliver decolonial concepts to secondary school year eight students. Using topics such as medicine and magnetism aligned with the school curriculum, Gandolfi adopted an intercultural history of science (HOS) and decolonial methods to adapt lessons within a 'storyline strategy.' For example, a lesson based on magnetism explored the use of magnets in ancient and present navigation, which led to global navigation, the impact of travel worldwide on economy, science and technology, politics, and the eventual intermixing of cultures. These topics were founded on efforts to uncover 'hidden' trajectories of 'knowledge and practices taught and learnt with the help of HOS,' revealing the many axes that modern science exists upon.

Gandolfi's research unveiled the transformative potential of a 'decolonial' approach to science curricula, providing students with an avenue to critically examine the contextual framework in which scientific knowledge is situated. This approach fosters a more organic integration of diverse perspectives rather than merely serving as an afterthought to address representational issues in the Global North. By embracing this approach, complex socio-scientific scenarios can be authentically explored and discussed within the curriculum.²³ Through the teacher engaging in conversations with students, the capacity for critical thinking and the ability to draw connections between ideas were vividly demonstrated:

Student H: It is different to other lessons.

Researcher: What is different from your other science lessons?

Student G: In normal other lessons we do not learn about scientists and with these lessons, as you learn about the development, you learn about the scientists, how they work and how things changed.

Reflections by the students and teacher showcase the ability of this work to expand curricula and its ability to teach global ideas and narratives that encompass stories beyond the Western canon. In this work, all five dimensions of the global awareness stated by Hanvey were fulfilled positively resulting in the participant students' exam marks being above the school A's average that year.²³

2.2.1.4 Decolonising the SPAIS Curriculum

In 2020, Lauren Hutfield, a final-year student from the School of Sociology, Politics and International Studies (SPAIS) at the University of Bristol, collaborated with Decolonising SPAIS volunteers and peers to produce an initial report titled “Decolonising the SPAIS Curriculum: Evaluating Mandatory Units.”⁴² This thorough report meticulously examines SPAIS' mandatory modules, mainly focusing on core modules within the undergraduate and postgraduate curriculum. The analysis extends to evaluate lecture content and unit summative assessments, providing a nuanced understanding of the diversity, breadth and depth of the SPAIS curriculum.⁴³ Students carrying out the task were encouraged to become more aware of the diverse pedagogy available and conscious of whose voices have been extracted or ignored from reading lists. A subsequent evaluation in 2021 revealed some progress but continued to highlight a need for addressing race, coloniality, and diversity. Notably, despite the inclusion of these topics in diverse modules like “Politics of the Global South,” only 11 % of the referenced authors are from the Global South. Similarly, in units that address race, such as the “Social Identities and Divisions” module, only 13 % were from a Global Ethnic Majority (GEM) background. Additionally, the report emphasized the need for a curriculum that fosters critical thinking about Eurocentric knowledge and power dynamics played out within the course content.⁴²

While the students conducting the analysis were already familiar with key concepts in their degree related to 'knowledge of global dynamics' and 'awareness of human choices,' this endeavour allowed them to examine these factors through a decolonizing, diversifying, and contextualizing lens, bringing to light issues of race and gender across the globe. One student's comment illustrates the motivation behind their participation in this review activity: “[I joined because of] my frustrations at the Eurocentrism of my curriculum as an international student of colour. after writing an essay on postcolonial thought and sociology...which opened my eyes to a world of scholarship and academic activism that I was shocked had not been a bigger part of my sociological education.” The sentiment expressed by another student further emphasises the significance of this work: "Our curriculum ignores our past, which has massively shaped the society that we see today. I want education to be fairer, less Eurocentric, and more representative of people from all backgrounds.” This underpins the importance of such efforts in broadening students' mindsets, enhancing their global awareness, and deepening their understanding of their course while challenging the perpetuation of colonial narratives.

The method employed by Hutfield et al.¹³⁷, involving students in critically analysing their course content, serves as a model for prospective initiatives within aerosol science training. This method empowers students to identify opportunities for diversification, contextualisation, and decolonisation within their curriculum, fostering an understanding of the social, political, and economic influences on their field of study.

2.2.1.5 Decolonising International Social Work

By engaging university students in conversations rooted in an understanding of the prevailing ‘hegemonic systems’ within the international social work course, Narda Razack was able to facilitate difficult social dialogues with a decolonial approach. Students discussed topics such as child labour in the Global South and differentiating funeral rituals, which challenged their worldview given the mixed cultural terrain of the classroom, consisting of students from the Global North and the Global South. The decolonial approach in these lessons allowed the voices of the students from different corners of the globe to be heard and not silenced while continuing to validate and hold everyone’s experiences within a safe space.⁴⁴

Through decolonising pedagogy that includes the competing social narratives and experiences within the classroom, Razack suggests that the binaries of us/them, good/bad, privilege/subordinate, propagated during the colonial era may be eradicated. The dialogues between students enabled them to shift their former belief systems over time, contributing to greater knowledge and self-awareness. Razack, reflecting on the process highlighted the importance of establishing “our own involvement in global issues,” highlighting ‘it is imperative that our texts and articles traverse global literature in order for our students to gain a broad perspective on social issues’ and provide an opening to challenge the relevance of contemporary education and its traditional pedagogical methods.

Razack's work offers valuable insights into navigating challenging discussions surrounding social, political, economic, and ethical issues within the aerosol science curriculum. By incorporating Razack's methodology, educators can create a supportive learning environment that encourages students to engage thoughtfully with contentious issues, leading to deeper insights and meaningful learning experiences.

2.2.2 Decolonising and Diversifying the Science Working Environment

2.2.2.1 Being BME in STEM Half-Day Conference

The initiative of “Being BME in STEM” was established in 2019 by Lara Lalemi, as a direct response to the challenges faced by Black and Minority Ethnic (BME²) staff and students in STEM fields, which were not being sufficiently addressed by the community. The event comprised of a discussion workshop which facilitated conversations around the experiences of underrepresented students and researchers and proposed strategies for positive action by the university, a panel discussion with EDI champions, and a networking session with local STEM businesses with an EDI statement. The recommendations

² Though BME was used at the time, the preferred term used in 2023 is Global Ethnic Majority (GEM)

generated from the event were subsequently compiled in a report by N. Pridmore, which outlined several primary suggestions (within 1-5 years of implementation)⁴⁵:

- Unconscious bias training for all University staff and students, mandatory for members of committees or interview panels, and for personnel involved in teaching.
- Instigate mentoring schemes aimed at supporting BAME-accepted applicants, students, and staff.
- Provide a diverse curriculum that includes BAME contributions to science and ensures diversity on teaching committees.
- Introduce anonymised applications in the undergraduate recruitment process.
- The presence of BAME role models at all career stages is encouraged to promote diversity and inclusivity. This can be achieved through various means, including organising outreach activities, inviting speakers from diverse backgrounds, and ensuring that the curriculum includes contributions made by BAME individuals to STEM.
-

Many of these objectives were either already being achieved or have since been fulfilled, indicating the positive impact of this workshop on the community. By creating opportunities for open discussions that prioritise the voices of underrepresented individuals, the aerosol community can effectively tackle issues related to the barriers remaining from colonialism, as well as the belonging and inclusion barriers that remain today. This also presents an opportunity to include more Global South voices in the conversation so that we can take a globalised approach to accessibility to the aerosol science community.

2.2.2.2 The Inclusive Research Collective Training Programme

The Inclusive Research Collective founded by Alessia Dalceggio, Dr. Caroline McKinnon and Amber Roguski, and later joined by Luke Burguete, Elle Chilton-Knight, Laura Mediavilla Santos, Rox Middleton and Lara Lalemi, devised a training programme for university researchers and staff to develop inclusive research practices. The course developed in 2022 consisted of five-hour long core training sessions which included self-reflection exercises, fun interactive activities, videos from external researchers and facilitated breakout rooms. The sessions culminated in a practical workshop run with Zebera Ltd. For course participants to develop an idea around inclusive research practice and how they wish to develop this within their own department and/or research group. The core sessions were set out as follows:

- Session 1: Enhancing Inclusive Research Practice through Contextualising Research. Primary aim was to contextualise research within the university structure that will explore the history of research, epistemology, ontology, and methodology.

- Session 2: Reflexivity for Researchers – understanding the impact of our personal identity on research. The primary aim was to introduce the concepts of reflexivity and positionality for researchers.
- Session 3: Inclusive Study Design & Data Collection. The primary aim was to explore sources of bias and the role these play in study design and data collection and introduce approaches to inclusive study design.
- Session 4: Inclusive Data Analysis & Research Dissemination. With the primary aim of exploring sources of bias and the role these play in data analysis and publication.
- Session 5: Beyond the Publication: Wider Impacts of Our Research. With the primary aim of discussion, the responsibility for what subjects and questions get researched and the ways in which that research is conducted.
- Session 6: Post-training Practical Workshop

This type of training program has the potential to be implemented by multiple aerosol science research institutions as a way to promote a holistic understanding of inclusive practices and environments in STEM for their students, researchers, and staff. These training sessions can be incorporated into the pre-CDT training for new students and partners, providing them with a better-informed and more contextualized perspective right from the outset.

2.2.2.3 Inspirational Bristol Scientists Board

The Inspirational Bristol Scientists Board, shown in Figure 2-2, honours the remarkable achievements in research, teaching, and community contributions of eight undergraduate and postgraduate students in STEM disciplines across the University of Bristol.⁴⁶ Launched by Lara Lalemi and Fred Manby in late 2019, the board was strategically positioned in the University of Bristol School of Chemistry building, adjacent to one of the busiest lecture theatres, and garners visibility among thousands of students and staff weekly. The board seeks to champion exemplary practices in academia, offer recognition to nominated individuals, and enhance visibility within the academic community. Individuals were chosen based on their achievements rather than their identity, though their identity played a role in the initial nominations. While this initiative does not replace efforts to decolonise the scientific working environment, it represents a step towards diversifying the university's academic landscape. In a world marked by a history of colonial oppression, the visual representations of scientists from across the globe that are not distorted or misappropriated become increasingly important.⁴⁷ By challenging the Eurocentric portrayal of prominent scientists commonly found in textbooks and throughout the university, the board provides a crucial visual representation of often marginalised faces who may not have received recognition for their contributions to science and engineering. This initiative quickly gained prominence across STEM departments university-wide, raising awareness of the

accomplishments of students and staff from different backgrounds within the Global North and South. The work here will be reflected in the decolonising educational initiatives detailed in Chapter 7.

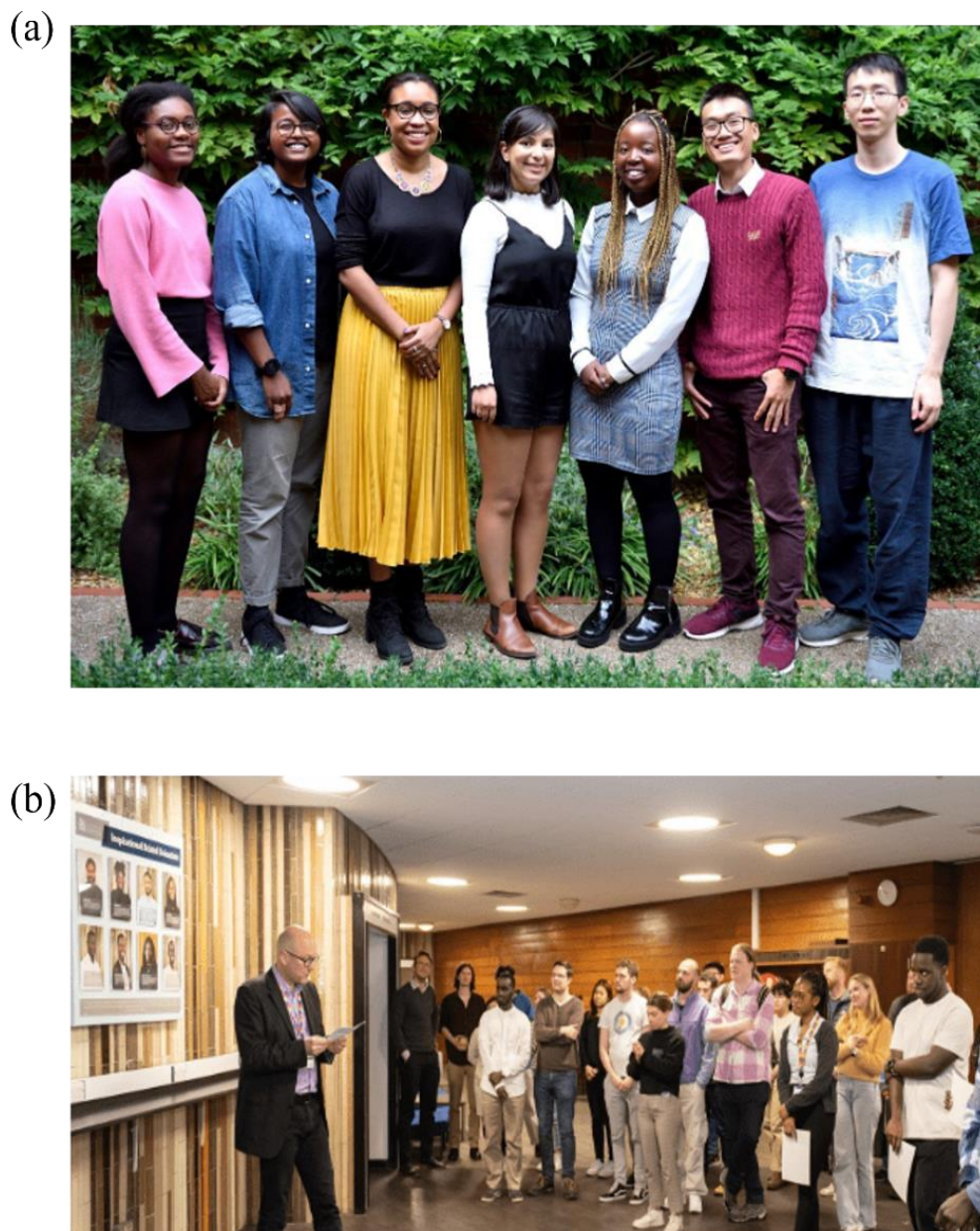


Figure 2-2: Images of (a) the 2019 eight inspirational Bristol scientists and (b) the awarding ceremony for the inspirational Bristol scientists in 2023. **Photographs taken by Bhagesh Sachania.**

2.3 Decolonising Aerosol Science Curriculum and Teaching Activities

The section herein describes a method centred on decolonising, diversifying and contextualising knowledge disseminated within the EPSRC Centre for Doctoral Training (CDT) in the Aerosol program. This work has a two-pronged approach: first, it includes a workshop that encourages students to discuss the social, political, and economic issues intersecting with aerosol science. By providing a space for discussion and learning, students can enhance their self-awareness and global consciousness using the Academic Wheel of Privilege and the framework within a workshop setting. The latter part of the

workshop consists of a facilitated discussion which draws inspiration from the Being BME in STEM half-day conference and work by Biomedical sciences team the University of Bristol, described in Section 2.2.1.1. and Section 2.2.2.1, respectively. The second prong is through the adaptation of course content and assessment tasks. This adaptation prompts students to engage in introspection and pose challenging questions throughout the program content, ensuring that this work is not perceived as merely an ‘add-on’ but rather an integral component of a scientist's everyday thought process. The approach here is crucial given the dynamic nature of aerosol science, which intersects with various disciplines and sectors, including medicine, environmental science, food storage, and the transmission of viruses and bacteria. Ultimately, by nurturing the self and global awareness of CDT postgraduate students, this initiative aims to prepare them for conducting inclusive scientific research, thereby contributing to a more equitable future in the field.

The EPSRC Aerosols CDT program, reflected in Figures 2-3 has been chosen for analysis because Reid and co-workers have provided fertile ground to build these conversations. The course already adopts a diverse and inclusive approach to its education and has ‘revolutionised’ aerosol science training.⁴⁸ Table 2-1 shows the nine PGR competencies guiding the course, confirming that there is an appropriate curriculum for this decolonial thinking and approach. For example, competency six states the program should ‘act in congruence with professional and ethical values and manage ethical dilemmas in formulating scientific solutions’; hence the course includes a UKRI-responsible innovation task to consider the broader impacts of their research. It is here where the framework will be implemented.

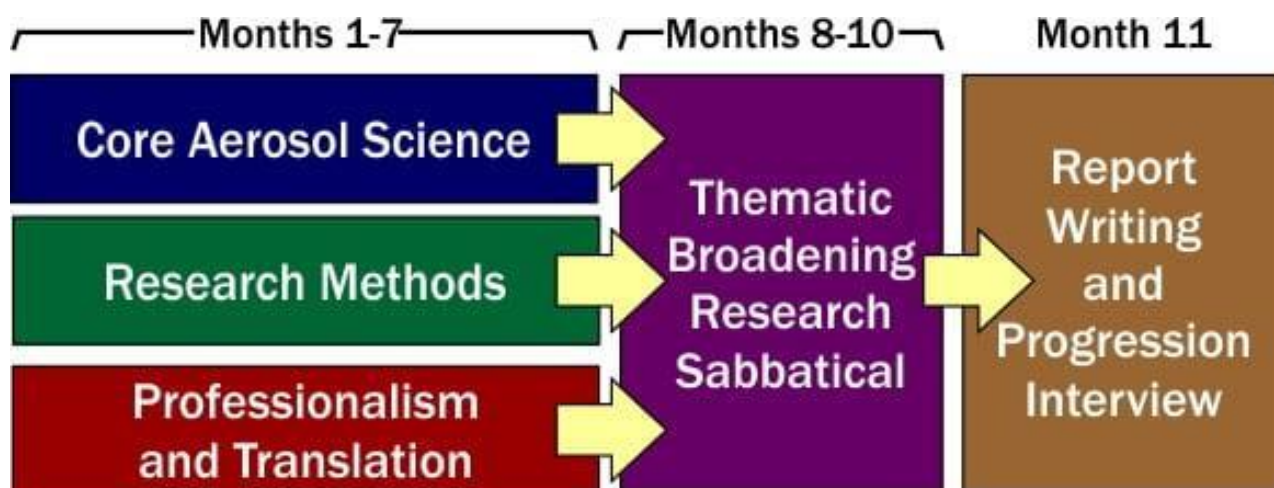


Figure 2-3: A structural overview of the EPSRC Aerosol CDT training program⁴⁸.

Table 2-1: The nine postgraduate research competencies set by Reid et al.⁴⁸

1. Apply theoretical knowledge of aerosol science across a range of problems of a chemical, physical, biological, or technological nature.

2. Undertake independent design and conduct experiments/models with technical mastery, as well as analyse and interpret data.

3. Identify, formulate, critique, and solve research problems within their specialised context to advance the understanding of aerosols.

4. Develop or adapt advanced methodological approaches to contemporary problems, recognising the complexity and tolerating the ambiguity that arises in real-world systems.

5. Synthesise new approaches to meet an identified outcome within realistic constraints such as economic, environmental, social, political, ethical, safety, manufacturability, and/or sustainability.

6. Act in congruence with professional and ethical values and manage ethical dilemmas in formulating scientific solutions.

7. Function effectively and confidently in multidisciplinary teams, acting autonomously and taking responsibility for the scientific activity of others.

8. Communicate and share research knowledge to both expert and non-expert audiences and guide the learning of those from outside their discipline.

9. Manage personal intellectual development as a self-critical, reflective scientist with the agility to respond to new challenges.

2.3.1 Methodology of Delivering the Framework

At the Variety in Chemistry Education and Physics Higher Education Conference (VICEPHEC) in 2019, the Decolonising the Science Curriculum working group was established. Comprised of educators from various institutions in the UK and the University of Bristol, this group was formed to initiate conversations, mobilise action, and educate the scientific community on the importance of decolonisation and diversification within STEM education. What initially began as a single workshop evolved into eight workshops conducted at universities throughout the UK. These sessions delved into the impact of European colonialism on the scientific field, explored the concept of decolonising the curriculum and environment, and facilitated discussions where participants could share their concerns and propose alternative approaches. This educational initiative within the scientific community has yielded a streamlined decolonising STEM framework, depicted in Figure 2-2. This framework empowers educators to scrutinise their curriculum and practices, and by doing so, students can explore the historical and ongoing impacts of colonialism on their subject matter.

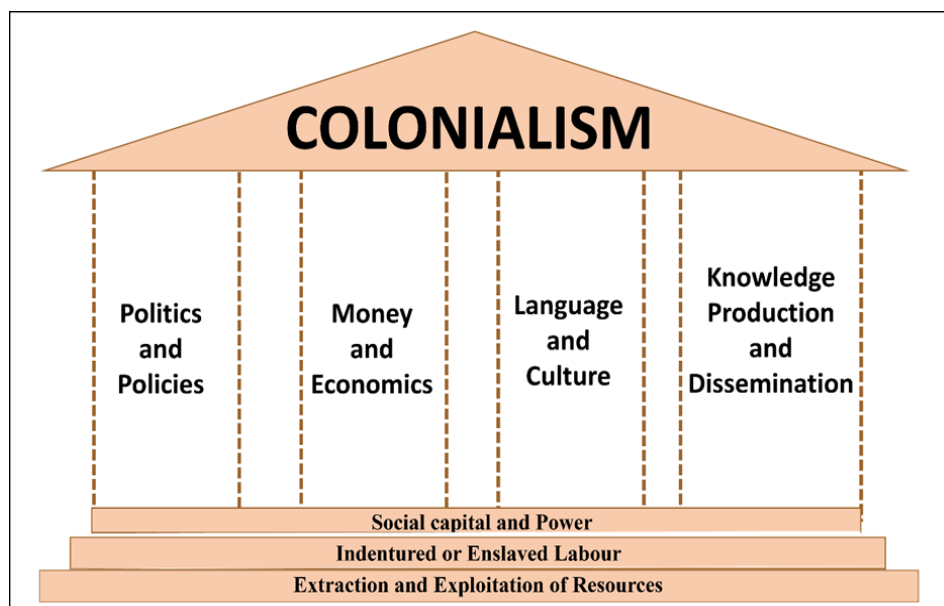


Figure 2-4: Simplified depiction of the elements upholding coloniality for academics, non-academics, and students to view their curriculum, teaching materials and research devised by the DSCWG.

The four pillars illustrated in Figure 2-3 signify the key areas where coloniality has exerted its influence: politics, economics, language/culture, and knowledge production and dissemination. A method has been developed to deliver the content to aerosol CDT students using this framework and the Academic Wheel of Privilege illustrated in Figure 2-4.

2.3.2 The Decolonising Aerosol Science Workshop

The workshop includes an Academic Wheel of Privilege exercise followed by group roundtable conversations with social, political, economic, and ethical scenario questions related to aerosol science for students to discuss and record their findings.

The Academic Wheel of Privilege detailed in Figure 2-5 encompasses twenty identity types across seven categories: lifestyle and culture, caregiving, education and career, gender and sexuality, race, health and well-being, and childhood and development. These identities are represented as circles connected to three concentric rings (outer, middle, and inner) of "identity" circles, with increasing privilege towards the centre. This configuration creates a funnel-like appearance, where proximity to the centre correlates with greater privilege levels.

Within a decolonising the aerosol science program workshop, the wheel is used as a primary discussion provocation as it is here where students begin to self-analyse and develop self-awareness concerning conducting scientific research. Students are asked to personally walk the wheel of privilege, relating it to themselves to interrogate their positionality, but are at no point encouraged to reveal theirs to others. In this work, positionality refers to the socio-political context that shapes an individual's identity based on factors such as race, class, gender, sexuality, and ability status. It also encompasses how one's identity impacts and may predispose one's perception and perspective of the world.⁴⁹

The students are asked three questions:

1. How does walking the wheel of privilege make you feel? Describe in three words.
2. How might one's position on the Academic Wheel of Privilege impact their experience as a science student within a Global North university?
3. How might one's position on the Academic Wheel of Privilege impact their experience as a scientific researcher across the globe?

Question one enables students to discuss emotions such as guilt, shame, sadness, and discomfort, which is often conveyed as a sticking point in introducing decolonising work.⁵⁰ By discussing this earlier with their peers, students are provided a safe space to recognise these emotions and have them acknowledged, which is a powerful position to start from. Questions two and three ask students to externalise their thinking, asking them to reach beyond their backgrounds and experiences to consider others who may not experience the same privileges. This provides a good foundation for discussion of the social, political, economic, and ethical influences on aerosol science and research.



Figure 2-5: The wheel of privilege showing the twenty identity types across seven categories: lifestyle and culture, caregiving, education and career, gender and sexuality, race, health and well-being, and childhood and development. **Reproduced under CC-BY Attribution 4.0 International from Elsherif, M. M., Middleton, S. L., Phan, J. M., Azevedo, F., Iley, B. J., Grose-Hodge, M., Tyler, S., Kapp, S. K., Gourdon-Kanhukamwe, A., Grafton-Clarke, D., Yeung, S. K., Shaw, J. J., Hartmann, H., & Dokovova, M. (2022). Bridging Neurodiversity and Open Scholarship: How Shared Values Can Guide Best Practices for Research Integrity, Social Justice, and Principled Education.**⁵¹

Figure 2-6 presents a series of scenarios stimulating student discussion and critical thinking. These scenarios are crafted to prompt students to reflect on their research practices within diverse contexts and experiences. By creating this space for contemplation, students are encouraged to consider how their research context and delivery may vary among different groups. This approach is aligned to foster students' global awareness and promote a deeper understanding of the societal implications of their research endeavours.

Scenario One

In developing countries like Nigeria, there exists a significant gap in understanding PM pollution. Abulude et al. aimed to address this gap by conducting PM 2.5 and PM10 aerosol studies across Nigeria. However, they noted a limitation in their study as the data was compared against WHO standards rather than Nigerian Environmental Standards, and much of the analysis was conducted outside the country.

As part of your research team, you aim to support Abulude in establishing these standards and comprehending the factors contributing to aerosol production across Nigeria, encompassing both rural and urban areas, utilizing cutting-edge instrumentation. Data collection will entail studies conducted in rural sacred land alongside rural communities.

In what ways could you take a decolonial/inclusive approach to undertaking this research project? Consider the different stages of the scientific approach, and what concerns and opportunities arise in each.

Scenario Two

In 2020, the Guardian reported on the landmark ruling of the death of Ella Kissi-Debrah who, having been living in Lewisham (ranked 7th in the most deprived areas in London in 2019), was determined to have been exposed to nitrogen dioxide and particulate matter (PM) pollution in excess of World Health Organization guidelines, the principal source of which were traffic emissions.

You and your research team have been tasked by combined UK authority to investigate and explore the disparities in exposure to air pollutants among different socio-economic groups and the resulting health outcomes.

In what ways could you take a decolonial/inclusive approach to conducting this research project with different communities in different socio-economic groups? Consider the different stages of the scientific approach, communication of research, and what concerns and opportunities arise in each.

Scenario Three

The nasal olfactory region is a potential route for non-invasive delivery of drugs directly from the nasal epithelium to the brain, bypassing the often impermeable blood-brain barrier. However, efficient aerosol delivery to the olfactory region is challenging due to its location in the nose.

You and your team wish to explore the use of bi-directional pulsatile airflow conditions to enhance the delivery of aerosols to the olfactory region for targeted drug delivery. This investigation is conducted using a computational fluid dynamics (CFD) model based on the specific nasal geometry of individual patient. Given that the nasal geometry varies amongst ethnic groups, how would you go about conducting this study so that is representative and inclusive. What ethical consideration need to be made in conducting this study.

Figure 2-6: Three scenarios that could be discussed within an aerosol science-related workshop to encourage students to think about how they may conduct scientific research bearing in mind the social, political, and economic sphere it exists within.

2.3.3 Adaption of the Aerosol Science Program Content

The framework depicted in Figure 2-3 can complement the development of educational materials. Figure 2-7 outlines the sequential stages of thought that teaching material developers can adopt to incorporate decolonial, diversified, and contextualised elements into their courses. This framework guides developers to:

1. Reflect on how colonial politics, economics, language/culture, and knowledge production and dissemination impact on what and how we teach and conduct research.
2. Consider how these factors may serve as barriers to the involvement of marginalised groups in science research and curriculum development, both in the Global North and Global South.

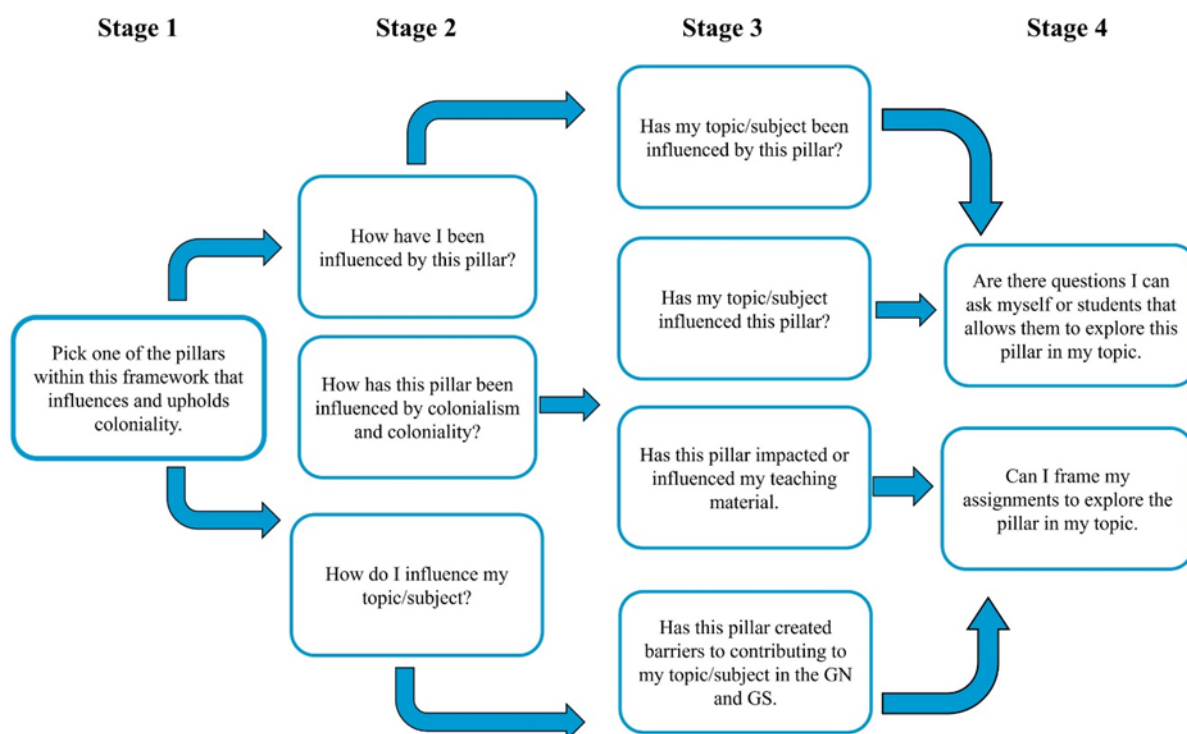


Figure 2-7: The simplified decolonial framework to provoke critical reflection of the self and one’s course.

Concerning the aerosol curriculum, the framework can be used to develop the program content, adapting particular areas using a research task method. For instance, in the core aerosol curriculum, developers can encourage students to investigate economic barriers to research from Global South and North perspectives or explore how language and culture affect aerosol science knowledge dissemination. The effectiveness of this approach stems from its ability to foster curiosity, facilitate critical examination, and stimulate inquiry into global issues. In this section, examples will be detailed, illustrating how to integrate these fundamental factors into developing the Aerosol Science CDT curriculum.

2.3.3.1 Knowledge Production and Dissemination in Aerosol Science

Aerosol science research and who produces the research holds immense global importance as it contributes to advancing understanding developing and managing the environmental impacts of pollution and climate change.^{128,138} For example, research on the viscosity of atmospheric organic aerosols is central to rationalising and predicting their atmospheric impacts on climate, visibility and air quality. Air quality research has contributed to legal restrictions such as London's congestion charging model, or odd-and even number plate bans in cities such as Madrid or Rome designed to prevent vehicular transport emissions.^{138,139} By incorporating tasks that enable university students to connect their fundamental aerosol science to policies and sectors that benefit from that knowledge, this method allows students to explore what work does the knowledge they produce do and who does or does not benefit from this work. Further research could delve into how the distribution of knowledge and power influences a country's capacity to conduct aerosol research and shape air quality policies or economic growth. Below is example of additional proposed tasks that students could undertake as part of this investigation:

Task one: Aerosol science is a rapidly expanding field worldwide. Explore the distribution of the global production of aerosol and atmospheric scientific knowledge and identify how has colonisation has contributed to the distribution.

Possible answer: In recent decades, there has been a notable surge in the number of scientific articles focusing on aerosol research, driven by increased investment from numerous countries in investigating various aspects of aerosols. This includes studying their chemical composition, formation and transformation mechanisms, and climate and human health impacts. Xie et al. in 2008 conducted an analysis of the ISI database on the production of aerosol science-related papers spanning from 1991 to 2006, revealing that the seven major industrialised countries (G7: Canada, France, Germany, Italy, Japan, the UK, and the USA), led by the USA, dominated total world production during that period.⁵² In 2015, the top ten world publishers collectively accounted for 54 % of the revenue from the 57 companies listed.^{52,53} Headquarters of major publishers, scholarly journals, and scientific societies and associations are predominantly located in the Global North. Similarly, a subsequent examination of 99,700 academic papers published in 2020, retrieved through a WebScience⁵⁴ search for 'aerosol science', revealed that 67 % of the papers and authors originated from the Global North (North America, Australia, and Europe). While scientists from developing countries have increasingly focused on aerosol research in recent years, their contributions still represent a growing but relatively smaller proportion of global publication output.

This unequal division of labour is highlighted by Kreimer and Zabala⁵⁵ where collaborations between Northern and Southern scholars often result in Northern scholars gaining publishable knowledge. In

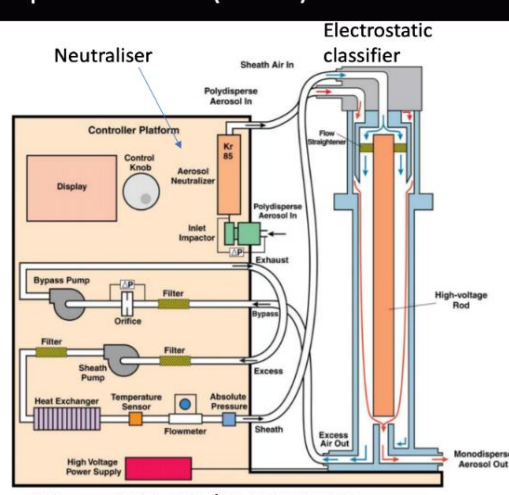
contrast, Southern scholars are relegated to the role of 'sub-contractors', producing knowledge that may not be deemed relevant in addressing local issues. Citation analysis (reviewed 99,700 studies and their country of origin¹⁴⁰) further underscores the unequal distribution of world knowledge production, revealing a tendency for scholars in the Global North to cite their own work and focus inward primarily. In contrast, scholars in the periphery predominantly cite publications from core countries. These dynamics significantly impact the aerosol science community and contribute to broader disparities in global knowledge production.

2.3.3.2 The Economy and Access to Funding in Aerosol Science

In Figure 2-8, a slide from the aerosol CDT teaching material discusses the instruments used to expand the study aerosols in the atmosphere. In the case of aerosol science, instruments include aerosol generators, particle counters, and analytical instruments that are expensive and require government funding to purchase. This economic barrier renders aerosol research difficult for scientists from low-income backgrounds or institutions with limited funding to access. While the primary focus of the lesson is to introduce aerosol study instruments, students can also be prompted to contemplate the feasibility of conducting aerosol-related research on a global scale given the barriers put in place by colonialism. This includes considering the challenges and obstacles associated with such research and brainstorming potential solutions. Another example of where this work could be effective is during the lesson on bioaerosols as shown in Figure 2-9. Tasks could centre around intersectional topics such as how socioeconomic and living status correlates to the increased likelihood of disease aerosol transmission or explore how bioterrorism and disease transmission benefited the colonial era.

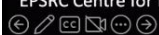
Scanning mobility particle spectrometer (SMPS)


- ~15 nm to ~1000 nm (1 μm)
- Use electrical mobility to size select.
- Poly-dispersed aerosol acquire a characterised charge distribution in a neutraliser
- They are then passed through the electrostatic classifier where only particles with the right charge and mass will make it to the exit.
- The number of aerosol at this size are then counter in a separate condensation counter where they are grown to a size where they can be detected with light.
- Watch this from 1 min 7 s: <https://www.youtube.com/watch?v=6yqdKTdlyJl>



C Kuang, 2016, DOE/SC-ARM-TR-147

EPSRC Centre for Doctoral Training in Aerosol Science





Engineering and Physical Sciences
Research Council

Figure 2-8: A lecture on the ‘Introduction to measuring aerosol particle distributions’ delivered by Dr. Ben Murray as part of the CDT Aerosol Science program.

(a) **What is a bioaerosol?**

- An aerosol of biological origin, including airborne suspension of viruses, pollen, bacteria and fungal spores, and their fragments
- Viable and non-viable.
 - Non-viable bioaerosols are not currently alive and, therefore, cannot multiply - can be allergens
 - Viable bioaerosols are living organisms that demonstrate microbiological activity and have the potential to multiply - can be infectious

(c) **Why bioaerosols are important?**

- Impact on the environment
 - CCN, ice nucleation
- Disease transmission
 - SARS, legionella, influenza
- Livestock and crop pathogens
- Bioterrorism
- Production facilities
 - Pharmaceutical, hospitals, food

Activity	Approximate particle count	Units
Smoking	40,000	Per cigarette
Boiled exhalation	20,000	Per breath
Yawning	1,000	Per event
Coughing	710	Per cough
Talking	36	Per 100 words

(b) **Research challenges**

Santl-Temkiv et al. *Aerosol Science and Technology*, pp.1-27.

(d) **Microbiomes of the Built Environment**

Figure 2-9: Lecture from the CAS 2.6 module on the ‘Introduction to bioaerosols’ delivered by Ian Colbeck. (a) slide four on What is a bioaerosol? (b) slide five on Why bioaerosols are important (c) slide 8 on the Research Challenges bioaerosols present and (d) slide 10 on the Microbiomes of the Built Environment.

Task one: Identify 2-3 economic or financial obstacles to conducting aerosol and atmospheric science studies across the world, compare different nations and continents. Investigate what continues to exacerbate these obstacles?

Possible answer: In a study by Abulude et al. in Nigeria¹⁴¹, the collected aerosol samples needed to be analysed abroad or outside the region, away from the site of collection, due to the inability to measure the samples where they were taken as a result to a lack of equipment, expertise, and funding. In 2023, Garland et al. emphasised the urgent need for comprehensive atmospheric science studies in Global South countries to address critical environmental issues, including various Sustainable Development Goals (SDGs).^{56,57} Garland highlighted a significant factor contributing to the disparity between research output in the Global North (GN) and Global South (GS) regions: the funding imbalance.^{53,58} Research spending in countries like China, the USA, and Europe is steadily increasing, but it remains stagnant or declining in regions such as Latin America, the Caribbean, and Sub-Saharan Africa. They pointed out a strong correlation between research expenditure per capita and research output, citing examples from the geosciences field where high-income countries spent significantly more per capita than African countries. For instance, in 2017, high-income countries spent an average of US\$1064 per capita on research, while Africa spent only US\$42 per capita.⁵⁹ This lack of funding also impacts the

number of researchers per million inhabitants, with Sub-Saharan Africa having significantly fewer researchers than Europe and Northern America. Specifically, while Europe and Northern America have approximately four thousand researchers per million inhabitants, Sub-Saharan Africa only averages 494, which is almost ten times lower. Consequently, the scientific capacity in Global South regions remains limited, hindering their ability to research to inform policies. Furthermore, the insufficient funding contributes to the perception that research produced in the Global South is less rigorous and applicable globally, highlighting a disparity in how research from different regions is perceived. Wild notes, “When researchers in the global North produce research, it is understood as if it was universal, whereas when research is done in the global South, then it is only local and applicable to those settings.”⁶⁰

Task two: Investigate ways the Global North aerosol science community can improve the ability to measure aerosols in lower-income countries. Discuss the power dynamics and benefits/costs of such a partnership.

Possible answer: International collaborative efforts whereby support from Western institutions helps to fund and train Global South researchers with the additional incorporation in research papers can begin to lower the economic barriers to aerosol and atmospheric chemistry research. Andarade-Flores et al. describe this form of action taken by the Commission on Atmospheric Chemistry and Global Pollution (iCACGP) and the International Global Atmospheric Chemistry (IGAC) Working group to improve research in the Latin America and Caribbean (LAC) region in 2013. Though research has been conducted in the LAC region for decades, the amount and quality of data collection and processing remains inconsistent, along with the number of local scientists needed to acquire the data. Additionally, international projects such as the Mexico City Metropolitan Area (MCMA) field campaign have increased scientific knowledge and capacity for research whilst acknowledging the contributions of local and international scientists in scientific publications.⁶¹

In West Africa, the West African Science Service Centre on Climate Change and Adapted Land Use (WASCAL) is a notable example of concerted efforts in climate-focused research over the past decade. Supported by the German Federal Ministry of Education and Research (BMBF), WASCAL has been instrumental in training young scientists in various climate change and atmospheric chemistry disciplines through its postgraduate and doctoral programs across the region. Additionally, WASCAL is a crucial hub for disseminating information and knowledge at local, national, and regional levels, offering valuable insights to its member countries in West Africa. These efforts aim to address the challenges posed by climate change and to formulate comprehensive strategies for building resilient and sustainable socio-ecological landscapes in the region.

Similar to Razack's work, these tasks allow students to contemplate potential disparities between the Global North and South, especially concerning the global allocation of funding. It is well-documented that colonialism has impacted the distribution of research funding and the availability of human

resources.^{142,143,144} Therefore, these tasks allow students to contextualise the impact of colonialism while also encouraging them to explore potential solutions they may contribute to in their careers.⁵³

2.3.3.3 Policies and Aerosol Science

Powel et al. highlighted that over the past decades since moving from an industrial to a knowledge-based economy, developed countries have expanded their scientific activity to benefit national economic development.^{62,63} This has increased the ability to research to inform environmental and healthcare policies. In ILO 6 of the CDT teaching material, particle sizes and their health impacts are discussed; see Figures 2-10. Students could be asked to consider what work knowledge of the health impacts of aerosols does for a nation and policies developed by that nation. This will strengthen students understanding of how the fundamental research they conduct can impact wider society.

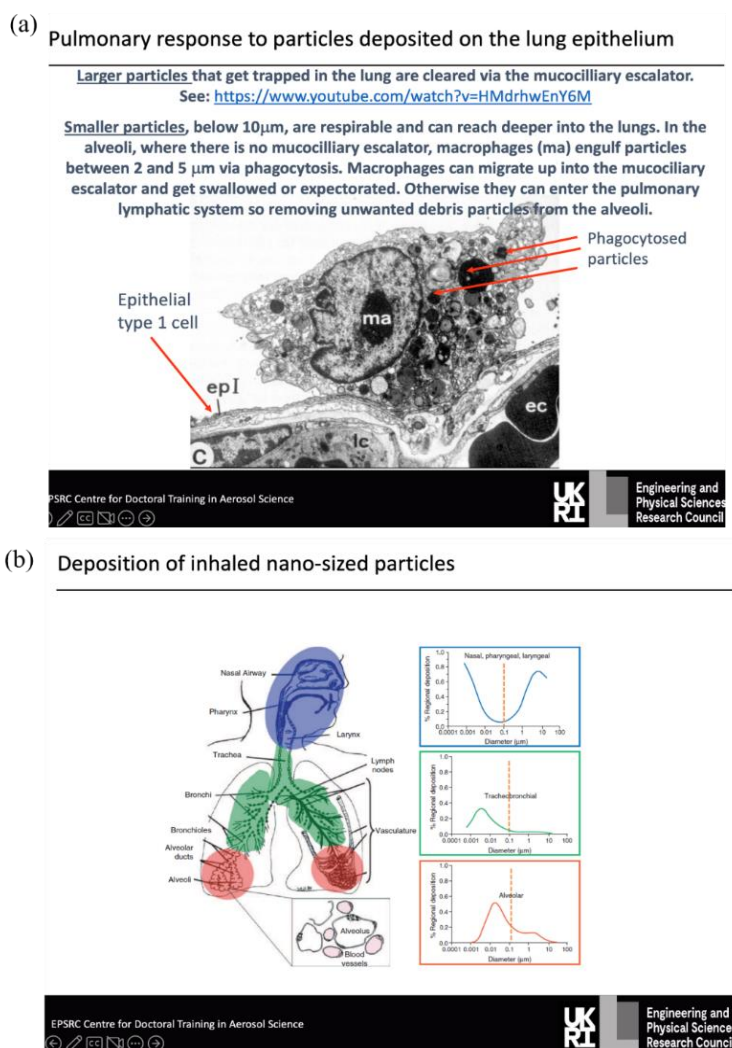


Figure 2-10: The ILO 6 lecture on the Interactions of particles with the respiratory epithelium delivered by Terry Tetley from National Heart and Lung institute at Imperial College London from the Aerosol CDT course, (a) slide 3 discussing the pulmonary response to particles deposited on the lung epithelium and (b) slide 4 discussing deposition of inhaled nano-sized particles.

Task one: How has the ability of a Western country like the UK to conduct aerosol science research impacted policies developed around PM_{2.5} and PM₁₀? Explore how this can vary between different communities across the world.

Possible answer: Haddad et al. highlighted how advancements in aerosol science contribute to our understanding of the health effects of outdoor particulate pollution, leading to formulating policies to mitigate these risks. In the UK, chronic exposure to ambient air pollution is estimated to result in 29,000 to 43,000 deaths annually.⁶⁴ These pollution levels primarily stem from emissions like greenhouse gases produced by burning fossil fuels. Measures to curb greenhouse gas emissions, such as transitioning to renewable energy sources like wind and solar power, adopting electric vehicles and enhancing energy efficiency, can yield significant health benefits by improving air quality. A review focused on the UK suggests that, overall, the health impacts of ambient air pollution are projected to decline in the future due to policies aimed at achieving net-zero emissions and implementing emissions controls. Policy initiatives like the Gothenburg Protocol, the Air Quality Directive of the European Parliament and Council, and Air Quality Standards Regulations (2010) have led to improved air quality levels in the UK since the 1970s. These improvements, primarily driven by policy interventions, have resulted in a 56% reduction in UK-attributable mortality due to exposure to PM_{2.5} and a 44 % reduction due to exposure to NO₂. Furthermore, a study by Macintyre et al. indicates that mortality rates are expected to decrease significantly in the coming decades as a result of current policies aimed at reducing emissions, with projected reductions of 31%, 35%, and 37 % by 2030, 2040, and 2050 respectively, assuming no changes in population.³⁴

2.3.3.4 Language, Culture and Aerosol Science

Effective communication and dissemination of aerosol science research hinges on understanding language and culture, which can significantly affect public engagement with aerosol-related concepts worldwide.⁶⁵ Governmental decisions on PM levels often take a technocratic approach, overlooking the intricate interplay of psychological, cultural, social, economic, and political factors. This approach risks encountering resistance or limited support from the grassroots level, such as what is encountered when implementing clean air zones or changing cultural practices such as wood burning.⁶⁶ Therefore, addressing the role of communication and cultural understanding early in a scientist's career is essential to their development as a science communicator.

As part of their training, CDT students engage in public outreach, making it crucial to discuss and grasp the impact of language and culture on public reception and perception of aerosol science research and policies. By setting tasks for students to discuss the importance of culturally sensitive communication in conveying policies and regulations, a new generation of globally aware students who are capable of effectively disseminating knowledge to diverse audiences could be raised.

Task one: Given the universalism of the English and western scientific language as a result of colonialism, provide examples of why the use of language becomes important in the communication of scientific research across the world.

Possible answer: *Example one-* Abulude and colleagues emphasise the importance of communicating scientific knowledge about the particulate matter to the local community to help them comprehend the potential health consequences.⁶⁷ Therefore, there is a need to enhance the dissemination of information and utilising local languages as a ‘medium of communication’ could assist in conveying the message effectively to individuals with diverse backgrounds. This would enable them to understand better the environment and the air quality management systems that are implemented in their area.

Example two: Language plays a pivotal role in comprehending aerosols and aerosol science worldwide. Aerosols have gained significant attention in the media due to their potential role in transmitting SARS-CoV-2, the virus responsible for COVID-19, highlighting the importance of a universally understood term for public health implications. However, a discrepancy exists between the public's understanding of the term and its scientific definition. While the public commonly associates "aerosol" with substances in pressurised containers like hair spray, scientists define it as small particles suspended in the atmosphere. Smith et al.⁶⁸ suggest this disparity may not dramatically alter public perception of aerosol science but it can lead to confusion and impede a comprehensive grasp of aerosol science concepts, representing a missed opportunity for enhanced public understanding. Improved communication and carefully chosen language to the public around aerosols and their significant impact on the climate, air quality, public health and drugs and medicines, particularly those from marginalised groups, could result in a better public perception and understanding of their role in our society.

Example three: Communities that are already marginalised often bear the brunt of environmental hazards and experience poorer public health outcomes for various reasons. Language plays a significant role in exacerbating this disparity, particularly considering that most COVID-related research is published in English, a language that may not be the first language for many affected communities. Moreover, scientific discourse is predominantly shaped by the dominant culture, further marginalising non-English speakers. By centring community leaders and involving them in interpreting research findings, marginalised communities can reclaim their knowledge, authority, and agency. A study by Polk and Diver demonstrated the value in engaging students in open and clear communication with the public and community leaders on environmental injustices.¹⁴⁵ The work was grounded on equity framing principles, which include asking science communicators to (1) become aware of their positionality and partial perspectives, (2) name sources of inequity that arise from uneven power relations, and (3) find intersections with initiatives that are rooted in the experiences of disadvantaged communities. The use of language and cultural awareness was vital to the success of the project and led

to heightened social relevance of scientific findings, increased trust in scientific knowledge, and a more comprehensive understanding of global issues.⁶⁹

Task two: Investigate three potential benefits of cross-cultural scientific research for the aerosol science community and decolonial collaborative practices.

Possible answer: Jenkins et al. relay a project conducted between the US and Senegal whereby NASA and the National Science Foundation funded the participation of US and Senegalese students to design, implement and maintain a rain-gauge network and a site for radar measurements. Students from the US not only learnt new radar measurement skills but also about the culture of Senegal, such as the music, customs and language, alongside the urban challenges facing Senegal, such as poverty, public health, electricity, and access to fresh water. This initiative was a positive step toward increasing social and cultural awareness among students and improving the scientific skills of student researchers.⁷⁰

The paper by M. Finucane explores the nature of creating climate science policies and actions by the government. Finucane proposes that while mitigations should be based on ‘sound science’ it must also include an ‘understanding of how the science is interpreted and translated into action in society’.⁷¹ Traditional environmental knowledge can be combined with modern-day technologies to increase the success of local people in dealing with the changing climate. Given the connection Māori and Samoan communities have with nature, the climate and spirituality, Finucane suggests policymakers should work with scientists, cultural leaders, theologians, philosophers and community groups to ‘identify and speak meaningfully’ about the changes that need to be made to reduce emissions with key stakeholders. This analysis by Finucane would enable postgraduate students to see how language and cultural understanding play a significant role in communication and subsequent investment in climate mitigations and comprehension.

The tasks and examples presented in this section demonstrate how adopting a decolonial and contextual approach to curriculum development can naturally enhance global awareness. While not all aspects of the aerosol science curriculum may integrate decolonial perspectives, wherever feasible, it is encouraged to provoke deeper thought and reflection among students.

2.4 Conclusion

Colonialism has profoundly shaped the landscape of science, scientific inquiry, and the scientific community, influencing our perceptions of valuable knowledge, who conducts research, and the scope of what is considered legitimate knowledge.^{72,73} Research by Harris et al. reveals how US public health researchers sometimes evaluate research abstracts from low-income countries less favourably.⁷⁴ Further studies by Harris indicate that a majority of participants associate "good research" with wealthier countries over poorer ones.⁷⁵ Implicit biases like these may disadvantage research from economically disadvantaged nations in areas such as research evaluation, evidence-based medicine, and the diffusion

of innovations.⁷⁵ Moreover, traditional indigenous knowledge has often been marginalised or derided when juxtaposed with Western science, as noted by Ora Marek-Martinez⁷⁶ in a Science article. Western scientific knowledge is often perceived as objective, quantitative, and rigorous, while traditional knowledge is seen as subjective and qualitative. However, it is acknowledged that Western science tends to isolate its subjects from their broader contexts by confining them to simplified, controlled experimental environments, thereby divorcing scientists from nature, the very object of their studies. In contrast, traditional knowledge is deeply rooted in context and local conditions.⁷⁷ These findings underscore the pervasive effects of coloniality on the scientific research community, including within aerosol science. To counter these narratives and challenge the hegemonic power structures established by colonialism, we propose embracing decoloniality as a potent means of dismantling and reconstructing a more globally aware scientific community that embraces diverse knowledge systems, perspectives, and experiences.

This chapter advocates for adopting a decolonial framework, including a workshop and curriculum development, to cultivate global consciousness among students and equip them with the skills needed to address humanity's future challenges. The proposed workshop prompts students to critically assess their positionality, the dissemination of knowledge within their field, and the contextual factors influencing knowledge production. By engaging students in discussions and tasks related to the impact of colonialism, they gain insights into how colonial legacies affect aerosol science and hinder participation from 'Global North' institutions and marginalised groups. Moreover, it encourages students in the Aerosol Science CDT to broaden their perspectives beyond the Eurocentric lens by presenting them with questions and scenarios to explore.

In the context of the framework created by the DSCWG, this chapter briefly highlights the social, political, economic, language and cultural barriers that impede participation in aerosol science, allowing students to grasp who can and cannot engage in aerosol science research due to inadequate funding and local policies. Access to funding is fundamental to the ability to conduct research. Globally, funding is skewed in favour of Global North countries, resulting in their increased ability to conduct research and dominate the scientific field, leading to a lack of diversity among researchers and researchers. Within the UK, access funding also has the additional racialised element as a result of colonial ideas, as BAME scientists are less likely to be funded than their white peers for academic research. In this chapter, students are urged to consider these issues, understand their origin and link to colonialism and research potential solutions they may contribute to in the future.

Language has long been used as a tool of marginalisation, with its exclusionary roots traced back to the colonial era and persisting to the present day. This perpetuates a significant issue of unequal access to knowledge and its benefits. The complexity of scientific language further exacerbates this problem, creating barriers to understanding research and acquiring knowledge, thereby privileging those with

access to higher education, policymakers, and individuals from higher socioeconomic backgrounds. Consequently, power and access to knowledge remain disproportionately distributed towards Western societal groups. In response to this challenge, the scenarios presented in this chapter aim to prompt students to consider the effective communication of complex scientific concepts to the public, particularly in light of the prevailing climate of science denial.⁷⁸

Additionally, understanding the cultural context of communities is essential for conveying and absorbing scientific information among the public and for implementing government policies on issues such as air pollution. As postgraduate students may pursue academic careers beyond the UK, they must develop an understanding of diverse cultures and customs, even within Western institutions. These barriers significantly impact the underdevelopment of education and science in certain regions, as well as differing political agendas and environmental challenges. Therefore, by introducing thought-provoking discussion questions and tasks, students can begin to explore these barriers and contemplate their role in dismantling them.

Finally, this chapter has served a dual purpose. Firstly, it has shed light on the various barriers within atmospheric, environmental, and aerosol science, effectively providing a comprehensive research impact statement encompassing social, political, economic, language, and cultural dimensions. Such impact statements should be included in the majority if not all, scientific theses to contextualise knowledge within its broader socioeconomic and political framework. Secondly, the insights gleaned from this chapter have informed the development of science education initiatives guided by a decolonial approach, as detailed in Chapter 7. Furthermore, Chapter 7 will outline potential future initiatives for the EPSRC CDT in the Aerosol Science Program, drawing from the themes explored in this chapter.

2.5 Final Remarks

In order to prepare future scientists to be well-rounded citizens and competent professionals capable of navigating the complexities of scientific systems and addressing the challenges faced by diverse communities worldwide, it is crucial to provide them with opportunities for open and guided discussions with one another. Such discussions that centre on the ethics, access, politics, and culture conditions behind fundamental science research can enable researchers to acknowledge how they impact society and how society impacts them. In this work we have opted to take a decolonial approach as it offers the ability for historical reflection and critical thought of the scientific system. By doing so, the aim is to educate students and educators about the foundations upon which science and society have been built, enabling them in theory to conduct better research that benefits the aerosol science field and the broader community. The ultimate objective behind integrating these concepts into the training curriculum for CDT postgraduate students is to enhance their capacity to position and critically analyse their scientific research. Ultimately, this approach aims to ensure that students adeptly incorporate a social, contextual justification for their research in their practical and final written work.

Chapter 3

Experimental Techniques and Methodology

3.1 Overview

In this chapter, key physical properties of picolitre droplets will be explored under different environmental conditions. To that end majority of the experiments detailed herein measure droplet shape distortions over time to determine surface tension and viscosity. Primarily, droplet surface tension experiments were performed using the droplet oscillatory method. The approach utilises droplet-on-demand dispensers (DoD) to retrieve surface tension measurements through examination of damped shape oscillations of the ejected droplet. The DoD droplet dispensers used in this work are widely employed in diverse ranging of experiments such as droplet drying and printed droplet microfluidics¹⁴⁶ due to their highly reproducibility in generating droplets of a specific size.¹⁴⁷ Upon generation of the fresh surface, these oscillations can be observed over surface ages < 1 ms compared to bulk solution approaches where the surface ages are > 10 ms.¹⁴⁸ In this work, the droplet oscillatory method was used to study the surface tension of inorganic and organic mixtures alongside the dynamic surface tension behaviour of three different surface-active agents (surfactants) under ambient conditions. The data retrieved from this method was compared to the bulk surface tension measurement techniques, the maximum bubble pressure tensiometer and the Wilhelmy plate.

In addition, two single droplet techniques have been used in this thesis. The first, holographic optical tweezers (HOT), enables the optical trapping of droplets $2 - 8 \mu\text{m}$ in radius and the second, the electrodynamic balance (EDB), allows droplets between $2 - 30 \mu\text{m}$ radius to be trapped in an electromagnetic field. Using Raman spectroscopy and light scattering, the HOT can capture subtle changes in the droplet radius and refractive index, and thus retrieve droplet properties such as viscosity and surface tension, changes in local RH as well as monitor changes in composition or photochemical reactions. For this work, the HOT was employed to collect viscosity measurements of proxy organic materials over a $0 - 80$ % RH range. The EDB uses the elastically scattered light from the droplet illuminated by a 532 nm laser, to accurately infer the droplet size under different RH conditions. Here, the EDB was used to monitor a photochemical reaction initiated by the interaction of a levitated sodium nitrate particle and a UV Light source under varying RH conditions ($30 - 80$ % RH).

3.2 Droplet Oscillatory Method

Since the 19th century, shape distortions in the form of oscillations have been subject to investigations, revealing information of the solution properties. Lord Rayleigh was among the first to interrogate the oscillation of liquid drops extended to include small amplitude distortions, excluding the effects of

viscosity and a uniform electric field.^{149,150} In his investigations, Rayleigh demonstrated that by considering inertial and capillary forces, the natural angular oscillation frequency for a given oscillatory mode, ω_l , can be found using Eq. 3.01.¹⁵¹

$$\omega_l^2 = \frac{l(l-1)(l+2)\sigma}{a^3\rho} \quad (3.01)$$

Where ρ is the density of the droplet, σ is the surface tension of the droplet, a is the droplet radius, and l denotes the deformation mode of each spherical harmonic as represented graphically in Figure 3-1.¹⁵² At $l = 2$, the droplet oscillates become axisymmetric, going through the prolate and oblate shape distortions. At this mode, the spherical harmonic can be reduced using a Legendre polynomial, it is this mode that is commonly used throughout this thesis.

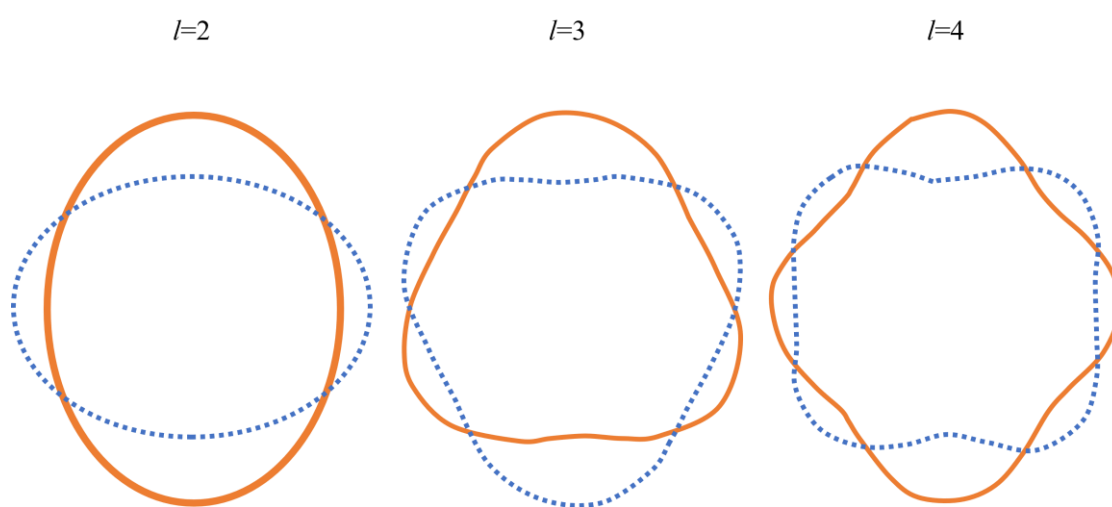


Figure 3-1: Three modes of oscillation in a spherical droplet. Each mode, l , represents the l th spherical harmonic. The solid orange line represents the droplet at $t=0$ and the dashed blue line represents the mode at $t=\omega_T/2$, where ω_T indicates the oscillation period.¹⁵²

Later, Lamb encompassed the effects of viscosity on the damping of small oscillations within the bulk of the particle and demonstrated that the rate at which the oscillations dampened was dependent on the droplet size, becoming extremely large for nanometre drops. Below the critical damping threshold, the time-dependent amplitude of the oscillating droplet was relayed in the form of Eq. 3.02, where $A_m(t)$ decays with the sum of the normal modes, $A_{0,l}$ designates the initial mode amplitude and α the modal phase shift:

$$A_m(t) = \sum_l \exp\left(-\frac{t}{\tau_l}\right) A_{0,l} \cos(\omega_l t - \alpha) \quad (3.02)$$

3.2.1 Droplet Oscillatory Method Setup

The droplet oscillatory method setup is shown in Figure 3-2. Initially, a repeating square waveform at a given pulse width and amplitude is used to trigger the DoD dispenser to generate a stream of uniform droplets. The waveform is designed using a custom-made LabVIEW program on a PC, generated using a waveform generator (Keysight 33500B Series, 1000GHz) and amplified with a custom made 10x amplifier. The amplifier increases the pulse amplitude from ~6V to ~60V; a pulse of this magnitude is required by the DoD dispenser due to the energy needed for the piezoelectric crystal to vibrate the capillary. The repeating voltage pulse delivered to the piezo microdroplet dispenser causes the capillary to contract, changing the volume of the liquid reservoir, and eject a stream of uniform droplets of the desired solution.¹⁵³ The breaking of the jet stream of solution is based on the Plateau-Rayleigh jet instability theory.¹⁵⁴ The maximum size of the droplet is determined by a number of factors: the dispenser capillary diameter (30 and 80 μm were used in this work), along with the amplitude, duration and shape of the voltage pulse.

Upon ejection from the dispenser orifice, hundreds of different but identical droplets are generated undergo an evolution of prolate and oblate spheroid distortions until a final spherical shape is reached. The time-evolution of droplet shape is observed by stroboscopic imaging along the horizontal plane.¹⁵³ The highly reproducible production of dispensed droplets enables the stroboscopic imaging to continuously capture droplets and produce a static image. The ability to produce such an image is possible due to the stability of the droplet velocity and trajectory, and the consistency of the droplet size.^{147,155} Typical droplet diameter size ranges from 10 – 45 μm , released at a dispensing frequency of at 20 Hz.

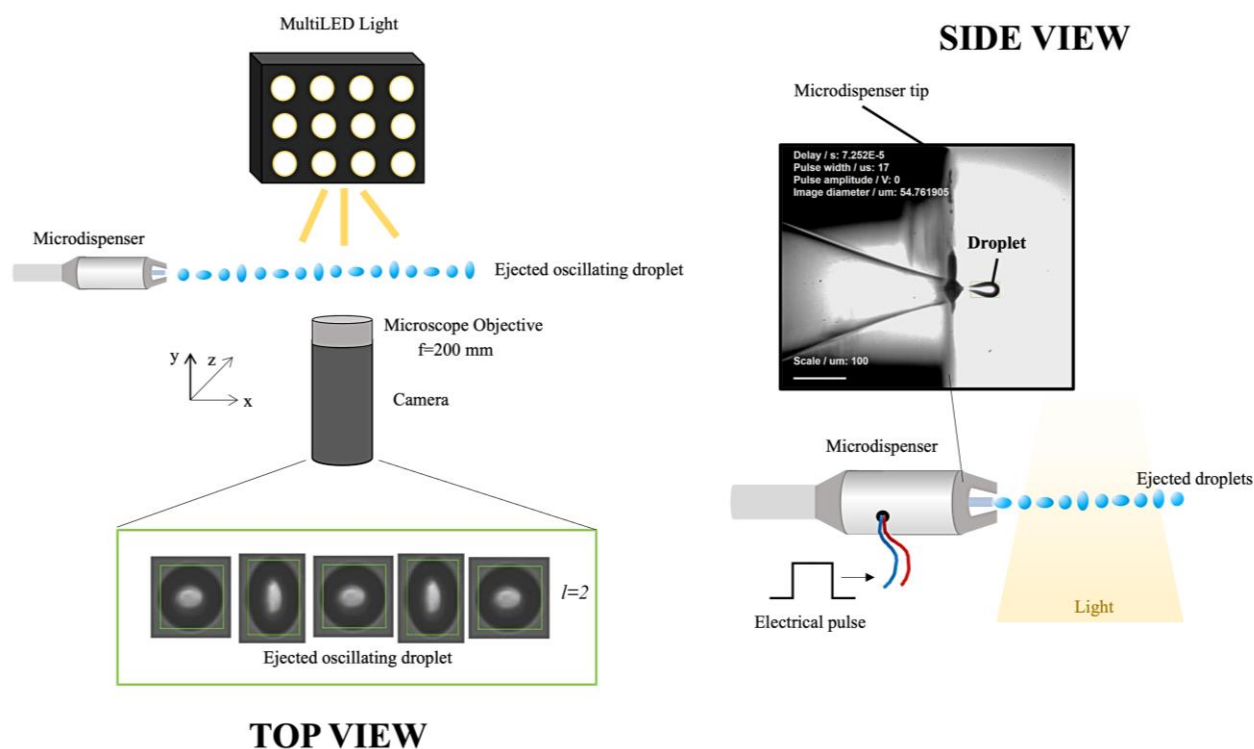


Figure 3-2: A top and side view schematic of the Droplet Oscillatory Method Instrument. Droplets propagate in a $l = 2$ oscillation mode along the x axis captured by the camera with a fitted microscope and illuminated by a strobing multiLED light.

The stroboscopic imaging assembly consists of a white multi-LED light (MultiLED QT, 150W 48V), image collection optics (a microscope objective (Optem 28-21-11, M Plan APO 20 \times) and Zoom lens module (Optem Fusion 7:1 Zoom Detent) and camera (JAI GO-24000M-USB). The LED and camera were triggered with a 500 ns pulse from the delay pulse generator (BNC Model 555), which itself was triggered using the pre-amplified DoD dispenser trigger pulse following the introduction of a user-controlled delay time (controlled by Quantum composers 9520 series). By varying the delay time between droplet generation and imaging, the temporal evolution of the droplet shape distortions can be investigated at a high time resolution. The user defined delay time is dependent on the size of droplet under investigation, for a $\sim 30 \mu\text{m}$ droplet the shift delay time is 6×10^{-7} s compared to 1×10^{-6} s for a $\sim 50 \mu\text{m}$ droplet. This can be attributed to the fact that larger droplets exhibit longer oscillation periods, hence requiring less precise time resolution. The droplet was identified in the images using a custom written software (LabView) using an 8-bit greyscale image to distinguish the edge of the droplet.¹⁴⁸

3.2.2 Droplet identification and Image Analysis

Droplets are identified by brightfield imaging which uses a custom software algorithm to detect the droplet by comparing the value of each pixel in the greyscale image against a set threshold value. Above the threshold value, the droplet can be isolated from the background due to the dense grouping of darker

pixels shown pictorially in Figure 3-3. At the points of colour gradation change, a box is fitted around the droplet to give the height (a_y) and width (a_x) of the droplet, in pixels. Aspect ratio (a_y/a_x) can be determined using the ratio of a_y to a_x , while the droplet diameter is inferred from the width of the superimposed box once an aspect ratio of one is reached. From pixel to SI units, the droplet radius was calculated by multiplying the number of pixels by their lengthscale, which was calibrated using a graticule before each experiment. Typically, the pixel length scale was $2.18 \mu\text{m}\cdot\text{pixel}^{-1}$. Motion blur, which can reduce the accuracy of droplet diameter determination, is reduced by keeping the LED pulse width within the range of 500 – 600 ns. The droplet size retrieved at the end of the experiment is equal to the droplet size at the start due to minimal solvent evaporation during the short experiment window. For comparison, the measurement timescales in this study reach a maximum of 1.2 ms which is considerably shorter than the time it takes for 30 – 60 μm diameter pure water droplet to evaporate, which is estimated to be between 1 – 10 s.¹⁵⁶

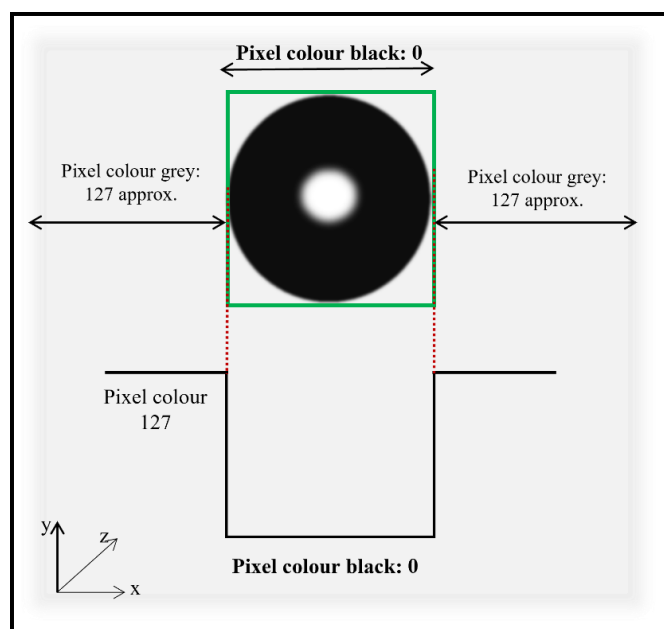


Figure 3-3: An illustration of how edge of an aerosol droplet is determined in the Droplet Oscillatory Method. On the 8-bit greyscale, the threshold denotes what is to be considered the droplet by the software. For example, here the threshold is set to 100 therefore all pixels below the threshold of 100 are considered part of the droplet and thus the green box can be superimposed around the droplet to determine the aspect ratio.

To ensure accurate droplet diameter retrieval, an appropriate threshold limit must be set. Water, the surface tension of which is widely documented (72.8 mN m^{-1}) was used to calibrate the instrument prior to each experimental measurement collection^{157,158,159}. Ejection from the dispenser induces multiple surface oscillatory mode orders, with high order modes dominating at the beginning of the droplet trajectory (e.g., $l = 4, l = 3, l = 2, l = 1$) dampening out quickly. For this work, the axisymmetric oscillations of the $l = 2$ mode were used to calculate surface tension and was identified at the point where the droplet's centre of mass was located at the central coordinates shown by Figure 3-4(a). To retrieve the angular oscillation frequency, a fast Fourier transform is applied to the droplet aspect ratios

from the time denoted as $l = 2$ onwards, Figure 3-4(c) and 3-4(d). As illustrated in Figure 3-4(d), a Lorentzian line shape was fitted to the fast Fourier transform to locate the peak position of the oscillation frequency as the line best fit the data points. Using the rearranged Eq. 3.01, Eq 3.03 was used along with the droplet diameter retrieved from image of the droplet ($\pm 0.2 - 1 \mu\text{m}$) standard deviations on average, to extract surface tension.

$$\sigma = \frac{r^3 \rho \omega_l^2}{l(l-1)(l-2)} \quad (3.03)$$

3.2.3 Determining Error in Calculations

For equilibrium surface tension measurements, detailed in Chapter 4, each surface tension is an average of three or more measurements at the same solution concentrations. The error in each measurement is calculated by the propagation of uncertainties from the radius and frequency typically resulting in an error between $\pm 1 - 3 \text{ mN m}^{-1}$. The uncertainty in the droplet radius is determined by averaging the last hundred data points of the droplet radius and calculating the standard deviation. The uncertainty in the oscillation frequency is quantified based on the goodness of fit of the Lorentzian line shape. The uncertainty in surface tension is predominantly influenced by the uncertainty in radius, as it scales proportionally with a cubic power factor. When studying the dynamic surface tension, described in Chapter 5, the surface tension data points were binned and averaged over a typical time interval of $50 - 100 \mu\text{s}$, leading to uncertainties of $\sim 0.1 - 4.0 \text{ mN m}^{-1}$.

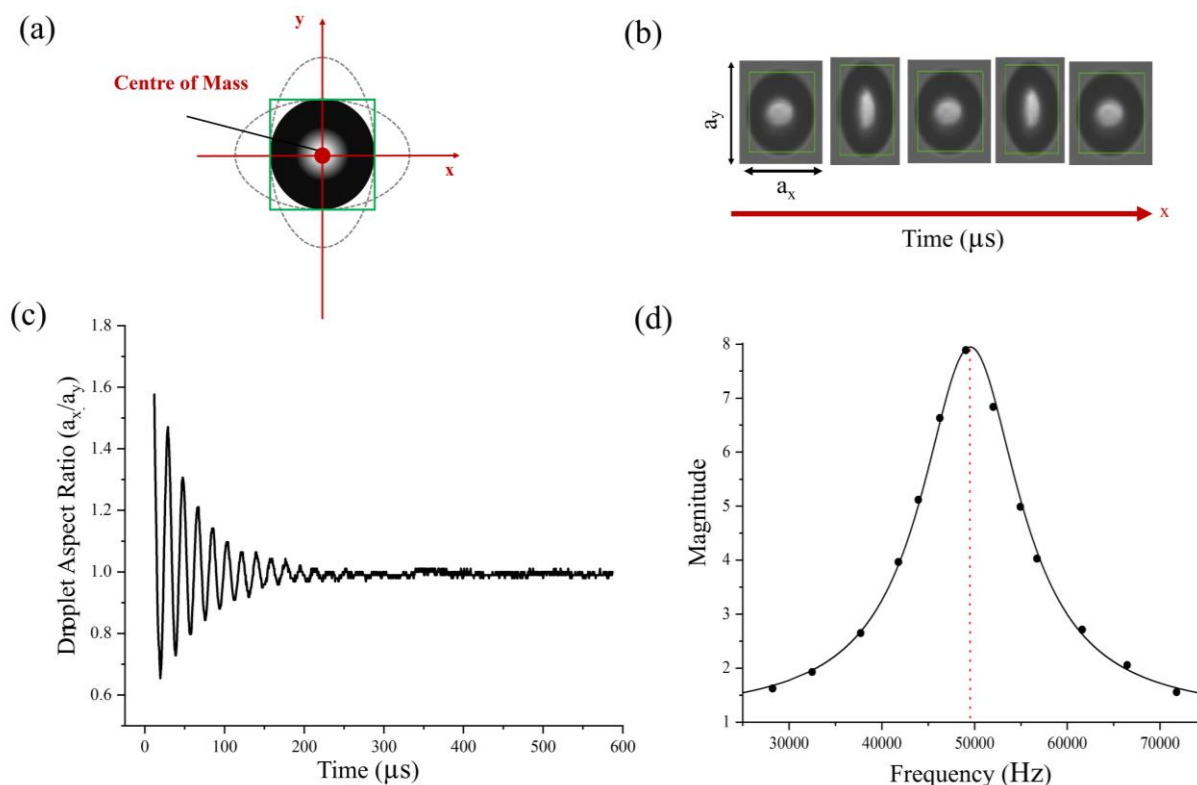


Figure 3-4: (a) The position of the centre of mass (b) after the droplet is ejected from the microdispenser, the droplet undergoes a series of damped oscillations as it relaxes to an aspect ratio of 1, from higher order modes to $l=2$ (c) Droplet aspect ratio is plotted against droplet delay time and then fast Fourier transformed (d) the fast Fourier transform is fit with a Lorentzian curve giving the frequency of the oscillations used to retrieve surface tensions.

3.3 Holographic Optical Tweezers

The holographic optical tweezer was used in this work to examine a change in viscosity as a function of relative humidity for two different ternary mixtures. Mixture one consisted of the sucrose, sodium nitrate and water while mixture two consisted of sucrose, citric acid, and water both of which are proxy systems for simple atmospheric aerosols.

3.3.1 Components of the Holographic optical tweezers

Since the first observation of particle trapping made by Arthur Askin in 1970, the contactless processing of aerosols via optical levitation has developed into the use of optical tweezers. The addition of diffractive optics allows for the confinement and manipulation of multiple droplets. Commonly termed holographic optical tweezers (HOTs), this is a widely applied technique in research across physics, biology, and medicine. Using elastic and inelastic (Raman) scattering along with brightfield microscopy, trapped particles can be characterised to study aerosol thermodynamics, kinetics, and hydrodynamics.

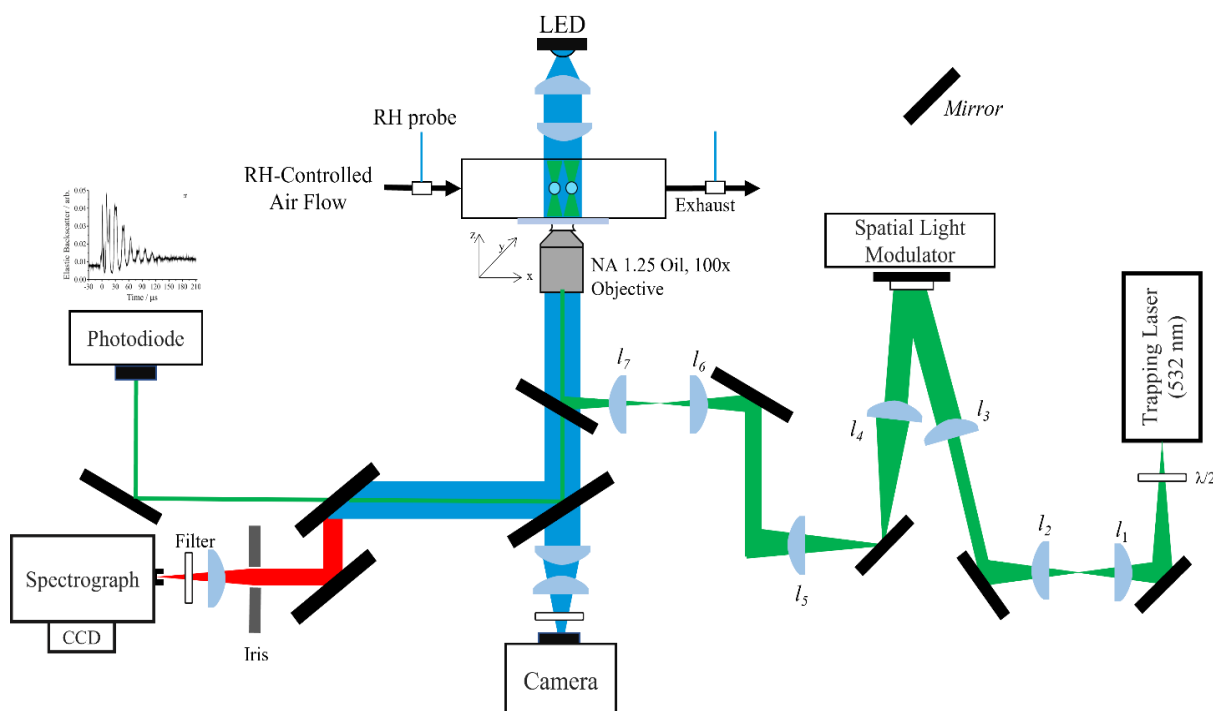


Figure 3-5: A schematic of Holographic optical tweezers (HOT) used in this work. The trapping beam at 532 nm is expanded by l_1 - l_3 to overfill the reflective face of the spatial light modulator, l_1 - l_2 forms a telescope with focal lengths of 40 mm (l_1) and 50 mm (l_2). Herein the SLM splits the beam into two optical traps projected into the back aperture of the microscope objective by l_2 - l_7 . Illumination is provided by brightfield microscopy via a blue LED light captured by the camera. Raman (Stokes) and elastic scattering are collected by spectrograph and imaged onto the CCD and a photodiode respectively.

Figure 3-5 illustrates a schematic representation of the HOT instrumental design used in this work. The trapping beam is a continuous wave Nd:YVO₄ laser light at 532 nm (maximum output of 3 W, Opus, Laser Quantum) vertically polarised by a half-wave plate. The trapping wavelength is chosen to correspond to the minimum in the complex refractive index (i.e., light absorption) of water, which is around 500 nm, as shown in Figure 3-6. The absorption of laser light by the aqueous droplet is leads to droplet heating on the order of just mK whilst promoting stable trapping. Droplet heating caused by light absorption could lead to a change in vapour pressure, phase behaviour and kinetics. The beam is expanded onto the spatial light modulator (SLM) such that it slightly overfills the reflective face by a four-lens system with focal lengths of $l_1=75$ mm, $l_2=450$ mm. The SLM, explored in Section 3.2.7, creates multiple traps from the expanded beam which are projected onto the back aperture of the inverted microscope objective via two lenses ($l_3=400$ mm, $l_4=250$ mm) and beam telescope ($l_5=175$ mm, $l_6=100$ mm). The telescope expands the beam to overfill the back aperture of the microscope objective to ensure the gradient force is as large as possible and the particles can be trapped at the beam focal point. Additionally, it is paramount for the beam to enter the objective normal to the back aperture to ensure issues derived from misalignment do not arise. In this configuration, the microscope chosen is a high numerical aperture (NA) oil immersion objective (Olympus ACH oil, 100×, infinity corrected, NA 1.25) to reduce beam arbitration.

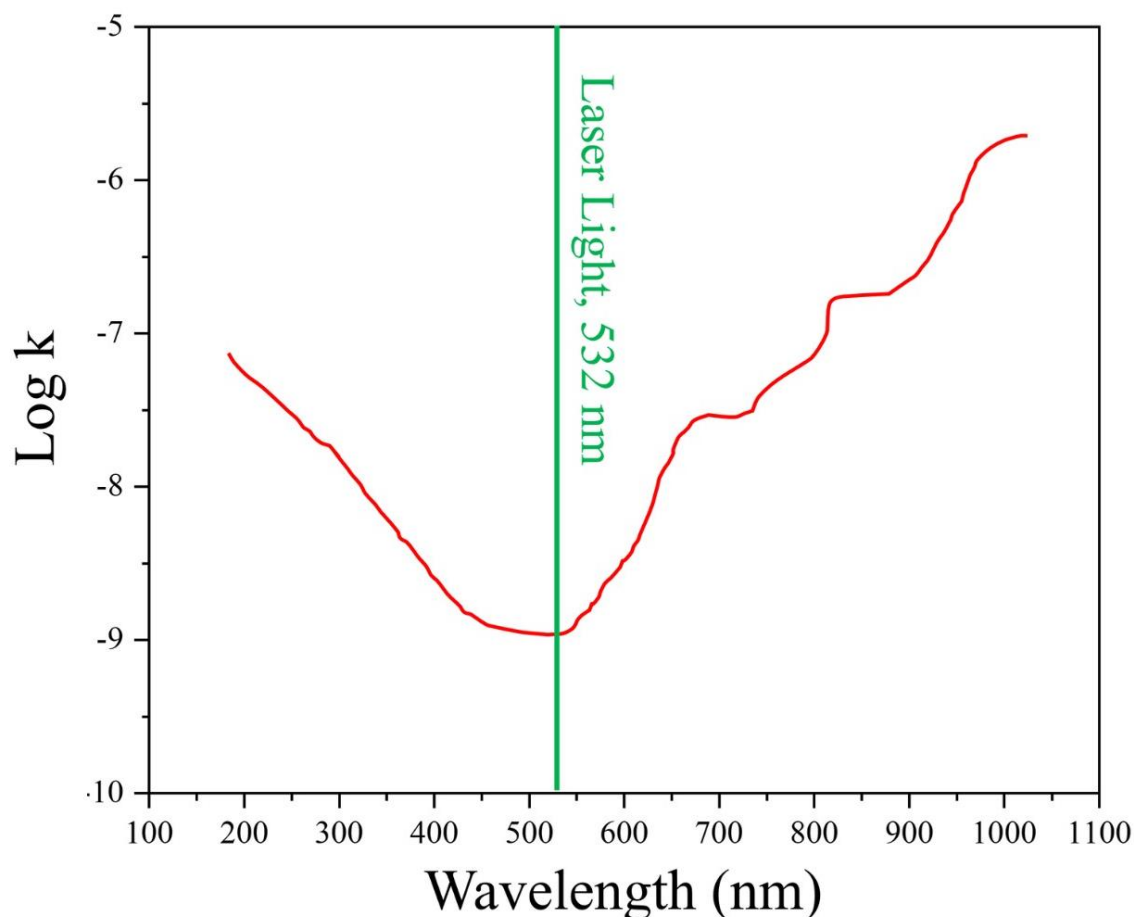


Figure 3-6: The imaginary part of the refractive index, k , for water against wavelength. The minimum absorption of light for water occurs at around 500 nm where the imaginary part of the refractive index is $\sim 1.6 \times 10^{-9}$.

The propagating beam is output as vertically polarised light. The SLM is optimised for vertically polarised light. Therefore, a half-wave plate is used placed between the laser and SLM to control polarity of the beam and ensure vertical polarity.

3.3.2 Aerosol Delivery and Trapping Cell Design

The ultrasonic nebuliser (NE U07, NE-U22-E MicroAir Omron) shown in Figure 3-7, was used to populate the HOT optical traps with droplets containing the desired aqueous solution. Droplets were generated with an ultrasonic medical nebuliser (1 – 5 μm average droplet diameter) at a flow rate of approximately 1 mL min^{-1} until droplets were trapped. With careful control of the laser power, the size of the captured droplets can be selected, with larger sized droplets stabilised by incremental increases in laser power. Droplets are drawn through the cell by a fume extractor (BVX-200, OK International) to encourage trapping, prevent deposition of the aerosol onto the coverslip and solution accumulation within the cell. Accumulation results from the large quantity of aerosol nebulised into cell to enable trapping within the small size of the effective trapping volume. The in-cell gas-phase water activity can quickly reach that of the bulk solution; therefore, nebulisation time and RH are monitored and meticulously controlled.



Figure 3-7: Medical Nebuliser, NE-U22-E MicroAir Omron

3.3.3 Trapping Chamber Design

The trapping chamber located vertically above the inverted microscope along the z-axis, see Figure 3-8, provides many functions and advantages when trapping an aerosol droplet. The confined nature of the trapping cell provides a discrete volume where particles can be isolated from air currents and the RH conditions can be controlled. Any dangers from beam transmission in the forward direction is restricted by 15 mm quartz window located at the top of the cell. It is through this window the blue LED light (455 nm) illuminates the droplet, enabling the capture of its behaviour within the trap.

The trapping of nebulised aerosol occurs in the trapping chamber depicted in Figure 3-8(a). The chamber is comprised of three components shown in Figure 3-8(b); the stainless-steel base, the Teflon cylindrical insert for RH control and a stainless-steel lid with a quartz window. The base is designed to have three ports (two inlets and one outlet) to allow for the delivery of humidified ultrapure N₂ gas, dry N₂ gas and the aerosol exhaust connected to a fume extractor. Inside the chamber, a 5 mm diameter borosilicate coverslip (Chance glass, No. 0, 85 to 130 µm thickness) coated in surfactant sits between the chamber and the microscope objective. A layer of immersion oil (Immersol G, RI=1.46, Carl Zeiss Ltd) is placed on the microscope objective to match the refractive index of the coverslip ensuring the continuity of the trapping beam with minimised spherical aberration.¹²¹

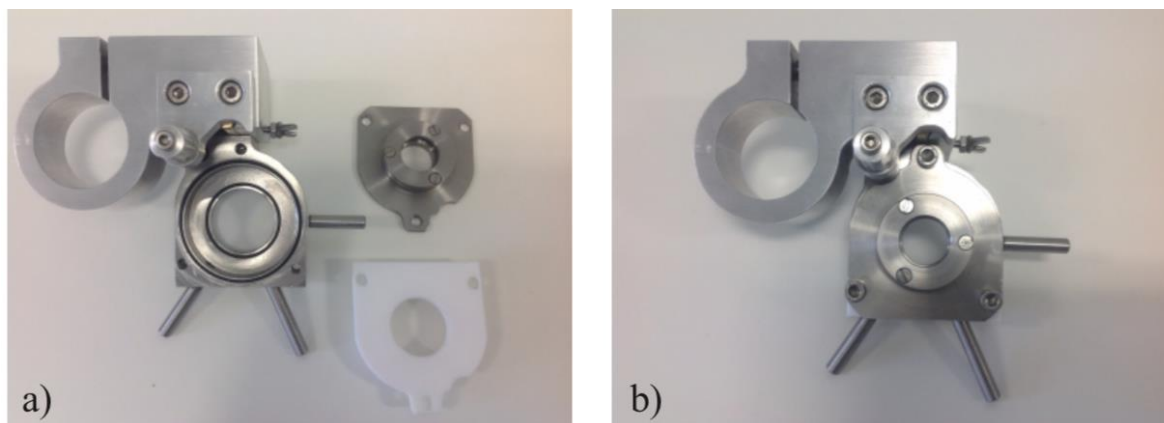


Figure 3-8: Trapping cell (a) The three separate components of the cell, showing inlets and the Teflon insert and the base of the chamber for the microscope objective (b) The fully assembled trapping cell. Optical access is provided in the beam propagation axis by a small quartz window located at the top.

The coverslip is pre-treated by soaking in an aqueous Decon 90 solution (50:50 water:Decon 90) to form a hydrophilic layer. This layer encourages nebulised droplets to spread evenly after sedimenting on the coverslip preventing discrete crystallised islands that may otherwise create an uneven refractive index profile and the aberration of the incoming laser beam, thus lowering trapping efficiency. Pre-treatment increases the wetting properties of the coverslip for even aerosol deposition.

3.3.5 Environmental Control of Gas Phase Conditions

Relative humidity control is an important factor in regulating droplet growth, preventing evaporative loss, and enabling a variety of water activities to be achieved. As key aerosol properties and processes are regulated by RH, it is vital to replicate the wide range of atmospheric conditions within the laboratory for accurate study of aerosol climate-relevant kinetics.

The schematic of the RH control and probe system is shown in Figure 2-8. The dry nitrogen (N_2) gas flow splits into two lines passing through mass flow controllers (MFC, Bronkhorst UK F-201C). One gas line remains dehumidified at an RH < 1 %, while the other line passes through the water bubbler reaching near saturation RH levels > 98 % of the water vapour. The two mass flow controllers allow for variation in the RH achieved in the cell by governing the ratio of wet to dry N_2 flow rates (0 – 200 mL min⁻¹). Figure 3-10 reveals a typical RH profile when the RH is progressively lowered. As the RH decreases, the droplet radius decreases, as the system is driven to more evaporative conditions.

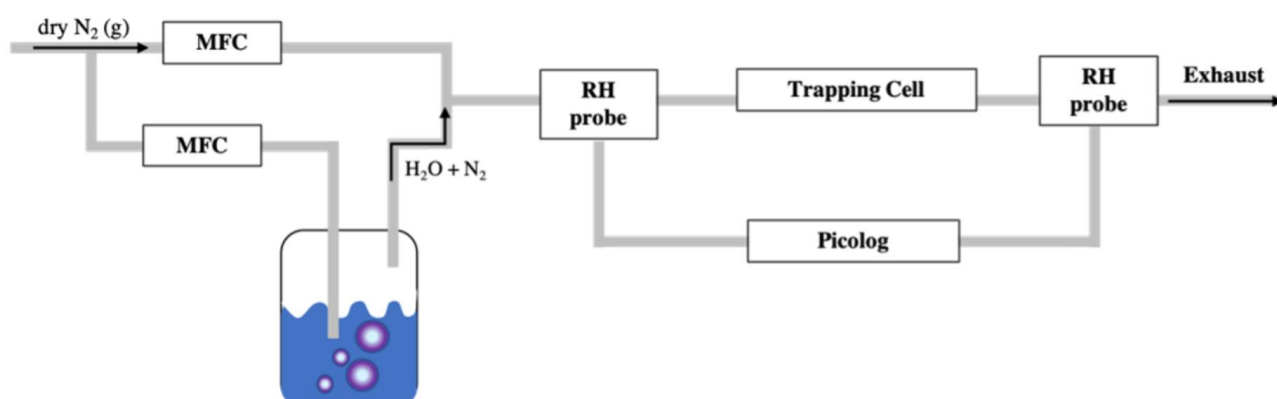


Figure 3-9: Environmental control system. RH is achieved using the Mass Flow Controllers which enable the wet and dry flow ratios to be adjusted. Dry air passes through a water bubbler, humidifying the air.

The capacitance probes (Honeywell, ± 2 % RH), located at the input and output exhaust ports, allow the RH within the trapping cell to be monitored and recorded.¹⁶⁰ Using a hygroscopic dielectric material placed between a pair of electrodes (creating a capacitor), the probe can detect moisture content through changes in dielectric constant of the material and sensor geometry. As RH is a function of ambient temperature and water vapour pressure, there is a correlation between the probe capacitance and the surrounding water vapour pressure within the cell.¹⁶¹ In the presence of moisture, more dielectric material exists between the electrodes (dielectric constant of water = 80 compared to 2– 15 for the porous dielectric material) leading to an increase in capacitance and the voltage measured. The voltage output is calibrated using a digital RH probe (Vaisala HMT 331) and plotting the linear relationship between probe voltage and measured RH. The RH probe data are measured and recorded using the Picolog software package, with an uncertainty typically around ± 2 %. It is customary for the before and after trapping cell probes to match in RH to ensure the correct RH has been achieved within the cell when conducting an experiment. Higher RHs require a longer time to achieve (10s of minutes) due to the cell having to uniformly equilibrate.

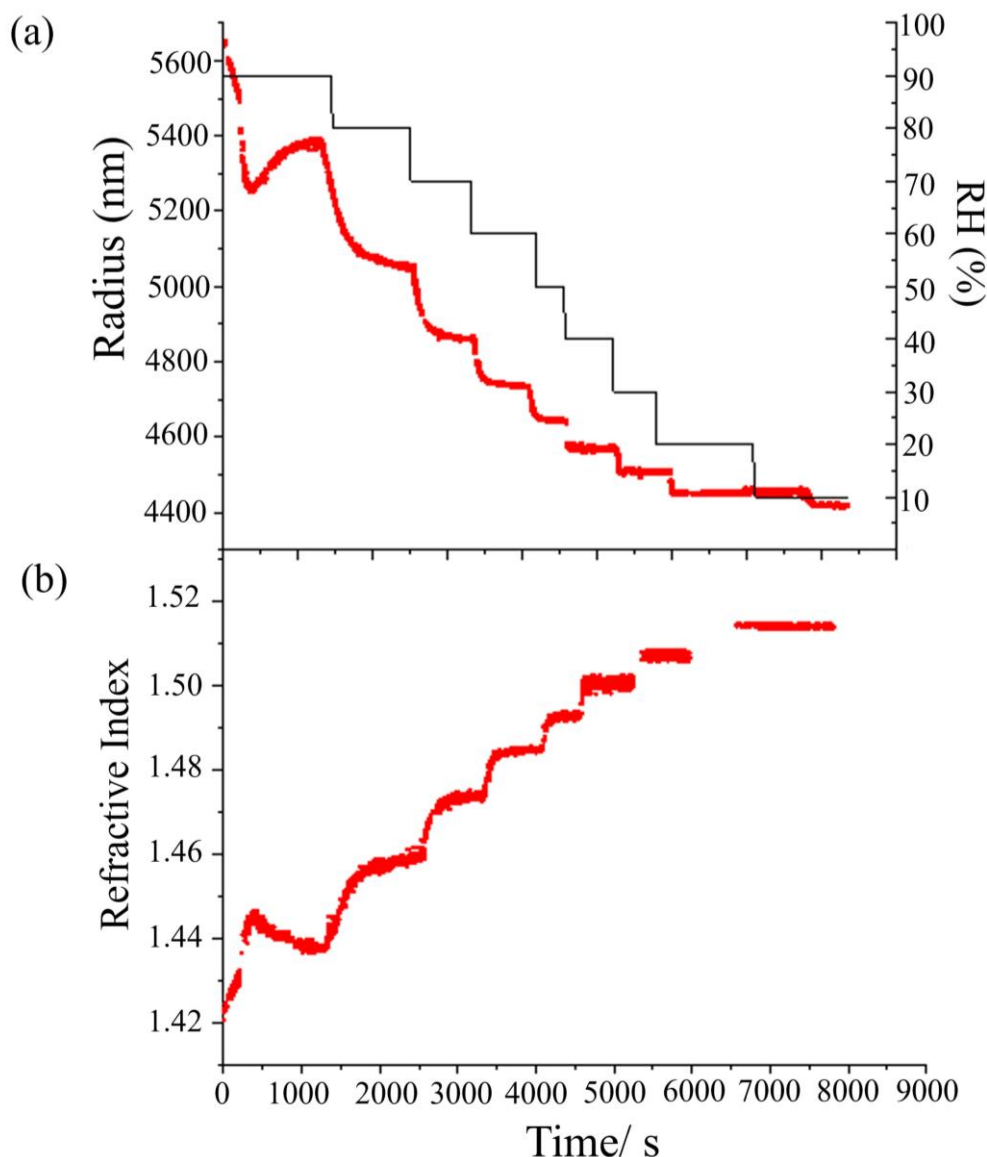


Figure 3-10: A typical HOT experimental profile, showing how changing (a) RH (black line) and radius in nanometres (red symbols) and (b) RI (red line) determined from Live Aerosol Raman Analysis (LARA).

3.3.6 Brightfield Imaging and Droplet Illumination

Brightfield imaging, used across many fields, has been used in this work to image droplets. This technique of imaging reduces light transmission through the particle compared to the background allowing for the particle to be clearly identified.¹⁶²

In this work, in-plane illumination of the trapped aerosol droplets is achieved using brightfield imaging microscopy to observe successful trapping of the droplet and to monitor coalescence. A lens directly below the LED is used to collimate and focus the blue LED light (Lumileds, Luxeon, royal blue) for illumination at 455 nm. This wavelength is chosen because it is easily isolated from the elastic and inelastic backscatter light that passes through the microscope objective to allow for imaging. The

brightfield image of the droplet is collected by a charge-couple device (CCD) camera (Dalsa Genie HM 640, CMOS) by a 10 cm focussing lens. Images and videos of the droplets can be recorded a 640 x 480 resolution with a maximum frame rate of 300 fps. The image obtained is subject to the position of the droplet relative to the coverslip, Figure 3-10 shows a brightfield image of two optically tweezed aerosol particles.

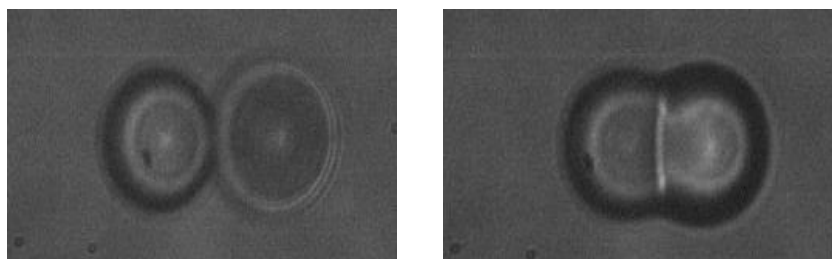


Figure 3-11: Example of brightfield imaging of a coalescing droplet imaged during an experiment.

3.3.7 SLM and Hologram Generation

Spatial Light modifiers freely modulate the wavefront of the incoming light using a series of kinoforms. The $4f$ lens system, described in Section 3.2.1 expands and collimates the laser beam to overfill the liquid crystal micro-display of the phase-only SLM (HoloEye LC-R 2500 SLM). The SLM image array (19.6×13.6 mm) has a resolution of 1024×768 pixels, of which only 768×768 pixels are impacted by the incoming vertically polarised light and conjugate with the back aperture of the microscope objective.

The liquid crystal alignment within each pixel is governed by electric circuits fabricated onto the silicon wafer (LCOS). Where an electric field is applied to a pixel, the liquid crystal orientation is altered resulting in a change in the refractive index along with the phase of the incident light and the outputted wavefront. Wavefronts of varying phase delays can be freely created by applying a unique voltage to on each pixel. The display is addressed with an 8-bit greyscale bitmap holographic image representing the optical function. Using software from Dr. Daniel Burnham et al.¹⁶³ a sequence of these holograms can be generated, with each pattern corresponding to a different optical position allowing for the translation of a particle in the 1st order trap relative to the 0th order along a predetermined trajectory. The zeroth order trap, generated from the direct reflection of a significant fraction ($\approx 50\%$) of the incident light, remains impervious to the holographic pattern displayed on the SLM, thus it remains the central immovable trap. The first order trap is controlled by changing the kinoform pattern which enables the manipulation of the trap relative to the zeroth order position. By refreshing the SLM at 60 Hz, manipulation of the traps can be achieved in discrete defined steps and example of which is shown in Figure 3-12. Upon coalescence, the droplets fall out of their traps and rearrange in between the traps until within milliseconds the composite droplet is recaptured in the higher intensity 0th order trap.

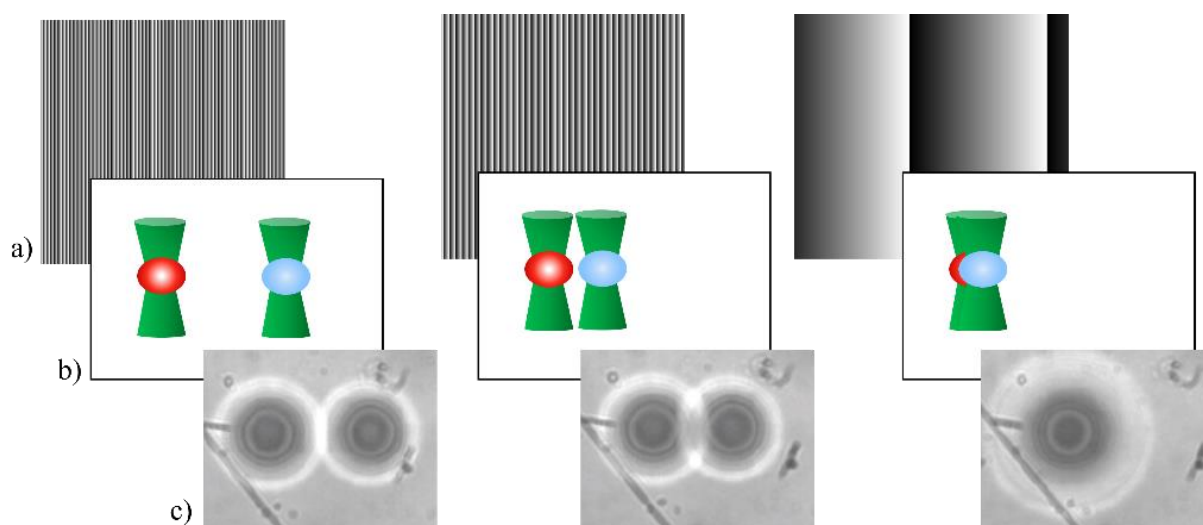


Figure 3-12: Schematic of the trap position as a function of the kinoform pattern and droplet position. a) The kinoforms that denotes the 1st order trap position. b) Using a series of kinoforms, the 1st order trap moves towards the 0th order trap in order to initiate coalescence. c) Brightfield imaging of the trapped droplets relative to one another. **Images acquired from Dr. Alison Bain.**

3.3.8 Raman Spectroscopy

Inelastically (Raman) backscattered light is used to probe and characterise droplet size and refractive index. Light is directed into the spectrometer by various high reflectivity mirrors and a final lens (100 mm) mounted onto a translation stage which aligns, angles, and focuses the light (Princeton Instruments, Acton, SpectraPro SP550i/SP500i). The adjustable slit at the entrance of the spectrograph is used to refine the light entering the spectrograph for better spectral resolution.

3.3.8.1 Spectrograph and CCD Detector

The Raman scatter is directed into the spectrograph through an entrance aperture i.e., slit, the width of is finely controlled. Too wide and the resolution of the spectrograph is limited, conversely, too narrow and intensity of light entering the spectrograph is reduced resulting in a low signal to noise ratio. After passing through the slit, the light expands towards the collimating mirror which converts the expanding rays into parallel rays. Once directed to the diffraction grating consisting of small parallel grooves, the light disperses into its constituent wavelengths and is subsequently reflected onto the CCD detector.

The groove density and dispersion of the diffraction grating is important to consider when optimising spectral resolution. The angle at which a given wavelength disperses is highly dependent on the density of diffraction grating grooves. A wider range of dispersion angles is achieved with a higher number of grooves per mm leading to enhanced spectral resolution, but a smaller detectable wavelength range recorded by the CCD, refer to Table 3-1.

Table 3-1: Spectrograph diffraction gratings and the associated CCD spectral range and resolution.

Grating	Wavelength range recorded (nm)	Spectral resolution (nm pixel ⁻¹)
300	~ 151	~ 0.12
600	~84	~0.063
1200	~38	~ 0.04
1800	~ 25	~ 0.03

Charge coupled device (CCD) cameras can detect weak Raman signals, measure the intensity of light at each given wavelength and convert that information into a digital signal. The CCD consists of a two-dimensional pixel array, cooled to -70°C by a Peltier cooling system and circulating air (Princeton Instruments, Pixis 256, 1024 x 256, Pixis 400, 1340 x 400). Background thermally generated electrons form the dark noise of the CCD array independent of those that are photon-generated. The region of interest (ROI) is the strip of light corresponding to light backscattered from the droplet, all other pixels beyond this region are excluded in the resulting spectra. This maximises the signal to noise ratio, improving quality of the collected spectra.

3.3.8.2 Acquisition of Spectra (LARA)

The software WinSpec 32 (Princeton Instruments) allows control of the spectrograph parameters such as the set grating and the ROI. Calibration of the spectrograph is necessary to ensure the accurate conversion pixel position to wavelength. A mercury lamp was used for the calibration. Light from the lamp is transmitted into the spectrograph via the trapping chamber and the peaks detected are compared against the reference peaks of the lamp. Errors in the spectral peak positions indicate recalibration of the spectrograph is needed.

The program LARA (Live Aerosol Raman Analysis) written by Dr. Jim Walker stipulates the spectral acquisition time and ROI parameters to be used. The acquisition time can vary between $0.1 > t > 10\text{s}$, with a preference for shorter times for dynamic measurements particularly during the initial equilibration stage of the droplet(s). However, shorter acquisition times lead to a decreased signal to noise ratio, thus a compromise must be reached to limit the broadening of the whispering gallery modes on the broad O-H band.

3.3.8.3 Analysis of Raman Spectra

Figure 3-13 is an example of a recorded Raman spectrum from a levitated sucrose droplet. The Stokes spontaneous signal is separated into the underlying spontaneous peaks such as a O-H and C-H band and the overlaid stimulated peaks, called whispering gallery modes (WGM). The broad, underlying Stokes (Raman) band is indicative of the chemical bonds present within the levitated particle, enabling changes

in particle chemical composition to be detected. The WGM arise from the ability of a droplet to act as a low loss optical cavity. A standing wave around the circumference of the droplet is created when the spontaneous Raman emission couples with the WGM. The propagation of the light around the droplet is intensified by this coupling such that sharp stimulated peaks are produced in the spectrum.

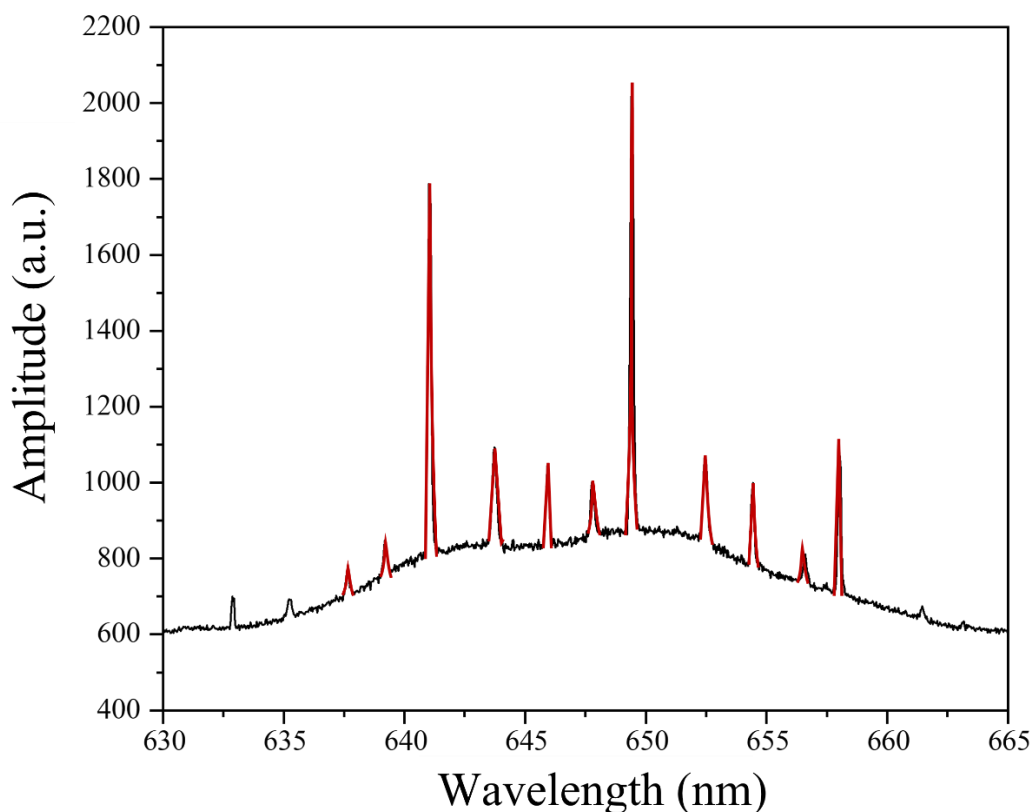


Figure 3-13: An example of a Raman spectrum of a levitated sucrose droplet. The spectrum consists of a spontaneous OH band onto which stimulated Raman peaks are superimposed (highlighted in red). These peaks enable the tracking of droplet radius and refractive index over time.

The stimulated peaks can be defined by two components: the mode number, n_{mode} , and the mode order denoted with the subscript, l . The mode number is defined by the number of wavelengths forming a standing radial wave around the circumference of the cavity. Larger droplets have higher mode numbers for the standing wave circulating the droplet at a given wavelength. The mode order refers to the number of radial maxima within a droplet and the specific light polarisation state defined as either transverse electric (TE) or transverse magnetic (TM). A TE mode and TM mode exist for each mode number and mode order and depend on whether the light has no radial dependence of the electric or magnetic component, respectively.¹⁶⁴ In a TE mode, the electric field of the wave is perpendicular to the direction of propagation, conversely, in the TM mode, the magnetic field of the wave is perpendicular to the direction of propagation, both types of mode are shown in Figure 3-14.¹⁶⁵

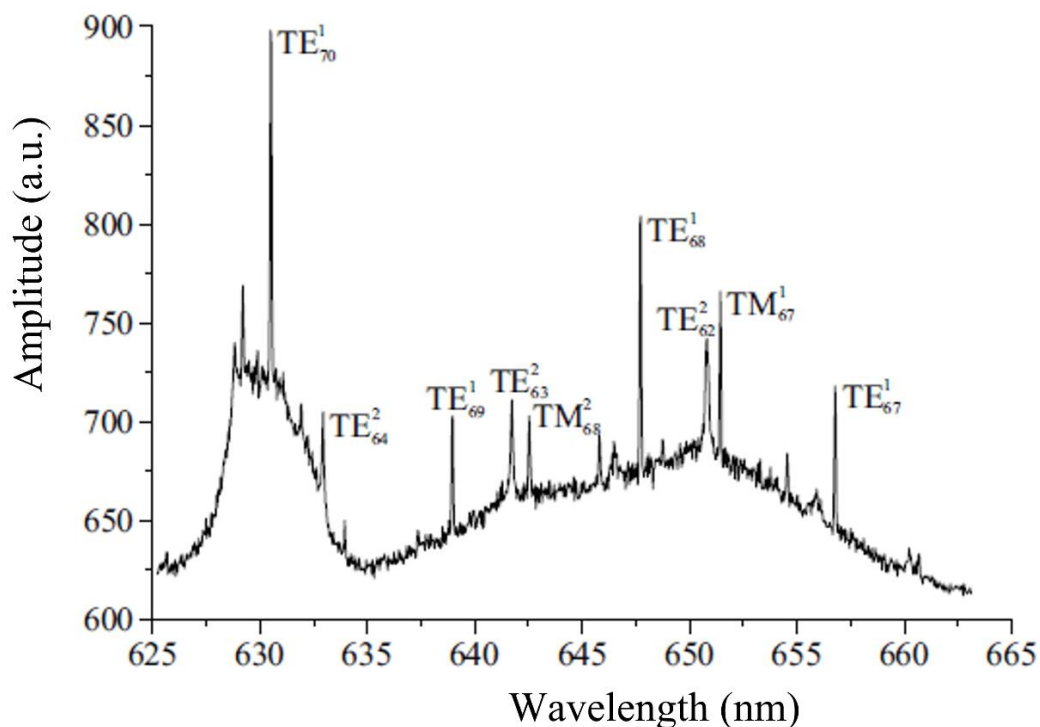


Figure 3-14: An optically levitated sucrose droplet spectrum showing the spontaneous band and stimulated peaks indicated as either transverse electric or transverse magnetic. **This image is taken from the journal articles by Bzdek et al.**¹⁶⁵

Mode positions are detected using a peak detection algorithm that isolates regions of spectral intensity exceeding the threshold. By fitting a Gaussian to each peak with a maximum spectral resolution reported as 0.037 nm/pixel, the position of the WGMs can be estimated to ± 0.01 nm.

Figure 3-15 shows a common spectrum of an OH stretching band arising from the excitation of the stretching vibration of water within an aqueous droplet. The excited system decays to a higher vibrational state than its initial state, and upon relaxation, light is radiated at a lower frequency (long wavelengths) than the incident light this is termed the Stokes shift as shown in Figure 3-14. The larger the droplet, the more stimulated peaks commensurate with the underlying spontaneous band due to the minimisation of spacing between the resonant modes of the same polarisation.

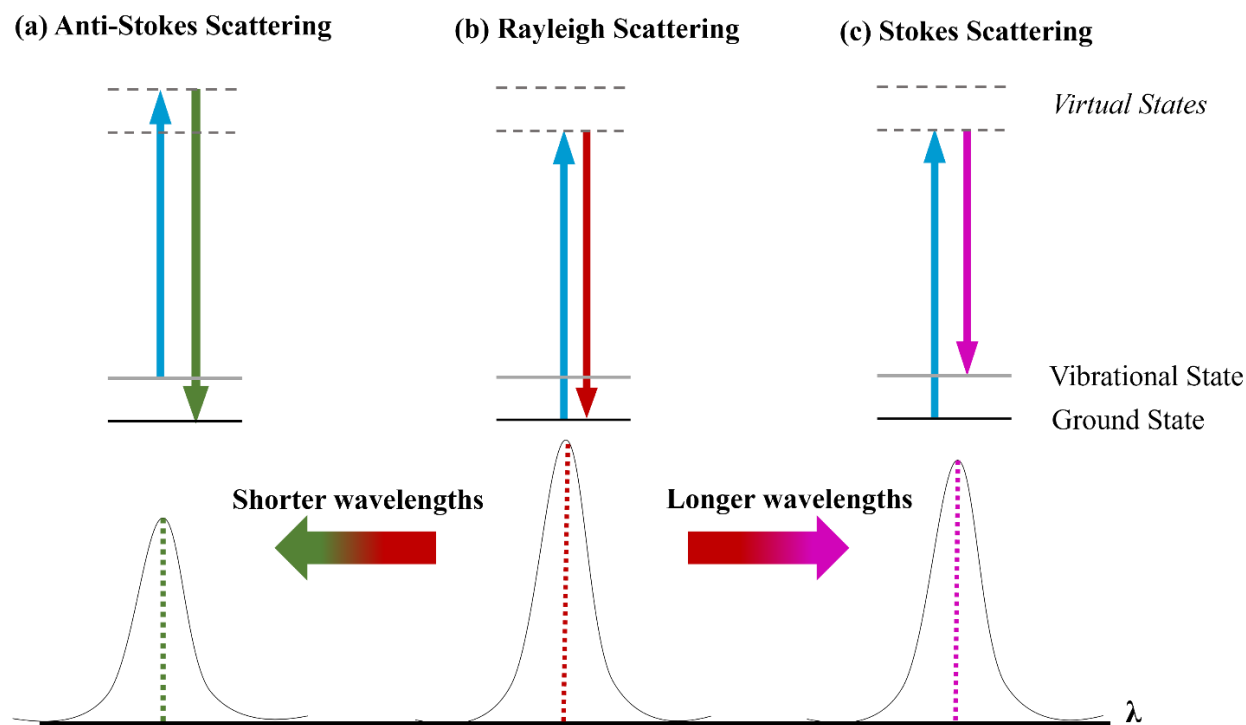


Figure 3-15: An illustration of the (a) anti-Stokes (b) Rayleigh and (c) Stokes scattering that occurs when an incoming light interacts with a droplet.

A precise measurement of the size and refractive index can be achieved when the experimentally observed WGM positions are compared to a library of Mie theory simulations. The rapid analysis of spectra can be conducted using the LabView program LARA to peak search and fit data in real time. To predict the size of a particle with a degree of confidence, a minimum of three whispering gallery modes is required and a mix of TE and TM modes. With only two or less WGMs for each wavelength, there is insufficient information to accurately determine the size of the droplet using Mie theory calculations. A Fortran software written and developed by Dr. Thomas Preston simulates mode positions. The program's high computational efficiency in fitting the mode positions in a 2D array, by simultaneously floating the size, refractive index, and peak wavelengths, is more advanced than previous methods used. From the desired ranges of droplet size, refractive index, mode orders, and number of peaks inputted the program, the size and refractive are outputted. This can be carried out online in real time at a spectral resolution of ~ 1 nm.

3.3.9 Calculating Viscosity

Optical tweezers provide a robust platform for the kinetic study of solutions in confined volumes and their properties, such as viscosity. Viscosity, η , can be defined as the resistance of a material to deformation and is a fundamental physicochemical property that provides valuable information on the diffusion constants, particle phase and intermolecular interactions.¹⁶⁶ Particles exist in a range of phase states, liquid ($\eta < 10^2$ Pa s), semisolid ($10^2 < \eta < 10^{12}$ Pa s), or solid/amorphous (above the $\eta > 10^{12}$ Pa s), determined by the external ambient conditions.¹²⁸ In this work the viscosity of inorganic and organic

materials, namely, sodium nitrate, citric acid and sucrose as proxies to atmospherically relevant organic aerosols which represent 50 % or more of the mass of the fine aerosol particle fraction.¹⁶⁷ In the absence of a surface, in the levitated state, droplets are able to reach supersaturated solute states unachievable in bulk solutions. For this reason, the holographic optical tweezers are used to investigate the viscosity of organic solutions over a range of relative humidities that are atmospherically significant.

3.3.9.1 Raman Spectrum of Coalescing Droplets

Figure 3-16 shows various methods of capturing the coalescence of two optically tweezed droplets. Power et al. demonstrated in Figure 3-16(a) the movement of the first order optical trap to within $\sim 5 \mu\text{m}$ of the zeroth order trap. This enables the droplet to be pulled into the zeroth order trap to coalesce with the droplet within it. Depending on the viscosity of the droplets and the critical dampening threshold, different experimental data collection methods are used to observe the coalescence event. At low viscosity (below the critical damping threshold), the fast relaxation of the oscillations is recorded with a high time resolution oscilloscope see Figure 3-16(b) and at high viscosities, the slow shape relaxation is monitored using brightfield imaging see Figure 3-16(c). Figure 3-16(d) shows the loss of Raman spectrum during coalescence as the particles rearrange in the trap and subsequently form a composite spherical droplet with a Raman spectrum once again.

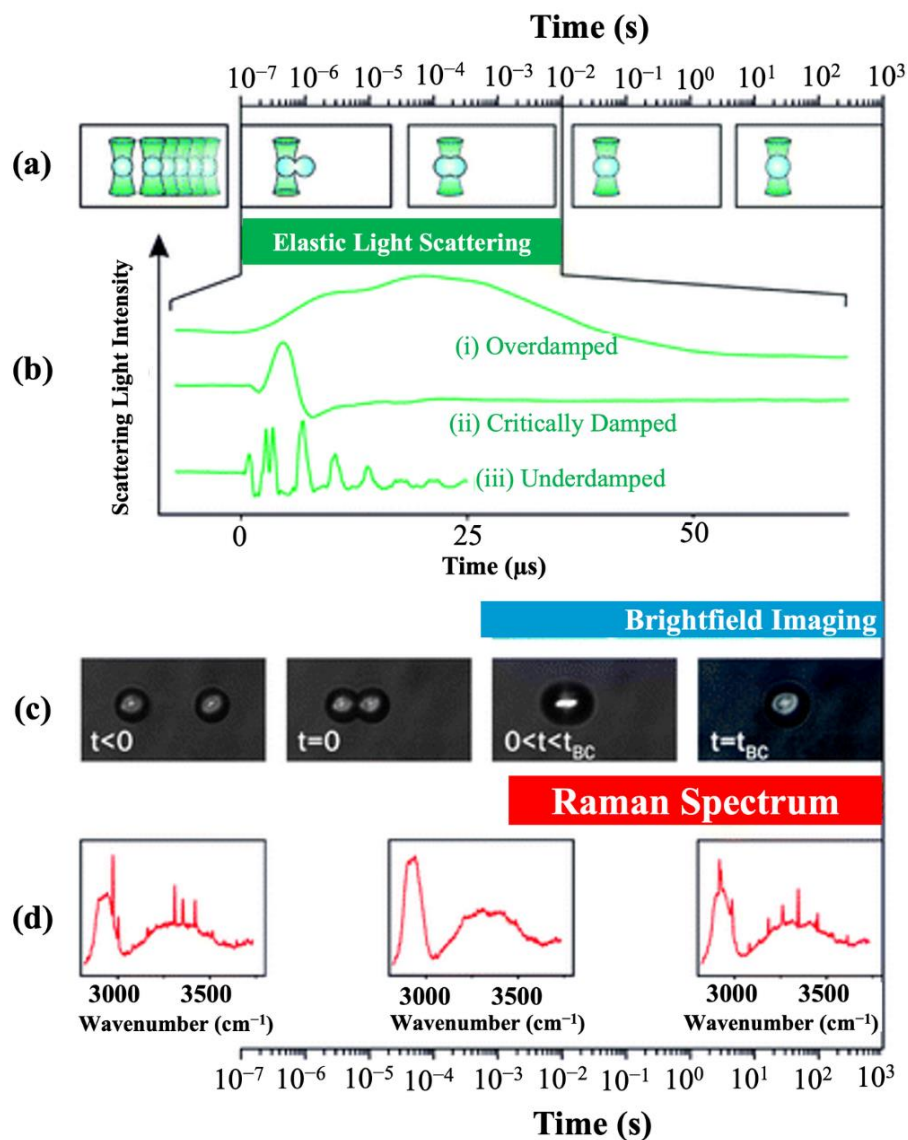


Figure 3-16: The methods used to calculate aerosol droplet viscosity. (a) Shows the coalescence of optically trapped droplets using the holographic optical tweezers. (b) The light intensity regimes of the composite droplet relaxation for (i) overdamping ($\eta > 0.01$ Pa s, sucrose droplets, 74.5 % RH), (ii) critical damping ($\eta > 0.01$ Pa s, sucrose droplets, 91.6 % RH) and (iii) underdamping ($\eta < 0.01$ Pa s, sodium chloride droplets, > 95 % RH).¹⁶⁸(c) Coalescing droplets which undergo a slow merge monitored by brightfield imaging over a given time $t > 1000$ s. (d) The temporal change in the Raman spectrum resulting in a loss of WGMs during coalescence and their return when a spherical shape is re-established. **This image and data are taken from a Power et al. paper.**¹⁶⁹

Chapter 6 will describe the significance of calculating viscosity in more detail. Herein, the equations used to calculate viscosity will be defined. The underdamped characteristic damping time, τ_l , scales with radius squared and is given by:

$$\tau_l = \frac{r^2 \rho}{(l-1)(2l+1)\eta} \quad (3.04)$$

Two regimes of oscillation decay that are dictated by the critical viscosity, η_{crit} are defined in Eq. 3.05. Chandrasekhar^{170,171} was the first to explore the oscillation of viscous spherical liquid droplets as

described in Eq. 3.04 details the decaying inertial mode and second a slowly creeping viscous mode as described on Eq. 3.06. Each have a different method of measurement. The critical viscosity that defines the point of transition between the two modes is given by Eq. 3.05.

$$\eta_{crit} = 0.76\sqrt{r\sigma\rho} \quad (3.05)$$

Above the critical viscosity, $\eta > \eta_{crit}$, for higher viscosities ($\eta > 10^8$ Pa s) there are no surface oscillations occur and relaxation proceeds via the overdamped regime, characterised by the slow merging of the droplets indicated using brightfield imaging. Here, Eq. 3.06 is used to define the viscosity. As the viscosity increases, the characteristic damping time, τ , increases as illustrated in Figure 3-17. For this reason, the coalescence event is often examined over a longer time periods (several minutes to days).

$$\tau = \frac{l(l+2)(2l+1)}{2(2l^2+4l+3)} \frac{\sigma}{\eta r} \quad (3.06)$$

Below the critical viscosity, $\eta < \eta_{crit}$, oscillations occur much faster than can be recorded using brightfield imaging and instead an oscilloscope is used (TeleCoy, HDO6033-ms, 350 MHz, High-definition mixed signal oscilloscope) shown in Figure 3-18. For droplets at the inviscid limit, a reduction in viscosity due to an increase in water content of the particle leads to more oscillations over time as water acts as a plasticiser, thus the characteristic damping time increases.¹⁵¹ Here, the regime region is termed underdamped as viscosity opposes inertial forces and follows the characteristic dampening time given in Eq. 3.07. Larger droplets are required for this measurement as within this regime, the smaller the particle size the fewer oscillations the particles undergo over the characteristic damping time.

$$\tau_l = \frac{2(2l^2+4l+3)}{l(l+2)(2l+1)} \frac{\eta r}{\sigma} \quad (3.07)$$

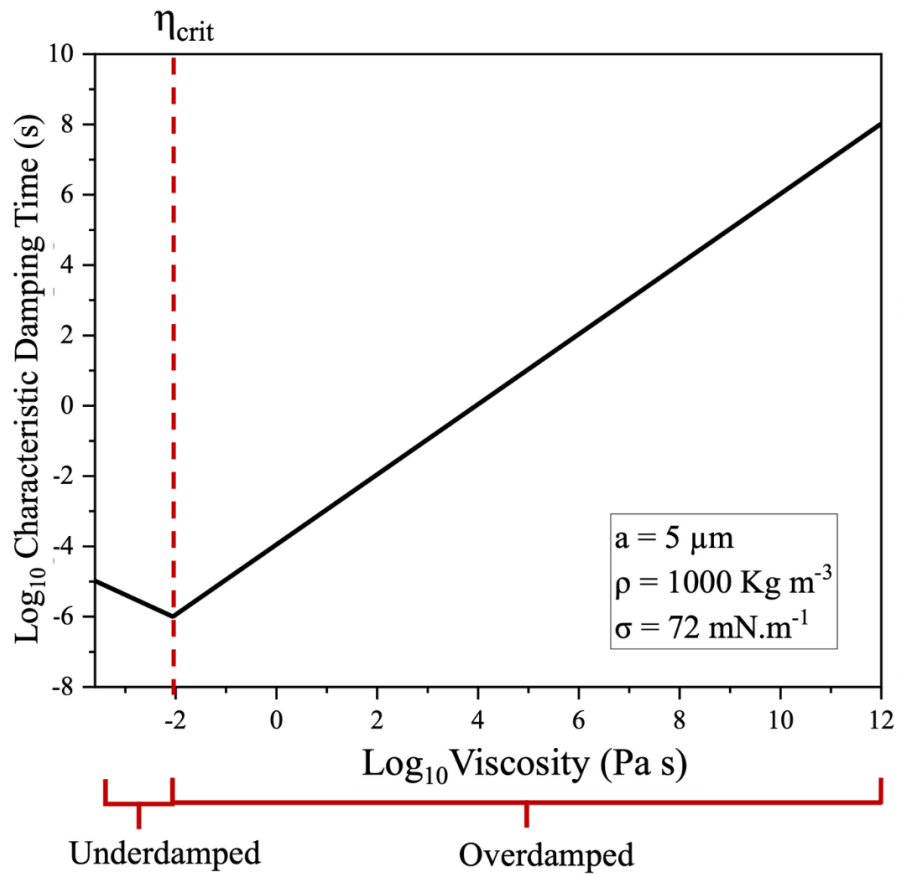


Figure 3-17: The characteristic damping time for relaxation in the particle shape against viscosity. Taken from the work of Rory Power et al. the damping time is calculated using Eq. 3.7 for the $l = 2$ distortion of a $5 \mu\text{m}$ radius water droplet.¹⁵¹

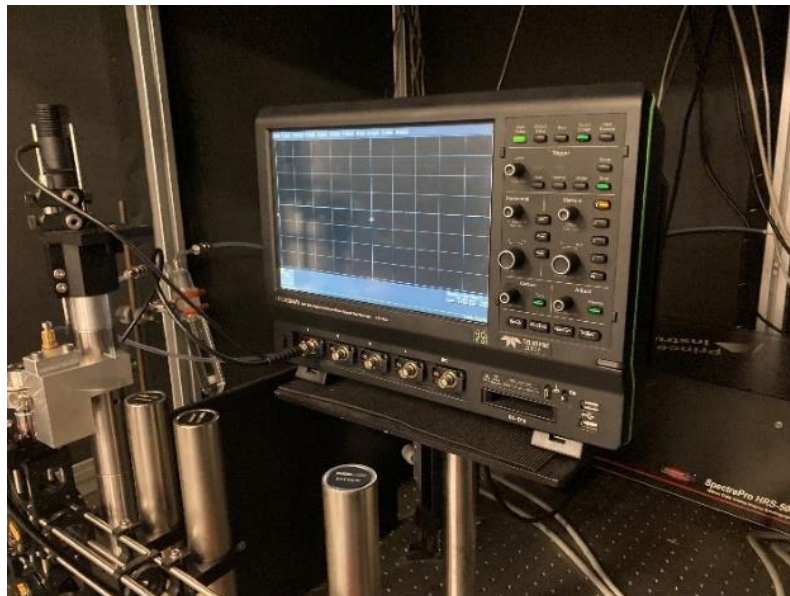


Figure 3-18: A picture to show the oscilloscope used to determine the damping time in the underdamped regime.

3.4 Electrodynamic Balance

The electrodynamic balance was used to levitate and probe sodium nitrate droplets with and without UV light illumination. These experiments form the preliminary measurements of a wider investigation into droplet photochemical reactions and the properties that reduce reaction rate such as viscosity or adsorbed surfactant molecules. Herein the technique used to examine the reduction in droplet radius (proportional to droplet mass) under different relative humidity conditions, in the presence of a UV light will be described.

3.4.1 The Experimental EDB Set-up

A modified electrodynamic balance (EDB) was used to study droplet radius change upon UV illumination of a photoactive levitated particle under different RH conditions. The experimental design shown in Figure 3-19 illustrates how the original concentric cylindrical of Heinisch et al. has been subsequently transformed by Allen Haddrell et al. to improve the capabilities of the experiment.^{172,173} The EDB facilitates the confinement of electrically charged droplets with a radius ranging from 5 to 30 μm , in a controlled environment, where aerosol kinetics and nucleation can be examined. In this section, the experimental approach and set-up used to determine the occurrence of a photoinitiated reaction following UV photoirradiation under certain conditions is shown in Figure 3-20.

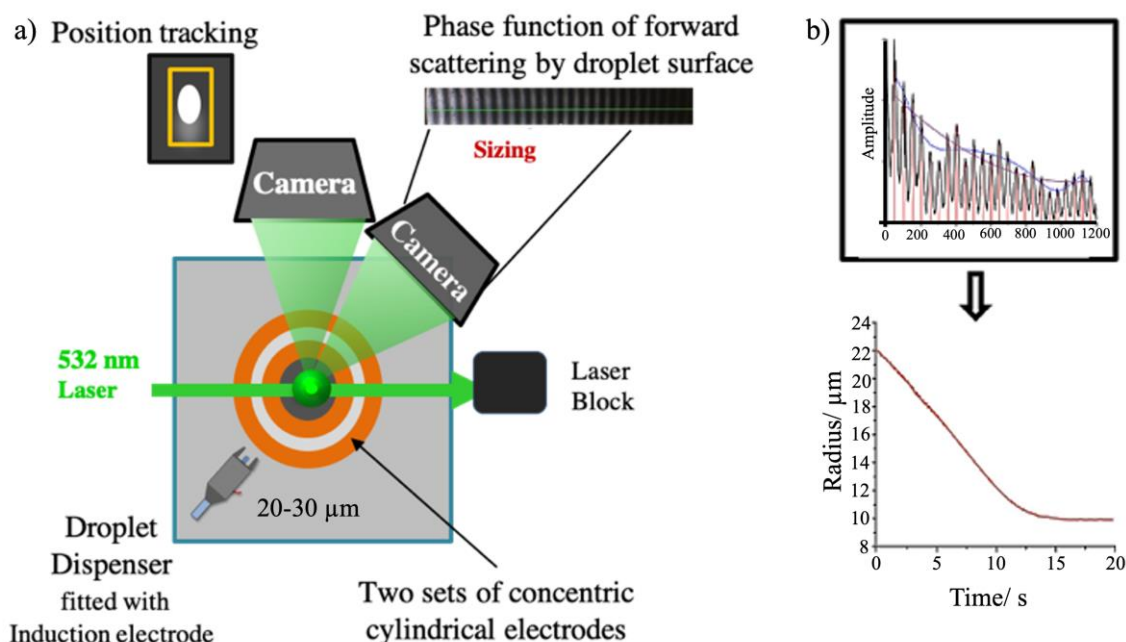


Figure 3-19: A top-view schematic of the open Electrodynamic Balance (EDB), (a) birds-eye view of the concentric cylindrical electrodes and a trapped droplet generating the phase function collected (b) and converted from the phase function to a radius versus time plot.

The two concentric cylindrical electrodes create an electric potential well within which a charged particle is trapped, described in Section 3.3.3. The dual electrode configuration, grounded with copper, produces both an AC voltage between 0 and 1000 V and DC voltage with a maximum range of -80 to $+80$ V to stably confine droplets. The application of an AC voltage enables restorative forces to re-centre the confined particle following lateral displacement from the centre of the well. Conversely, net downward displacement due to gravitational forces is counteracted by the DC voltage along the vertical axis of the trapped droplet.

A droplet on-demand dispenser generates a stream of sample droplets, charged by conducting rings mounted onto a 3D printed holder also containing the dispenser. Droplet illumination and characterisation of the droplet size, shown in Figure 3-19, is achieved with a 532 nm continuous wave, green Laser Quantum Ventus diode laser operating at a maximum of 50 mW. Angularly resolved elastic scattering is collected, for particle sizing, in the near forward scattering direction by a CCD camera positioned at a 45° angle. The particle vertical position is monitored by a CCD camera positioned at 135° to the trapped droplet.

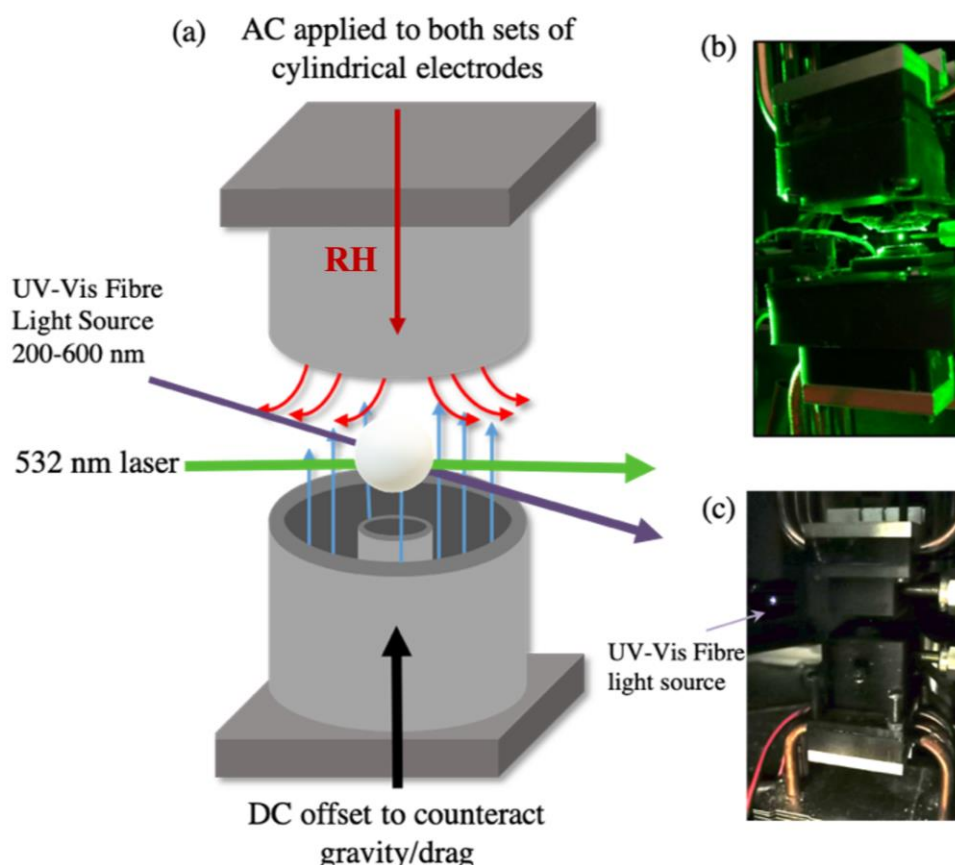


Figure 3-20: A side-view schematic of the EDB (a) with both environmental controls and electrodynamic fields are controlled through the device creating adjustable environmental conditions. A 532 nm laser illuminates the droplet at a $\sim 97\mu\text{m}$ diameter, approximately 45° angle to the incoming UV-Vis light (b) a photograph shows the EDB an illuminated trapped droplet (c) a photograph to show an UV-Vis illuminated droplet.

3.4.2 Droplet Delivery and Generation

In this work, a continuous stream of liquid droplets is generated using a piezoelectric dispenser (MicroFab dispenser, MJ-APB-01) with an orifice diameter of 30 μm . Using a displacement pipette (Pipetman, Gilson), $\sim 20 \mu\text{L}$ of sample solution fills a small piece of plastic tubing affixed to the end of the microdroplet dispenser.

An in-house LabView software via a DAQ card activates a piezoelectric crystal resulting in a stream of droplets produced from the dispenser tip. The square waveform applied to the dispenser must be of a sufficient amplitude to enable droplets to travel the minimum distance, approximately 50 mm, to reach the trapping region. The pulse voltage supplied to the dispensers lies between 3 and 6 V with a pulse frequency of 10 Hz and a pulse width of 35 μs . When a droplet is trapped, the scattered light from the droplet is registered by the CCD camera; if a droplet is not confined, another is dispensed immediately. The dispenser tip is continuously purged of fresh solution using a continuously pulsed wave with a low amplitude at a rate of 10 Hz. The amplitude is such that a constant jet of droplets is produced that do not affect the experiment.

3.4.3 Droplet Confinement

Charge is placed on a droplet upon generation by an induction electrode consisting of a conductive ring fitted to the front of the dispenser holder. The induction electrode is supplied with a voltage of 500 – 700 V and creates a charge imbalance as the droplet is being produced at the tip. If the induction electrode is at a negative voltage, positive charges populate the meniscus of the droplet before ejection, whereas negative charges migrate away from the meniscus. Once the droplet is ejected from the dispenser with a net positive charge, it can be confined within an electrodynamic field shown in Figure 3-20. Each minimum of the absolute value of the electric field corresponds to a position where the charged droplet can be stably confined within.¹⁷²

When a droplet is confined within a pure AC field with a gas flow and additional gravitational or drag forces, it continuously oscillates. To control these oscillations, particularly along the vertical axis, a DC voltage is applied to the upper electrode in order to offset permanent forces.

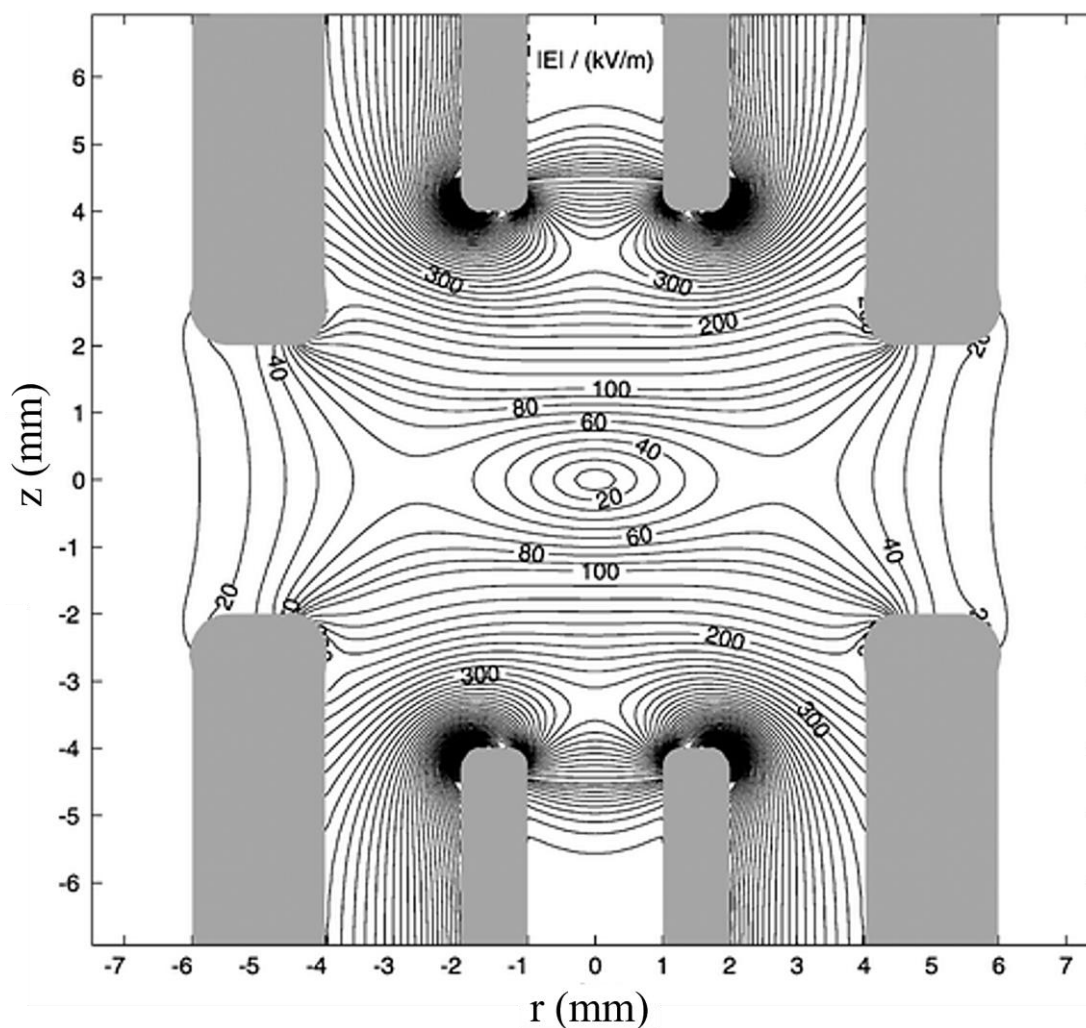


Figure 3-21: Illustration of the calculated absolute value of the electric field in the cross-section of the modified electrodynamic trap. The simulated the electric fields within an EDB are shown in the figure. The cross-section of the electrodes is depicted by the grey areas, with the trapping region located at its centre. **This image has been extracted from the work of Heinisch et al.**¹⁷²

3.4.4 Environmental Control

Figure 3-21 displays the open atmosphere EDB configuration used for this experiment. The instrument is enclosed in a large black box which isolates the trapped droplet from some air currents and fluctuations, however, due to the open-air structure of the EDB it is necessary to minimise these fluctuations within the lab as much as possible.

An airflow (200 mL min^{-1}), formed from the mixture of wet and dry nitrogen gas flows allows RH control over the confined droplet as well as forms a protective sheath over the droplet from the ambient environment. Both the upper and lower electrodes have their own air flow that can be independently controlled and manipulated such that the droplet experiences two different RH levels. The temperature inside the EDB can be controlled regulated by Peltier cooler fitted into each of the copper grounded electrodes enabling the heating or cooling of the entire electrode. The experimental data collected for this thesis is performed at the room temperature (298 K).

3.4.5 Estimating Droplet Size

Droplet illumination shown in Figure 3-22 is achieved with a continuous wave laser at 532 nm (Quantum Ventus diode) operating at a maximum of 50 mW. Interference between reflected light rays from the surface of the droplet and refracted rays from light passing through the droplet, leads to a pattern of light and dark fringes known as a phase function. The phase function is highly dependent on refractive index. The uncertainty in the droplet radius can be defined to a ± 50 nm accuracy.

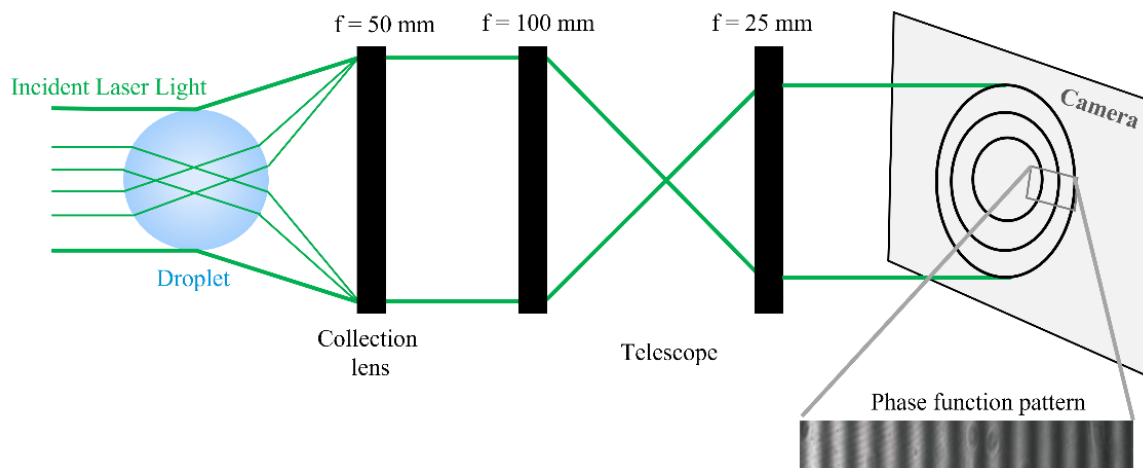


Figure 3-22: The EDB sizing system showing the reflected and refracted light from the illuminated droplet. In-phase interferences lead to the phase function pattern.

In 1908, Mie et al. found an analytical solution to the Maxwell equation used to describe the scattering of light by a spherical particle, enabling information of the droplet dimensions and properties to be gained. Droplet size information can be retrieved through two different data analysis methods. One approach based on the fully comprehensive Mie calculation of scattered light, encompasses iterative fitting between recorded and simulated phase functions. Hence, the less computationally demanding geometric optics approximation is used, based on the work of Glantschnig and Chen (1981).¹⁷⁴ The droplet radius r is estimated from the angular separation, $\Delta\theta$, between the phase function fringes taken across a linear profile of the camera image where iterative fitting,

$$r = \frac{\lambda}{\Delta\theta} \left(\cos\left(\frac{\theta}{2}\right) + \frac{n \sin\left(\frac{\theta}{2}\right)}{\sqrt{1 + n^2 - 2n \cos\left(\frac{\theta}{2}\right)}} \right) \quad (3.08)$$

where θ is the central viewing angle, n is the droplet refractive index and λ is the laser wavelength. The ability to estimate the radius in real-time using this approximation approach is advantageous for this study. The accuracy of the approximated radius has previously been shown to be ± 100 nm.¹⁷⁵

3.4.6 UV-Vis Droplet Illumination

An aqueous sodium nitrate droplet was equilibrated to a selected ambient humidity (80, 60, or 30 RH %) over several seconds. The confined, equilibrated droplet was irradiated overnight for 5 – 15 hours in the dark with UV light from a broadband UV Fibre Optic light source (200 – 600 nm). The time range is defined as the length of time between when the droplet equilibrates, $t=0$ and the point at which the droplet falls out of the trap. As a separate control experiment, equilibrated droplets were also held in the dark without illumination for the same period. Figure 3-23 illustrates the typical photochemical reactions that the aqueous sodium nitrate droplet may undergo when illuminated with the UV.

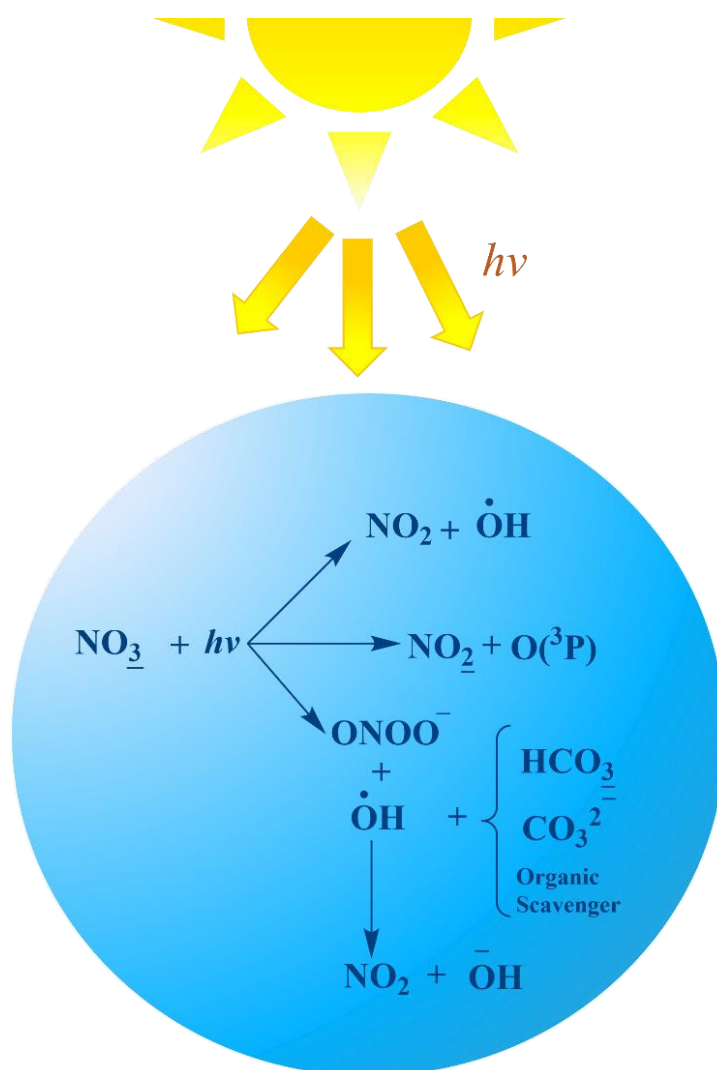


Figure 3-23: Primary photoinitiated processes and subsequent reactions during NO_3^- photolysis. The main absorbances at $\lambda \sim 200$ nm, $\epsilon = 7200 \text{ M}^{-1} \text{ cm}^{-1}$ and the actinic wavelength $\lambda \sim 302$ nm, $\epsilon = 7.2 \text{ M}^{-1} \text{ cm}^{-1}$.^{176,177}

3.5 Bulk Phase Measurements

Bulk phase measurements played a crucial role in this study as they were used to measure the surface tension of the bulk solutions and compare them with the droplet measurements. Chapter 4 utilises bulk phase measurements to validate the droplet oscillation method and its accuracy in measuring surface tension. In Chapter 5, bulk phase measurements were employed to calculate surfactant diffusion coefficients and other essential properties of the surfactant solution, providing detailed information on its surface activity and behaviour.

3.5.1 Maximum Bubble Pressure Tensiometer

In processes where interfaces are rapidly produced such as spraying, foaming, cleaning, printing, emulsifying, or coating, the equilibrium surface tension and the kinetics of the interface forming are important.¹⁷⁸ Surface tension measurements in these processes can be used for the indirect determination of the concentration of cleaning or wetting agents in industrial baths and therefore is a useful property to determine both industrially and atmospherically. Since Simon et al. first used the maximum bubble pressure method in 1851, it has been used, refined, and adapted.¹⁷⁹ The bubble pressure tensiometer BP100c (KRÜSS Model) used in this work is a valuable technique in the measurement of surfactant solutions, reliably analysing the surfactant molecules' mobility.¹⁸⁰ How the BP100 determines surface tension will herein be described.

3.5.2 Determining the Surface Tension

Figure 3-24 shows the BP100 instrument used in this work. Purified air is pumped into the instrument, passing through a gas flow capillary that measures the gas flow rate and into the capillary submerged in the desired solution. The capillary generates gas bubbles within the solution, the surface age of which is defined by the start of the bubble formation to the point when the maximum pressure is reached. The surface tension plotted as a function of surface age is measured by varying the speed of bubble formation at regular time intervals. The BP100 can adjust the required surface age exactly between 5 to 2×10^5 ms enabling the dynamic surface tension of a solution to be measured. The surface tension determination occurs in stages shown in Figure 3-25(a)-(d).¹⁷⁹



Figure 3-24: Photographic pictures of the BP100 maximum bubble pressure tensiometer taken in the KRÜSS lab.

Figure 3-25(a)-(b) illustrates the initial bubble formation. The air bubble appears at the end of the capillary with a radius of curvature larger than the radius of the capillary. As the bubble increases in size, the radius of curvature decreases. The pressure inside the bubble continues to rise and passes through its maximum. Figure 3-25(c) demonstrates that at this point the air bubble radius is the equal to the radius of the capillary and therefore is a hemispherical shape. From this point the surface tension is calculated using Young-Laplace equation, Eq. 3.09^{181,182}

$$\sigma = \frac{(p_{max} - p_0) \cdot r}{2} \quad (3.09)$$

Where p_{max} is the maximum bubble pressure, p_0 is the hydrostatic pressure and r is the inner radius of the capillary. After the maximum, the ‘dead time’ denoted τ_d begins.¹⁷⁹ The pressure of the bubble decreases as the radius of the bubble becomes larger and subsequently the bubble detaches from the capillary tip and a new cycle begins, Figure 3-25(d).¹⁸⁰

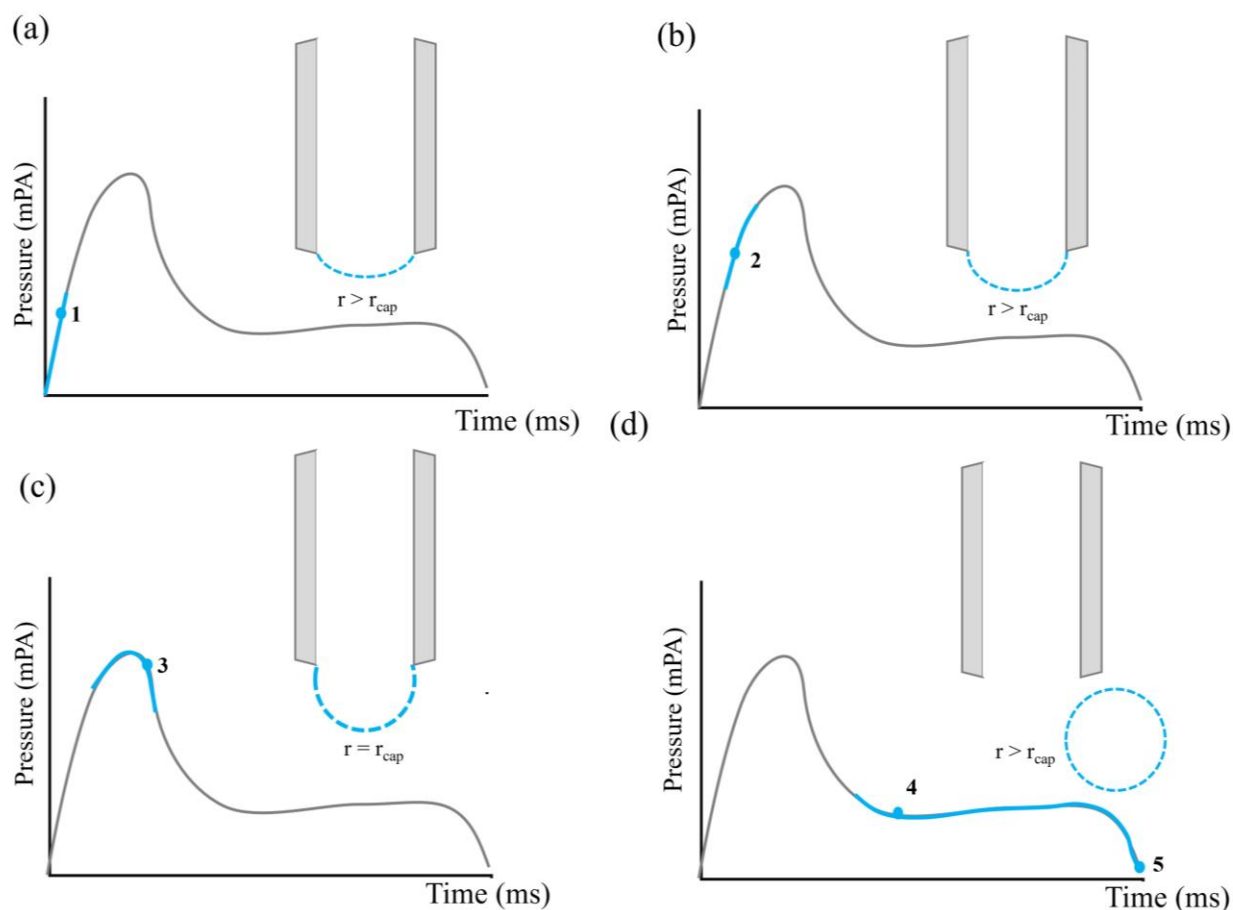


Figure 3-25: Droplet at the tip of the capillary begins to grow and the pressure increase (a) as the pressure increases, the radius of the air bubble equals the radius of the capillary (b) once beyond the maximum the surface tension can be calculated using Eq. 2.2 (c), droplet detaches, and the cycle begins again (d).¹⁸³

3.5.2.1 Hydrostatic pressure, p_0

The hydrostatic pressure is determined by the weight of the desired solution acting on an area. The additional pressure component (not a feature of the surface tension) acting on the pressure sensor must therefore be subtracted from the maximum pressure.

$$p_0 = \rho \times g \times \Delta h \quad (3.10)$$

where ρ is the density of the selected solution, g is the acceleration due to gravity and Δh is the height of the column defined as the immersion depth capillary.

3.5.3 Measuring Surface Tension

The size of the capillary is a key feature in the calculation of surface tension. Using a glass vessel, 30 ml of a reference solution, for example, water is placed in the BP100, and the capillary diameter is detected using Eq. 3.8. Capillaries used in this measurement are relatively small in size (0.15–0.25 mm) allowing the buoyancy force created when the bubble deforms to be neglected and the surface tension to be calculated from the bubble pressure alone.¹⁸⁴

The bubble pressure tensiometer can measure the dynamic surface tension, enabling surfactant kinetics and the mechanism of adsorption to be determined. The technique requires both the capillary (SH2031) and the glass vessel to be exceedingly clean as minor impurities within the system lower the surface tension. This is particularly true when measuring the surface tension of the surfactant, sodium dodecyl sulfate used in this work, with its highly surface-active impurities such as the dodecyl alcohol or polyvalent inorganic.¹⁸⁵ A hydrophobic coating is formed over the surface of the glass capillary by means of a salinizing solution in order to prevent the penetration of the sample solution into the capillary itself. If a liquid film can form on the inner walls of the capillary, the effective capillary diameter will be reduced throughout the measurement causing the surface tension to be too high. The capillary tip is immersed into the desired solution at a pre-determined depth (10 mm) which is the distance between the surface and the tip of the capillary during the measurement. The value of the depth is important as too low leads to the measurement being falsified by pressure variations when the rising bubbles contact the surface.

By inputting the solution density and viscosity, the LabDesk program produces a plot shown in Figure 3-25 of surface age against pressure. From this, one can determine the thermodynamically significant equilibrium values and the kinetically driven diffusion and adsorption coefficients as will be discussed in Chapter 5.

3.6 Wilhelmy Plate Method

The Wilhelmy plate method has been widely used to study both the equilibrium surface tension of a liquid and the contact angle between a liquid and solid.^{186,187} Commonly, a metal or glass cleaned plate with a known weigh and width is used to measure the liquid-solid interface. A platform raises the liquid until the contact angle between the surface of the solution and the plate is registered, as illustrated in Figure 3-26.

The surface tension of the liquid acts on the plate upon contact with the surface, therefore the vertical force required to pull the plate until it detaches from the liquid surface can be measured using a force sensor. This force as shown in Eq. 3.11 can be used to calculate the surface tension of the liquid.

$$\sigma = \frac{F}{L \times \cos \theta} \quad (3.11)$$

where σ is the surface tension of the solution, F is the force acting on the sensor, L is the wetting length and θ is the contact angle. In this work, a thin roughened platinum plate is optimally wetted such that the contact angle is virtually 0° , so $\cos \theta = 1$. Only the measured force and the wetting length need to be accounted for. Within this highly accurate method ($\pm 0.1\%$), it is not necessary to know solution densities nor are correction calculations needed.^{188,189}

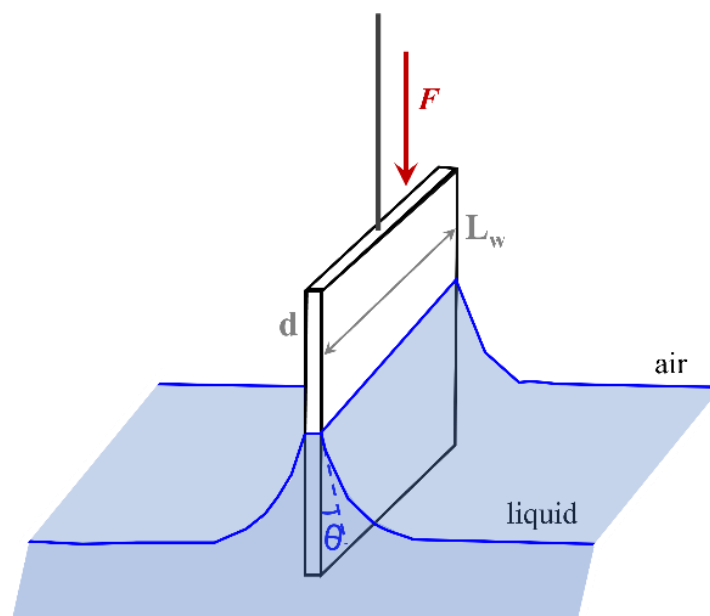


Figure 3-26: An illustration of the Wilhelmy plate method where L_w is the wetting length, d is the thickness of the platinum plate and F is the force exerted on the plate by the liquid.

3.6.1 Determining the Critical Micelle Concentration

The Wilhelmy plate method enables the calculation of the critical micelle concentration (CMC) of a surfactant. Surface active agents (surfactants) consist of a ‘hydrophilic’ head and a ‘hydrophobic’ tail. In an aqueous solution, the surfactant molecules enrich the surface with the hydrophilic tail protruding from the surface, creating a layer of surfactant molecules with a given thickness. Once the surface sites are fully occupied, the surfactant molecules begin to agglomerate inside the solution, i.e., form micelles. The CMC is intrinsic to the characterisation of surfactant behaviour and efficiency, knowledge of which is important in industries such as cleaning where the formation of micelles is desirable. The washing effect of surfactants is predicated on their ability to store hydrophobic substances such as fats or soot within the micelle.

From the CMC it is possible to derive variables such as the area per surfactant molecule and the maximum surface excess concentration that allow the characterisation of the surface adsorption. Surface excess concentration in this work was used to calculate diffusion and adsorption coefficients alongside the dynamic surface tension collected from the bubble tensiometer.

3.6.2 A Standard Measurement

The CMC was determined by conducting surface tension measurements on a series of different surfactant concentrations. Each concentration required three separate surface tension measurements to determine a mean value and standard deviation. Surfactants exhibit different behaviour above and below the CMC. Below the CMC, surfactant molecules continue to enrich the water surface, occupying available adsorption sites with increasing surfactant concentration. During this phase the surface tension decreases linearly with the logarithm of the surfactant concentration until the CMC is reached. At this

point, the adsorption sites are occupied, and the surface is saturated, thus any increase in surfactant concentration will not decrease the surface tension further, as shown in Figure 3-27. The CMC is then acquired from the intersection of straight lines for the concentration-dependent portion and concentration-independent portion.

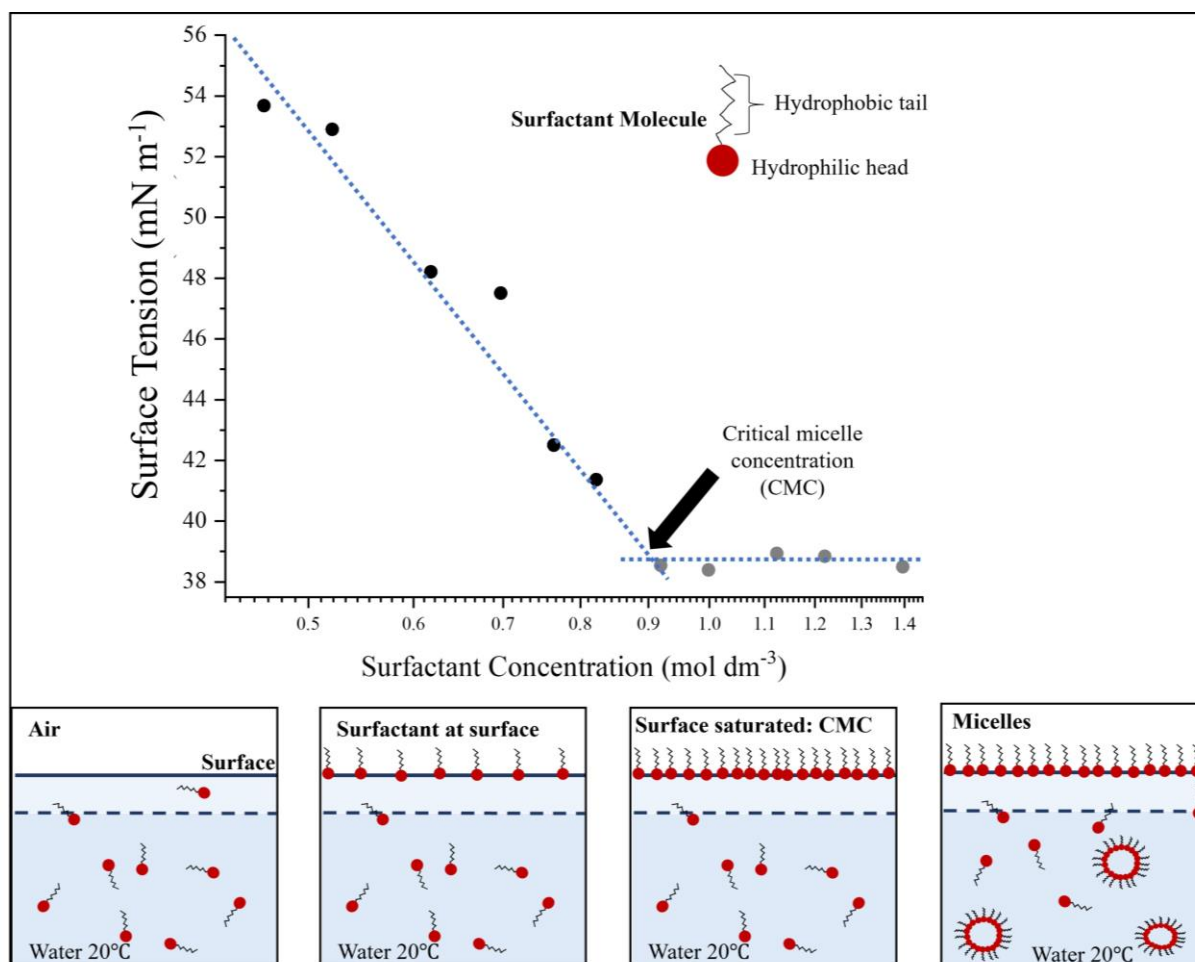


Figure 3-27: By increasing the surfactant concentration until an equilibrium surface tension is reached the surfactant critical micelle concentration can be determined as shown here.

3.7 Conclusion and Future Work

This chapter has addressed the techniques used in this thesis to characterise droplet and bulk properties. To investigate surface tension, three main instruments were discussed: the droplet oscillation method, the maximum bubble pressure tensiometer and Wilhelmy Plate techniques. The droplet oscillation method was applied for equilibrium and dynamic droplet surface tension measurements. The maximum bubble pressure tensiometer was employed for dynamic bulk measurements and the Wilhelmy plat was used for equilibrium bulk phase measurements. The ability of the droplet oscillation method to capture highly time resolved droplets along the droplet trajectory was introduced and used to generate novel

droplet dynamic surface tension measurements. These methods will be explored in Chapter 3 and Chapter 4 of this thesis.

With regard to the measurement of droplet viscosity, the holographic optical tweezer was discussed. The developed design of the HOT coupled with a Raman spectrometer has been explored including the method of populating the optical traps with the desired solution. The ability of the HOT to calculate highly accurate size and refractive index of a levitated droplet has been examined along with the ability to control the environment experienced by the droplet within the trapping chamber. The results from this experimental method will be discussed in Chapter 6. Finally, the newly developed electrodynamic balance, EDB, detailed further in Chapter 6 was used to levitate single aqueous droplets. By collecting elastic light scattering from the laser illuminating the droplet, the radius could be inferred. In this work, SPEL was used to examine the photoinduced droplet radius variations over time periods between 9 – 15 hours.

The techniques employed and discussed in this chapter offer a breadth of approaches to studying fundamental aerosol properties as well as the ability to collect data between microseconds to hours. This renders these methods ideal for increasing the understanding of aerosol droplet growth.

Chapter 4

The Surface Tension of Organic Acids, Inorganic Salts, and Their Mixtures

4.1 Overview

This chapter focuses on determining the surface tensions of aqueous solutions of organic acids, inorganic salts, and their mixtures. The composition of an aerosol plays a significant role in the droplet surface tension governing the growth beyond the critical supersaturation barrier into a cloud condensation nucleus, explored fully in Chapter 1. Conducting this work in the aerosol phase in comparison with the analogous bulk phase provides the opportunity to work at high surface-to-volume ratios, super saturated solute states, and higher surface curvatures, all of which impact surface tension and particle activation. The droplet oscillation method was used to observe the surface oscillations in droplet shape following droplet ejection from a droplet-on-demand dispenser. Having captured shape oscillations over microsecond timescales, surface tension can be retrieved to a high accuracy on droplets with very short surface ages. Droplet surface tensions are compared to bulk measurements taken with a Bubble Pressure Tensiometer.

Herein, the measured surface tension will be compared to statistical thermodynamic model predictions. In doing so, we can identify processes that the model may or may not be accounting for in its predictions of surface tension. Models such as these can go on to inform larger climate models, helping to decrease the large uncertainty associated with the aerosol indirect effect on climate.

4.1.1 The Surface Activity and Tension of Organic Acids

The main components of tropospheric fine particles are: 1) water-soluble and electrolytic inorganic substances, 2) organic and elemental carbon (carbonaceous material), 3) insoluble inorganic substances (oxides or salts of silicon, calcium, iron and aluminium).¹⁹⁰ Globally, carbonaceous aerosol is a key constituent of PM_{2.5} and PM_{0.1} particles. In the US, carbonaceous aerosol represents 10 – 65 % of the total mass of fine atmospheric PM_{2.5} particles while in Japan a study revealed organic and elemental carbon accounted for 51 – 57 % and 83 – 89 % of PM_{2.5} and PM_{0.1}, respectively.¹⁹¹ Saxena et al. proposes there are two main fractions of organic compounds; the first is the hydrophobic fraction.¹⁹⁰ Originating from primary emissions, compounds within this fraction display soap-like behaviour with one water repelling end and one water attracting end with a propensity to form a film that prevents the uptake of water. The second is the hydrophilic fraction whereby compounds are formed from atmospheric processes such as oxidation of gases display a high affinity to water.¹⁹⁰ These compounds

tend to be condensable, low molecular weight carboxylic acids, dicarboxylic acids, alcohols, aldehydes, nitrates and polyfunctional molecules. This work focuses on the latter fraction, namely water soluble organic compounds (WSOC) as Tuckermann et al.⁴⁷ found the concentration of organic compounds in solution was integral to the overall droplet surface tension of collected aerosol samples.¹⁹²

Cadle and Groblicki¹⁹³ found water soluble compounds were dominant in the total organic mass (average of 40 %) in Denver samples, while Mueller et al.⁶⁵ found 34 – 77 % of the total carbon in their samples taken in urban southern California consisted of water-soluble compounds. In measured aerosol and fog water samples taken in Po Valley, Facchini et al. showed increasing WSOC content within the samples resulted in a 10 – 20 % decrease in surface tension with respect to pure water.¹⁹⁴ Samples with little to no WSOC, did not exhibit surface tension reduction to the same extent.¹⁹⁵ In these samples, mono- and di-carboxylic acids were found to be the highest proportion of WSOC (in ppm) but it was the polycarboxylic acids analogous to humic like substances (HULIS) that resulted in the highest reduction in surface tension. Conversely, work by Kiss et al.¹⁹⁶ confirms HULIS account for 60 % of water soluble organic carbon across thirty-two samples causing a decrease in surface tension by 25 – 42 %, enhanced in the presence of ammonium sulfate.¹⁹⁶

Gas-liquid exchange processes and liquid phase chemical reactions as well as droplet nucleation and growth are influenced by changes in surface tension.¹⁹⁷ It is well documented that some organic substances including organic acids are surface active and their presence has a significant impact on the surface tension of cloud droplets. Organic compounds that adsorb at the surface tend to cause a lowering of the droplet surface tension. The extent of this adsorption is dictated by the polarity and asymmetry of the organic molecule according to P. Meissner et al.¹⁹⁸ The decrease in surface tension causes a lowering of the barrier to cloud droplet activation by reducing critical supersaturation ratios. In doing so, a larger fraction of atmospheric aerosol can be activated into cloud droplets and contribute to the indirect effect of aerosols by increasing the cloud lifetime and albedo.¹⁹⁹ The mono- and di-carboxylic acids: oxalic acid, malonic acid, pyruvic acid and levulinic acid, shown in Figure 4-1, are investigated in this work. These compounds were specifically chosen to enable comparison between organic molecule chain length which varies from two to five carbons and the number of carboxylic acid groups, subsequently investigating their impact on surface tension. The importance of these compounds is discussed further in Chapter 1 Section 1.3.1. The longer the chain length, the lower the surface tension at a given mole fraction will be. For compounds with four or more carbon atoms the surface tension decreases linearly with the logarithm of the mole fraction of the solute compound.¹⁹⁸

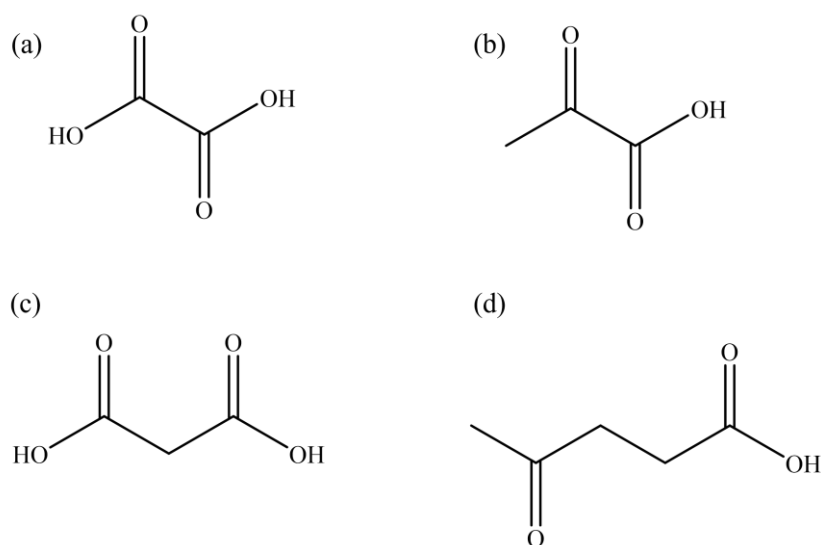


Figure 4-1: The structures of the organic compounds used in this work. (a) oxalic acid with two carbons, (b) pyruvic acid with three carbons, (c) malonic acid with three carbons and (d) levulinic acid with five carbons.

The emission of organic compounds from natural and anthropogenic sources such as fossil fuel burning is set to rise in the near future and in turn influence our climate, health and technology.¹⁴⁸ Characterising the impact of these compounds will be intrinsic to the improvement of climate models and understanding of cloud droplet growth.

4.1.2 The Surface Activity and Tension of Inorganic Salts

One of the major constituents of atmospheric aerosol is ammonium sulfate and therefore it is the inorganic salt of interest in this thesis. Several studies have shown the prevalence of ammonium sulfate within the troposphere. Sulfates are known to form CCN at low cloud supersaturations and impact the reflectivity of cloud droplets thus altering the Earth's albedo, and countering the global warming effect of greenhouse gases.²⁰⁰ Ammonium sulfate and ammonium bisulfate play a key role in the heterogeneous hydrolytic reactions of N_2O_5 into HNO_3 by providing a reaction surface.²⁰¹ These reactions affect the oxidising capacity of the atmosphere through impacting the NO_x , O_3 , and OH global budgets by an average of 25-50%.²⁰² Mkoma et al.²⁵ found the main anionic component within their samples was SO_4^{2-} accounting for 23 % and 37 % of the total species in $PM_{2.5}$ and PM_{10} , respectively.

Ammonium sulfate forms from the transformation of SO_2 to SO_3 , conversion to concentrated sulfuric acid (H_2SO_4 , > 40 wt%) and neutralisation by ammonia in tropospheric aerosol.²⁰³ According to Tu et al. $(NH_4)_2SO_4$ is expected to dominate the continental aerosol composition while NH_4HSO_4 dominates marine aerosols.²⁰⁴ MD simulations of ammonium sulfate show that it is not surface active and resides within the bulk of the droplet for a number of reasons as shown in Figure 4-2. The doubly charged sulfate anion has a small surface affinity due to the electrostatic penalty of bringing the dianion close to the surface. It is therefore more favourable for the SO_4^{2-} ions to solvate within the droplet bulk. The positive ammonium ion, also favouring the bulk of the droplet, is able to form four hydrogen bonds

with the surrounding water molecules. This hydrogen bonding increases the change in the surface energy to surface area ratio thus increasing surface tension above that of water (72.8 mNm^{-1}).

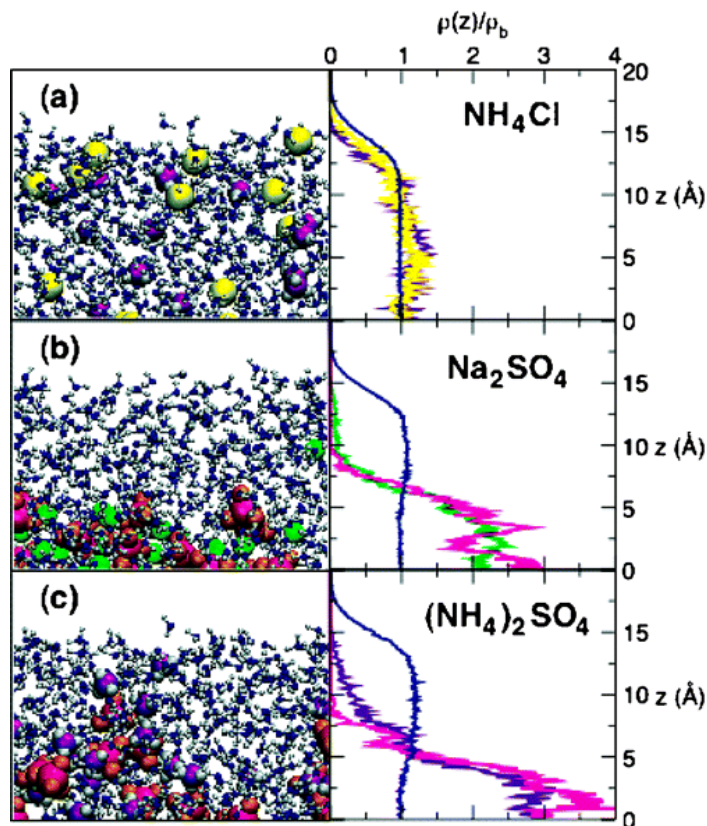


Figure 4-2: On the left-hand side: A snapshot of 1.2 M aqueous solution of (a) ammonium chloride, (b) sodium sulfate, and (c) ammonium sulfate MD simulations. On the right-hand side: Right panels: Density profiles relating to the centre of the slab ($z = 0$) to the air/water interface at 15 \AA . Colour scheme: hydrogen, grey; water oxygen, blue; chloride, yellow; sodium, green; ammonium, purple; sulfate S, pink; sulfate oxygen, orange. **This image is taken from the paper by Gopalakrishnan et al.**²⁰⁵

4.1.3 Surface Tension of Inorganic and Organic Mixtures

Atmospheric aerosols are complex chemical mixtures, containing both inorganic and organic compounds.⁴⁶ The complexity is owed to the thousands of organic compounds with varying surface activities emitted from anthropogenic and biogenic sources and generated through nucleation.²⁰⁶ Frosch et al. stated that the mixing of inorganic and organic to result in two main effects, one being the partial replacement of organic compound with inorganic salt leads to an increase in surface tension and the second effect, shown at high inorganic acid concentrations, leads to a further decrease in the surface tension due to the inorganic salt decreasing the solubility of the organic species forcing the organic component to the solution interface.⁴⁶ Data collected by Saxena et al., in urban and non-urban areas found organic species alter the aggregate hygroscopic properties of inorganic particles.¹⁹⁰ On the one hand, for the non-urban location (Grand Canyon, United States) predominantly hydrophilic organic species exist and account for 25 – 40 % of the total water uptake by the inorganic salt present. On the other hand, in the urban area (Los Angeles, United States) where more hydrophobic organic compounds can be found, at relative humidities between 88 – 93 RH % the uptake of water is diminished by

25 – 35 %.¹⁹⁰ Relative humidity cycles play an important role in the phase state of mixed organic and inorganic aerosols dictating the phase transition and uptake of gaseous species.²⁰⁶ Studies that have been conducted on mixed organic-inorganic salt particles have found the organic component to influence the deliquescence and efflorescence RH along with liquid-liquid phase separation of the inorganic salt.^{207,208} In the case where liquid-liquid phase separation does not take place the DRH and ERH of the inorganic salt are significantly lowered such that the particle may remain in a homogenous liquid state with the potential to further impact air quality and visibility.

4.1.3.1 The Salting Effects

In the presence of an inorganic salt, the aqueous solubilities of organic compounds decrease, this is known as the salting-out effect. The classical Setschenow equation is used to quantify this decrease in solubility using the following equation²⁰⁹:

$$\log(\gamma/\gamma_0) = \log(S_0/S) = K_s [\text{salt}] \quad (4.01)$$

where γ_0 and γ represent the activity coefficients of the organic solute in pure water and in the salt solution respectively, S_0 and S denote the solubilities of the solute in pure water and salt solution, respectively.²¹⁰ K_s is the empirical Setschenow or salting out coefficient (M^{-1}). The equation may also be written as follows:

$$\log(k_{1/\text{salt water}}/k_{1/\text{water}}) = K_s [\text{salt}] \quad (4.02)$$

Where $k_{1/\text{water}}$ and $k_{1/\text{salt water}}$ are the equilibrium partitioning coefficients of an organic solute in an aqueous solution and aqueous salt solution, respectively.²¹¹ A positive value of K_s signifies the partitioning equilibrium shifting towards the non-aqueous phase and the non-electrolyte is pushed towards the surface as solubility decreases. Ultimately an increase in organic species at the solution interface will lead to greater surface tension depletion.²¹² Conversely, the salting-in effect which results in an increase in solubility of the organic component is often caused by salts with a large partial molar volume and have lower K_s values than the salting out coefficient.^{210,213} Sareen et al. found these two effects in glyoxal²¹⁴ and methylglyoxal-inorganic solutions.²¹⁵ Glyoxal salts-in in the presence of salts such as ammonium sulfate, ammonium nitrate and sodium chloride due to strong interactions between the OH groups and electrolyte ions in the hydration shell. Methylglyoxal, however, salts-out in the presence of the same salts as a result of the increase in size due to the additional methyl group adding to the steric hindrance when fitting into the ion hydration shell.²¹⁵

The salting-out by electrostriction theory by et al.²¹⁶ and Conway et al. posits a K_s increase occurs in tandem with an increase in the size of the salt ions, the volume and polarizability of the organic species.^{214,216} Sulfate ions are large ions which require more solvation than chloride ions. To solvate a

sulfate ion requires twelve water molecules to form the first hydration shell. This depletes the number of water molecules available to hydrate the organic molecules and decreases the solubility. When analysing the effect of anions on the salting-out coefficient between SO_4^{2-} , NO_3^- and Cl^- , the SO_4^{2-} coefficients were higher than Cl^- . This may be due to the doubly charged anions having a significantly larger salting-out effect than singly charged anions as Xie *et al.* demonstrated in their K_S values. The study found Na_2SO_4 coefficients to be larger than NaCl across all the organic compounds investigated.²¹⁷

4.1.4 Modelling Surface Tension of Inorganic and Organic Mixtures

Surface tension models and experimental measurements remain important to understanding the interactions between solution components, such as inorganic salts, organic acid, aqueous mixtures, as well as their surface and bulk propensities and their energy barriers associated with adsorption at the surface.^{93,218,219} Various surface tension models have surfaced over the last few decades to predict the behaviour of these more complex systems, two of which will be used in this chapter (Langmuir-Szyszkowski and Boyer *et al.* models).^{93,220}

Wang and co-workers successfully merged separate models which described electrolytes, non-electrolytes, and mixed solvents.²¹² Their framework represented the surface tension of a variety of solution compositions across a wide range of concentrations, however, the model was limited as it disregarded interactions between the solutes, curtailing its use in higher complexity systems. Wexler and Dutcher used an extended model of the Brunauer-Emmett-Teller (BET) and Guggenheim-Anderson-de Boer (GAB), and Ally and Braunstein single monolayer isotherm, which included multilayers with their own individual energy and entropic configuration.^{221,222} Using statistical mechanics to derive an equation for the surface tension as a function of solute activity, Wexler *et al.* developed a binary model whereby the interface consists of water molecule sites. Akin to the Langmuir-Szyszkowski model, the adsorption of solute at the surface displaces r water molecules, where r accounts for the size of the adsorbing molecule and is a parameter derived through fitting the following equation:

$$\sigma = \sigma_w + \frac{k_B T}{r S_w} \times \ln \left(\frac{1 - K a_s}{1 - K a_s (1 - C)} \right) \quad (4.03)$$

where σ_w is the surface tension of pure water, k_B is Boltzmann's constant, T is temperature, S_w is the surface area occupied by one solvent molecule, and a_s is the solute activity. The model parameters are K and C , which represent the energies of the solute molecule in the bulk and at the surface, respectively. Expressed as $K \equiv \exp(\varepsilon_{SB}/k_B T)$ and $C \equiv \exp(\varepsilon_{SS} - \varepsilon_{SB}/k_B T)$. ε_{SS} is defined as the surface energy while ε_{SB} represents the bulk energy. Few binary surface tension models have been successfully extended beyond binary solutions to mixtures with two or more components without the further addition

of parameters and assumptions. This study employs an adsorption isotherm and a statistical thermodynamic model, as previously outlined by H. C. Boyer et al.⁹³, to extend our understanding and predict the surface tensions of ternary solutions in comparison to experimental measurements.

4.1.4.1 Origin and Derivation of Binary System Models

By defining the subsurface/dividing surface at which the chemical potential of the solvent is zero, Gibbs derived the thermodynamic relationship between surface tension and surfactant surface concentration detailed in Chapter 1 Section 1.5.4 and shown in Eq. 4.04.

$$\frac{d\sigma}{d(\ln C_{\text{bulk}})} = -\Gamma_2 RT \quad (4.04)$$

In this equation, the bulk chemical potential and surface concentration of each solution component, along with the relationship between surface tension and solution concentration are described.²²³

$$\Gamma = -\frac{1}{RT} \times \left(\frac{\delta\sigma}{\delta C_{\text{bulk}}} \right)_T \quad (4.05)$$

An additional equation is required to describe the relationship between the bulk and surface concentration. Langmuir derived such an equation (see Eq. 4.06) for dilute ideal solutions and revealed when in combination with Gibbs equation, the previously noted semi-empirical Szyszkowski equation was described.²²⁴

$$\frac{\Gamma}{\Gamma_{\text{max}}} = \frac{C_{\text{bulk}}}{C_{\text{bulk}} + a} \quad (4.06)$$

where Γ_{max} is the maximum surface excess concentration of the surface-active species and a is the ratio of the adsorption to desorption. Szyszkowski in 1908 recognised upon examination of aliphatic acids, their effect on surface tension of water and derived the equation shown in Eq. 4.07 to better describe the relationship between surface tension and the concentration of the solute present.

$$\sigma = \sigma_0 \left(1 - B \times \log_{10} \left(1 + \frac{C}{\beta} \right) \right) \quad (4.07)$$

Where σ_0 is the surface tension of pure water (72.8 mN m⁻¹) at 20 degrees; σ is the surface tension of the aqueous solution (mN m⁻¹); C denotes the concentration of solute (mol L⁻¹) with B and a as a constant for all the acids and a constant characteristic of each acid respectively. To account for the reduced solubility of higher molecular weight compounds in water, C , is replaced with mole fraction, x , as follows¹⁹⁸:

$$\sigma = \sigma_0 \left(1 - B \times \log_{10} \left(1 + \frac{x}{a} \right) \right) \quad (4.08)$$

Eq. 4.08 enables surface tension to be calculated for a number of different dilute aqueous organic solutions with a 3 % accuracy according to Meissner and Michaels.¹⁹⁸ However the equation cannot be applied to solutions with > 1 mole % of the low molecular weight compounds. The constant B is related to the Gibbs adsorption equation by Eq. 4.09 and is said to be same value for acids, alcohols, esters, ketones, and amines which orient themselves almost identically at the surface.

$$\frac{B}{2.3} = \frac{RT\Gamma}{\sigma_0} \quad (4.09)$$

In 2004, Tuckermann expressed Eq. 4.09 and 4.10 as a first order approximation of the semi-empirical equation. Eq. 4.09 can be used to calculate surface concentration and the inverse Langmuir absorption coefficient, β .^{199,47}

$$\sigma = \sigma_0 - \Gamma_{\max}RT \cdot \ln \left(1 + \frac{C}{\beta} \right) \quad (4.10)$$

where Γ_{\max} is the maximum surface excess concentration (mol/m²); R is the universal gas constant (mN m K⁻¹ mol⁻¹); T is the temperature in Kelvin; C denotes the solute concentration (mol L⁻¹). Assuming equilibrium between the bulk phase and the surface layer, the well-known Gibbs equation (Eq. 4.10) can be used to calculate to the Γ_{\max} of the droplet and bulk solution.²²⁵

It is recognised that the Szyszkowski equation neglects solute interactions between the surface and the bulk and therefore can only be valid for ideal solutions or pure water. The Langmuir-Szyszkowski equation is a modified equation from the one proposed by Szyszkowski. This approach treated the movement of molecular species from the bulk to the surface as a process requiring the water molecules which occupy adsorption sites to be displaced in a reversible reaction. This treatment is valid for dilute solutions and begins to break down at more concentrated solutions:

$$\sigma = \sigma_0 - aT \cdot \ln(1 + bC) \quad (4.11)$$

Where T is the temperature and, C is the solution concentration (mol L⁻¹). Both a (g s⁻² K⁻¹) and b (L mol⁻¹) are empirically found parameters using a least squared fit analysis that systemically minimises the error.

4.1.4.2 Derivation of Multicomponent System Models

The Schwier (2013)²²⁶ and Tuckermann (2007)⁴⁷ model (Eq. 4.12) is derived from the Langmuir-Szyszkowski (L-S) equation and has been used to describe more complex mixed systems. In 2007, Tuckermann extended the L-S equation to account for the effect of electrolytes on surface tension of mixed inorganic-organic solutions with the addition of a term to model the salt-organic interactions. Schwier later adapted the model to what is shown in Eq. 4.12. The model parameters a and b were

found by fitting to the binary aqueous organic solutions and k ($\text{mN m}^{-1} \text{ L mol}^{-1}$) was found by first conducting a least squares regression using the mixed inorganic-organic solutions.

$$\sigma(T) = \sigma_{H_2O} + \left(\frac{\Delta\sigma}{\Delta c_{salt}} \right) c_{salt} - aT \ln(1 + bC) + kc_{salt} \ln(1 + bC) \quad (4.12)$$

4.1.4.3 Boyer et al. Model

The Boyer model²²⁷ uses work from Dutcher et al.²²² and Ohm et al.²²⁸ who were able to successfully model binary systems by using multilayer adsorption isotherm and accounting for solute long- and short-range interactions. The Boyer et al. model 2016 incorporates a solution model where water molecules adsorb to sites on the organic, and an interface model where the organic displaces water molecules at the surface, along with the partial dissociation of the organic acids. The partial dissociation constants are gathered from literature and allow consideration of both neutral and dissociated forms of the acid. In this way the model for binary organic systems in this study is able to account the change in surface tension over a range of concentrations. The binary statistical thermodynamic model was successfully expanded by Boyer et al.⁹³ to ternary systems showing excellent agreement between predictions and measurements of electrolyte-electrolyte solutions, organic-organic solutions, or single organic, single electrolyte solutions. The model allows organic and electrolytes to compete for surface adsorption sites with equal probability with each model parameter (r, K, C) decoupled for each of the solutes. These solutes are defined as either A or B which can adsorb and desorb from the surface as depicted in Figure 4-3. The temperature of the model is set at 298 K and uses 72.0 mN m^{-1} for surface tension of pure water.

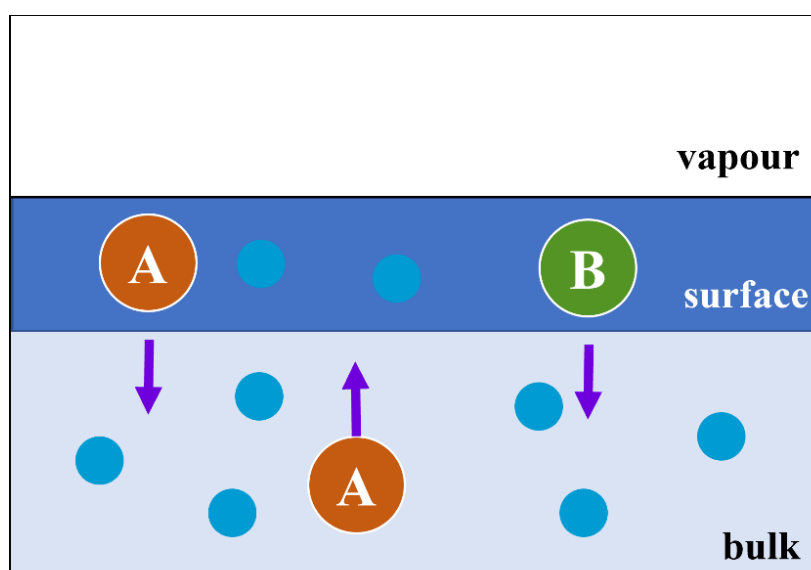


Figure 4-3: A depiction of how the model treats the separate components in a multi-component solution, A and B are used to denote different organic species. Image recreated from research article Boyer et al 2016.²²⁷

4.2 Measurement Techniques

The experimental techniques used to characterise the surface tension of organics, inorganic salts and their aqueous mixtures are described in Chapter 3 and will be briefly summarised. The specific systems examined in this chapter are not highly surface active. Based on the droplet compositions studied (organic acids and inorganic salts), the droplet surface tensions are not anticipated to deviate significantly from the bulk organic acid solution due to rapid surface-bulk partitioning (as opposed to the slow diffusion and adsorption properties observed in true surfactants). Therefore, these systems serve as a suitable test for the method, as the measurements taken from the droplets and bulk solution should match. Table 4-1 details of the compounds used in this study to analyse low different systems in aqueous solution alter surface tension.

Table 4-1: The chemical information of each compound used in this experiment. Information was (a) PubChem²²⁹, (b) Fernandez et al.²³⁰, (c) Chemical Book²³¹.

Compound	Molecular weight (g mol ⁻¹)	Density (g cm ⁻³)	Solubility limit in water (g L ⁻¹)	O:C Ratio
Oxalic acid	90.0 ^a	1.9 ^a	220.0 ^b	2.0
Malonic acid	104.1 ^a	1.6 ^a	730 ^a	1.3
Pyruvic acid	88.1 ^a	1.3 ^a	1000.0 ^a	1.2
Levulinic acid	116.1 ^a	1.1 ^a	675.0 ^c	1.4
Ammonium Sulfate	132.1 ^a	1.8 ^a	706.0 ^a	N/A

4.2.1 Droplet Oscillatory Method

When droplets are ejected from a microdispenser they undergo shape oscillations observed and captured by stroboscopic imaging. By superimposing a box around the droplet, the aspect ratio over a given time can be determined and converted into an oscillation frequency using fast Fourier transform (FFT) with a Lorentzian fit to the data. From the frequency acquired from the FFT the surface tension of the droplet can be derived. The uncertainty in the surface tension measurement is calculated from the error found in the Lorentzian fit of the frequency and the uncertainty found in the droplet diameter by taking these values and generating a maximum and minimum surface tension which is then used to calculate the uncertainty in the surface tension. The droplet diameter and its uncertainty are determined by taking the average and standard deviation of the last one hundred diameter recorded data points, where the droplet has relaxed to a spherical shape. The standard deviation in the diameter and surface tension varied no more than 0.1 – 0.3 μm and $\pm 3 \text{ mN m}^{-1}$ respectively.

4.2.2 Maximum Bubble Pressure Tensiometer

By creating bubbles at the tip of a capillary within the solution and measuring the time it takes to reach the pressure maximum, the surface tension of the solution over time can be deduced. Initially, the radius of the capillary tube must be determined with a known reference solution, water (72.8 mN m⁻¹, 298 K). Once the radius of the capillary is calculated, the surface tension can be determined from the pressure maximum p_{max} . The hydrostatic pressure p_0 from the immersion of the capillary in the liquid is subtracted from p_{max} automatically by the KRUSS bubble tensiometer software and from this the surface tension is computed, see Eq. 4.13. The uncertainty in the bulk measurements is ± 1 mN m⁻¹.

$$\sigma = \frac{(p_{max}-p_0) \times r}{2} \quad (4.13)$$

4.3 Results and Discussion

4.3.1 Summary of study

To characterise the closeness to bulk surface tension and the reproducibility of the droplet oscillation method, the surface tension of binary organic, inorganic salt and their ternary mixtures were investigated as a function of concentration or mole fraction. Droplets ejected from a microdispenser are captured using stroboscopic imaging set a delay time from the initial voltage pulse. By observing oscillation over a given time period, typically between 300 – 800 μ s depending on the solution, the aspect ratio can be retrieved, and fast Fourier transformed into a frequency. In turn this oscillation frequency can be used to calculate the droplet surface tension. The $l=2$ is determined to be point when the centre of mass equates to one and the droplet is said to be oscillating axisymmetrically. Earlier data points that correspond to higher order oscillation modes $l \geq 2$ (see Chapter 3, Section 3.1) are removed from the data. The surface tension of aqueous binary organic acid mixtures behaves similarly to pure water as shown in Figure 4-4. It does not exhibit surfactant-like behaviour hence the peak position in Figure 4-4 remains consistent over time. A shift in the peak position is indicative of dynamic-like behaviour taking place. The surface tension measurements are referred to as the equilibrium droplet surface tension, a characterisation supported by corresponding bulk phase equilibrium surface tension measurements.

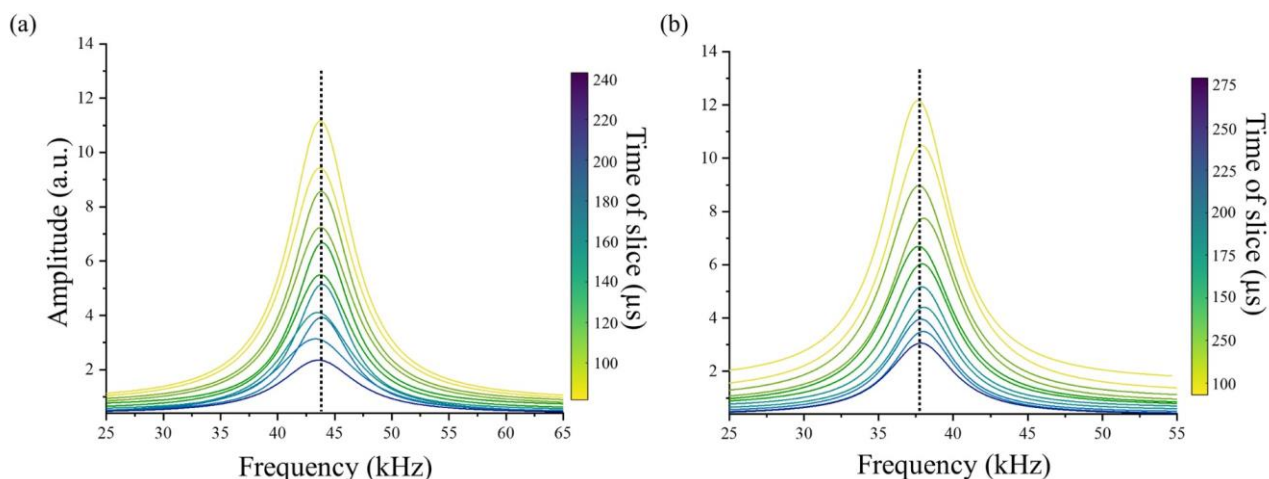


Figure 4-4: Dynamic behaviour of (a) water (b) a binary solution of aqueous levulinic acid. Each colour represents the time at which the data was sliced, and the data prior is removed. Both (a) and (b) identically show very little shift in the peak position of the oscillation frequency over time. This demonstrates that there is no dynamic molecular behaviour during the experimental time frame and the solution has reached equilibrium before the surface tension measurement commenced.

The bulk surface tension measurements were collected using a maximum bubble pressure tensiometer. By generating bubbles in a solution, the tensiometer is able to determine the maximum at which the bubble bursts which is associated with the surface tension of the solutions. The surface tension was collected at the final time point of the measurement 10^5 ms. Figure 4-5 shows the excellent agreement between the binary organic solution measured in the bulk using the maximum bubble tensiometer (MBT) and in the droplet measured by the droplet oscillation method.

Two models discussed in Section 4.1.4 will be compared to experimental data. The Boyer et al. 2016 model was compared to the droplet and bulk data to see the goodness of fit between the model to the measurements.²²⁷ The better the fit, the better the model is able to reflect the surface tension profiles of binary organic mixtures. The Langmuir-Szyszkowski equation was used to calculate the parameters by fitting the equation with method of least squares fitting to the experiment and bulk data to determine Γ , a , and b . Similarly, the Szyszkowski equation also known as the Gibbs equation was fitted to the droplet data to calculate the Γ_{max} and β of each compound and compared to the literature. The Langmuir-Szyszkowski equation was also used because it includes a term for the effect of temperature on the adsorption isotherm, while the Szyszkowski equation is a more general equation that relates the surface tension of a solution to the surface excess concentration of solutes at the surface.

4.3.2 Surface Tension of Binary System

4.3.2.1 Surface Tension of Organic Acids

Here, the dependency of surface tension on the solution concentration is explored. These systems were chosen as they are compounds found in the atmosphere or can act as models for surfactant are atmospherically relevant. Figure 4-5 shows excellent good agreement between the binary equilibrium surface tension values measured in the bulk and droplet. The L-S equation fitted line one denotes the fit when conducted on the surface tension of the bulk solutions and fitted line two describes the fit when conducted on the droplet-phase measurements. The surface tension for both malonic and oxalic acid are comparable within approximately $\pm 2 - 9\%$ and $\pm 1 - 4\%$ of the literature data, respectively, whereas the literature surface tension for pyruvic acid and levulinic acid are currently unavailable for comparison.

From Figure 4-5, we observe pyruvic, malonic and levulinic acid behave like surface-active agents whereas oxalic acid does not. A possible explanation for this behaviour can be found in the study by Mahiuddin et al.¹⁶ Using computational simulations, Mahiuddin et al.¹⁶ shows the surface behaviour of oxalic acid has the weakest surface propensity when compared to citric, succinic, and maleic acid. The oxalic acid molecule exhibits a density profile with both surface and bulk solvation showing signals in both areas.¹⁶ Pyruvic acid depresses the surface tension to the same level as its C3 counterpart malonic acid: both compounds have a moderate surface propensity confirmed by their similar maximum surface excess concentrations in Figure 4-6. As the number of carbons increases from oxalic acid < malonic acid = pyruvic < levulinic acid, the reduction in surface tension is increased as illustrated in Figure 4-4. For example, between 0-3 mol L⁻¹, the five-carbon levulinic acid reduces the surface tension by 19 mN m⁻¹ whereas the two-carbon oxalic acid reduces the surface tension by 3 mN m⁻¹. All models used in this study echoes these findings, showing an increase in the number of carbons per molecule leads to a greater surface tension reduction.²²⁷

The Boyer et al. model fit shows an agreement with the oxalic, malonic acid and levulinic acid bulk measurements within approximately $\pm 1 - 2$ mN m⁻¹). Pyruvic acid shows an unexpectedly poor agreement with the model at high concentrations as the model was skewed by the bulk phase measurement at 1.5 mol L⁻¹ whereby the surface tension equated to 50 mN m⁻¹. As these are simple binary systems, the Langmuir-Szyszkowski equation (Eq. 4.11) can be used to fit the data. The surface tension data was fitted to Eq. 4.10 taking $\sigma_0 = 72.8$ mN m⁻¹ for water. Multiple fits were conducted with the Langmuir-Szyszkowski equation to obtain the best agreement with the measurement data as possible. The droplet and bulk data for malonic, pyruvic, oxalic and levulinic acid are within $\pm 0 - 2\%$ agreement with the Langmuir-Szyszkowski model calculations. In both cases, the model fits are in very good agreement with the literature data found for oxalic acid and malonic acid as shown in Figure 4-5.

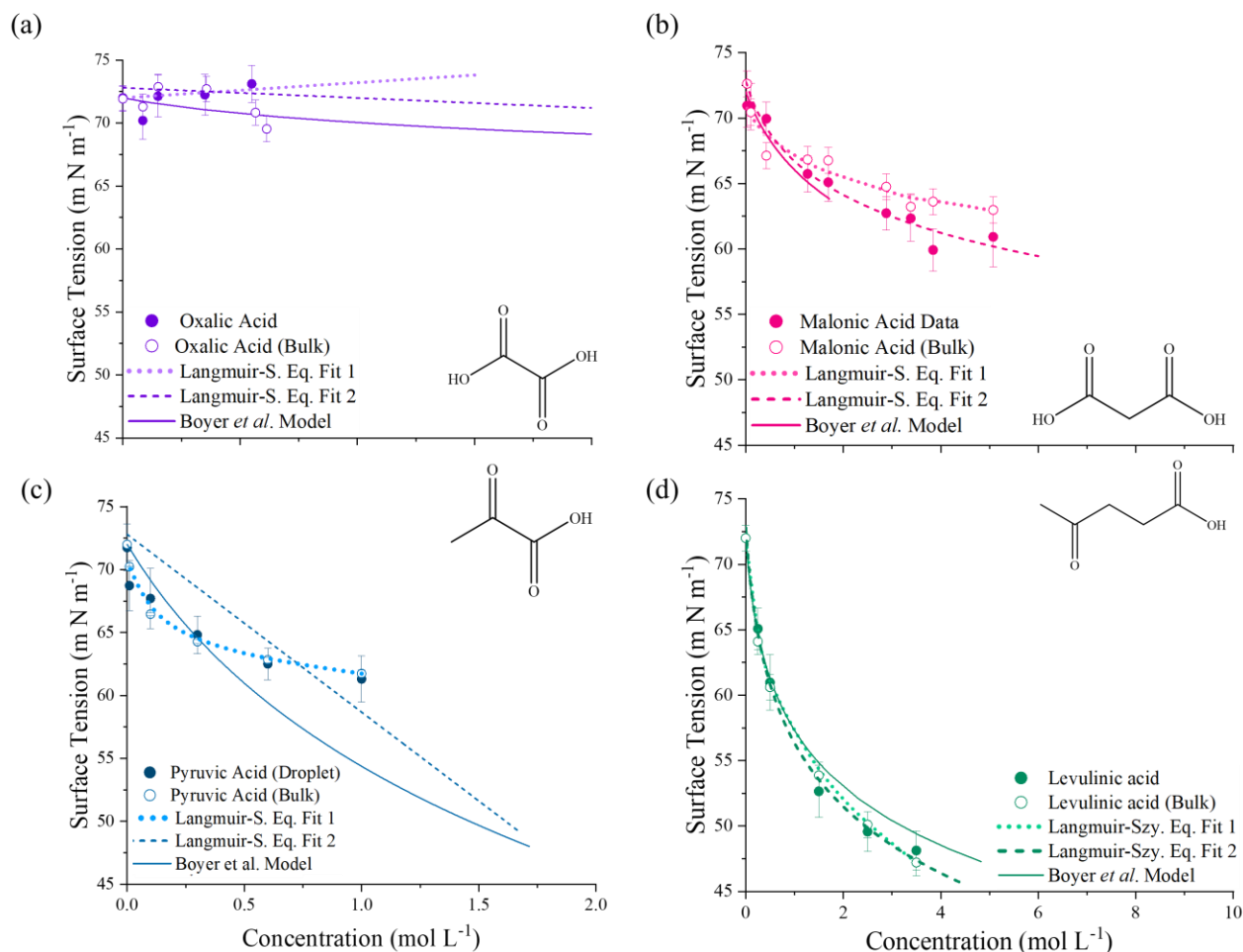


Figure 4-5: Surface tension of (a) oxalic acid (purple symbols), (b) malonic acid (pink symbols), (c) pyruvic acid (blue symbols) and (d) levulinic acid (green symbols). Filled symbols symbolise data collected using the droplet oscillatory method and empty symbols denote data collected using the Bubble pressure tensiometer. Shown for comparison with the experimental data are the predictions of surface tension from the model of Boyer et al. and the two different fits performed with the Langmuir-Szyszkowski equation.

Figure 4-6 presents Γ_{max} in relation to the number of carbons and Table 4-2 shows the concentration of adsorbed molecules at the surface fraction (θ). The Γ_{max} describes the maximum excess of a substance at the surface compared to the bulk whereas the surface concentration Γ_i refers to the concentration of a substance at the surface boundary. For oxalic acid Γ_{max} and θ are the lowest of the four compounds which resonates with the Mahiuddin et al. study showing the low surface propensity of the compound.¹⁶ Note, though pyruvic acid shows the highest overall surface concentration, it is levulinic which shows the greatest reduction in surface tension with an increase in organic concentration. This could be due to the area per molecule and number of carbons in levulinic acid as discussed below.

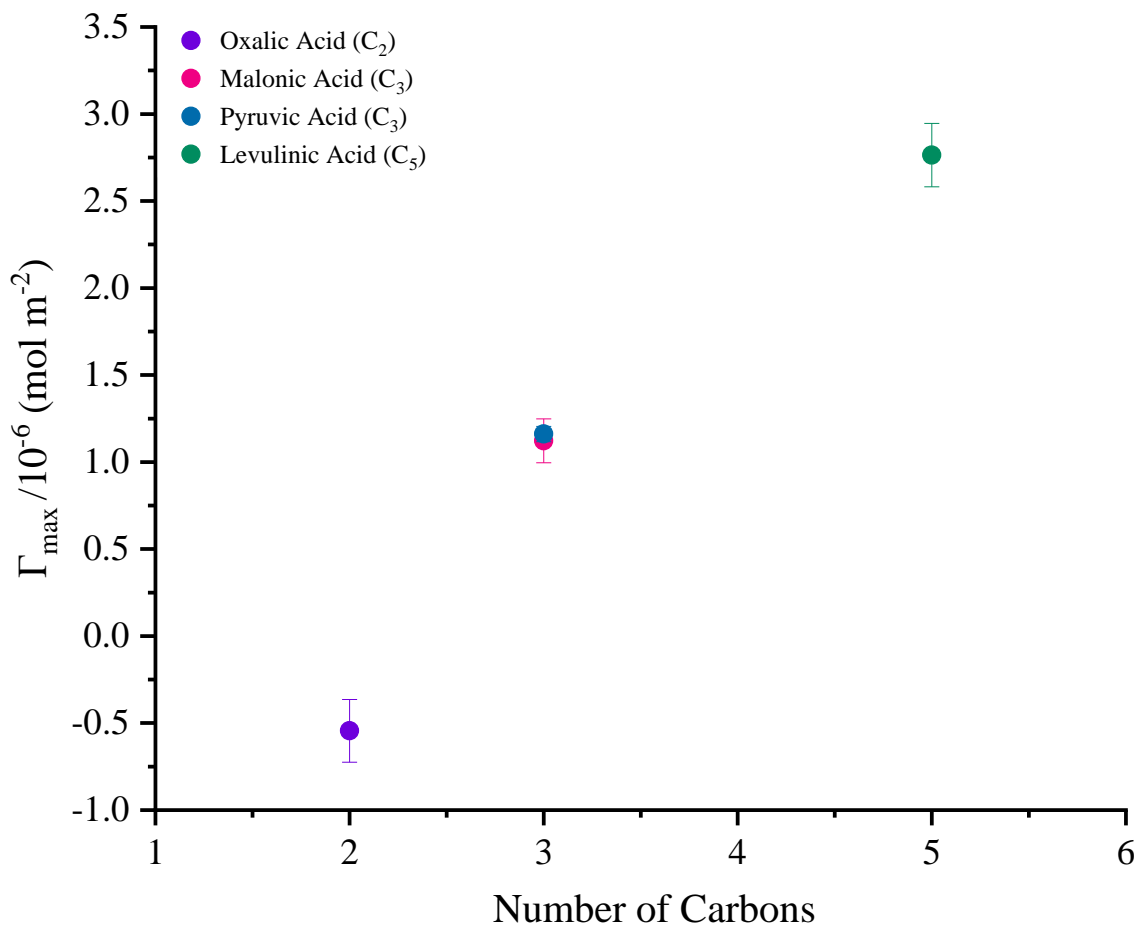


Figure 4-6: Maximum surface excess concentration for oxalic acid (purple filled symbol), malonic acid (pink filled symbol), pyruvic acid (blue filled symbol) and levulinic acid (green filled symbol). The graph shows a linear relationship between the number of carbons and the surface excess concentration. The positive values indicate the solute reduces the surface tension of the solution below that of water.

Table 4-2: The fraction of surface coverage by the adsorbed molecules at the surface calculated alongside the parameter a and b from the experimental data using the Langmuir-Szyszkowski equation ($\sigma = \sigma_0 - a\Gamma \ln(1 + bC)$).

Oxalic acid		Malonic acid	
Concentration (mol L ⁻¹)	Γ (mol m ⁻²)	Concentration (mol L ⁻¹)	Γ (mol m ⁻²)
0.55	2.30 × 10 ⁻⁵	5.10	0.78
0.35	1.40 × 10 ⁻⁵	3.80	0.71
0.15	6.10 × 10 ⁻⁶	3.40	0.70
0.09	3.40 × 10 ⁻⁶	2.90	0.64
		1.70	0.48
		1.30	0.40
		0.40	0.17
		0.10	0.05
		0.03	0.01

Pyruvic acid		Levulinic acid	
Concentration (mol L ⁻¹)	Γ (mol m ⁻²)	Concentration (mol L ⁻¹)	Γ (mol m ⁻²)
1.00	0.98	3.50	0.89
0.60	0.97	2.50	0.84
0.30	0.93	1.50	0.74
0.10	0.82	0.50	0.45
0.01	0.31	0.25	0.29

In the Langmuir-Szyszkowski equation, detailed in Eq. 4.11 is fit to the bulk (fit 1) and droplet (fit 2) shown in Table 4-3 using the least squares fitting method. The equation can be used to calculate the surface coverage and parameter ' a ' and ' b '. The constant ' a ' depends on the nature of the solute, and ' b ' denotes the Langmuir adsorption constant related to the concentration of the solute at the interface. At first these values are chosen arbitrarily and systematically optimised to the data using the estimation method of least squares regression. The constant a is related to the nature of the solute and the strength of its interactions with the solvent molecules at the surface. The larger the value of a , the stronger interactions at the surface and greater the surface tension depression. From Table 4-3, as expected the value of a in Fit 2 trends as levulinic acid > malonic acid > oxalic acid, in order of highest value first. However, pyruvic acid does not conform predictions as it shows the lowest value of a . This may be due to poor fitting of Eq. 4.11 to the experimental data, to understand this further, comparison with literature and measurement data would be needed.

Conversely, the Langmuir adsorption constant, b does not follow the same trend as parameter a . The parameter b characterises the strength of the interaction between the solute molecules and the surface. Given the relationship between number of carbons in each compound and surface affinity, the trend of parameter b is expected to follow levulinic acid > malonic acid > pyruvic acid > oxalic acid in order of highest to lowest. Both fits do not follow the trend as expected. In fit 1, pyruvic acid exhibits the highest value of parameter ' b ' as expected from Table 2, however the fit to the bulk data (fit 2) suggests levulinic has the higher value. Further work to understand this difference is required.

Table 4-3: The fitted parameter a and b from the Langmuir-Szyszkowski equation. As these values are found via a least squares regression, uncertainty values cannot be obtained. Fit 1 corresponds to fitting the L-S equation to the bulk-phase data and Fit 2 corresponds to the optimised fit to the droplet data.

Oxalic Acid			Malonic Acid		
	Fit 1	Fit 2		Fit 1	Fit 2
a	-7.24	-10.94	a	0.02	0.02
b	-5.70×10^{-5}	-2.50×10^{-4}	b	1.50	2.60

Pyruvic Acid			Levulinic Acid		
	Fit 1	Fit 2		Fit 1	Fit 2
a	-7.07×10^{-3}	-268.06	a	2.12×10^{-2}	0.026
b	44.97	-2.00×10^{-4}	b	2.02	7.51

Szyszkowski Equation

Another method of investigating the decrease in surface tension of binary systems is to fit data to the Szyszkowski equation, Eq. 4.07. The surface tension measurements from this study were conducted at 293 K and literature 298 K. The difference in the temperature leads to a $\leq \pm 1$ % discrepancy between the measurement and the estimated surface tension data. This shows that a temperature difference of this magnitude does not have a significant impact on the estimated surface tension. Table 4-4 exhibits the Szyszkowski equation calculated values for Γ_{max} , β and A_{min} . The maximum surface excess concentration, Γ_{max} , of a compound refers to the excess amount of a substance present in a given surface area. A positive value signifies the compound's capacity to elevate surface tension, whereas a negative value indicates the contrary effect. The parameter β represents the characteristic adsorption constant and is a measure of a compound's affinity to the surface. A_{min} describes the area per molecule which indicates the degree of packing and orientation of adsorbed molecules at the surface of the droplet or solution.

Oxalic Acid

Table 4-4 shows an increase in the Γ_{max} moving from oxalic and levulinic acid, a change likely to be an increase in the number of carbons in the organic chain and increased affinity for the surface. All organic species with the exception of oxalic acid have a positive value for Γ_{max} . In contrast to the other organic systems, the surface tension increases slightly above that of pure water (72.8 mN m^{-1}) as the oxalic acid concentration increases. This leads to a negative Γ_{max} , a characteristic often associated with inorganic acids. As the variation in surface tension is within error of the surface tension of water, the increase should be disregarded. Table 4-4 shows for the Γ_{max} and β values, oxalic acid is an order of magnitude lower than the values found in the literature, a discrepancy which could be due to the low number of data points and the scatter within the measurements taken. Additional data is needed to be collected to better characterise the surface tension of binary oxalic acid. Both in the bulk and droplet measurements the A_{min} is large suggesting oxalic acid does not closely pack at the surface of the solution or droplet which is expected from its lower surface affinity evident in the low β values.

These measurements imply that oxalic acid is unlikely to be a surface-active organic compound and is more likely to be situated in the vicinity of the bulk phase of a droplet or solution. Hence, it may not play a significant role in reducing the surface tension of atmospheric aerosols.

Malonic Acid

The values of Γ_{max} and A_{min} for the aqueous malonic acid droplet and bulk measurements exhibit a reasonable agreement with the literature data from Tuckermann et al.⁴⁷. For the droplet data, Γ_{max} and A_{min} is comparable within $\pm 2\%$ and 1% of the literature data while the bulk phase data is $\pm 2\%$ and 19% , respectively. Both malonic acid and pyruvic acid show similar values Γ_{max} and A_{min} but vastly different values for β , possibly indicating that malonic acid has a higher surface affinity than pyruvic acid. The large discrepancies in the values for β between the measured and literature remains under further investigation.

Levulinic Acid

In Table 4-4, it is evident that levulinic acid not only demonstrates the highest maximum surface excess concentration but also consistently presents the lowest area per molecule. This aligns with the observed trend in the studied series of carboxylic acids, specifically, levulinic acid < pyruvic acid < malonic acid < oxalic acid. The levulinic molecules are able to pack closer together, with a high affinity and stability on the surface and thus it is capable of reducing the surface tension to highest degree of the droplet or solution. It is probable that organic compounds that possess analogous structures to levulinic acid, which are frequently detected in the atmosphere, can act to decrease surface tension to a value below that of pure water.

Table 4-4: The Γ_{max} denotes the maximum surface excess concentration, inverse activity coefficient β of various organic species and A_{min} is the area per molecule, calculated from the Langmuir-Szyszkowski equation, ^a Lee et al. (2014)¹⁹⁹, ^b Aumann et al. (2010)²³², ^c Hyvärinen et al. (2006)²³³, ^d Tuckermann et al. (2007)⁴⁷. The units used for Γ_{max} were 10^{-6} mol m⁻²; β , 10^{-3} mol L⁻¹ and A_{min} , Å² Molecule⁻¹. The measurements from this study were conducted at 298 K as in the literature.

Oxalic acid								
Droplet			Bulk			Literature		
Γ_{max}	β	A_{min}	Γ_{max}	β	A_{min}	Γ_{max}	β	A_{min}
-0.54 ± 0.18	270 ± 23	305	0.098 ± 0.19	80 ± 40	1700	1.20 ± 0.14 ^a	640 ± 192 ^a	143
						1.50 ± 0.39 ^a	1700 ± 501 ^b	108
						0.31 ± 0.04 ^a	35 ± 15 ^c	536

Malonic acid								
Droplet			Bulk			Literature		
Γ_{max}	β	A_{min}	Γ_{max}	β	A_{min}	Γ_{max}	β	A_{min}
1.10 ± 0.13	990 ± 36	150	0.95 ± 0.20	1080 ± 108	174	2.00 ± 0.12 ^a	590 ± 88 ^a	83 ^a
						1.10 ± 0.06 ^a	230 ± 44 ^c	150 ^a

Pyruvic acid								
Droplet			Bulk			Literature		
Γ_{max}	β	A_{min}	Γ_{max}	β	A_{min}	Γ_{max}	β	A_{min}
1.20 ± 0.044	270 ± 20	140	1.60 ± 0.044	270 ± 38	104	-	-	-

Levulinic acid								
Droplet			Bulk			Literature		
Γ_{max}	β	A_{min}	Γ_{max}	β	A_{min}	Γ_{max}	β	A_{min}
2.80 ± 0.18	1300 ± 550	60	2.30 ± 0.12	1300 ± 180	68	-	-	-

4.3.2.2. Surface Tension of Monovalent Inorganic Salts

Inorganic species such as ammonium sulfate have been shown to reside in the bulk of the solution and typically increase the surface tension above that of pure water. The first approximation Eq. 4.17 can be used to describe the linear function surface tension against the solute concentration and compare between the data in this study and the literature.⁴⁷ The $\Delta\sigma/\Delta C$ found in this study equates to 2.72 ± 0.32 kg mol⁻¹ mN m⁻¹ and compares well to literature values from Lee et al.⁴³ (2.33 ± 0.04 kg mol⁻¹ mN m⁻¹) and Svenningsson et al.²³⁴ (2.36 kg mol⁻¹ mN m⁻¹).

$$\sigma = \sigma_0 + \frac{\Delta\sigma}{\Delta C} C \quad (4.14)$$

From Figure 4-7, as expected, as the concentration of the inorganic increases, the surface tension increases for both the droplet and bulk measurements. The present study demonstrates a high degree of concordance between droplet and bulk data, thereby reaffirming the usability of the droplet oscillatory

method as a reliable technique for measuring surface tension. The droplet and bulk measurements deviate from the model by Boyer et al. however remains within error of the E-AIM model data shown in Figure 4-7 and 4-8.

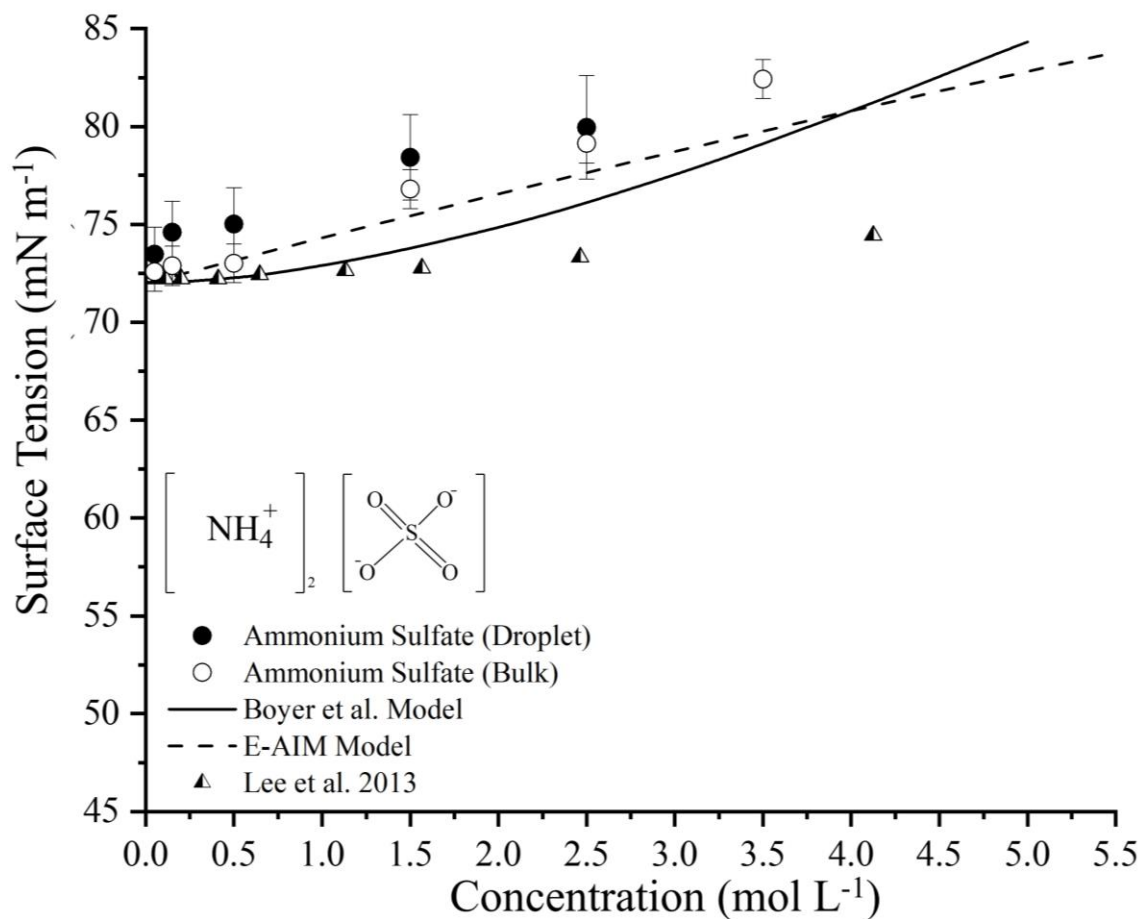


Figure 4-7: Surface tension of ammonium sulfate measured using the droplet oscillatory method (black filled symbols) and bubble tensiometer (black empty symbols). Our results are compared against the E-AIM model, Boyer et al. model.^{43,235}

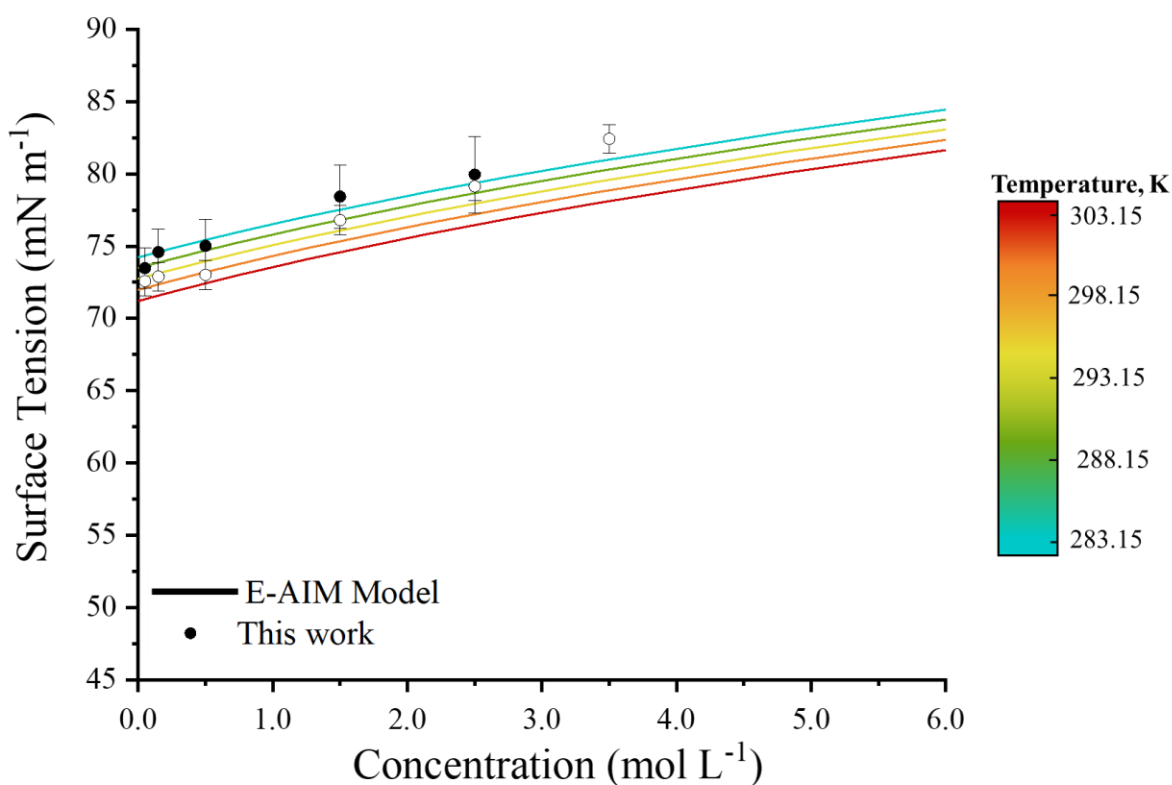


Figure 4-8: Surface tension of ammonium sulfate measurement compared to the surface tension given by E-AIM model at different temperatures ranging from 278.5-303.15 K.²³⁶

4.3.3 Surface Tension of Ternary Systems

Herein we will discuss the measurements collected that contain three components, organic acid, inorganic salt, and water making up our ternary systems. The surface tension of four different organic acids were measured at varying ratios with ammonium sulfate both in the bulk and droplet phase. The inorganic salt content was increased to analyse the impact of increasing the inorganic salt content on surface tensions of organic mixtures. These results have been compared to the model detailed in a previous paper by Boyer et al. and the Tuckermann 2007 models to assess how well the models reflect the measurement data.

Table 4-5: The chemical composition of mixtures which have been used in the experiments.

Compound	Mixture Ratio (inorganic salt: organic acid)
Ammonium Sulfate: Oxalic acid (AS:OA)	1:1
Ammonium Sulfate: Malonic acid (AS:MA)	1:1 4:1 8:1
Ammonium Sulfate: Pyruvic acid (AS:PA)	1:1 2:1 4:1
Ammonium Sulfate: Levulinic acid (AS:LA)	T: 4:1 16:1

4.3.3.1 Setschenow Coefficients

In this study AIOMFAC, a group contribution model, was implemented to computationally derive the activity coefficients of organic compounds in both pure water and salt solutions at 298 K. Subsequently, the Setschnow coefficient was determined using Eq. 4.01. In instances where the Setschnow or salting-out coefficient is positive, it signifies a shift in the solvation of organic species due to the presence of an inorganic salt, resulting in a diminished solubility of the organic compound and a further reduction in the surface tension. The organic compounds, levulinic, malonic and pyruvic acid all show positive K_s in Table 4-6, indicating the salting-out is in effect. Conversely, oxalic acid has a negative K_s value which shows the salting-in effect may take place as the concentration of the organic species increases. This may be a result of the increased polarity of oxalic acid with its two carboxylic groups that can interact strongly with salt ions and water molecules leading to an increase in solubility.

Table 4-6: Setschenow constants calculated from the thermodynamic model, AIOMFAC with the salt concentrations used in this study.

Ammonium sulfate: Oxalic acid			Ammonium sulfate: Malonic acid		
Inorg:Org	Salt Concentration (mol L ⁻¹)	K _s	Inorg:Org	Salt Concentration (mol L ⁻¹)	K _s
1-1	0.19	-0.04	1-1	3.36	0.018
	0.15	-2.91		1.68	0.021
	0.10	-3.16		0.96	0.021
	0.04	-4.15		0.48	0.012
4-1			4-1	2.20	0.019
				0.80	0.017
				0.40	0.009
8-1			8-1	2.64	0.017
				1.68	0.021
				0.96	0.019
				0.48	0.012
Ammonium sulfate: Pyruvic acid			Ammonium sulfate: Levulinic acid		
Inorg:Org	Salt Concentration (mol L ⁻¹)	K _s	Inorg:Org	Salt Concentration (mol L ⁻¹)	K _s
1-1	0.98	0.11	1-1	1.58	0.18
	0.62	0.11		1.01	0.19
	0.35	0.11		0.58	0.21
	0.18	0.12		0.29	0.23
2-1	1.30	0.11	4-1	2.26	0.22
	0.83	0.11		1.44	0.22
	0.47	0.12		0.82	0.22
	0.24	0.12		0.41	0.23
	0.12	0.12		0.21	0.25
4-1	2.84	0.13	16-1	3.68	0.28
	2.37	0.12		2.53	0.25
	1.66	0.12		1.38	0.23
	0.95	0.12		0.92	0.23
	0.47	0.12		0.46	0.23

The surface tension of the inorganic and organic aqueous mixtures at different mole ratios were measured by varying the mole fractions to determine the impact of increasing the salt concentration on the surface tension of the organic species. The results of the bulk and droplet measurements are detailed in the following section and show similar in values validating the droplet oscillation method for these systems.

4.3.3.2 Ammonium Sulfate: Oxalic Acid

Figure 4-9 shows the effect of increasing the total solute mole fraction (tMF) on the surface tension of an AS:OA 1:1 mixture. As the tMF was increased, the surface tension of the mixture remained relatively constant and within error of the ammonium sulfate and oxalic acid measurements. Contrary to the AIOMFAC derived Setschenow constants both sets of measurement data (droplet and bulk) do not appear to be impacted by the ‘salting-in’ effect. Interestingly, the Boyer et al. model predicts the

opposite result, and the model suggests the ‘salting-out’ could be an effect of the ammonium sulfate and oxalic acid mixture causing a decrease in surface tension below the binary oxalic acid solution. In comparison, the Tuckermann equation (Eq. 4.11) models the 1:1 mixture well across the tMF range showing little to no increase in surface tension as the organic concentration is increases until the end of the measurement data. After this, the Tuckermann model predicts a decrease in surface tension with an increase in the tMF. The predicted changes in this system were relatively small rendering the data quantitatively difficult to resolve for either model.

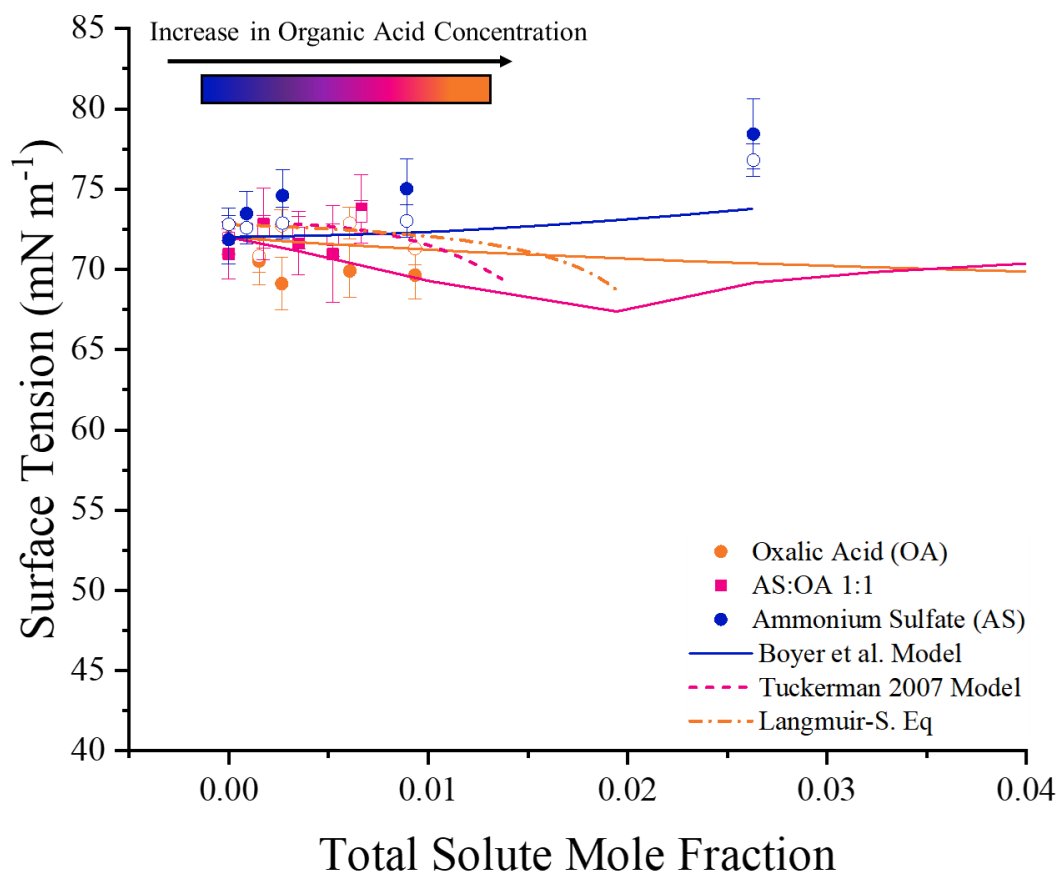


Figure 4-9: Surface tension of ammonium sulfate (blue symbols), oxalic acid (orange symbols) and the mixed aqueous ammonium sulfate:oxalic acid (1:1, pink symbols). The Boyer et al. model is indicated by the solid straight lines, the Langmuir-Szyszkowski model for aqueous organic systems represented by the short, dotted line and the Tuckermann (2007) model for mixed inorganic and organic symbols indicated by the short, dashed line.

4.3.3.3 Ammonium Sulfate:Malonic Acid

Figure 4-10 shows a comparison of AS:MA mole ratio across a wide tMF range with the Boyer and Tuckermann models. As the inorganic component in the mixture is increased, the surface tension increases showing the strong influence ammonium sulfate has on the surface tension. For example, at tMF value ~ 0.06 , the mole ratio of 1:1 ammonium sulfate to organic acid, the surface tension was reduced by 5 mN m^{-1} . Whereas at the same mole fraction, with the mole ratio of 8:1 ammonium sulfate to organic acid the measured data shows an increase of 3 mN m^{-1} .

The K_s constant show a relatively low salting effect on the AS:MA mixtures which supports a lack of an effect seen in the measurement data. Though Clegg et al.²³⁷ observed malonic acid salt out in low concentrations of electrolyte and salting in at high concentrations, increasing the solubility of the solution above ~ 8 to 10 mol dm^{-3} of acid. It is possible the data in this work does not reflect previous data due to the low concentrations used.

The Boyer model is in good agreement with the experimental data as this is a well-known and studied system. Tuckermann 2007 model shows better fit with measurement data points, estimating the surface tension across the total solute fraction range in very good agreement. For example, observing the 4:1 mixture, Tuckermann model deviates from the Boyer et al. predictions, following the measurement data more accurately as Figure 4-10. Both models remain within error of the droplet data across all mole fractions therefore both would be appropriate in estimating the surface tension profiles of the droplet ternary mixtures.

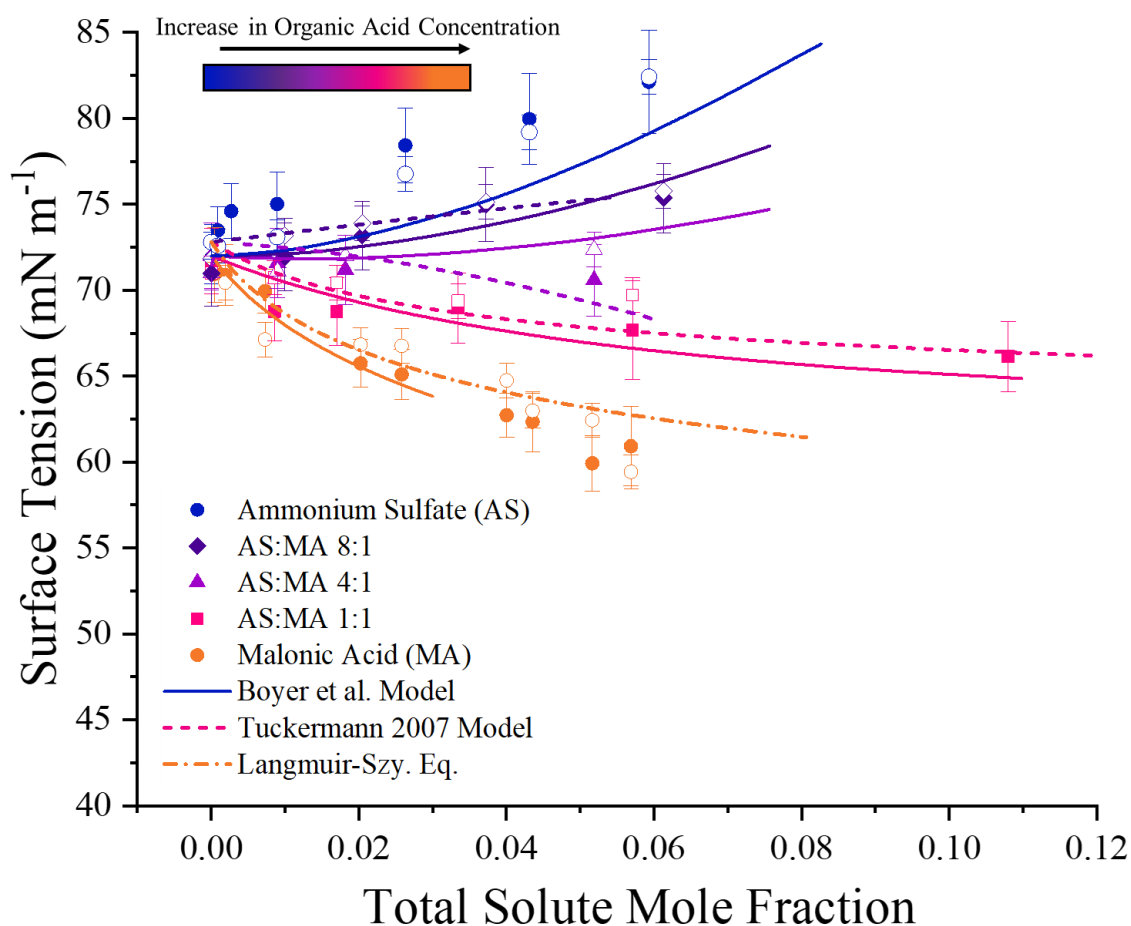


Figure 4-10: Surface tension of ammonium sulfate (blue symbols), malonic acid (orange symbols) and the mixed aqueous ammonium sulfate:malonic acid (1:1, pink symbols; 4:1, light purple symbols, 8:1 dark purple symbols) as a function of the total solute mole fraction. The Boyer et al. model is indicated by the solid straight lines, the Langmuir-Szyszkowski model for aqueous organic systems represented by the short, dotted line and the Tuckermann model for mixed inorganic and organic symbols indicated by the short, dashed line.

4.3.3.4 Ammonium Sulfate:Pyruvic Acid

The results of surface tension measurements on aqueous solution of AS and PA are plotted in Figure 4-11. The droplet and bulk surface tension of pyruvic acid remain similar to its C3 counterpart malonic acid at same mole fraction. From the binary Langmuir-Syskoski equation parameters a and b , a lower affinity for the surface would be expected for pyruvic acid than malonic however here a similar if not greater affinity is seen in the presence of ammonium sulfate. This observation corresponds to the higher salting out coefficients found in Table 4-6 for pyruvic acid compared to malonic acid. Figure 4-11 shows the ternary Boyer et al. model replicates the measurement ammonium sulfate/pyruvic acid data closely, showing the most coherent fits of all the systems. The Tuckermann model shows a good fit to the measurement data showing the assumptions made within the model hold true for this system. The model aligns with the surface tensions for all three mixed systems at low mole fractions however begins to increase surface tension for the 1:1 mixture. This is because it is a semi-empirical model which relies on data to fit more accurately, hence in the absence of data as shown > 0.04 tMF, the model deviates from its expected trend.

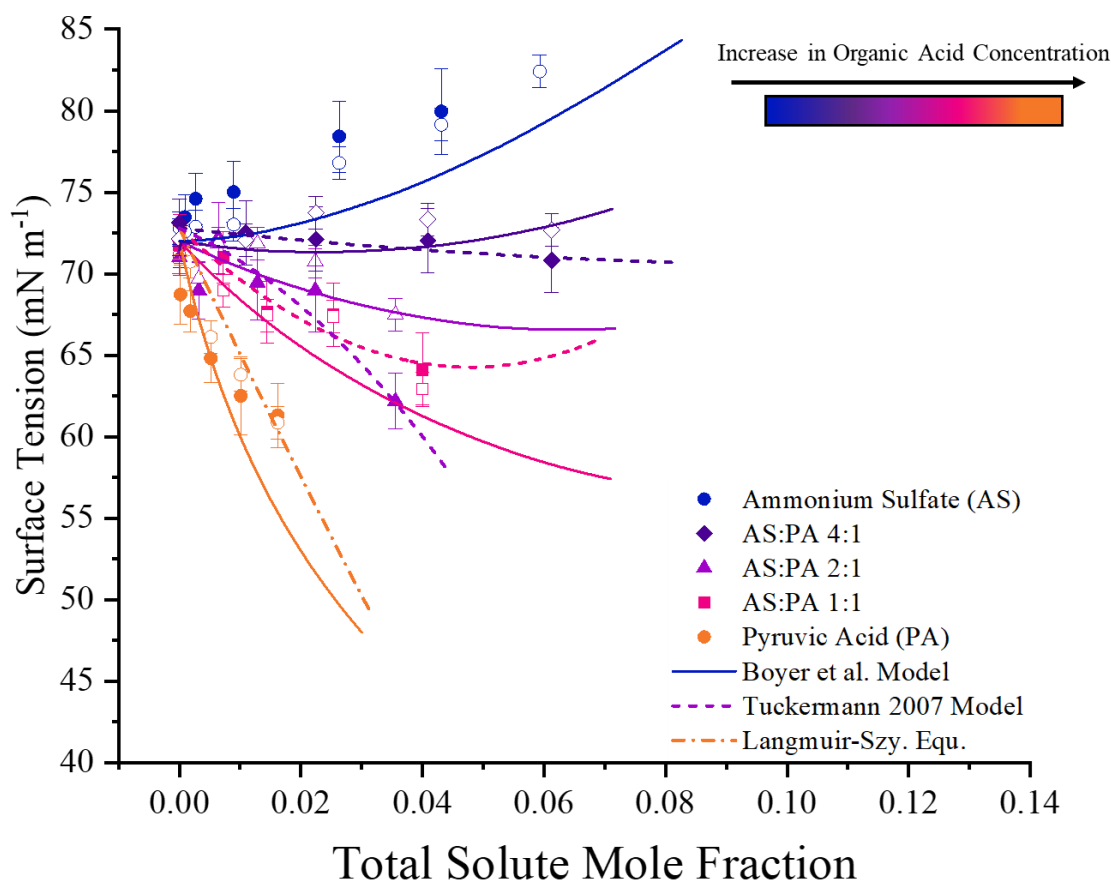


Figure 4-11: Surface tension of ammonium sulfate (blue symbols), pyruvic acid (orange symbols) and the mixed aqueous ammonium sulfate:pyruvic acid (1:1, pink symbols; 2:1, light purple symbols, 4:1 dark purple symbols) as a function of the total solute mole fraction. The Boyer et model is indicated by the solid straight lines, the Langmuir-Szyszkowski model for aqueous organic systems represented by the short, dotted line and the Tuckermann model for mixed inorganic and organic systems indicated by the short, dashed line.

4.3.3.5 Ammonium Sulfate: Levulinic Acid

The capacity of levulinic acid to lower the surface tension is supported by the observations presented in Figure 4-12. For instance, at a mole fraction of 0.06, levulinic acid exhibits a surface tension reduction of 17 mN m^{-1} relative to pure water, which surpasses the 14 mN m^{-1} reduction observed for pyruvic acid and the 6 mN m^{-1} reduction observed for malonic acid. The findings align with the predictions of the binary mixture, highlighting that levulinic acid is a potent surface-active species that necessitates a considerably higher inorganic concentration to elevate its surface tension. Consistent with the analysis of binary systems, levulinic acid showcases the highest surface tension reduction capability in binary and ternary mixture.

Upon comparison of the experimental data with the model predictions, it is discernible that the model exhibits overprediction of the surface tension across all mole fraction ratios. Since levulinic acid is employed in this study as a surrogate for five-carbon monocarboxylic acids and given that it is a relatively uncommon organic acid in the atmosphere, literature data on its properties, including surface tension, is limited. As a result, the Boyer et al. model tends to overemphasize the influence of inorganic salts on the surface properties, as it assumes levulinic acid to be a less potent surface-active molecule than the experimental evidence indicates.

Where the Boyer et al model exhibits overprediction of the surface tension, implying that a thorough analysis of the model parameters for levulinic acid mixtures is necessary to enhance its predictive accuracy. The Tuckermann model shows a good fit to the experimental data following the trend of the data closely, this is most likely because it is semi-empirical model. Both models align with the uncertainty of the measured data, demonstrating a satisfactory degree of data prediction that could be used in future inorganic-organic ternary mixture estimations.

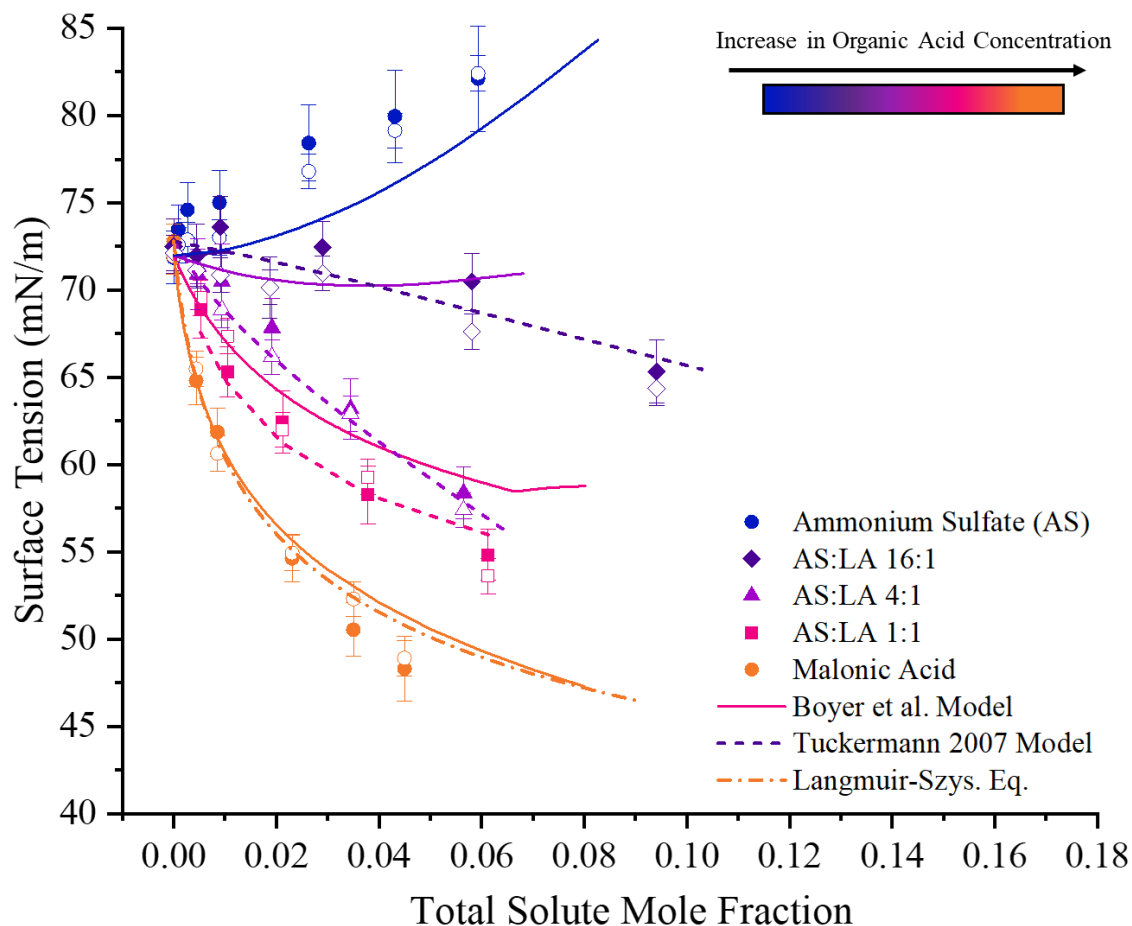


Figure 4-12: Surface tension of ammonium sulfate (blue symbols), levulinic acid (orange symbols) and the mixed aqueous ammonium sulfate:levulinic acid (1:1, pink symbols; 4:1, light purple symbols, 16:1 dark purple symbols) as a function of the total solute mole fraction. The Boyer et al. model is indicated by the solid straight lines, the Langmuir-Szyszkowski model for aqueous organic systems represented by the short, dotted line and the Tuckermann and Schwier model for mixed inorganic and organic symbols indicated by the short, dashed line.

The Organic Fraction in the System

If the surface tension is represented solely as a function of the organic component, rather than the total mole fraction of ammonium sulfate and the organic species, a more comprehensive view can be obtained. As illustrated in Figure 4-13, the surface tension of levulinic acid mixtures collapses onto a single curve, thereby highlighting the remarkable capacity of the organic component to significantly lower the surface tension, to levels as low as 55 mN m^{-1} within a narrow range of 0.02 tMF, which is not achieved by any other organic species in this work. The distribution of surface tension measurements at each mole ratio shows pyruvic is able to reduce the surface tension to greater extent than malonic acid but remains affected by the presence of ammonium sulfate. Figure 4-13 (b) shows majority of the data overlaps the organic binary data with the exception of the 8:1 mole ratio of malonic acid which shows a deviation from the binary organic measurements. This deviation could possibly be

due to the low concentrations of organic used in the mixture and the strength of the inorganic component resulting in an increase in surface tension.

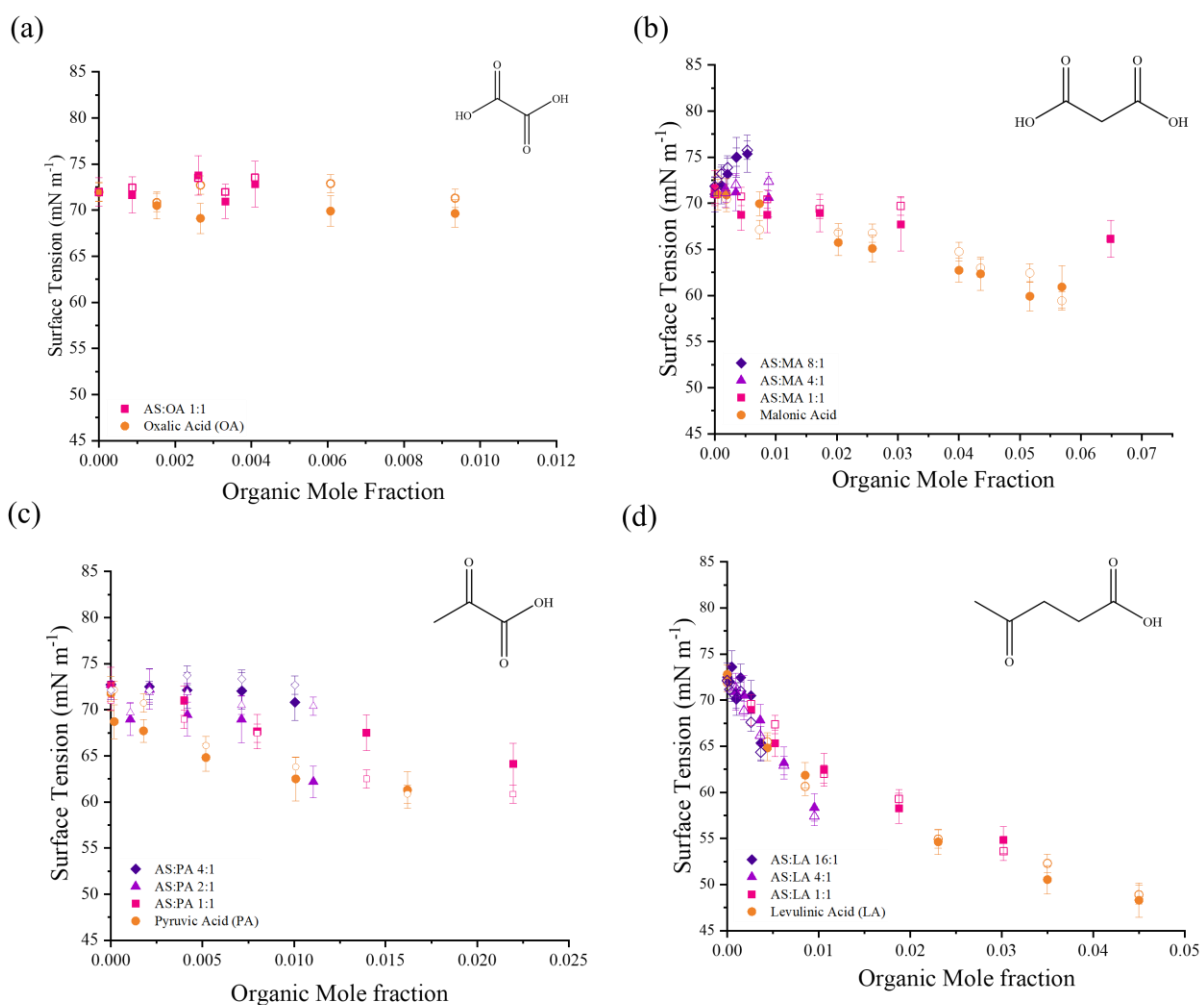


Figure 4-13: Surface tension as a function of the organic mole fraction for the systems (a) oxalic acid (b) malonic acid (c) pyruvic acid and (d) levulinic acid, the closed symbols represent the droplet phase measurements while the open symbols denote the bulk phase data.

4.4 Conclusion and Future Work

The surface tension of binary organic and inorganic aqueous solutions and ternary inorganic-organic aqueous mixtures were measured using the droplet oscillatory method and the MBT technique. The droplet oscillation method enabled the surface tension of droplets to be calculated using the aspect ratio dataset and the fast Fourier transformation of the data. From this transform, a frequency is produced which enables the surface tension to be deduced. The MBT was used to collect bulk equilibrium measurements of each system because no dynamic behaviour is observed in these solutions at ambient conditions. Overall, a good agreement was observed between the bulk and droplet measurements of each system further validating the calculation of surface tension via the droplet oscillation method.

The surface depression ability of the studied organic compounds increased with an increase in the number of carbons in the compound chain. Levulinic acid showed the highest reduction in the surface tension as the concentration of the organic acid was increased. Both the Boyer et al. model and the Langmuir-Szyszkowski equation adeptly conform to each binary organic compound, effectively capturing the observed decrease in surface tension. The experimental droplet and bulk phase data for ammonium sulfate were in excellent agreement closely following the predicted surface tension of the E-AIM model. The models used to accurately predict the binary behaviour however a more precise fit can be observed from L-S equation due to its semi-empirical nature.

Laboratory studies found that the addition of mono-and di-carboxylic acids can substantially change the surface tension of the monovalent inorganic salt, ammonium sulfate in aqueous solutions. The effect of the organic acid in the mixtures vary based on the surface-active nature of the organic compound with the more surface-active compound leading to a greater reduction in surface tension. The data shows ammonium sulfate: oxalic mixtures lead to a minor increase in surface tension as found in the Lee et al.⁴³ but as the data remained within error of one another this small change was disregarded. The malonic acid, pyruvic acid and levulinic acid systems lower the surface tensions of aqueous ammonium sulfate. Both models compared to experimental data performed better for mixtures with the same number of carbons namely, malonic, and pyruvic acid. Conversely, neither the Tuckermann nor Boyer et al. model characterise oxalic acid or levulinic acid closely with an underestimation of the surface tension in oxalic acid mixtures and an overestimation in levulinic acid mixtures. In conclusion the Tuckermann model serves as the better model due to its ability to closely agree with the droplet and bulk data without requiring the compound to be broadly documented in the literature.

In future work, the surface tension of more atmospherically relevant systems will be measured to build a greater picture of how chain length and functional groups impact surface tension. For example, organic systems to be investigated could include succinic acid, maleic acid, and oleic acid shown to be present in the atmosphere and all of which are reported within the literature. The inorganic salt systems that should be investigated further are, ammonium nitrate and sodium nitrate. Both maleic acid and sodium nitrate have been shown to be photoactive, therefore conducting droplet surface tension measurements following irradiation would prove to a valuable iteration of this work.

In subsequent work, this study would progress to examining the effect of varying pH on the surface tension. Commonly tropospheric aerosol pH exists between 3 and 5 however pH can reach 0 in the presence of sulfuric acid and 8 in the presence of sea salt.⁶ Depending on the organic and inorganic component the surface tension can be increased due to increased solubility at low pH levels or decreased at higher pH levels. In these the K_s values would be important to collect in order to understand the partitioning to the surface in the presence of the inorganic salt. Further work could incorporate

examining mixtures of organics with varying chain lengths as previous studies have shown these factors to impact surface tension by lowering aerosol pKa, increase the fraction of ionized molecules and increase the solubility of long-chain fatty acids.^{238,239}

Furthermore, the study of these mixtures and their ability to act as CCN would complete understanding of their ability to impact the climate by the indirect effect.⁴⁶ To continue to improve climate model predictions more mixed systems should be investigated to estimate and analyse the surface tension of real atmospheric droplets. Neglecting to do so may cause an overestimation in the surface tension within mixtures and errors within cloud droplet number predictions at the point of supersaturation.

Chapter 5

Explorations of Surfactant Partitioning in Microscopic Droplets and Bulk Solutions

5.1 Overview

Surfactants are surface-active, amphiphilic molecules that display unique dynamic behaviour and are widely utilized in various industrial sectors, including agrochemicals, enhanced oil recovery, and pharmaceuticals.^{240,241,242} Unlike organic acids studied in Chapter 4, surfactants can reduce surface tension by many fold at concentrations as low as mM. The preferential adsorption of surfactants to air-water interfaces reduces the interfacial tension, which lowers the energy cost of forming a new surface, droplet growth and wetting.^{87,243} Surfactants have a wide range of uses, including in the food industry where surfactants such as lecithin are used to stabilise dispersions containing fats and water at the oil/water and water/air interfaces.²⁴⁴ Surfactants may also be used to hinder processes such as coalescence due to their repulsive properties. Surfactant molecules present in the film on the surface of each droplet can cause both electrostatic and steric repulsion, reducing the film's ability to thin. This lack of thinning film establishes a gradient that induces Marangoni stresses that counteracts drainage and coalescence.⁸⁸

In the environmental context, surfactants are important due to their potential influence on cloud albedo and droplet growth, as shown in Figure 5-1, which in turn later impacts the climate and public health. The observations of Ruehl et al. reveal larger droplet sizes at the point of cloud activation than expected by Köhler theory for droplets containing surfactants, which they attribute to a reduced surface tension caused by the compressed film layer.²⁴⁵ Gérard et al., reported lower surface tensions than pure water in atmospheric aerosol samples containing surfactants.⁵³ Despite this, the impact of surfactants is currently ignored in the parametrization of κ -Köhler for predicting cloud condensation nuclei (CCN) activation, which assumes the surface tension of droplets to be that of pure water.²⁴⁶ The term ' κ ' denotes the single hygroscopicity parameter that represents the quantitative measure of aerosol water uptake characteristics and CCN activity.²⁴⁷ To understand the significance of surfactants in droplet growth studies, it is necessary to consider a more comprehensive examination of surfactant-containing aerosols and their behaviour under ambient conditions.²⁴⁸

Surface tension, σ , can be described as the change in energy required to create a unit of surface area, ΔA , where $\Delta E = \sigma \Delta A$.²⁴⁹ Dynamic Surface Tension (DST) refers to the variability of surface tension over

time, which is commonly observed in surfactant solutions and plays a crucial role in various biological processes, such as the proper functioning of lung alveoli across the phospholipid bilayer.⁸⁷

In general, when a new surface is formed, its surface tension reflects that of the solvent, typically water. Unlike surfactant molecules at the interface, bulk surfactant molecules have a symmetrical distribution of molecular neighbours, leading to a reduced net force experienced by each molecule. In the bulk of the droplet, there are a greater number of translational and rotational microstates available to the surfactant molecules, leading to a larger entropy per molecule compared to the surface-dwelling molecule.

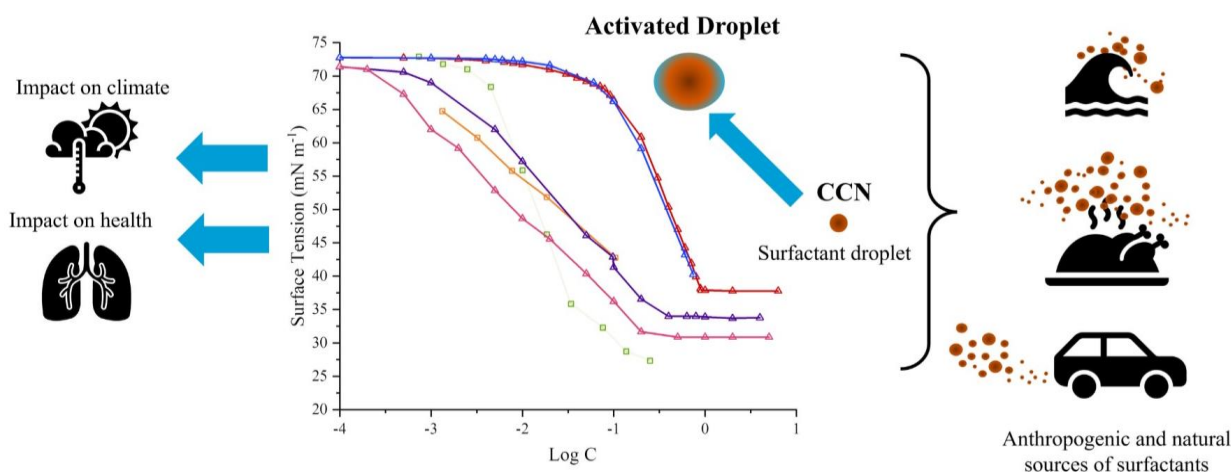


Figure 5-1: A schematic representing the sources of surfactant and the change in surface tension as the droplet grows and becomes an activated particle.

Prior to discussion of adsorption dynamics, it is important to explore the surfactant equilibrium adsorption behaviour, typically characterised by an adsorption isotherm. In this work, the Langmuir and Frumkin isotherm models described in Chapter 1, Section 1.5.4.3 will be used to describe the equilibrium adsorption behaviour of surfactants.

5.1.1 Modelling surfactant dynamics and behaviour

The dynamic behaviour of surfactants in solution is difficult to directly observe, therefore, it must be inferred through the measurement of surface tension as a function of time and modelling these systems. The two predominant models utilized to describe the transport of surfactant monomers and the resulting adsorption at the interface are the diffusion-controlled adsorption model and the kinetic-controlled adsorption model.⁸⁷ These models serve as a theoretical framework for understanding the behaviour of surfactants in solution and help to deduce the impact of surfactants on the surface tension over time.

5.1.1.1 Diffusion-Controlled Adsorption Model

The first model proposed here assumes that the surfactant molecule adsorbs to the interface directly after diffusing from the bulk of the droplet. Therefore, diffusion is denoted as the rate limiting step with adsorption occurring over a short timescale. The rate of diffusion increases with an increase in bulk concentration below the CMC as more molecules are situated near the surface of the droplet thus must diffuse over a shorter distance. In 1907, Milner²⁵⁰ suggested monomers diffusing from the bulk phase led to the formation of the interface following dynamic surface tension (DST) measurements of sodium oleate. However, it was Ward and Tordai, in 1946 who accounted for the adsorption process being diffusion controlled, forming Eq. 5.01²⁵¹:

$$\Gamma(t) = 2C_{\text{bulk}} \sqrt{\frac{D_c t}{\pi}} - 2 \sqrt{\frac{D_c}{\pi}} \int_0^{\sqrt{t}} C_s d(\sqrt{t} - \tau) \quad (5.01)$$

where $\Gamma(t)$ is the surface concentration at time, t , C_{bulk} denotes the bulk concentration, $\pi = 3.14$, D_c is the diffusion coefficient, C_s is the concentration in the subsurface, and τ is a ‘dummy’ variable of the integration.⁸⁷

The kinetic model of surfactant adsorption, as proposed by Ward and Tordai, asserts that the rate-limiting step in the adsorption process is diffusion. Eq. 5.02 represents the diffusion-controlled adsorption mechanism, and its validity requires a correlation between the observed dynamic surface tension (DST) and time and a consistent order of magnitude for the diffusion coefficient.²⁵² The equation also accounts for the back diffusion of molecules from the surface to the bulk once the surface-active sites are saturated. Limiting cases can be applied to Eq. 5.01 when the DST approaches the equilibrium value, σ_{eq} , or when it is close to the σ of the solvent. The short-time approximation can be applied to the equation when $t \rightarrow 0$ and $\sigma \rightarrow \sigma^0$, as it assumes that back diffusion is not significant at the early stages of the adsorption process when there are still numerous unoccupied surface sites. Hence:

$$\Gamma(t) = 2C_{\text{bulk}} \sqrt{\frac{D_{\text{diff}} t}{\pi}} \quad (5.02)$$

At low surfactant concentrations the Henry isotherm as shown in Eq. 5.03 can be invoked, where $n=1$ for non-ionic surfactants and $n=2$ for ionic surfactants.

$$\Pi = nRT\Gamma \quad (5.03)$$

Where Π denotes surface pressure and σ^0 is the surface tension of the pure solvent. Inserting Eq. 5.03 into Eq. 5.02 yields the short time approximation Eq. 5.04:

$$\sigma_{t \rightarrow 0} = \sigma^0 - 2nRT C_{\text{bulk}} \sqrt{\frac{D_{\text{diff}} t}{\pi}} \quad (5.04)$$

where D_{diff} is the diffusion coefficient. As $t \rightarrow \infty$, back diffusion must be accounted for in what is termed the *long-time approximation*. The subsurface concentration nears that of the bulk concentration such that c_s re-enters the equation:

$$\Delta c_{t \rightarrow \infty} = C_{\text{bulk}} - C_s = \Gamma \sqrt{\frac{\pi}{4D_{\text{ads}} t}} \quad (5.05)$$

where D_{ads} is the adsorption coefficient. By applying Gibbs equation denoted in Eq. 5.06 and rearranging the equation to Eq. 5.07:

$$\Gamma_{\text{max}} = - \frac{1}{nRT} \cdot \left(\frac{d\sigma}{dC_{\text{bulk}}} \right)_T \quad (5.06)$$

$$d\sigma = - nRT \Gamma dC_{\text{bulk}} \quad (5.07)$$

And then inserting Eq. 5.05 into Eq. 5.07, the long-time diffusion approximation can be derived as:

$$\sigma_{t \rightarrow 0} = \sigma_{\text{eq}} - \frac{nRT \Gamma_{\text{eq}}^2}{C_{\text{bulk}}} \sqrt{\frac{\pi}{4D_{\text{ads}} t}} \quad (5.08)$$

As $\Delta c_{t \rightarrow \infty}$ tends to zero i.e. as the subsurface and bulk concentration become unity and an equilibrium is reached the surface excess concentration at equilibrium is expressed as Γ_{eq} . According to Eq. 5.1 at short times, adsorption kinetics stipulate DST varies with $t^{0.5}$ and at long times Eq. 5.8, DST changes with $t^{-0.5}$ from which the diffusion and adsorption coefficient can be calculated.²⁵³ Both of these approximations are diffusion controlled, however, at the dilute solute concentrations the short-time approximation is often used. Figure 5-2 shows how the short- and long-time approximations fit to the DST of Triton X-100 at a $C_{\text{bulk}} = 1.5 \text{ mol dm}^{-3}$ studied in this work. To make the short- and long-time approximations, the surface tension at a given concentration is plotted against either $t^{0.5}$ or $t^{-0.5}$ and the gradient of the graph used to determine the rate of diffusion. For the long-time approximation, the Γ_{eq} was derived from fitting the surface tension against concentration to the Frumkin isotherm. The blue line in Figure 5-2 was fitted to cross the x-axis within an error $\pm 2 \text{ mN m}^{-1}$ of the surface tension of water (72.8 mN m^{-1}). Alternatively, the long-time approximation is used at higher solute concentrations and the red line fitted through the equilibrium surface tension value within error of $\pm 2 \text{ mN m}^{-1}$.

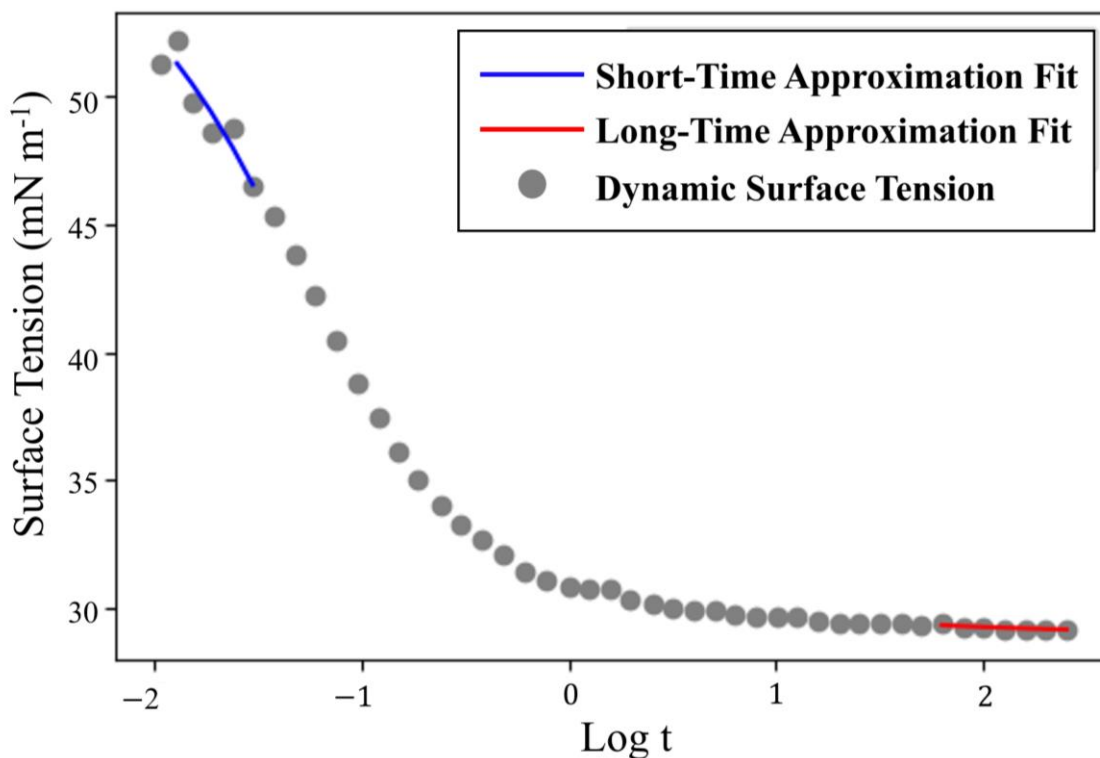


Figure 5-2: Short and long-time approximation fits to the DST collected data of Triton X-100 at $C_{bulk} = 1.5 \text{ mol dm}^{-3}$ yielding a diffusion coefficient, $D_{diff} = 1.10 \times 10^{-10} \text{ m}^2\text{s}^{-1}$ and $D_{ads} = 1.33 \times 10^{-10} \text{ m}^2\text{s}^{-1}$. Values were produced from a first principle approximation using the input parameters of Γ_{eq} , derive from the fitting of the Frumkin model to equilibrium surface tension data.

5.1.1.2 Kinetic-Controlled Adsorption Model

Under the kinetically controlled regime, the process of surfactant monomer adsorption to the interface is hindered by various barriers. The surface pressure, Π , must be overcome by the monomer in order to adsorb to the surface.^{87,254} Additionally, the monomer must adopt the proper orientation at the interface, which can be impeded by the presence of long surfactant chains that may become entangled.²⁵⁵ The probability of the surfactant molecule successfully adsorbing to a vacant site at the interface constitutes a statistical barrier. The persistence of micelles with long break-up lifetimes can also hinder the adsorption process. These hindrances shift the characterisation of surfactant adsorption from a thermodynamic relation to a kinetic limitation, as observed by Pugh et al. in their study of the DST of solutions containing cellulose polymers.²⁵⁶

5.1.1.3 The Presence of Micelles and Their Impact on Adsorption

When the surfactant concentrations exceed a critical value, known as the critical micelle concentration (CMC), structures called micelles are formed in the bulk phase. At concentrations above the CMC, the number of available sites at the surface becomes limited, making it energetically more favourable for surfactant molecules to aggregate and form micelles.²⁵⁷ Figure 5-3 shows that by fitting experimental data to an isotherm such as the Frumkin equation over the region where the surface tension changes with

concentration, and fitting a straight line when it plateaus, the CMC of a surfactant solution can be determined at the intersection of the lines.

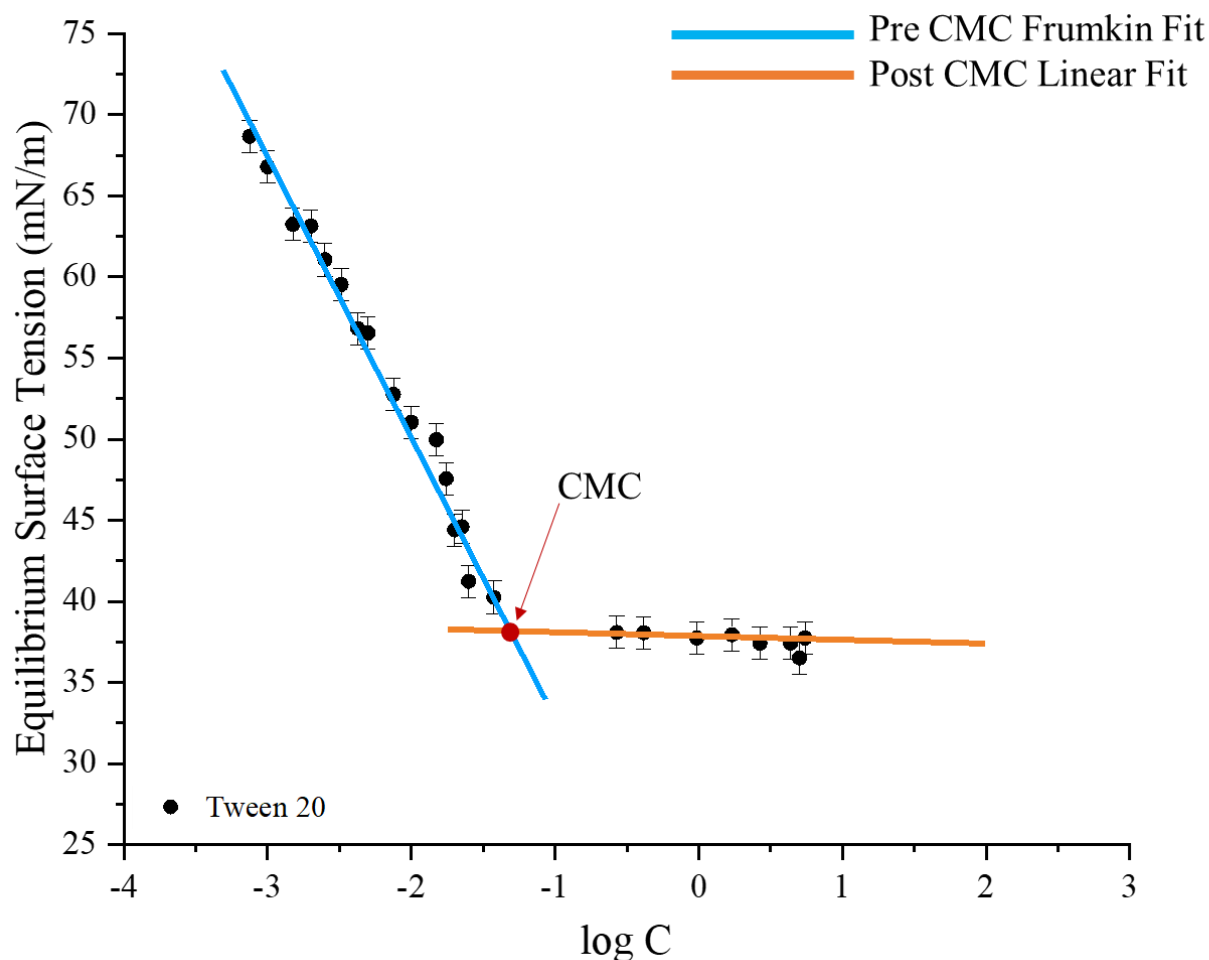


Figure 5-3: An illustrative graph showing how the critical micelle concentration can be determined from fitting the two regions i.e., pre-CMC to the Frumkin equation and beyond the CMC applying a linear fit. The data is taken from Tween 20 data collected by the Wilhelmy Plate.

Now above the CMC, energy is required for a surfactant monomer to dissociate from the highly stable micelle and adsorb to the surface. As a result, the surface tension of surfactants remains constant above the CMC and does not vary with increasing bulk concentration. The dynamic behaviour of micelles is determined by their break-up lifetimes which may render some molecules unavailable for adsorption.²⁵⁸ The transport and adsorption of surfactant monomers at the surface is therefore related to the surfactant monomers in the micelles. A micelle can serve as a dynamic reservoir for surfactants, functioning both as a supplier of molecules and as a repository (sink) for molecules. The micelle acts as a sink depending on the molecule affinity to aggregation and rate of desorption from the micelles.²⁵⁹

5.1.1.4 Adsorption Energy Barrier

The contributions of Liggieri and Ravera noted the presence of an energy barrier faced by surfactant molecules in the kinetic regime.²⁶⁰ Their model introduced a renormalized diffusion coefficient, D_a , in Eq. 5.09 to describe the monomer transport to the surface via diffusion and overcoming the energy barriers to adsorb (ε_{ads}) or desorb (ε_{des}).^{260,261}

$$D_a = D_c \exp\left(\frac{-2\varepsilon_{ads}}{RT}\right) \quad (5.09)$$

Here D_c is the diffusion coefficient of the surfactant from or to the bulk phase, R is the gas constant ($8.31 \text{ J mol}^{-1} \text{ K}^{-1}$) and T the temperature in Kelvin. The modified Ward and Tordai is as follows:

$$\Gamma(t) = 2c_0 \sqrt{\frac{D_a t}{\pi}} - 2 \sqrt{\frac{D_a}{\pi}} \int_0^{\sqrt{t}} c_s d(\sqrt{t-\tau}) \quad (5.10)$$

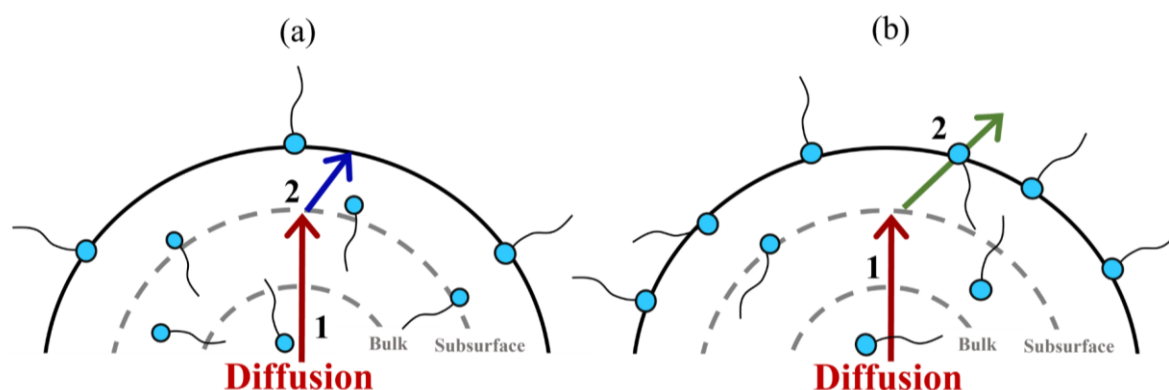


Figure 5-4: A depiction of (a) the diffusion-controlled adsorption mechanism (blue arrow) and (b) the kinetic controlled mechanism, note the surfactant molecules rearranging at the surface (green arrow).

The work of defining surfactant dynamics is necessary in accounting for the surfactant partitioning behaviour between the bulk and surface within a droplet or bubble. As the size of the droplet becomes small and its surface-area-to-volume ratio becomes large, it becomes important to also consider surfactant depletion in the droplet bulk.

5.1.2 Bulk surfactant depletion within a droplet

Molecules can diffuse over a defined lengthscale via Brownian motion along concentration gradients. When surfactant molecules adsorb onto a surface, they create a depletion zone in the bulk of the solution if there is a limited availability of surfactant molecules. The depletion zone is defined by the natural lengthscale called the depletion depth which compares the mass removed to the surface and the mass available within the bulk region.⁹⁶ Depletion depth is a phenomenon that can impact the stability and functionality of a surfactant solution for example in a foaming system, bulk depletion can cause the foam to collapse due to insufficient surfactant concentration.²⁶² As the surface area to volume ratio increases from a bulk solution to a droplet, the interfacial chemistry plays more of an important role

relative to bulk chemistry. Much of the work by Alvarez et al. refers to the bubble radii, b , but can be similarly applied to a liquid droplet with the radii, r hence the same equations are used in this study.

The planar depletion depth, h_p , denotes the number of molecules accumulated at the surface of the spherical interface, at equilibrium compared to the number of surfactant molecules found within a given volume as shown in Eq. 5.11.

$$h_p = \frac{\Gamma_{eq}}{C_\infty} \quad (5.11)$$

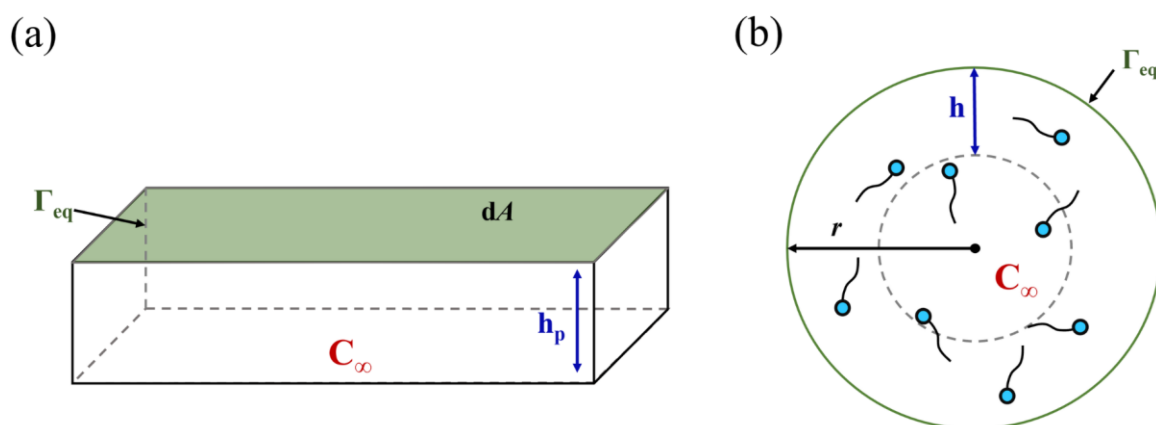


Figure 5-5: A depiction of (a) a defined volume planar interface and (b) a spherical droplet interface. Γ_{eq} is defined as the equilibrium surface excess concentration at equilibrium, dA as the surface area, C_∞ concentration of the bulk, r , as the radius of the spherical interface, h is the characteristic length scale over which diffusion occurs and h_p as the planar depletion depth.

Depletion arises where there is a finite solution volume, V , small bulk surfactant concentration, C_∞ , and large surface area, A . For a planar interface, $\Gamma_\infty dA$ represents the number of molecules that could be adsorbed per unit area, see Figure 5-5. When observing the depletion depth in a spherical droplet, one must also factor in the droplet radius which introduces an additional lengthscale, h_s :

$$h_s = r \left(\left(\frac{3h_p}{r} + 1 \right)^{1/3} - 1 \right) \quad (5.12)$$

When the droplet radius, r , is equal or less than to the depletion depth, depletion is significant because there is no reservoir of surfactants to replenish the depleted area.⁹⁶ As the droplet concentration increases, the spherical depletion depth decreases as more surfactants populate the subsurface and bulk.

The characteristic timescale for surfactant transport via diffusion, as described by Eq. 5.13, exhibits a linear relationship to the radius. This linear relationship arises from the increase in the surface area-to-volume ratio as the droplet radius decreases, resulting in a greater number of surfactant molecules in proximity to the interface in smaller droplets, reducing the timescale for diffusion. Consequently,

smaller droplets attain equilibrium faster compared to larger ones due to the increased diffusion timescales and decreased characteristic lengthscale. Jin et al. proposed Eq. 5.13 where the characteristic timescale scales proportionally with droplet radius and inversely proportionally to the diffusion coefficient.²⁶³

$$\tau_{D_{sphere}} = \frac{h_p r}{D_c} \quad (5.13)$$

An investigation by Alvarez and co-workers found inconsistencies in the scaling of $\tau_{D_{sphere}}$ previously proposed by Jin et al. One inconsistency is that the time scale does not approach that of the planar interface as the radius grows large and the curvature approaches zero.²⁶⁴ From Eq. 5.13 it appears that the time scale increases infinitely with radius. Another inconsistency is that as concentration increases, the timescale decreases without consideration of other kinetic limitations at play. Therefore, new characteristic time scales which overcome these limitations were developed by Alvarez et al. and represented in Eq. 5.14 for planar diffusion and Eq. 5.15 for the spherical diffusion. The spherical timescale accounts for the approach towards limit of planar diffusion time as large droplet radii as well as an increase in concentration tending towards h_p .

$$\tau_{D_p} = \frac{(h_p)^2}{D_c} \quad (5.14)$$

$$\tau_{D_s} = \frac{(h_s^3 h_p)^{0.5}}{D_c} \quad (5.15)$$

Where τ_{D_p} is defined as the diffusion timescale in planar coordinates and τ_{D_s} describes the spherical diffusion coefficient. From these equations it is evident that droplet size and surfactant concentration impact the characteristic timescale for diffusion to the surface.

5.1.2.1 Comparing Droplet Size and Curvature

The degree of curvature at the interface of a droplet plays a crucial role in controlling the characteristic time scale for diffusion-limited adsorption. The higher surface area-to-volume ratio of smaller droplets results in a greater concentration of surfactant molecules near the subsurface and thus, a higher rate of mass transfer to the spherical surface.²⁶⁵ This, in turn, leads to a reduction in the diffusion timescale. The non-linear dependence of the spherical depletion depth and planar length scale on the diffusion timescale is governed by equations 5.14 and 5.15.

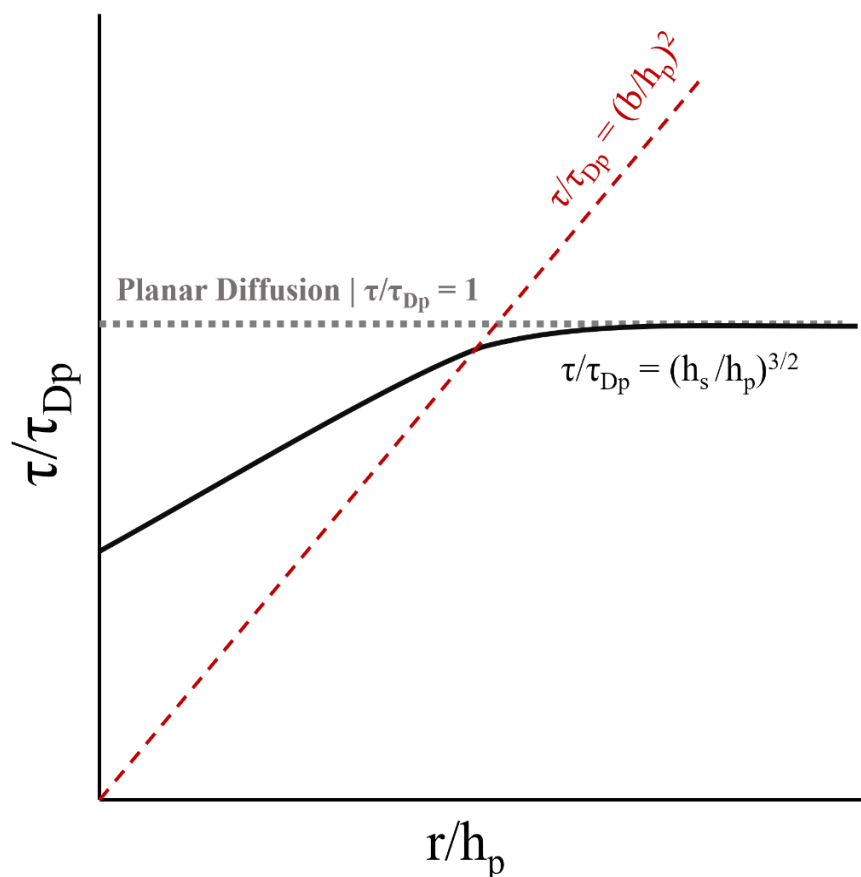


Figure 5-6: To show the different characteristic timescale regimes for planar diffusion, diffusion from inside the confined volume (red dashed line), which is used in this study, and diffusion from an infinite reservoir outside the interface (black solid line) against r/h_p where $h_p = \Gamma_{eq}/C_\infty$.

The red dashed line in Figure 5-6 shows that as the droplet radius decreases and the timescale for diffusion becomes shorter, the dynamics become faster as more surfactant molecules occupy the subsurface. As droplet grows the timescale for diffusion reaches the limit of planar diffusion. The figure also illustrates as the bulk concentration increases the normalised timescale approaches that of a planar surface. If there is a good agreement between $(r/h_p)^2$ and the experimental data, then it can be assumed adsorption is diffusion limited.²⁶⁶ A deviation from this line would mean kinetic processes of adsorption and desorption are significant when determining the characteristic time scale..²⁶⁵

Figure 5-7 demonstrates how the characteristic time for spherical diffusion varies with the droplet radius and concentration. As the concentration of SDS increases from left to right, the characteristic diffusion timescale for a spherical interface (τ_{D_s}) decreases due to a higher proportion of surfactant molecules occupying the surface phase, resulting in a shorter diffusion distance. Similarly, a decrease in droplet radius from $r = 40 \mu\text{m}$ to $r = 2.5 \mu\text{m}$ reduces the distance surfactant molecules must travel from the bulk, leading to a corresponding decrease in τ_{D_s} .²⁶⁵

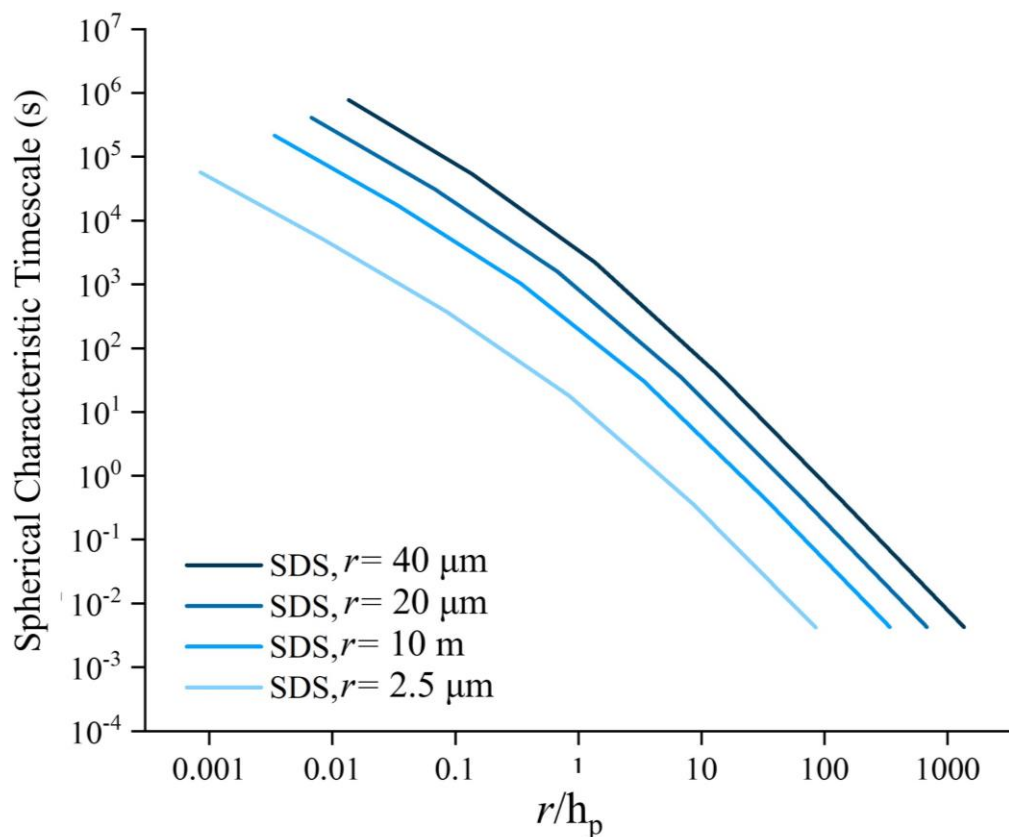


Figure 5-7: The spherical characteristic timescale decreases with a decrease in droplet radius as diffusion becomes faster due to more surfactant molecules being near the surface of the droplet. This data was modelled on an aqueous SDS system between the concentrations 3-100 mM.

5.1.2.2 Bulk Surfactant Depletion Within a Droplet

As mentioned in Section 5.1.2, surfactant molecules at equilibrium adsorb and desorb from the interface due to entropic costs of remaining within the bulk. During adsorption, near the surface is depleted of surfactant molecules allowing a concentration gradient to be established such that the subsurface is repopulated with surfactant molecules from the bulk. As the droplet becomes smaller (r decreases), the surface area relative to its volume increases. This requires a great number of bulk surfactant molecules to diffuse to the surface and reestablish an equilibrium, thus depletion becomes significant. Notably, an increase in the total concentration of dissolved surfactant molecules within the droplet bulk, compared to the total count of adsorbed molecules, mitigates the depletion phenomenon.

The surface area-to-volume ratio for a droplet is given by $A/V = 3/r$ hence:

$$\frac{3\Gamma_{eq}}{C_{\infty}r} < 1 \quad (5.16)$$

Using Eq. 5.16, Alvarez et al. defined two parameters to describe the impact of depletion on the equilibrium and dynamic surface tension.⁹⁶ The left hand side of Eq. 5.16 denotes the fractional potential mass loss of the surfactant to the droplet surface and is represented as the maximum mass loss parameter, ζ . In addition, for a spherical droplet a concentration ratio parameter, f , Eq. 5.17 is used alongside ζ to

describe the minimum concentration required to populate a surface relative to the surface activity of the surfactant, where C_i is the initial bulk concentration.⁹⁶

$$\zeta \equiv \frac{3\Gamma_{eq}}{C_i r} \quad (5.17)$$

$$f \equiv \frac{3\Gamma_{eq}}{a r} \quad (5.18)$$

In Eq. 5.18, a represents is the kinetic ratio of k_{ads} to k_{des} , it characterises the critical concentration at which adsorption of surfactants at the surface is significant. The smaller the value of f , the less surfactant that is required to diffuse from the bulk to the surface to achieve CMC and hence the less bulk depletion occurs. As this parameter is proportional to the surface area-to-volume ratio, it means f increases as the droplet size decreases. At equilibrium, ζ and f in combination with an isotherm model can be used to derive an expression, Eq. 5.19 for the depleted bulk concentration:

$$\frac{C_{eff}}{C_i} = \frac{1}{2} \left(1 - \zeta - \frac{\zeta}{f} \right) + \frac{1}{2} \sqrt{\left(1 - \zeta - \frac{\zeta}{f} \right)^2 + 4 \frac{\zeta}{f}} \quad (5.19)$$

where C_{eff} represents the depleted bulk concentration normalised to C_i which is the initial bulk concentration. To observe the effect of droplet radius on the depletion concentration, Eq. 5.19 was modelled as a function of C_i in Figure 5-8. As the droplet radius decreases from 50 μm to 1 nm, f increase and the A/V is large, therefore more surfactant molecules will be found at the surface relating to a large maximum mass loss parameter. Indeed, Figure 5-8 also shows that as the initial concentration increases, the bulk depletion ratio tends to a value of one and bulk depletion becomes negligible. Surfactants with a small a and thus small f values indicate highly surface-active surfactant molecules. Note that the ratio of adsorption and desorption used here by Alvarez et al. is the inverse of the ratio used in the Langmuir-Frumkin model, $a = 1/K_L$.

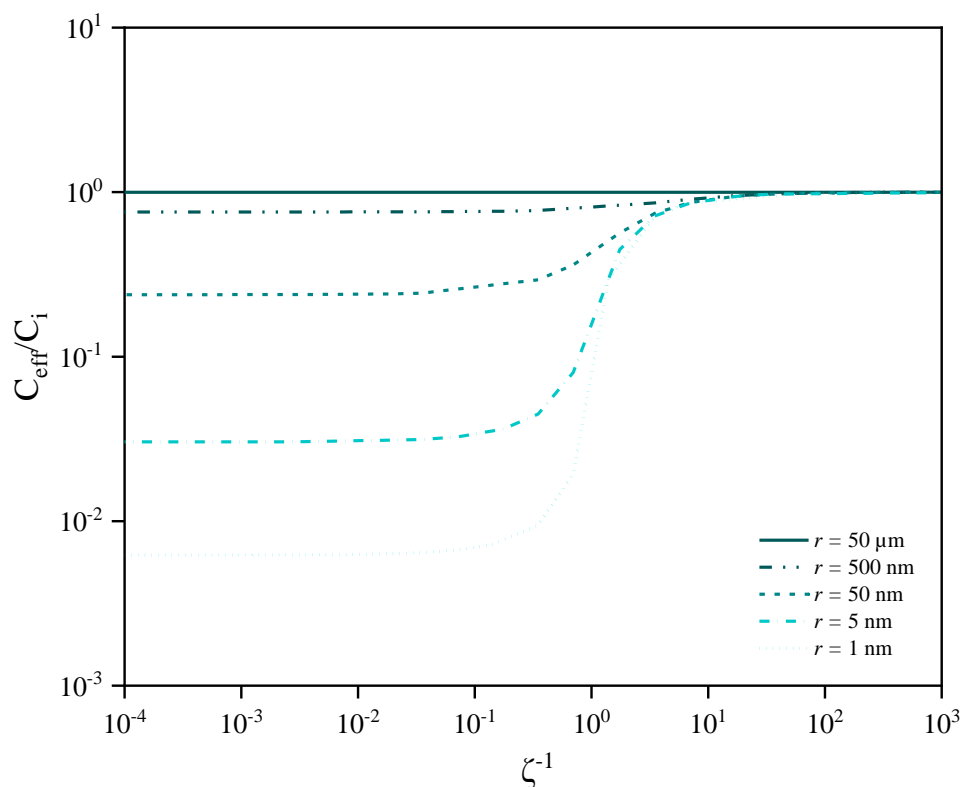


Figure 5-8: The normalised depletion bulk effective concentration as a function of C_i . Each line corresponds to different values of the radius r and the f . The graph is based on data collected by Alison Bain of SDS and 0.5 M NaCl. The constant a (k_a/k_d) had the calculated value of $89.57 \text{ m}^3 \text{ mol}^{-1}$.

As previously mentioned, the dynamic behaviour, surface adsorption, and bulk depletion of a surfactant are determined by its properties and structure. The use of proxy surfactants with similar behaviour to surfactants found in the atmosphere can complement field studies and expand understanding of surface tension observed in atmospheric aerosols samples.⁵³ In order to understand the complex mixtures of surfactants in aerosol, simple model systems need to be need systematically characterised. In this work, we study three such model systems, aqueous sodium dodecyl sulfate (SDS), Tween 20 and Triton X-100 (TX-100).

5.1.2.3 Comparing Surfactant Properties and Structure

The many types of surfactants all share the property of amphiphilicity; the molecule can be separated into partially hydrophilic and hydrophobic components.²⁶⁷ The presence of the hydrophilic portion enables the molecule to be soluble in aqueous solutions which is beneficial to many industries and central to their physicochemical properties. Surfactants can be classed as anionic, cationic, non-ionic, or Zwitterionic based on the charge on their polar head group.²⁶⁸ Gérard et al. found anionic and non-ionic surfactants formed a major fraction of samples taken at the Baltic station on Sweden while cationic surfactants were present in small quantities, often below the detection limit.⁵³

The order in terms of surfactant strength is as follows: (a) biosurfactants, (b) fatty acid sodium salts, (c) ambient aerosol samples, (d) aromatic dicarboxylic and tricarboxylic acids, (e) nonaromatic organic acids. Petters and Petters illustrate that some surfactants can reduce surface tension at concentrations $> 10^{-6} \text{ mol L}^{-1}$ which when compared to a modelled Köhler theory droplet shows most surfactants are capable of reducing surface tension and thus the activation barrier to droplet growth.⁵¹ Biosurfactants are the strongest naturally occurring surfactants produced by microorganisms and lofted into the atmosphere by wind and wave action.⁵¹ A study by Ekström et al.²⁶⁹ demonstrated atmospheric biosurfactants such as rhamnolipids, galactolipids and lipopeptides have the ability to reduce surface tension below that of pure water (72.8 mN m^{-1}) to $< 30 \text{ mN m}^{-1}$ between concentrations of 10^{-4} to 10^{-5} M. The aerosol samples were collected via aerosol field campaign in Aspövreten, Sweden across coastal and forested regions, Stockholm Archipelago $\sim 20 \text{ km}$ at sea, Sweden during an algae bloom, the temperate forest of Finland and tropical forest in Brazil. The samples showed low surface tensions, which is consistent with where the samples were taken, i.e. over the sea where there is large presence of microorganisms.²⁶⁹ Within this study, it was suggested that the presence of biosurfactants could lead to increased cloud nucleating efficiency. Other surfactants such as humic-like substances (HULIS) substances found in oxidised soot and biomass burning samples and ambient organic compounds have also been found to reduce the surface tension of atmospheric aerosols.²⁷⁰

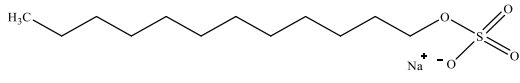
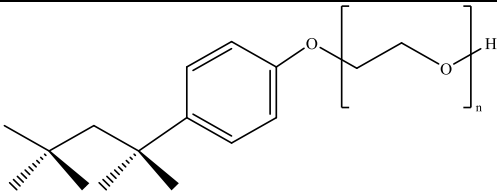
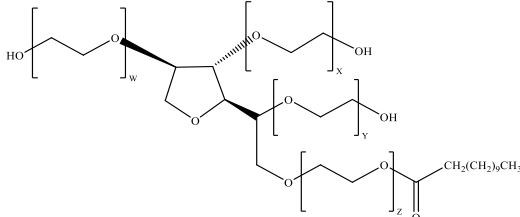
The non-ionic polyethylene glycol tert-octylphenyl ether compound (Triton X-100 or TX-100) is a highly water soluble and widely used surfactant particularly within the biology and pharmaceutical fields.^{271,272} The surfactant is able to serve as a model system for atmospheric aerosols, and it has been known to reduce surface tension almost as effectively as a biosurfactant.⁵¹ According to Bzdek et al., TX-100 is capable of reducing surface tension to 33 mN m^{-1} at concentrations above the CMC making it an efficient surfactant.⁵⁰ Table 5-2 shows the molecular structure of TX-100 where the average value of n is 9.5.^{271,273}

Fatty acid sodium salts such as sodium dodecyl sulfate (SDS) have been used as model systems for long-chained carboxylic acids that are detected in atmospheric aerosol samples.²⁷⁴ SDS is an anionic surfactant composed of a hydrocarbon tail ($c = 12$) attached to an anionic sulfate group head, both contributing to its adsorption behaviour as shown in Table 5-2.²⁷⁵ SDS is used in both industry and studies because of its non-toxic, chemical and physicochemical properties. It can be commonly found in toothpastes, detergents and drugs.²⁷⁶

Polysorbates are an important group of non-ionic surfactants which are amphiphilic and model systems for large, more complex biosurfactant systems.²⁷⁷ Matrix-assisted laser desorption/ionization time-of-flight mass spectrometry (MALDI-TOFMS) analysis has shown Tween 20 to be composed of polysorbate monolaurates, polysorbate monomyristates, and polysorbate monopalmitates.²⁷⁸ Tween 20 is a type of polyoxyethylene sorbitan that is used widely due to its effectiveness at low concentrations

and low toxicity.²⁷⁹ Table 5-2 shows the chemical structures and properties of the surfactants used in this study.

Table 5-2: The chemical structures and details of the surfactants used in this study.

Surfactant Name	Molecule	Surfactant Type	CMC (mM)	RMM (g mol ⁻¹)
Sodium dodecyl Sulfate (SDS)		Anionic	8.1-8.2 ²⁸⁰	288.372
2-[4-(2,4,4-trimethylpentan-2-yl)phenoxy]ethanol (Triton X-100)		Non-ionic	0.22-0.24 ^{281,282}	647
2-[2-[3,4-bis(2-hydroxyethoxy)oxolan-2-yl]-2-(2-hydroxyethoxy)ethoxy]ethyl dodecanoate (Tween 20)		Non-ionic	0.059 ^{283,284}	1226

In this work, the dynamic behaviour of the different surfactant molecules will be probed using both droplet and bulk measurement techniques. This chapter will explore the use of both the Langmuir and Frumkin isotherm models to examine the diffusion-controlled regimes and will investigate the effect of decreasing droplet size on the rate of surface tension change over time.

5.2 Experimental

5.2.1 Droplet Dynamic Surface Tension Measurements

The droplet oscillation method is used to quantify the surface tension of aqueous surfactant solutions at room temperature (298 K) of SDS, Triton X-100 and Tween 20 at different concentrations, dispensing frequencies, and droplet sizes. This approach measures the dynamic surface tension of picolitre volume droplets by observing the excitation of the droplet oscillatory surface modes as previously described in Chapter 3 and 4. The results from this method have been compared with the bulk phase measurements acquired from the maximum bubble pressure tensiometer, Wilhelmy plate, and the Langmuir-Frumkin isotherm model to determine the regimes at play for different surfactant concentrations.

Similar to other surfactants, SDS is plagued with the presence of contaminants such as dodecanol formed by hydrolysis. Difficult to remove, dodecanol is the most commonly found contaminant and has been shown to alter surface tension measurements of SDS.^{185,285} Therefore the SDS used in this study was purified through recrystallization to increase its purity relative to commercially available SDS.

5.2.2 Bulk Dynamic and Static Surface Tension Measurements

As described in Chapter 3, the maximum bubble pressure tensiometer (MBT) was used in this work to determine the bulk dynamic surface tension of each surfactant solution. The nature of this measurement technique enables the surface tension to be determined at discrete timepoints between 10 ms and 2×10^5 ms showing the dynamic behaviour of a surfactant solution. The equilibrium value for the surfactant solutions is taken as the last data point at the time 2×10^5 ms, though it is important to recognise some surfactants, such as Tween 20, do not reach their equilibrium value within the time frame of the MBT and therefore techniques such as the Wilhelmy plate are needed. The Wilhelmy plate technique enables the static surface tension to be determined by measuring the equilibrium surface tension. Measurements from both methods are used to calculate the parameters in the Langmuir-Frumkin isotherm model.

5.3 Results and Discussion

5.3.1 Bulk Surface Tension Measurements

5.3.1.1 Dynamic Bulk Surface Tension Measurements

Bulk dynamic surface tension measurements of three surfactant systems (SDS, TX-100 and T20) were taken using a maximum bubble pressure tensiometer at a range of concentrations. Bubbles are formed by the injecting gas into the surfactant solution and increasing the pressure until the maximum pressure is reached. The point at which the maximum is reached is related to the surface tension of the surfactant solution. The DST as a function of time and the effective adsorption time ($t^{-0.5}$) is shown in Figure 5-9(a) to (c) and Figure 5-9(d)-(f), respectively, across the different bulk concentrations. As expected, DST decreases with time, approaching the minimum surface tension value determined using Wilhelmy plate. The data of the DST decay are compared to one another to observe a difference in the

dynamic behaviour between surfactant type. In contrast to SDS and Tween 20, TX-100^{286,287} displayed a strong dynamic profile. For example, at the [TX-100] of 0.05 mM compared to the [SDS] of 0.50 mM, an order of magnitude higher, the rate of surface tension decay ($d\sigma/dt$) is two orders of magnitude greater than SDS.

According to Bak et al. if the σ versus $t^{-0.5}$ plots that show a linear relationship at longer times, then it can be assumed that adsorption is diffusion controlled.²⁷⁹ Figure 5-9(d) and (e) show SDS and Triton X-100 follow a linear dependence at long times therefore it can be assumed that surfactant adsorption is diffusion-controlled. However, in examining Tween-20, the linear relationship between the surface tension and longer times is not replicated thus this assumption does not hold true.

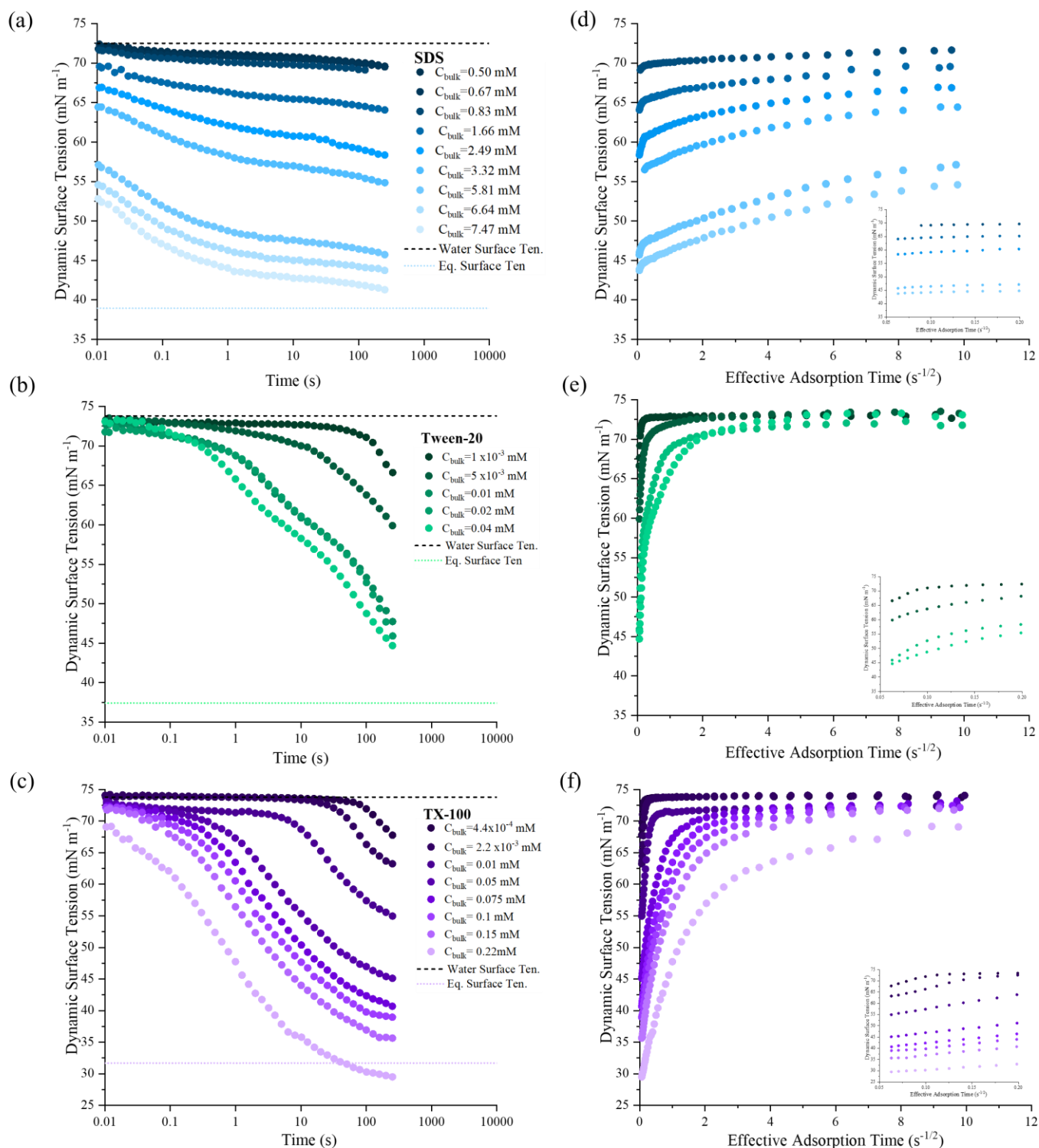


Figure 5-9: The macroscopic dynamic surface tension plotted against time collected using the MBT of (a) SDS (b) Tween 20 and (c) TX-100 showing a gradual increase in monotonic behaviour from (a) to (c). The black dashed line on graphs (a)-(c) indicates the surface tension of water (72.8 mN m^{-1}) and the coloured dashed line indicates the equilibrium surface tension value for each surfactant solution. The surface tension is plotted against the inverse square root of time from (d) to (f) showing increasing linear behaviour at long times for (d) and (f) and non-linear relationship for Tween 20. The linearity of the relationship indicative of a diffusion-controlled adsorption mechanism.

Figure 5-10 presents a summary of both short-time and long-time diffusion coefficients obtained by averaging individual values at concentrations above and below the critical micelle concentration (CMC) using the Ward and Tordai equation, Eq. 5.01. At short times, where surface coverage is low, the dynamic behaviour can be closely represented by a diffusion-controlled mechanism. However, at longer times, as the bulk concentration approaches the CMC and surface coverage increases, the regime potentially transitions to a mixed kinetic-diffusion control mechanism. Miller et al. reported a similar observation while examining the protein t-BPh-EOIO10.^{87,264} Specifically, the short-time diffusion equation strongly described the initial stages of adsorption when the surface coverage was low, and the adsorption barrier was weak. However, as the bulk concentration increased, the diffusion-only approach underpredicted the decay of the measured data. Consequently, the use of the long-time diffusion coefficient was more appropriate when fitting the data.

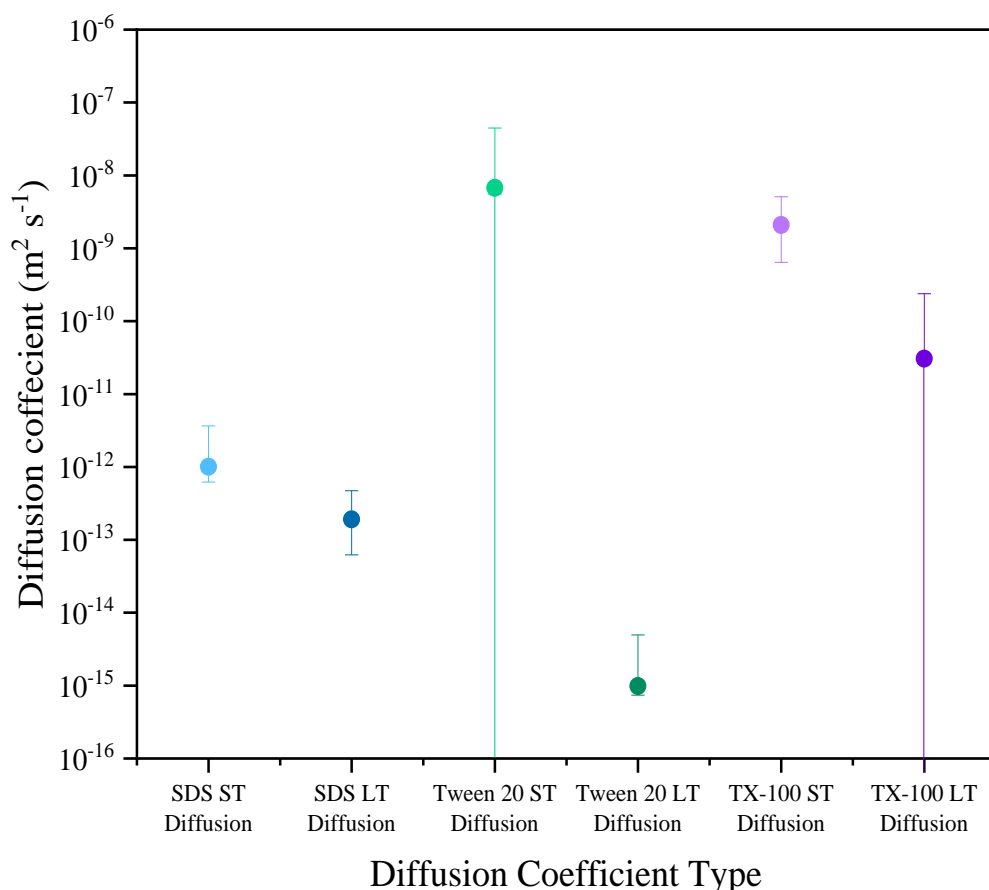


Figure 5-10: Diffusion coefficient plotted against the diffusion coefficient type, i.e., short time (ST) and long-time (LT) diffusion approximations of each surfactant type used in this study. Where no minus error can be seen on a data point it has been hidden by the data point (T20 LT diffusion)

The distinctions among the effective diffusion coefficients of SDS, TX-100, and Tween-20 can be easily discerned by examining Figure 5-10. The short time and long-time diffusion coefficients cover a range of values spanning from 10^{-10} - 10^{-13} , 10^{-9} - 10^{-11} , and 10^{-8} - 10^{-16} m² s⁻¹ for SDS, TX-100 and Tween-20, respectively, from surfactant concentrations between 1 – 50 mM. For SDS, the effective diffusion

coefficients $3.26 \times 10^{-13} \text{ m}^2 \text{ s}^{-1}$ obtained at the concentrations 3.32 mM is three orders of magnitude faster than the value reported in the literature while at 7.47 mM the diffusion coefficient is two orders of magnitude higher than the previously published data displayed in Table 5-3.

Table 5-3: The literature data of the effective diffusion coefficients of SDS, TX-100 and Tween 20.

Surfactant type	Surfactant Concentration (mM)	Diffusion Coefficient ($\text{m}^2 \text{ s}^{-1}$)	Literature Reference
SDS	3.40	4.30×10^{-16}	Noziere et al. ²⁸⁸
	7.00	1.10×10^{-14}	
TX-100	7.70	5.50×10^{-11}	Weinheimer et al. ²⁸⁹
	15.50	5.80×10^{-11}	Giglio and Vendramini ²⁹⁰
Tween 20	0.01	1.90×10^{-10}	Wu et al. ²⁹¹
	1.00	1.00×10^{-8}	Bak et al. ²⁷⁹

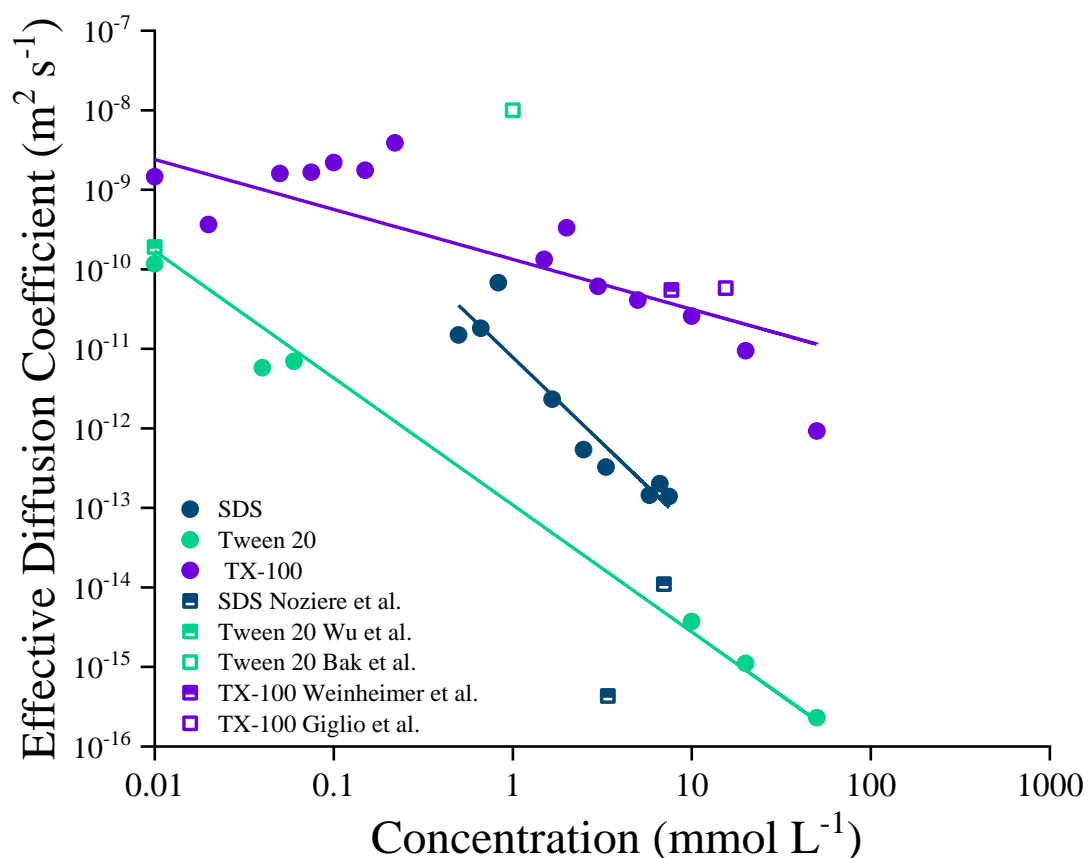


Figure 5-11: The effective long time diffusion coefficient as a function of bulk concentration. SDS is represented by the blue circle symbols, TX-100 in purple circle symbols and Tween 20 as green circle symbols, with the linear fit represent by the solid lines.

Consistent with the results depicted in Figure 5-10, TX-100 exhibited the highest effective diffusion coefficient relative to other surfactant types. Furthermore, our findings for TX-100 demonstrate good agreement with previously published data, as illustrated in Table 5-3. Specifically, at TX-100 concentrations of 5 mM, 10 mM, and 20 mM, the effective diffusion coefficients were determined to be 4.10×10^{-11} , 2.58×10^{-11} , and $9.46 \times 10^{-12} \text{ m}^2 \text{ s}^{-1}$, respectively. A $\pm 10\%$ error is assigned to each diffusion coefficient as an error for each calculation not determined. This is based on the bubble tensiometer error of $\pm 1 \text{ mN m}^{-1}$ surface tension which equates to approximately $\pm 10\%$ uncertainty.

Contrary to expectations based on Figure 5-9, the findings from Figure 5-11 indicate that Tween 20 does not exhibit a higher long time diffusion coefficient than SDS. Wu et al. reported a possible explanation for this behaviour, relaying that a decrease in the diffusion rate of Tween 20 resulted from an increase in concentration.²⁹¹ This phenomenon is also observed in our study, where short-time and long-time diffusion coefficients show a significant reduction with increasing concentrations of Tween 20. Additionally, Table 5-3, shows the experimental data aligns closely with previous literature, specifically, at a concentration of 0.01 mM, the short-time diffusion coefficient of $5.98 \times 10^{-8} \text{ m}^2 \text{ s}^{-1}$ and a long-time diffusion coefficient of $1.17 \times 10^{-10} \text{ m}^2 \text{ s}^{-1}$.

From the literature data that was collated and compared to the data collected in this study, discrepancies of 2-3 orders magnitude have been observed. This can be attributed to Ward and Tordai model used to calculate the diffusion coefficients being sensitive to the slope of the σ versus $t^{0.5}$ plots hence even a slight variation can lead to substantial deviations in the computed diffusion coefficient.

5.3.1.2 Equilibrium Bulk Surface Tension Measurements

The equilibrium bulk surface tension was measured using the Wilhelmy Plate technique and refers to the surface tension at which a surfactant solution is at thermodynamic equilibrium with the bulk. The force required to remove a thin platinum plate from a surfactant solution is used to determine the surface tension of the liquid. Surfactant properties such as the surface concentration, adsorption/desorption constant and area of the molecule shown in Table 5-4 can be calculated using the change in equilibrium surface tension over surfactant concentration and fitting to the Langmuir and Frumkin Model. The CMC determined at the cross section of the Frumkin isotherm fit to the concentrations below the CMC and a linear fit to the concentrations above the CMC which plateau. The CMC, Γ_{max} and A_{min} for all systems agree well with the previously published data in Table 5-4 which validates the accuracy of the experimental method and reliability of results. The increase K_L values from SDS to Triton X-100, indicates an increasing ability for the surfactant to remain stable at the surface hence TX-100 is able to stabilise at the surface more effectively and reduce the surface tension. The values for area per molecule calculated and shown in Table 5-4 do not reflect the closely-packed insoluble monolayers of single-chain surfactants ($\approx 20 \text{ \AA}^2$) and the effective close-packed area of hydrated ions ($\approx 16 \text{ \AA}^2$) hence they are assumed to be reasonable values.²⁵⁹

Table 5-4: To show the calculated CMC, the maximum surface excess concentration, area per molecule and K_L , the ratio between k_{ads} and k_{des} calculated using the Frumkin isotherm alongside literature data.

		This Study				Literature Data		
CMC (mM)		Γ_{max} (10^{-6} mol m $^{-2}$)	A_{min} (\AA^2)	K_L (m 3 mol $^{-1}$)	CMC (mM)	Γ_{max} (10^{-6} mol m $^{-2}$)	A_{min} (\AA^2)	K_L (m 3 mol $^{-1}$)
TX-100	0.29	2.86 ± 0.14	59.30 ± 2.87	1140 ± 242	$0.22^{50}, 0.24^{51}$	$2.78^{62}, 2.91^{48}, 2.90^{25}$	$59.70^{25}, 57.10^{63}$	-
Tween 20	0.05	1.84 ± 0.10	90.30 ± 4.66	890 ± 130	$0.06^{52,53}$	3.53^{48}	47.00^{46}	-
SDS	8.07	4.56 ± 0.56	35.40 ± 4.00	0.40 ± 0.08	$8.10-8.20^{49}$	$5.50^{64}, 10.00^{25}$	$30.20^{58}, 33.00^{25}$	1.10^{25}

Using the Frumkin Model, the surface coverage was determined for each surfactant solution and indicates the degree to which the surfactant molecules occupy the liquid-air interface. The surface coverage has a significant impact on surface properties such as stability and reactivity. Both TX-100 and Tween 20 reach a total surface coverage at lower concentrations compared to SDS due to their higher surface activity leading to a greater reduction in surface tension confirmed by Figure 5-12. The surface coverage SDS compares closely to published data from Mysels in 1986¹⁸⁵ and Gilsson 1957.²⁹²

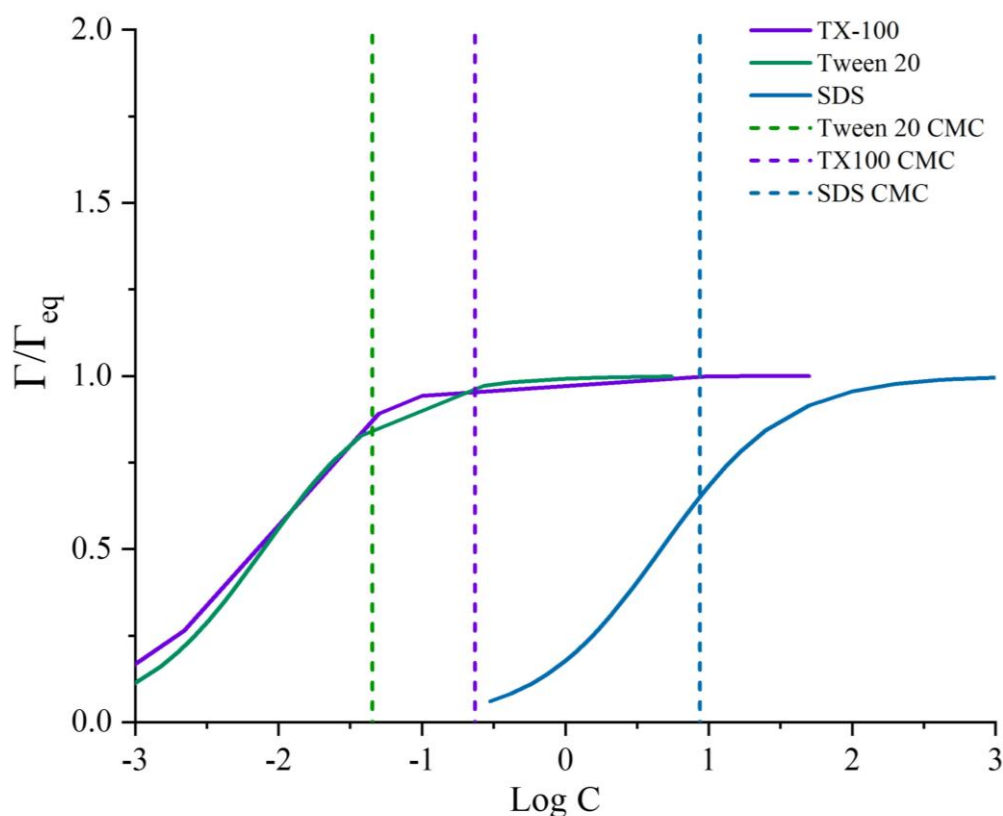
**Figure 5-12:** The surface coverage defined as Γ/Γ_{max} as a function of the log C for surfactants TX-100, SDS and Tween 20 indicated by the solid lines. The dotted lines denote the position of the CMC shown in Table 4-4.

Figure 5-13 shows the equilibrium surface tensions of SDS, TX-100 and Tween 20 as a function of the concentration fitted to both the Langmuir-Szyszkowski and the Frumkin models. By examining this figure, it is possible to see both models fit the equilibrium surface tension of SDS, TX-100 and Tween 20 well. Both TX-100 and Tween 20 show a higher capacity than SDS to reduce surface tension at low surfactant concentrations which corresponds to the total surface coverage at low maximum surface excess concentrations observed in Figure 5-12.

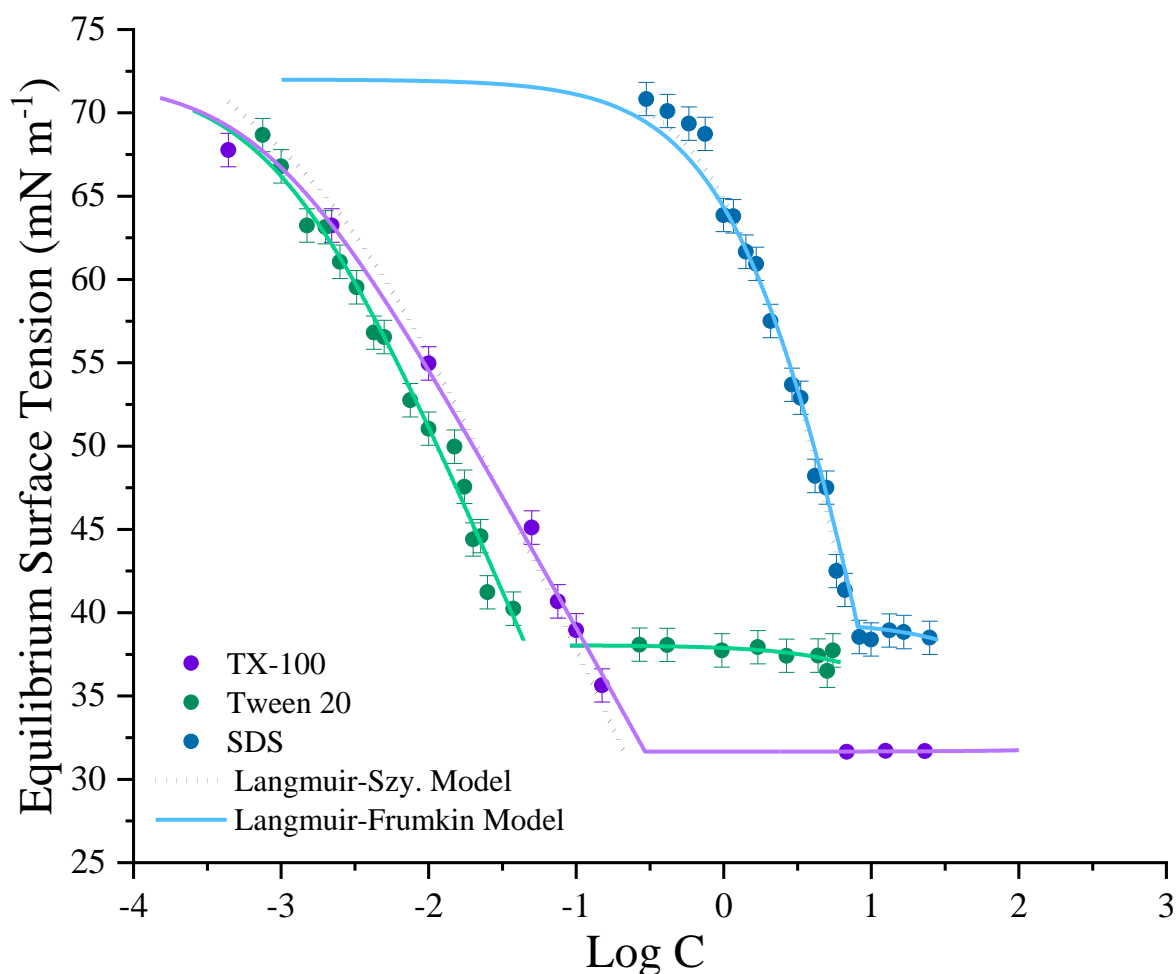


Figure 5-13: Comparing the Frumkin model (solid lines) and Langmuir-Szyszkowski equation (dotted lines) with experimental data taken using the Wilhelmy Plate for SDS (blue closed symbols), TX-100 (blue closed symbols) and Tween-20 (blue closed symbols). Notice how SDS and Tween 20 have very good fits to both models shown by their overlap whereas the Frumkin model appears to represent TX-100 the best.

The primary objective of this study is to investigate the potential of commercially available surfactants, such as SDS, TX-100, and Tween 20, to act as atmospheric surfactant proxies. To assess their efficacy, Figure 5-14 presents the equilibrium surface tension and surface surfactant activities, derived from Eq. 5.20, in comparison to biosurfactants and surfactants isolated from aerosol samples. Rhamnolipid and Surfactin are highly potent natural surfactants that exhibit comparable surface tension reduction capabilities to the synthetic surfactants TX-100 and Tween 20 investigated in this study. In terms of

concentration dependence, the natural surfactants can begin reducing the surface tension at remarkably low concentrations, ranging from 10^{-6} to 10^{-5} M.²⁶⁹ On the other hand, the proxy surfactants demonstrate surface tension reduction at concentrations an order of magnitude higher at 0.4 μ M and 1 μ M, This directly compares to the study by Petters and Petters which showed Triton X-100 can begin reducing surface tension at concentrations of 10^{-3} mM.²⁹³ From Figure 5-14 we can also observe TX-100 and Tween 20 relate strongly to other natural surfactants such as those found in samples taken from the Amazonian Forest, HULIS and Marine Algae Bloom, in terms of their surface tension reduction capabilities.¹⁹⁶

$$\sigma = \sigma^0 + \frac{RT}{\omega_w} \ln a_w^S \quad (5.20)$$

The TX-100, TX-114, and SDS measurements reported by Zdziennicka et al. demonstrate good agreement with the TX-100, SDS, and Tween 20 measurements conducted in this study, as reflected by the similarity in their surfactant surface activity plots.⁹⁰ The SDS profiles in particular show strong agreement between the present work and literature data.²⁶⁹ As anticipated, increasing the surfactant concentration results in a rise in the surface activity of the surfactant molecules, with TX-100 exhibiting the highest a_w^S value (defined in Chapter 1 Section 1.5.4) among the measured surfactants. In terms of atmospherically relevant samples, Rhamolipid-2 and Surfactin exhibit the highest activity due to their highly surface-active nature.

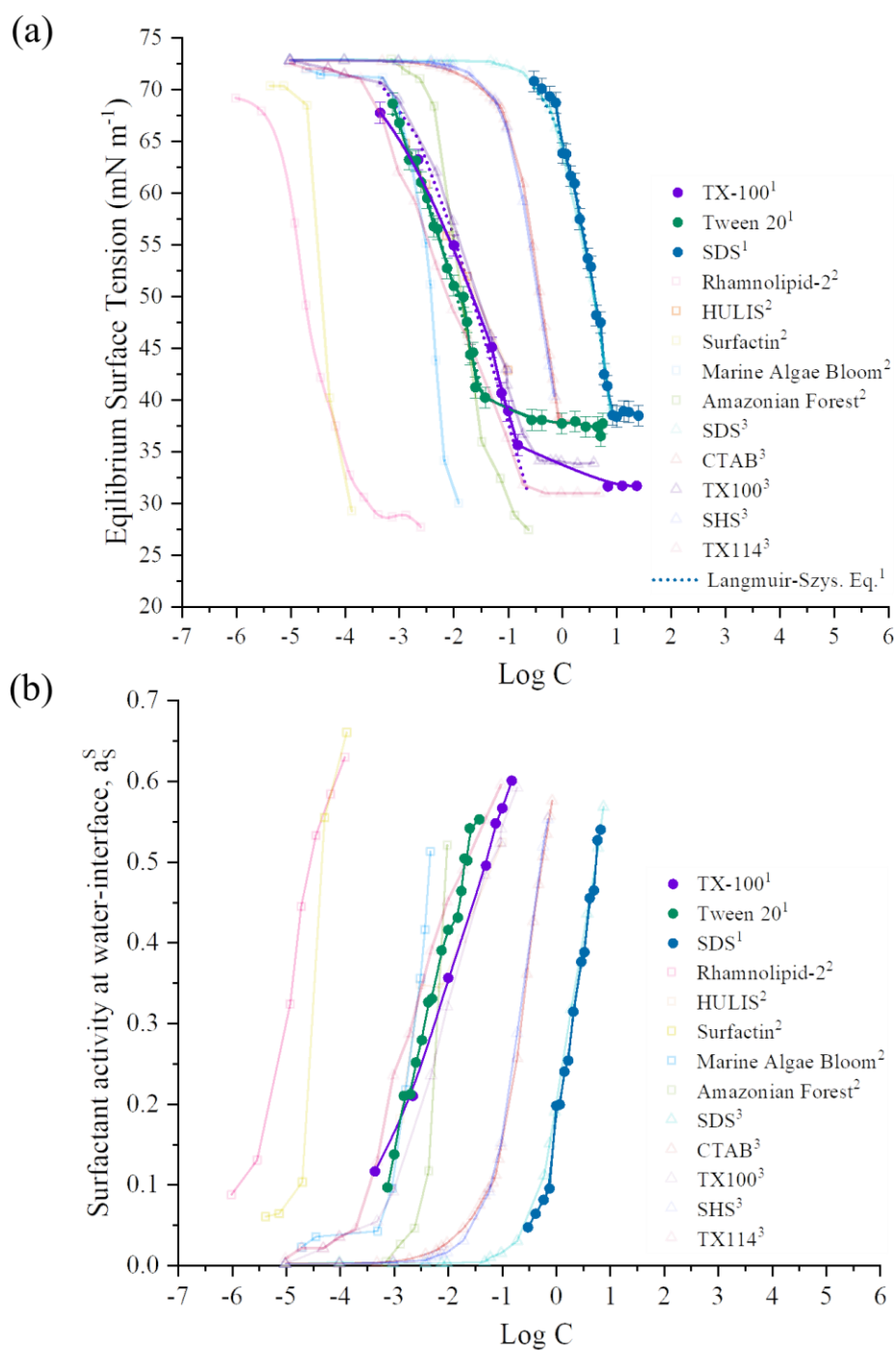


Figure 5-14: The log concentration of surfactants plotted against (a) the equilibrium surface tension and (b) the surfactant surface activity at the air water interface. The measurements taken in this work are indicated by emboldened curves where TX-100 is represented by the purple closed symbols, Tween 20 indicated by the green symbols and SDS denoted by the blue symbols. ¹ denotes data collected from this study, ² represents data from Ekstrom et al.²⁶⁹ and represents the data collected by Zdziennicka et al.⁹⁰.

5.3.2. Droplet Dynamic Surface Tension Measurements

A series of oscillating droplet of SDS, TX-100 and Tween 20 were observed using the droplet oscillation method to determine their surface tension in ambient conditions. At equilibrium, as mentioned previously in Section 5.1.2, the droplet radius and initial bulk concentration can be used to indicate bulk depletion. The C_{eff}/C_i ratio was calculated using the parameters f and ζ^{-1} which are dependent on the surface area-to-volume ratio as well as the important geometric length scale, r_g , with the range of $15 \mu\text{m} < r_g < 20 \mu\text{m}$. Figure 5-15 demonstrates the normalised depleted bulk concentration C_{eff}/C_i plotted as a function of the SDS, TX-100 and Tween 20 initial concentrations. A distinct curve exists on which data points sit indicating the modelled bulk depletion for droplet sizes and concentrations used throughout this work.

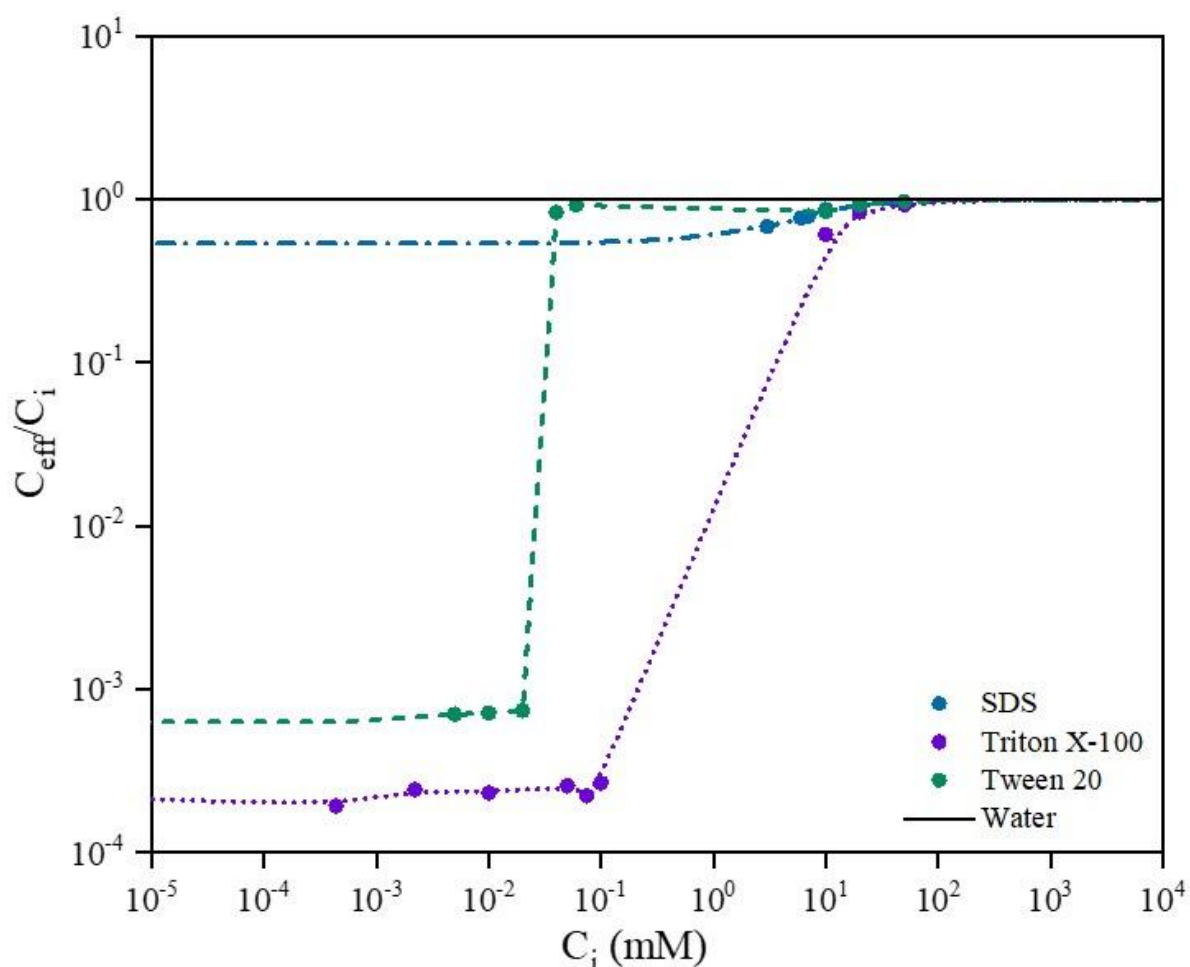


Figure 5-15: The normalised effective bulk depletion concentration as a function of the initial bulk concentration, C_i . Each line represents a different surfactant, the blue dash-dot line denotes SDS, the green dashed line corresponds to Tween 20 and TX-100 is indicated by the purple dotted line. The filled symbols indicate the concentrations and droplet sizes in the range $15 \mu\text{m} < r < 20 \mu\text{m}$ used in this work.

The shape of each surfactant curve in Figure 5-15 shows as the concentration increases from left to right on the x axis, the fractional mass lost to the surface decreases and depletion becomes negligible. From Figure 5-15, at the large concentrations of SDS used in these experiments, the depletion ratio is near

one i.e., very little or no depletion is expected. TX-100 and Tween 20 have a high bulk depletion at the low concentrations (10^{-4} to 10^{-1} mM), but this becomes less significant at higher concentrations. This substantial bulk depletion at low concentrations is consistent with the spherical depletion lengthscale, h_s , shown in Table 5-5. If the h_s is larger than the droplet radius (a common occurrence at lower concentrations), bulk depletion of the droplet is significant. Depletion can have a large impact on the rate at which surfactant adsorption approaches equilibrium.

The characteristic timescale for spherical diffusion, τ_{D_s} , can be calculated using Eq. 5.16 and reveals the relationship between diffusion and bulk concentration and droplet radius. In this present study, τ_{D_s} is normalised to the characteristic timescales for planar diffusion for each surfactant type as demonstrated in Figure 5-16.

Table 5-5 The spherical depletion length scale h_s in comparison to the droplet radii for each type of surfactant used in this study.

Concentration (mM)	r (μm)	h_s (μm)
SDS		
3	17.91	0.93
6	17.77	0.48
7	17.82	0.41
10	22.33	0.29
20	18.85	0.15
50	21.76	0.06
Tween-20		
0.005	19.71	67.84
0.04	19.69	25.19
0.06	20.10	20.23
10	20.24	0.28
20	19.87	0.14
50	20.72	0.06
Triton X-100		
0.00044	15.88	173.85
0.0022	19.95	109.39
0.05	20.79	27.41
0.1	21.34	18.66
10	18.39	0.39
20	21.42	0.20
50	19.11	0.08

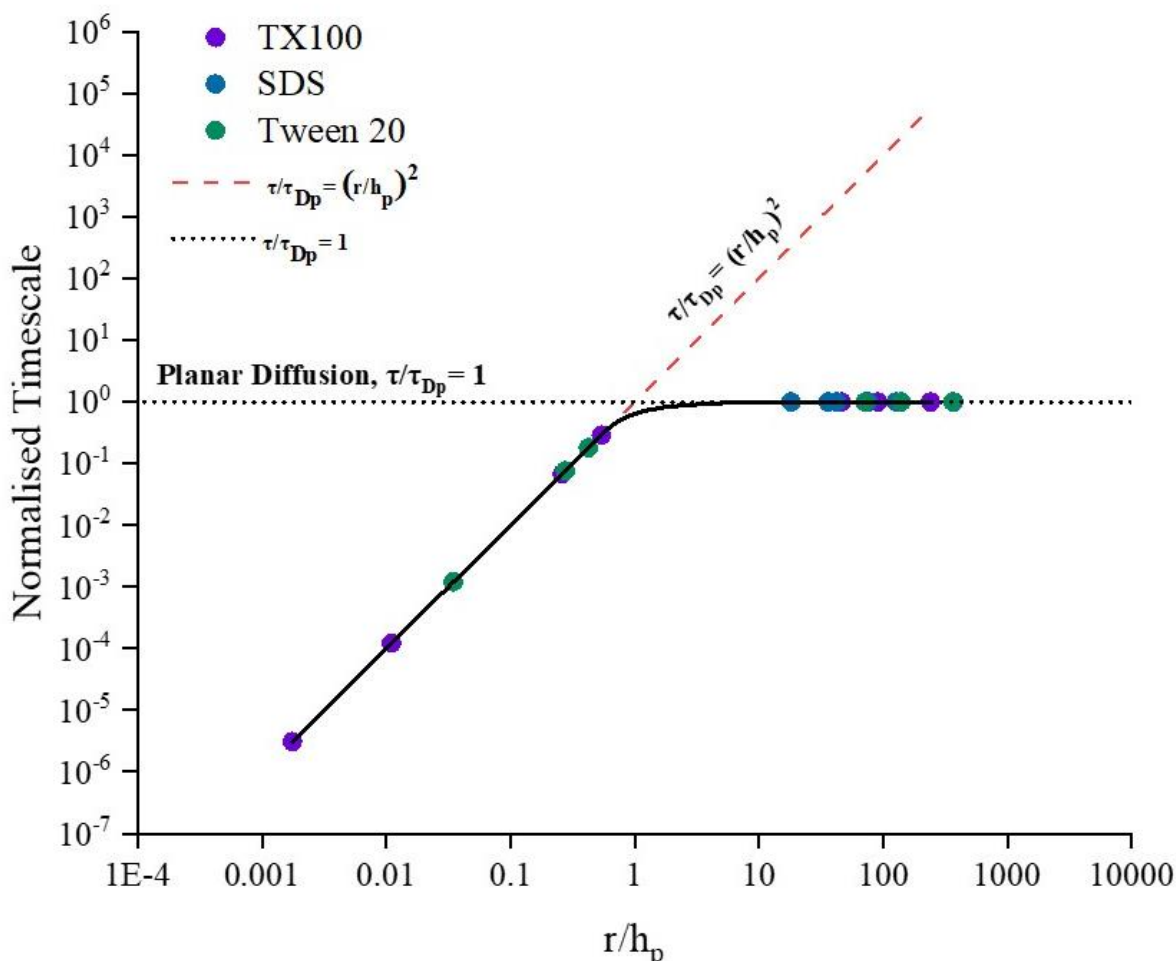


Figure 5-16: Characteristic timescale for diffusion of the surfactants to a spherical surface as a function of the normalised droplet radius r/h_p . The filled purple symbols indicate Triton X-100 which show fast normalised timescales at low concentrations and planar-like diffusion at higher concentrations. The filled blue symbols denote SDS which show planar-like diffusion in all concentrations used and the filled green symbols correspond to the characteristic timescale for Tween 20 which demonstrates the same behaviour as TX-100 at low and high concentrations. The normalised timescale $(\tau_{Ds}/\tau_{Dp})=(r/h_p)^2$ until the upper limit of 1 is reached after which planar diffusion is assumed. The solid black line is used to guide the eye.

To present the capability of the droplet oscillation method to produce time-dependent surface tension measurements the (1) surfactant type and concentration, (2) droplet size and (3) dispensing frequency were varied in this work. In Figure 5-17, time $t = 0$ is defined as the point at which the voltage pulse is applied to the droplet dispenser, with the time points thereafter defined by the user-imposed delay time set at 6×10^{-7} s for 30 μm orifice microdispenser and 1×10^{-6} s for 80 μm orifice microdispenser. The delay time denotes the time between the voltage pulse and the start of the stroboscopic imaging, separation from the dispenser tip, droplet stream and the operation of higher modes mean the earliest time the aspect ratio can be collected is approximately $\sim 120 \mu\text{s}$. The duration of oscillations and the eventual relaxation to aspect ratio one depends on the droplet size, solution concentration and dispensing voltage however on average relaxation occurs after 300 – 800 μs .

Droplet aspect ratios are retrieved after the higher order modes (explanation to be found in Chapter 3) relax to the $l=2$ mode within $\sim 10\text{-}60\ \mu\text{s}$.¹⁴⁸ The aspect ratio dataset was systemically shortened by removing earlier data points and the oscillation frequency determined by performing a fast Fourier transform on the remaining data. By fitting a Lorentzian line shape to the FFT data, the peak oscillation frequency could be located and used to calculate the surface tension. Each coloured Lorentzian line in Figure 5-17(b) corresponds to the data that undergoes a FFT to the right of the same-coloured line in Figure 5-17(a) for the water droplet measured. For example, in Figure 5-17 (b), the red Lorentzian line shape is fit to the FFT of the aspect ratio plot from 29 to 341 μs whereas the yellow Lorentzian line fit corresponds to the aspect ratio plot from 68 to 341 μs . Though the magnitude of the peak diminishes due to a reduction in data, there is little to no shift in the peak of the Lorentzian lines and no reduction in the surface tension over time. This is owing to the lack of dynamic behaviour observed in water droplets in ambient conditions. Conversely, for the 6 mM SDS droplet shown in Figure 5-17(d), the shift in the Lorentzian lines towards lower oscillation frequencies is indicative of surfactant diffusion or adsorption processes being operative at the surface over time. Using this shift in the oscillation frequency peak characteristic of surfactant solutions, the dynamic surface tension can be calculated.

During measurement collection approximately four to eight surface tension measurements were taken at each concentration (10^{-4} to 10^2 mM), droplet size (between 30 and 50 μm) or frequency (between 2 and 200 Hz). The typical dispensing frequency used for the different concentrations and droplet sizes was 20 Hz. The data were collated into 20 μs time bins which allowed sufficient data points within each bin (2 to 6 points on average). The surface tension was averaged, and a standard deviation of the data points used was taken to be the uncertainty in the y axis. Similarly, the standard deviation of the binned times was taken as the x axis uncertainty.

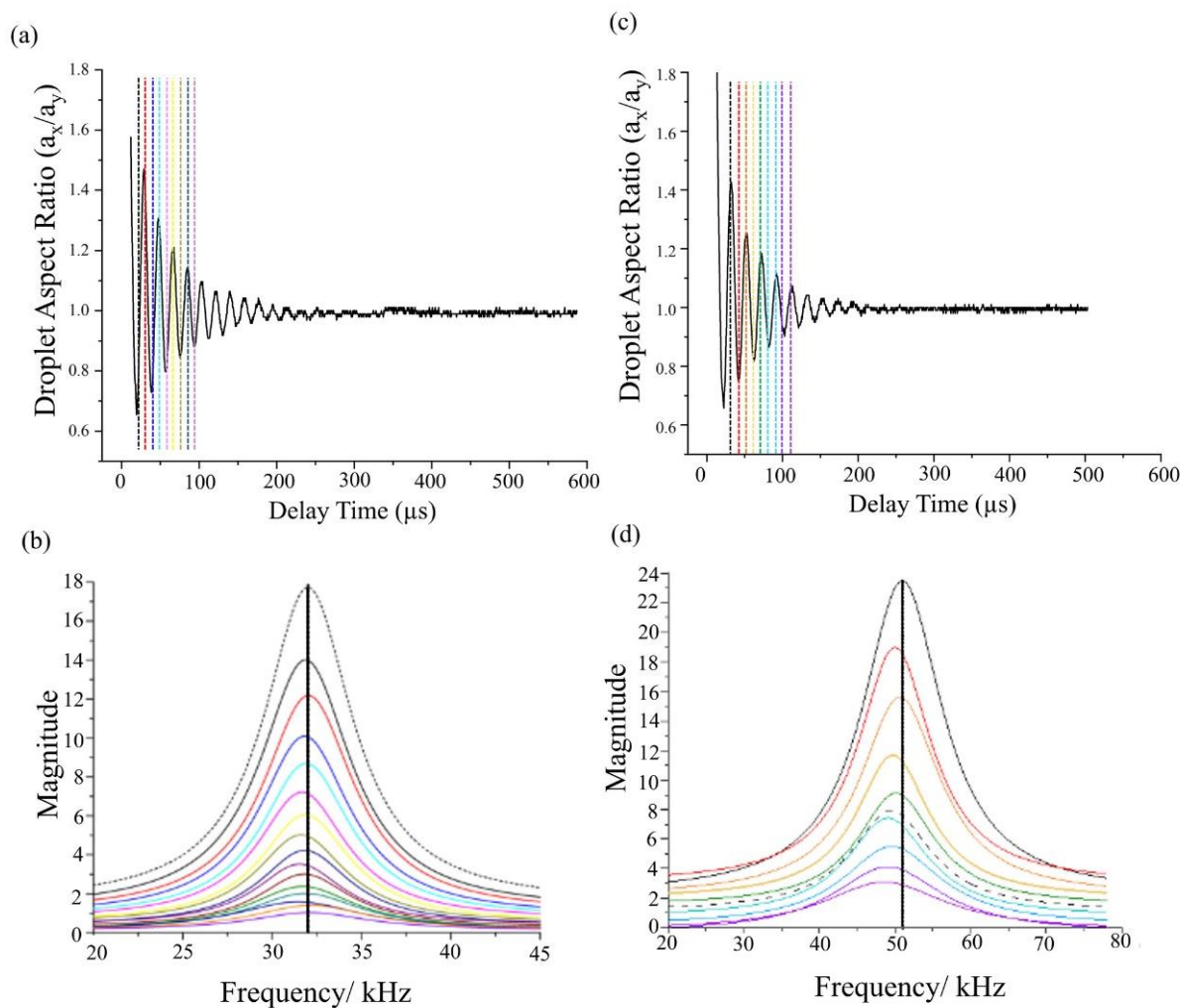


Figure 5-17: Droplet aspect ratio plotted against delay time and associated Lorentzian line fit. The data to the right of each vertical dotted line underwent a separate FFT and plotted with a Lorentzian fit (a) Analysis of a $21 \mu\text{m}$ radius water droplet, $l=2$ determined at $t=7.2 \times 10^{-5} \text{ s}$, with a complete droplet oscillation time of $1.2 \times 10^{-5} \text{ s}$ (b) the Lorentzian fits for the water droplet in (a), and (c) a $15.5 \mu\text{m}$ radius SDS droplet, $[\text{SDS}]_{\text{aq}}=6 \text{ mM}$, $l=2$ at $5.8 \times 10^{-5} \text{ s}$ with a complete droplet oscillation time delay time of $1.3 \times 10^{-5} \text{ s}$ (d) the Lorentzian fits for the spliced SDS droplet in aspect ratio plots shown in (c). These measurements were conducted at a dispensing frequency of 20 Hz.

5.3.2.1 Characterization of Surface Tension in Relation to Surfactant Concentration and Type

As previously discussed, there are three interrelated phenomena taking place at the droplet interface, namely, diffusion, adsorption, and desorption. Surfactant molecules adsorb and desorb from the interface due to a balance between entropic costs and enthalpic forces, leading to subsurface depletion. At low concentrations this process results in bulk depletion, as surfactant molecules diffuse from the bulk to the surface and to adsorb at the surface. Upon reaching an equilibrium where the number of adsorbing molecules is equal to the number of desorbing molecules, a minimum surface tension is reached. Both the DST and the characteristic timescale for diffusion are influenced by various factors, including the type of surfactant, its surface activity, bulk concentration, and molecular diffusivity. The

surfactants described herein were chosen based on their different dynamic behaviour over time and their potential use as atmospheric proxies for biosurfactants and organic surfactants.

As discussed in Chapter 3, the delay time is defined as the variable time delay between the voltage pulse sent to the dispenser and the brightfield imaging strobe. In Figure 5-18 to Figure 5-20, x axis refers to the delay time at which the data is spliced and the FFT taken thereafter. An increase in the surfactant concentration brings the system closer to the equilibrium surface tension between 10-300 μs for SDS, Tween 20 and TX-100. Each surfactant has a unique profile of surface tension decay above and below their CMC. As the measurements in this study were performed over short timescales (microseconds), there is insufficient time for the requisite number of surfactant molecules to reach the surface and attain equilibrium with the bulk. Refer to Table 5-6 for the equilibrium surface tension collected from the Wilhelmy plate and averaged over the concentrations above the CMC.

Table 5-6: The equilibrium surface tension of SDS, TX-100 and Tween 20.

Surfactant Type	Equilibrium Surface Tension (mN m^{-1})
SDS	38.60 ± 0.20
Tween 20	37.40 ± 0.40
TX-100	31.70 ± 0.03

The relationship between surfactant concentration and surface tension reduction varies with surfactant. Figure 5-18 shows the time-dependent surface tension profile SDS which shows dynamic behaviour above and below the CMC. At the SDS concentrations 20 and 50 mM, the DST plots overlap with each other, which may suggest that diffusion is no longer the rate-determining step, and the presence of a strong adsorption barrier may have become the limiting factor. From Figure 5-18 it is evident that longer oscillation windows will be needed to reach the equilibrium surface tension measured in the bulk.

AE

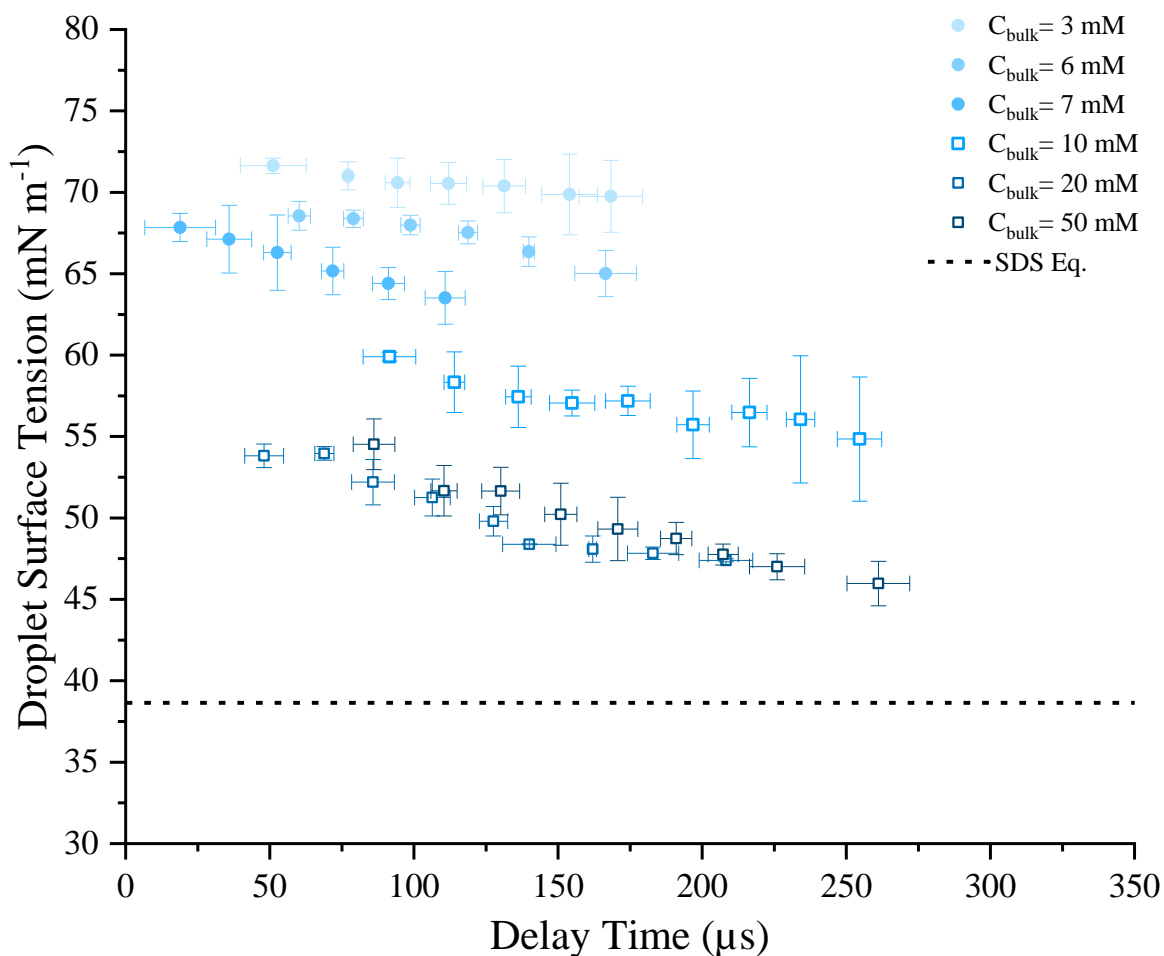


Figure 5-18: The droplet surface tension plotted against the delay time for SDS surfactant concentrations below (closed symbols) and above (open symbols) the CMC of sodium dodecyl sulfate in aqueous solution. The dotted line represents the equilibrium surface tension when concentration $>$ CMC ($\sim 38 \text{ mN m}^{-1}$) measured using the Wilhelmy plate.

Figure 5-19 shows the retrieved surface tensions for TX-100. Below the CMC, when the concentration is low, no obvious dynamic behaviour is observed due to low mass transport. At concentrations $>$ 10 mM, TX-100 shows greater decay of the surface tension than both SDS and Tween 20. For example, at a concentration of 50 mM, TX-100 shows a significant change in surface tension ($\Delta\sigma = 13 \text{ mN m}^{-1}$) between 50 – 150 μs , while over the same period of time and at the same concentration, SDS and Tween 20 show notably lower at values of $\Delta\sigma = 5 \text{ mN m}^{-1}$ and $\Delta\sigma = 0.79 \text{ mN m}^{-1}$, respectively. This observation correlates well to the bulk data collected and described previously in Section 5.31. Figure 5-20 shows the change in surface tension decays below and above the CMC point, notably, the rate of change distinctly increases from 10 to 50 mM. This is consistent with the findings by Alvarez et al., which showed an increase in concentration results in reaching the equilibrium faster as r/hp is proportional to the spherical diffusion timescale.⁹⁶

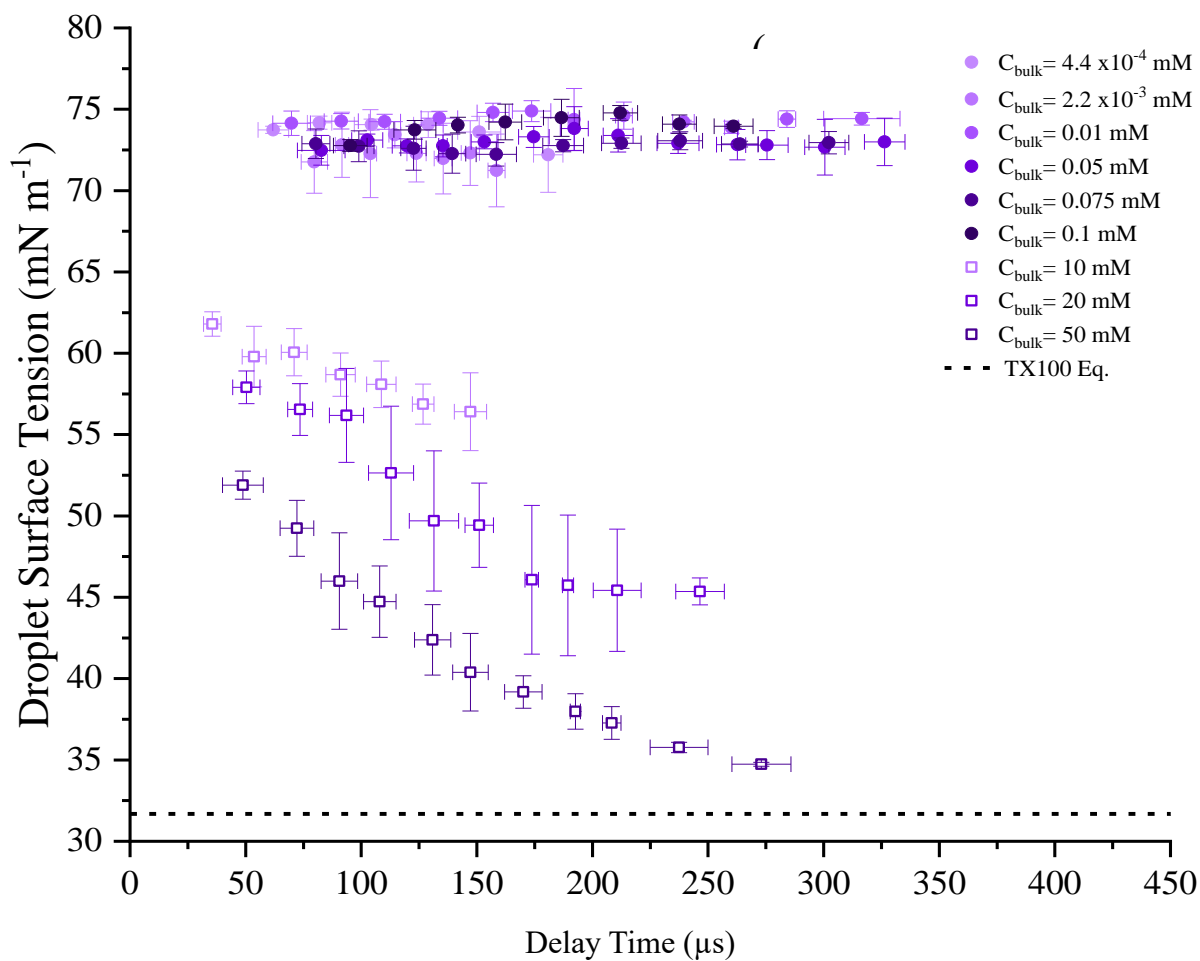


Figure 5-19: The droplet surface tension plotted against the time for TX-100 surfactant concentrations below (closed symbols) and above (open symbols) the CMC of Triton X-100 in aqueous solution. The dotted line represents the equilibrium surface tension when concentration > CMC (~ 31-32 mN m⁻¹) measured using the Wilhelmy plate and MBT.

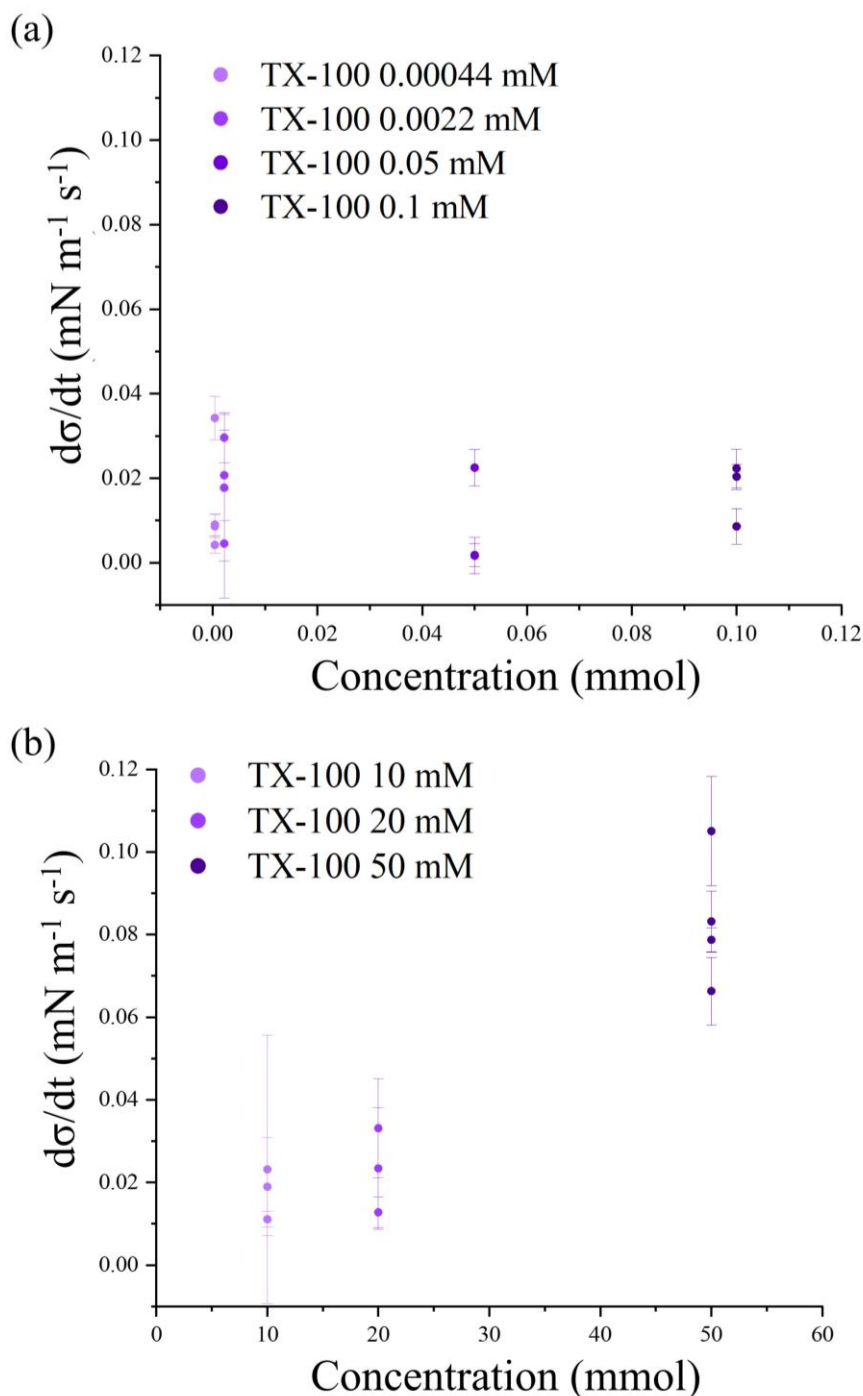


Figure 5-20: The rate of surface tension change over given time duration (time window = 150 μ s) plotted against surfactant concentration (a) below and (b) above the CMC of Triton X-100 in aqueous solution.

Figure 5-21 illustrates the temporal evolution of the surface tension of aqueous Tween 20 droplets. Similar to TX-100, below the CMC, Tween 20 demonstrates limited reduction in surface tension as a result of low mass transport resulting in accordance with the low concentration. At concentrations above the CMC (10 mM to 50 mM), Tween 20 shows a slight change in the decay rate of the surface tension

over time, which could be due to the slow diffusion rates as observed in the bulk. However, Tween 20 is able to reduce the surface tension to greater degree than the other surfactants showing it is a strong and useful surfactant. This observation is consistent with bulk measurements that demonstrate Tween 20 to be a strong surfactant at low concentrations compared to SDS and other proxy surfactants, see Section 5.3.2.2 (Figure 5-13), as indicated by its prominent surface tension reducing abilities.²⁷⁹

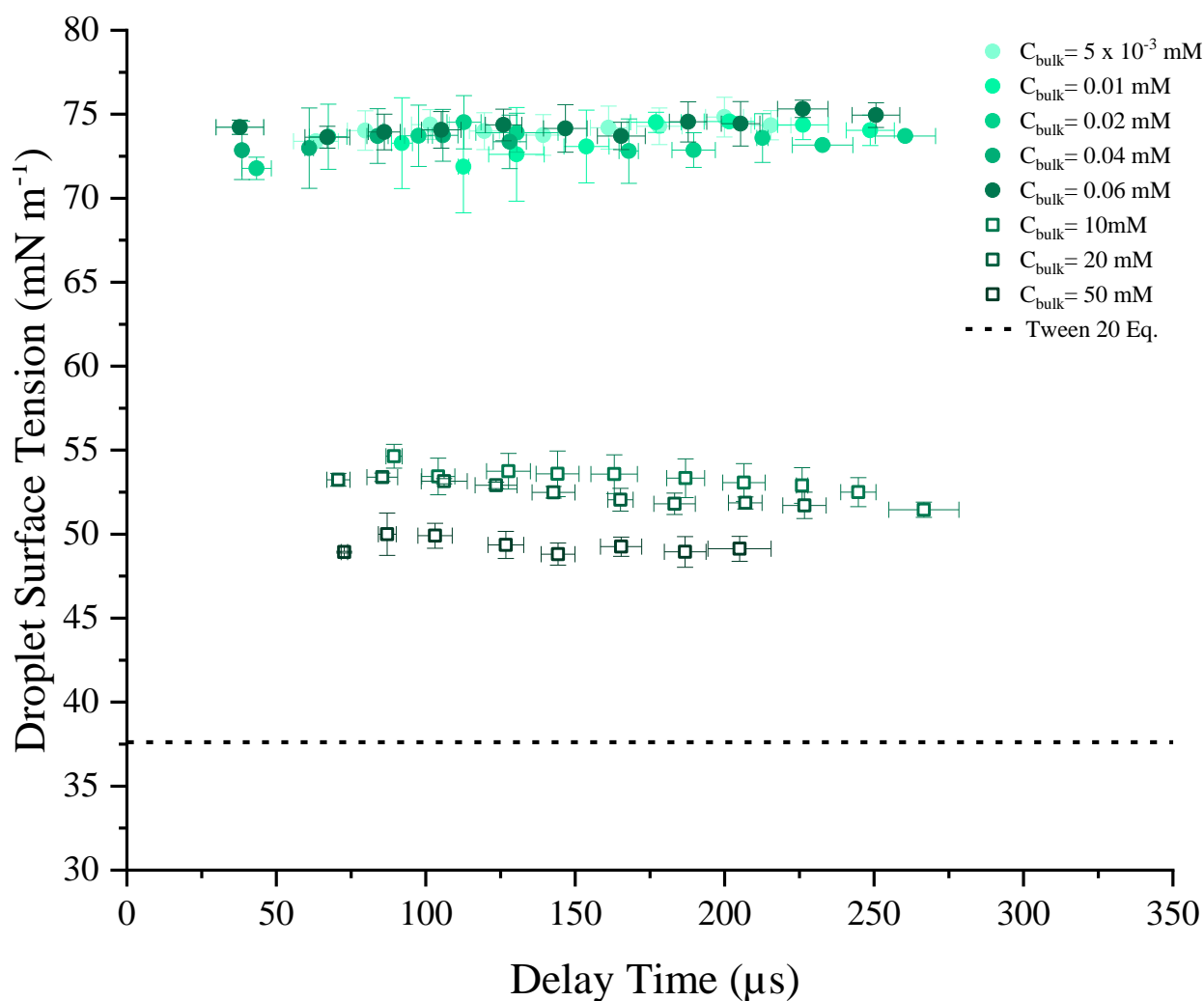


Figure 5-21: The droplet surface tension plotted against the time for Tween 20 surfactant concentrations below (closed symbols) and above (open symbols) the CMC of Tween 20 in aqueous solution. The dotted line represents the equilibrium surface tension when concentration $>$ CMC (~ 35 - 37 mN m^{-1}) calculated using the Wilhelmy plate and MBT. These measurements were conducted at a dispensing frequency of 20 Hz.

5.3.2.2 Characterization of Surface Tension in Relation to Droplet Size and Dispensing Frequency.

Figure 5-22 shows how the normalised spherical diffusion timescale varies with radius using the work of Alvarez and co-workers.²⁹⁴ To examine whether diffusion within droplets with a $r > 10 \mu\text{m}$ behaved like planar diffusion, droplet sizes was varied between 30-50 μm using a 30 μm and 80 μm orifice microdispenser at a constant concentration of 20 mM for each surfactant. Figure 5-23 demonstrates the variation in the rate of surface tension decay which shows no trend with increasing droplet radius. The lack of a trend is expected from Figure 5-22 and attributed to the size of the droplet radii and high concentrations leading to droplet diffusion reaching the planar diffusion limit where the rate of surface tension change will remain similar. Only when the droplet radius is lowered by two orders of magnitude will a notable change in the surface tension decay be observed, this is beyond the ability of the microdispensers used in this study.

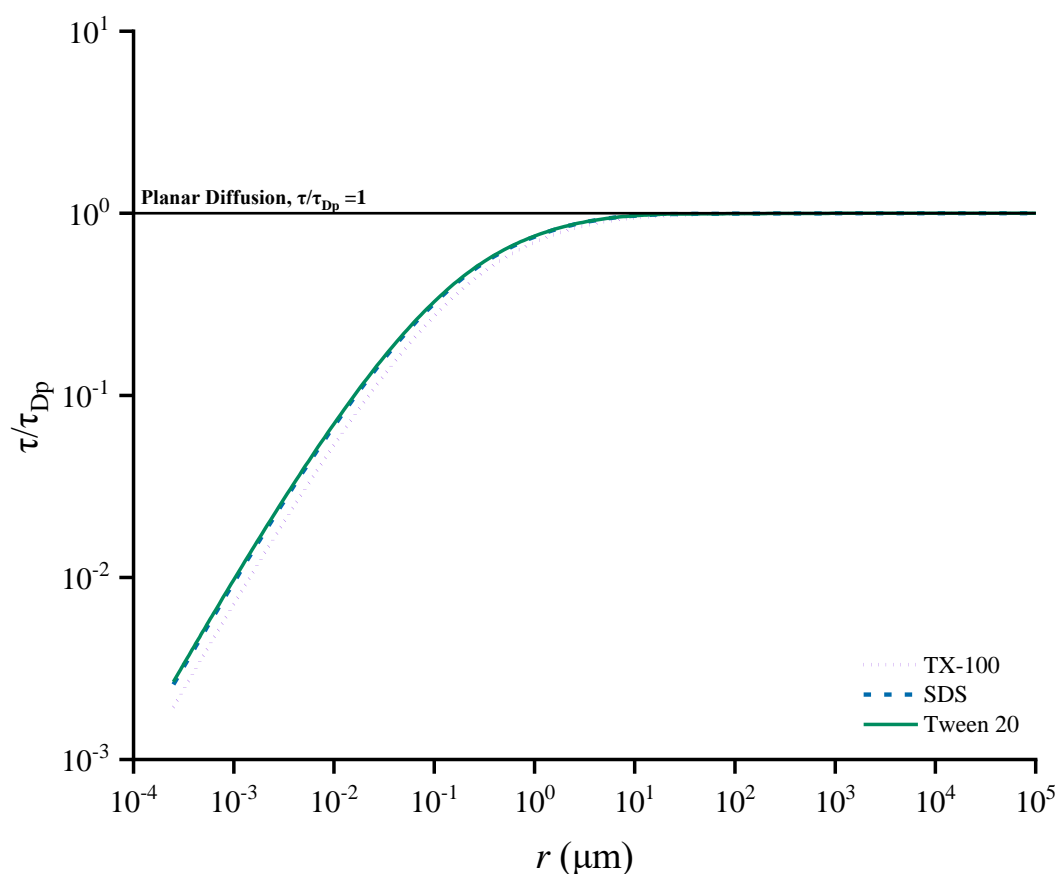


Figure 5-22: The normalised characteristic timescale for diffusion as a function of the droplet radius at a constant concentration of 20 mM. SDS indicated by the blue dashed line, TX-100 shown in the purple dotted line and Tween 20 shown with the green solid line.

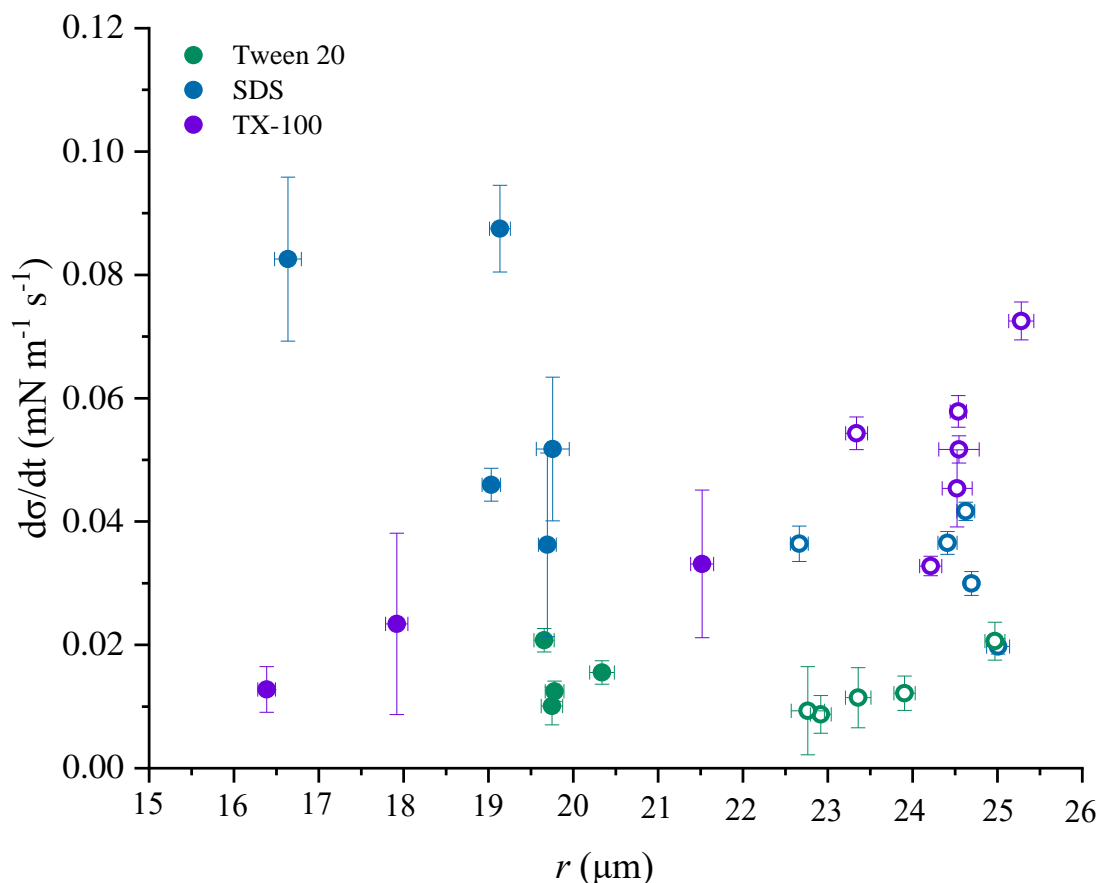


Figure 5-23: The rate of surface tension decay in a 150 μs time duration plotted against droplet radius for each surfactant type at the concentration of 20 mM. The closed symbols represent the 30 μm orifice microdispenser and open circles denote the 80 μm orifice microdispenser.

During these measurements a novel advantage was found to using two different microdispenser orifice sizes. Using a 30 μm orifice microdispenser, as in previous work¹⁴⁸ results in relatively short measurement time windows $t < 250 \mu\text{s}$ for surfactants to partition to the surface, which could be too short for certain surfactants to the surface in further work. Figure 5-24 shows how by using the 80 μm orifice microdispenser the window of measurement can be extended without impacting the rate of surface tensions decay as confirmed by Figure 5-23. This offers investigators the ability to combine measurements from both dispensers and extend the time period over which the surface tension can be measured, particularly in the case of SDS and TX-100.

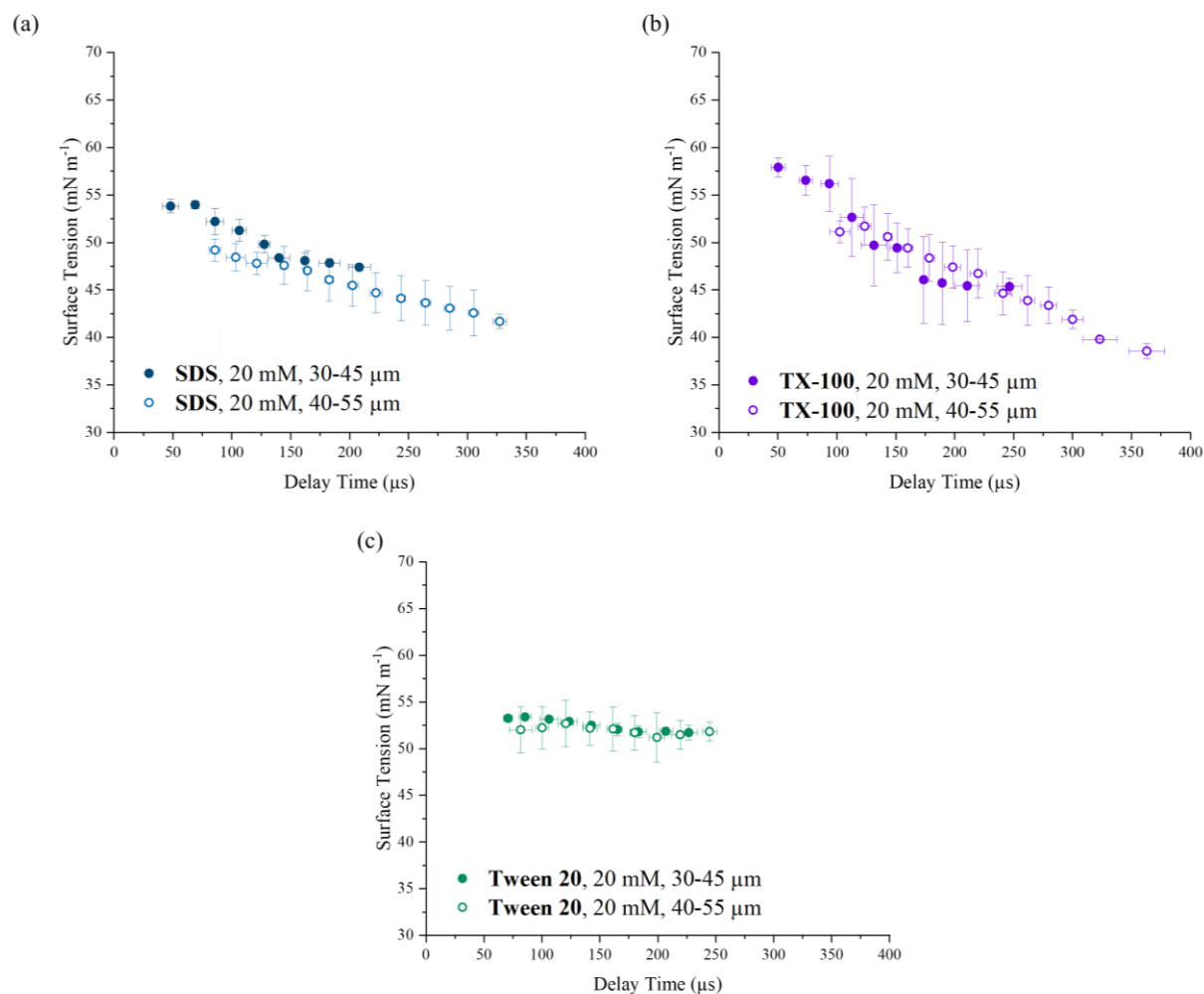


Figure 5-24: The surface tension plotted against time for (a) SDS (b) TX-100 and (c) Tween 20 at a concentration of 20 mM with the closed symbols representing droplet diameters between 30-45 μm and open circles denoting droplet diameters between 40-55 μm.

Next, the frequency at which the droplets are ejected from the microdroplet dispenser is explored to determine if this impacts the starting surface tension of the droplet. The lower the dispensing frequency, the longer the meniscus age of the dispensing droplet hence the more time surfactant molecules at the tip have to diffuse to the surface and reduce the surface tension before beginning their oscillation journey as depicted in Figure 5-25. By comparing different dispensing frequencies, it is possible to confirm which dispensing speed was most appropriate to use during this study.

The study employed 20 Hz as the dispensing frequency as it is the most appropriate frequency to use upon examining Figure 5-26. Specifically, this frequency exhibits significant overlap with 200 Hz, but less so with 2 Hz. This finding suggests that meniscus age effects remain in operation at the lower frequency of 2 Hz impacting the droplet. Therefore, the selected dispensing frequency of 20 Hz is scientifically justified based on the observed overlap with relevant frequencies and the continued operation of meniscus age effects at lower frequencies. In addition, the most stable droplet trajectories were found at 20 Hz making it a more desirable frequency to work with.

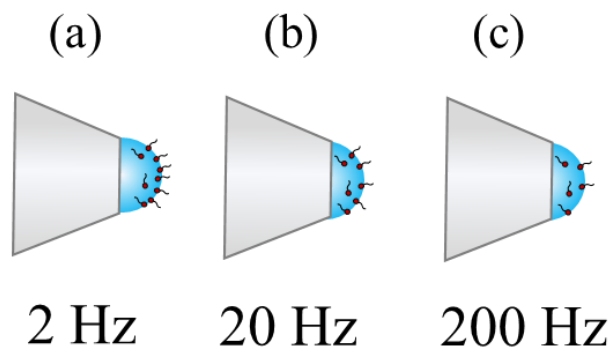


Figure 5-25: A schematic to demonstrate the population of surfactant monomers at the droplet meniscus before dispensing from the microdispenser tip at (a) 2, (b) 20 and (c) 200 Hz which corresponds to 0.5 s, 0.05 s and 5 ms respectively between the dispensed droplets.

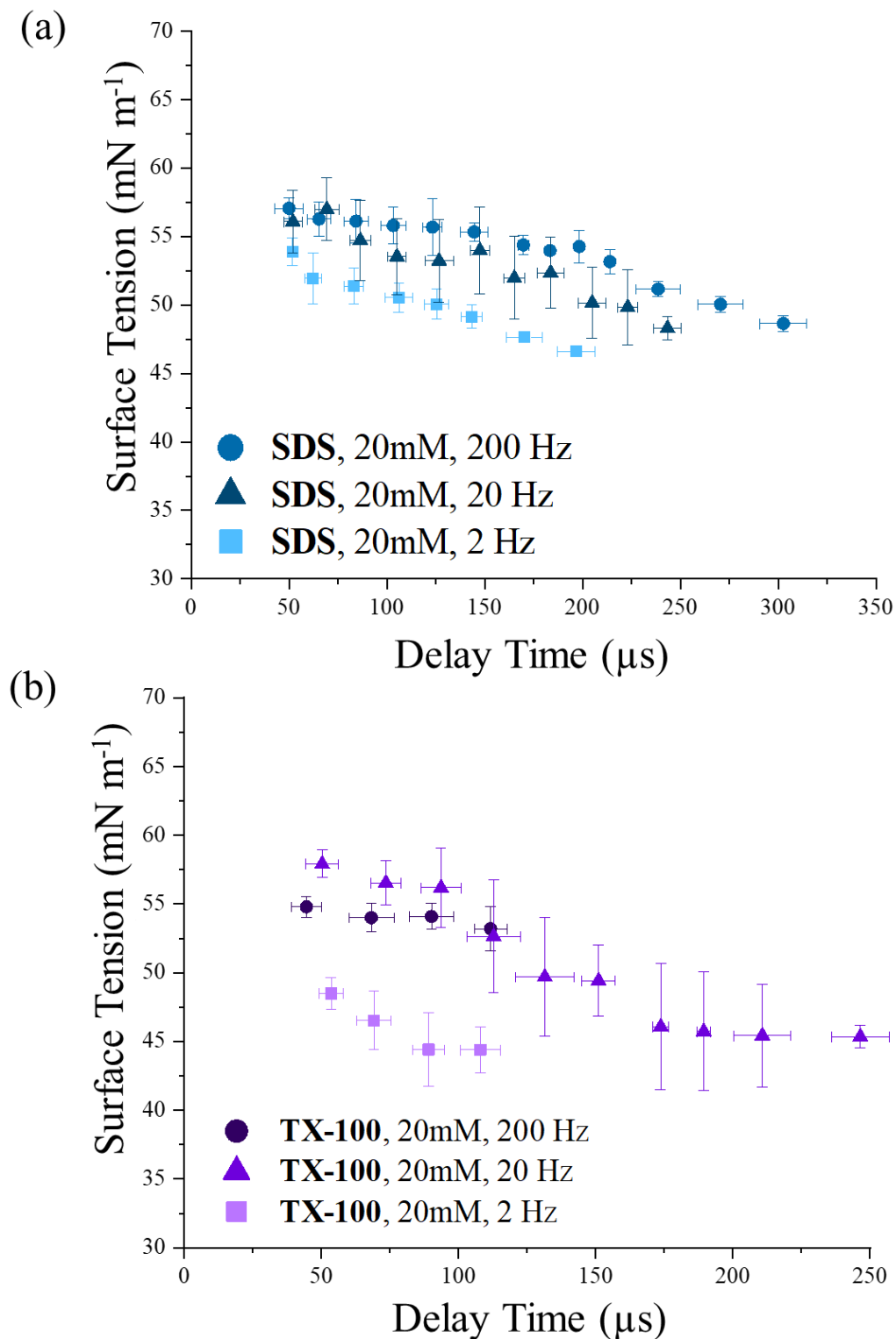


Figure 5-26: Surface tension plotted against delay time, at dispensing frequencies of 2 Hz (square symbols), 20 Hz (triangle symbols) and 200 Hz (circle symbols) for (a) SDS and (b) Triton X-100 at the concentration of 20 mM.

5.3.2.3 Combining Droplet and Bulk Data using the Hua-Rosen Equation

Figure 5-27 shows the combination of droplet and bulk dynamic data modelled using the Hua-Rosen semi-empirical Eq. 5.32 where n (dimensionless) and t^* (units of time) are constants. There is an excellent fit between the model and the TX-100 solution at a concentration of 10 mM. At the concentration of 20 mM, there is agreement between the model and measurement data within error. The value of n for both concentrations is similar ($n_{10\text{mM}}=0.45$ and $n_{20\text{mM}}=0.46$) indicating that the interactions between the surfactants and the surface are equally strong. Contrary to expectation, t^* which represents the rate of adsorption and desorption is higher for 10 mM than 20 mM however as both are within same order of magnitude this difference can be treated as negligible.

Table 5-7: A table for the constants, n and t^* , calculated from the fitting of the Hua-Rosen Approach to the experimental droplet and bulk dynamic surface tension data.

TX-100		
Concentration (mM)	t^* (ms)	n
10	0.43 ± 0.02	0.45 ± 0.01
20	0.10 ± 0.01	0.46 ± 0.06

Overall, the ability to account for surfactant activity at very short and long times will prove useful to many industries along with improvements to our understanding and modelling of surfactants and their dynamics within the atmosphere.

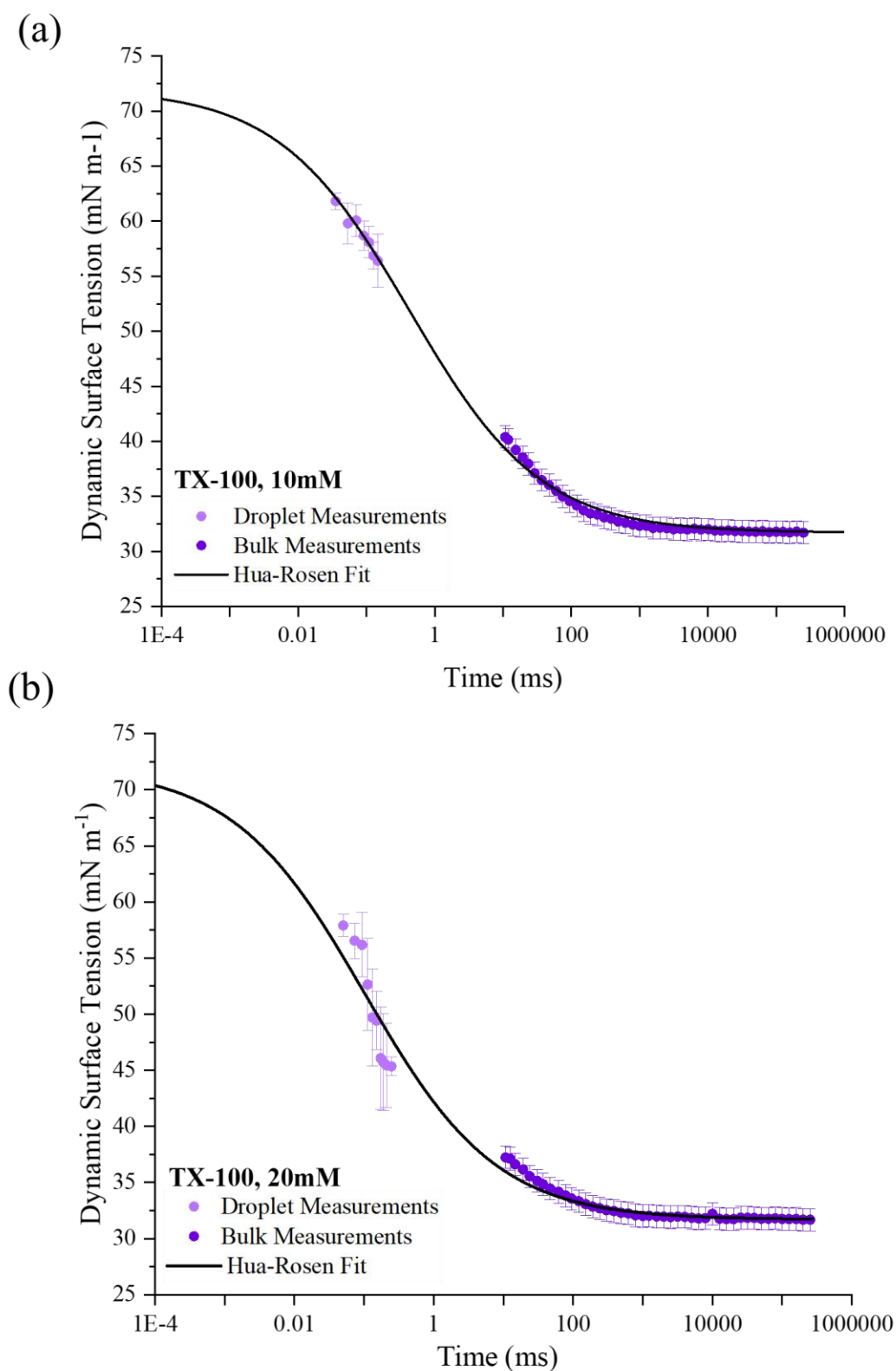


Figure 5-27: Dynamic surface tension of droplet and bulk measurements plotted against time and fitted to the Hua-Rosen model for (a) $[\text{TX-100}] = 10 \text{ mM}$ and (b) $[\text{TX-100}] = 20 \text{ mM}$. The light purple symbols indicate droplet measurements collected using the droplet oscillation method; while the dark purple symbols represent the bulk measurements obtained by MBT. Here surface age and delay time are treated as the same.

5.4 Conclusion

The work herein describes the investigation of droplet dynamic surface tension (DST), bulk DST, and bulk equilibrium surface tension using various measuring techniques. The Wilhelmy plate method uses the force needed to remove a plate from the surfactant solution to determine the equilibrium surface tension. Using the Langmuir and Frumkin isotherms, key surface properties such as CMC, Γ_{∞} , A_{\min} for each surfactant solution were calculated and used to infer their surface propensity and stability. Overall good agreement is observed between the published data and those collected in this study showing the validity of the measurements collected. In comparison to the equilibrium surface tension profiles of biosurfactant samples and other synthetic surfactants, TX-100 and Tween 20 profiles show they can act well as proxies for atmospheric aerosol surfactants for laboratory studies.

The MBT approach was used to determine the dynamic bulk behaviour of the aqueous sodium dodecyl sulfate (SDS), Triton X-100 (TX-100), and Tween 20 solutions. The bubbles produced by a gas reach maximum pressure used to determine the surface tension. It was assumed from DST profiles of Tween 20 and SDS that adsorption followed diffusion-controlled mechanism due to the linearity of the plot at long times. By fitting the DST profiles of the surfactants to the short time and long-time approximations derived from the Ward and Tordai equation, diffusion coefficient which are in good agreement with the literature could be calculated. At short times where diffusion is dominant the SDS shows the lowest diffusion coefficient whereas at long times when adsorption is the limiting factor, Tween-20 has the lowest diffusion coefficient which is expected. The MBT approach cannot account for the unique properties observed within the confined volume of a droplet or the dynamic behaviour at early surface ages, hence another method was employed to do so.

This work describes the droplet oscillation approach to measuring the droplet DST at delay times ≤ 1 ms. Stroboscopic imaging captured oscillating droplets ejected from a microdispenser from which the surface tension can be retrieved. This method is used to collect nascent dynamic surface tension data for aqueous SDS, TX-100, and Tween 20 solutions at different concentrations, droplet sizes and dispensing frequencies. The most notable system is TX-100 which displayed the most dynamic behaviour over a given time ($\sim 100 \mu\text{s}$) above the CMC showing it is a highly surface-active surfactant. The data showed Tween 20 to be the strongest surfactant system above the CMC, by its ability to lower the surface tension to a greater degree below that of water. For the SDS system the surface tension decay profiles overlap at the higher concentration 20 to 50 mM, potentially because of the concentration and diffusion no longer being a limiting factor in adsorption to the surface and the subsequent surface tension reduced. Additional concentrations would need to be measured in order determine if this theory is correct. The ability to measure the dynamic surfactant behaviour in liquid droplets over the early time range was the most useful result to come from this work as this is not reflected in the literature.

Interestingly, investigation into the effect of droplet size of diffusion lead to finding a method to extend time over which the droplet measurements are taken, thus extending the DST surfactant profiles towards the equilibrium value derived from the Wilhelmy plate measurements. This may be useful in future studies and should be explored further.

5.5 Future Work

With the scope of this current study there are several areas for future work, which will be discussed in detail in this section. Firstly, there is a need to broaden the range of surfactant types studied by choosing more anionic, cationic, and non-ionic surfactants, as well as biosurfactants, in order to capture and model the surfactant dynamics that could be seen in atmospheric aerosols.⁵³ Another avenue for future investigation will be the study of surfactants and inorganic salt mixtures.²⁹⁵ At short timescales, inorganic salts have been shown to enhance the performance of some surfactant molecules performance, lowering the CMC and equilibrium surface tension which will in turn impact cloud droplet growth.

296,297,298

The acidity of suspended atmospheric aerosols has been known to have an adverse effect on watersheds, marine and terrestrial ecosystems.²⁹⁹ As aerosols form in part from clouds evaporation, cloud chemistry may affect the acidity and composition of aerosols when they evaporate. Equally as aerosols are precursors to clouds, they can affect the pH of the cloud droplets or ice crystals. Solution pH conditions impact the rate of adsorption and desorption of surfactant molecules in droplet and bulk dynamic surface tension. For example, Hernainz et al. showed a reduction in surface tension as the concentration of the SDS solution increased and the pH decreased between pH 4 and 8.³⁰⁰ Given that the pH levels found within aerosols can vary five orders of magnitude between pH -1 and 7²⁹⁹, future work will examine this pH range using compounds such as sulfate organics (pH -1).

Eastoe et al. observed that increasing the temperature leads to faster surface tension decay and lower surface tension of di-(C5-Glu) profiles, with an effective diffusion coefficient that increased by two orders of magnitude from 283 K to 323 K.⁸⁷ Given that the temperature profile of the troposphere varies between 222 to 290 K, this temperature range would be used in future studies of surfactant solutions.

Finally, investigations into chain length, steric hindrance, hydrophobicity, and barriers to reorientation at the surface could help to better understand the impact of these factors on dynamic surface tension. For example, Bykov et al.³⁰¹ showed that the surface tension decreases with increasing chain length of C_nTAB (*n* varies between 8 and 16) using CTAB/DTAB mixtures, a trend confirmed by Smit et al. Further studies will be necessary to elaborate on the relationship between chain length, surface tension, and the rate of decay, as well as the aggregate structure of surfactants.^{301,302} Studies such as these will help to improve our understanding of aerosols and the climate models they feature in.

Chapter 6

The Measurement of Viscosity and Photoinduced Size Change in Aerosol Droplets Under Different Humidity Conditions

6.1 Overview

From this thesis, it is apparent that organic and inorganic aerosol particles play key roles in cloud formation and lifetime, absorbing and scattering light, altering atmospheric composition, and impacting human health, see Figure 6-1.^{128,303} Conventionally, particle partitioning models have assumed the phase state of atmospheric organic aerosols to be liquid with a low viscosity which has led to incorrect constraints on chemical reactivity, hygroscopicity and component volatilities. These partitioning models predict that aerosol particles attain equilibrium with the surrounding environment instantaneously, resulting in a homogenous, well mixed composition in short diffusion timescales.⁴⁰ Recent measurements have shown contrasting findings whereby laboratory and field measurements indicate the existence of highly viscous, semi-solid and even amorphous solid particles.³⁰⁴ Particles with a high viscosity are predicted to be less reactive to gas composition changes than those with a low viscosity.³⁰⁵ Particle viscosities in both laboratory and field measurements have been shown to range from 10^{-3} to 10^{12} Pa s, values spanning water and tar pitch, respectively.

Viscosity is a fundamental physicochemical property that has important implications on aerosol heterogenous and photochemical reactions, climate forcing and transboundary pollution across the globe.^{166,306} The viscosity of atmospheric aerosols can vary in different environments because of changes in ambient relative humidity: water acts as a plasticiser within aerosols and increases the mobility of organic matrix within an aqueous droplet.³⁰⁷ Highly viscous SOA particles are often found in low relative humidity, cold conditions and exhibit slower uptake and penetration of trace gases and SVOCs coupled with slower diffusional rates within the particle. Slow diffusion can change the growth and therefore size of SOA particles moving from absorptive to adsorptive partitioning and reduced evaporation.^{308,132,309} An example of this, by Gervasi et al.³⁰⁶ in 2020, noted the increased shielding from oxidation by species such as the hydroxyl radical (OH), nitrate radical (NO₃), and ozone (O₃) in viscous droplets which culminates in the increased time organic species spend within the aerosol phase.³⁰⁶ This increased time in turn allows the particles to undergo long range transport that contributes to transboundary pollution.³¹⁰ Primary aerosol particles containing soot, black carbon or polycyclic hydrocarbons undergo chemical reactions at the surface rather than the bulk due to the quasi-solid state.¹⁰² Oxidation reactions in viscous SOA particles also have an impact on the climate. In 2018, Liu

Chapter 6- The Measurement of Viscosity and Photoinduced Size Change in Aerosol Droplets Under Different Humidity Conditions

and colleagues found that the formation of brown carbon aerosol may be restricted by viscosity.³¹¹ As a result, secondary organic aerosols that would typically undergo browning due to multiphase chemical reactions become transparent because the reactions are slowed down. This transparency causes the aerosols to scatter solar radiation rather than absorb it. The inhibition of brown carbon formation by viscous organic compounds has a direct impact on aerosol-radiation-climate effects, while the phase state of secondary organic aerosols may also have an indirect impact on climate and weather.³¹¹

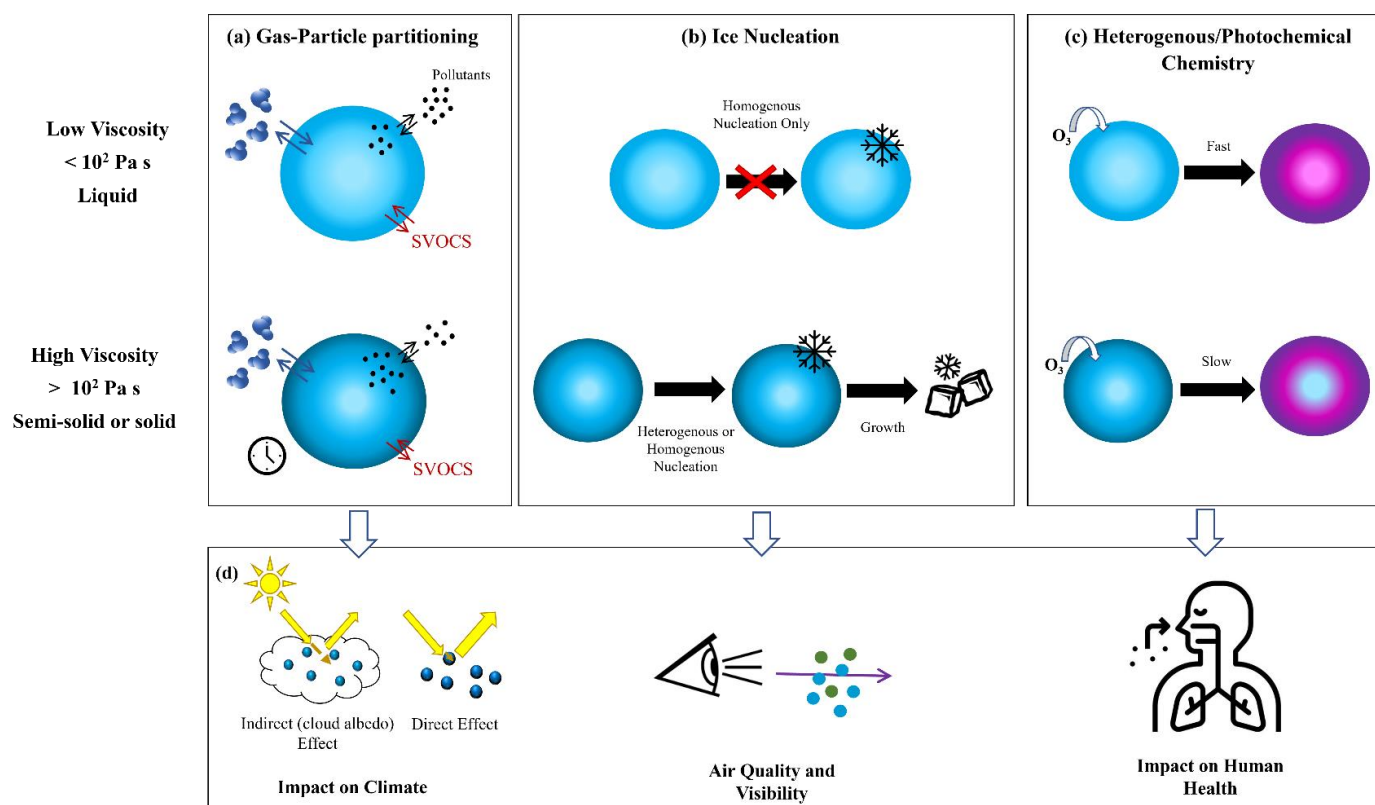


Figure 6-1: Impacts of particle viscosity on (a) the time taken to achieve equilibration through gas-particle partitioning of water, pollutants and semi volatile organic compounds (SVOCs) (b) the ability to form ice nucleating particles which high viscosity particles are able to do via homogenous and heterogenous nucleation (c) the photochemical and heterogenous rate of reactivity which is faster in low viscosity particles (d) the climate, air quality and visibility and human health. This image has been created based on the paper by **Reid et al.**¹²⁸

Marshall et al.⁴⁰ examined the ozonolysis of the ternary maleic acid (MA)/sucrose/water mixture at different mass ratios under various environmental conditions. MA was exposed to ozone and the photochemical oxidation of the C=C was measured by following the reduction in the vinylic band in the droplet's Raman spectrum.⁴⁰ As the viscosity of the droplet increased with decreasing relative humidity, the loss of the vinylic band intensity was less pronounced. This study also found that an increase in particle viscosity leads to a decrease in the inferred diffusion coefficient and to the suppression of the effective vapour pressure of MA. Indeed, at lower relative humidities, viscosity impedes the diffusion of MA molecules, reducing the effective MA volatility. Consequently, the observed droplet size change is smaller than the amount expected based on measurements of wet (low viscosity) droplets. Hinks et al.³¹² observed a similar trend when examining SOM mixtures impregnated

Chapter 6- The Measurement of Viscosity and Photoinduced Size Change in Aerosol Droplets Under Different Humidity Conditions

with the atmospherically relevant, photodegradable compound 2,4-dinitrophenol (2,4-DNP). At lower temperatures and RH, the SOM viscosity increases, leading to slower photodegradation rates in all three model systems. The increase in viscosity is believed to reduce the motion of the molecules in the SOM matrix, hindering their respective photochemical reactions.³¹²

Figure 6-1 illustrates differences between low and high viscosity particles. Highly viscous particles can serve as ice nucleating particles (INP) and ice crystals in glaciated clouds.^{128,131} The INPs found in the atmosphere can be formed via deposition nucleation, a heterogenous process, or immersive freezing, a homogenous process. The deposition of mineral dust particles or bacteria on a droplet at a given temperature can induce ice formation while homogenous freezing of pure water or solute particles must occur below 236 K and at high water supersaturations.³¹³

To fully understand the implications of viscosity on atmospheric aerosols and the climate, we must quantify the impact on environmental conditions (like relative humidity) on SOA viscosity. Additionally, photochemical reactions are important in determining the chemical composition of the atmosphere. Accounting for the influence of relative humidity on photochemical reactions is important because RH constantly cycles from high to low values in the atmosphere which can lead to different reaction rates dependent on the ambient conditions. In this chapter, the viscosity of two different systems, namely, sucrose/citric acid/H₂O and sucrose/nitrate/H₂O (data for which was acquired in L. Lalemi Master's degree) have been investigated in relation to the relative humidity using a holographic optical tweezers. Additionally, preliminary data are reported on the change in droplet size caused by the UV irradiation of aqueous sodium nitrate droplets under different relative humidity conditions using an electrodynamic balance.

The viscosity of liquid water in ambient conditions is $\sim 10^{-3}$ Pa s which is orders of magnitude lower than semi solid aerosols found between $\sim 10^2$ to $\sim 10^{12}$ Pa s and glassy particles which can exceed viscosities of $\sim 10^{12}$ Pa s. It was Einstein who first established a correlation between the increase in viscosity of the medium and slower diffusional motion. Hence the Stokes-Einstein equation is commonly used to relate the viscosity, η , to the molecular diffusion coefficient, D_c , as follows³¹⁴:

$$D_c = \frac{k_B T}{6\pi\eta r_m} \quad (6.1)$$

where k_B is the Boltzmann constant, T is the temperature in Kelvin, and r_m is the radius of the diffusing molecule. The viscosity and radius are inversely proportional to the diffusion coefficient hence when both increases, the diffusion coefficient decreases.¹⁰² The characteristic time of mixing by molecular diffusion, τ_{mix} , is defined by Eq. 6.02 where r is the radius of the particle.

$$\tau_{\text{mix}} = \frac{r^2}{\pi^2 D_c} \quad (6.02)$$

According to Shiraiwa et al.³¹⁵, within the accumulation mode size range, defined in Chapter 1 ($D_p \approx 10^2$ nm), τ_{mix} can vary between microseconds to milliseconds for non-volatile organic species, seconds to years for semisolids to years for solids (Figure 6-2). Such a range in mixing times has resulted in kinetic rather than thermodynamic frameworks being used to model SOA formation due to the kinetic limitations to growth as well as evaporation arising from high particle viscosities.

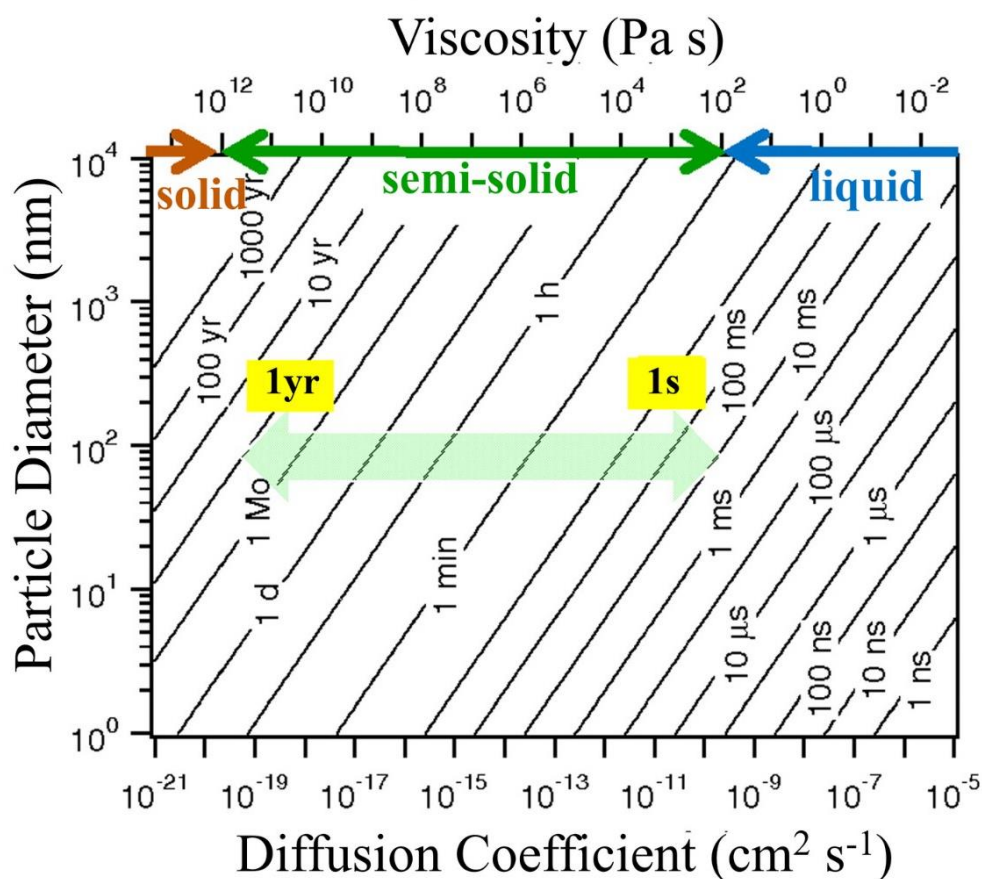


Figure 6-2: The characteristic time of mass-transport and mixing by molecular diffusion (τ_c) in particles of liquid, semisolid, and solid states can be expressed as a function of their diffusion coefficient and diameter. In the accumulation mode ($D_p \approx 10^2$ nm), semisolid particles exhibit a wide range of τ , spanning from seconds to years, as indicated by the light green arrow. **This image was taken from free access paper by Shiraiwa et al.**^{102,315}

6.1.1 The Impact of Particle Composition on the Viscosity of Aerosol Particles

Within this study and previous work, sucrose is selected as a proxy system for SOA particles found in the atmosphere and is used as a high viscosity compound. Comparatively, inorganic salts and acids, termed electrolytes have lower viscosities and have been known to partially or fully dissociate in liquid solutions, affecting the neutral organic compounds via the salting-out effect.^{316,317} Previously described in Chapter 4, the ‘salting-out’ effect can drive non-polar organics out of the mixed phase into the gas phase or an alternative organic-rich phase hence establishing liquid-liquid separation and a new equilibrium state.³¹⁸ The presence of electrolytes tends to increase polarity in the aqueous phase while

Chapter 6- The Measurement of Viscosity and Photoinduced Size Change in Aerosol Droplets Under Different Humidity Conditions

decreasing it in the organic phase.³¹⁹ This phase behaviour significantly influences the surface characteristics and morphology of the aerosols which in turn affects the organic compounds reactivity toward gas-phase oxidants.^{320,316,321,322} In 2017, Bateman et al. examined particles located in central Amazonia consisting of biogenic organic compounds, sulfates, and black carbon and found them to be in a non-liquid state where $\eta > 10^2$ Pa s at higher RH.³²³ Additionally, in laboratory studies, Power et al. 2013 showed specific example of a system where the viscosity of sucrose particles can be altered in the presence of sodium nitrate.³²¹ As the sodium nitrate content increased the viscosity of the sodium nitrate: sucrose mixtures decreased. Similarly, Rovelli et al. showed a decrease in the viscosity of sucrose particles upon adding the sodium nitrate or citric acid content.³²⁴ Song et al. demonstrated atmospherically relevant mixtures of sucrose and $\text{Mg}(\text{NO}_3)$ or $\text{Ca}(\text{NO}_3)$, which were used due to their presence in mineral dust and sea salt particles, had lower viscosities than binary sucrose mixtures.³²⁵ Consequently, over the last decade, several approaches have been used to measure the viscosity of individual particles and their compositions. For instance, rheometry techniques have been used to infer the viscosity of aerosols. However these bulk solution methods are unable to reach the supersaturated solute states that can be attained in aerosols.³⁰⁵ The bead mobility technique uses an external gas blowing to move melamine beads within a droplet. The movement and flow of these beads within the droplet is used to derive the viscosity using fluid bead dynamics. Bzdek et al. further developed the technique of using a coalescence event of two droplets which undergo shape oscillations at the droplet surface following controlled coalescence in the underdamped regime.¹²⁴ In the overdamped region, the timescale for slow merging particles (between seconds to days) can be used to calculate particle viscosity whereas oscillations are used in the underdamped region as discussed in Chapter 3. Reid et al. review provided a comprehensive analysis of the various methods used to derive particle viscosity.¹²⁸ A commonly used technique stated in this review was the poke and flow method.³¹⁴ Droplets are deposited on a hydrophobic substrate within a flow cell and poked with a sharp microneedle. The time it takes for the particle shape to relax from a half-torus geometry to a spherical cap morphology is monitored by optical microscopy. When compared to fluid dynamic simulations the droplet viscosity can be calculated.

6.1.2 Predicting Viscosity Using Mixing Models

Two viscosity modelling approaches are used in this work namely, AIOMFAC and the mixing binary model which incorporates the ZSR approach in order to predict the viscosity of mixed organic compound sucrose/inorganic salt or acid / H_2O at different weight percent mixtures. The AIOMFAC model accounts for the ion-organic interactions effects on activity coefficients using group contribution to derive viscosity, while the Bosse et al. mixing rule calculates viscosities using the subcooled pure component viscosities of each constituent of the mixture. The Zdanovskii-Stokes-Robinson (ZSR) approach determines viscosity using the water activity-dependent mixing of binary viscosity data and considers the interaction between mixture components.

6.1.2.1 AIOMFAC Viscosity Model

The Aerosol Inorganic-Organic Mixtures Functional Groups Activity Coefficients (AIOMFAC) model is a thermodynamic model used to predict the physical and chemical properties of atmospheric aerosols.³²⁶ It has been developed and tested in hundreds of experimental datasets to investigate the effects of aerosols on climate, air quality, and human health due to its accuracy.³¹⁶ Designed by Zünd et al. to simulate complex mixtures of inorganic and organic compounds, AIOMFAC is a group contribution model that describes the deviation of the activity of a substance in a mixture from its ideal behaviour (Raoult's law).³¹⁷ The non-ideality of mixtures has an impact on the gas-partitioning within an aerosol and affects the particle physical state resulting in the possible liquid-liquid phase separation.

The model considers the different functional groups present in the aerosol particles, including hydroxyl, carboxyl, carbonyl, and amine groups, and uses their chemical interactions with water and inorganic ions to calculate the activity coefficients of the aerosol components.³¹⁸ The AIOMFAC model offers the ability to predict the thermodynamic properties of aerosols, including their vapour pressure, solubility, and hygroscopicity. The model has been shown to accurately predict the behaviour of atmospheric aerosols under a wide range of environmental conditions from dilute to highly concentrated solutions in supersaturated conditions. Hence in this work it has been used to provide predictive estimates of mixture viscosity for sucrose/citric acid and sucrose/sodium nitrate across a range of relative humidities.

6.1.2.2 Mixing Binary Model

In the ZSR approach, using the example of a sucrose/citric acid/water mixture, the mass fraction of each solute was first calculated using Eq. 6.03 and Eq. 6.04 and the mass based hygroscopicity parameter [$\kappa_m(a_w)$] values were retrieved from Marsh et al.³²⁷

$$w_s = \left\{ 1 + \kappa_m \left[\frac{a_w}{(1 - a_w)} \right] \right\}^{-1} \quad (6.03)$$

$$\kappa_m(a_w) = \sum_i \varepsilon_i \kappa_{m,i}(a_w) \quad (6.04)$$

Where w_s is the total mass fraction of dry solutes in the particle, a_w , water activity of solution, ε_i describes mass fraction of the i th component in the dry particle and the hygroscopicity parameters is denoted κ_m . and $\kappa_{m,i}(a_w)$ denotes the mass weighted hygroscopicity parameter of the i th solute, with parameterized dependence on water content.

Using the ZSR equation (Eq. 6.05), the mass fraction of water can be derived for each binary mixture (sucrose/water, citric acid/water) and used to calculate the total mass of water in a system assumed to be ideally distributed between the two solutes (solute1 and 2). The water activity of the binary solutions

is then obtained using Eq. 6.03 and the “partial” viscosity $[\eta_i(a_w)]$ for each solute component calculated using a parameterisation of each binary mixture from model data. Overall, with the Arrhenius mixing rule, the viscosity of the ternary mixture can then be calculated using Eq. 6.06.

$$m_{H_2O} = m_{H_2O,1} + m_{H_2O,2} = \varepsilon_1 \times m_{H_2O} + \varepsilon_2 \times m_{H_2O} \quad (6.05)$$

$$\ln[\eta_i(a_w)] = \sum_i x_i \ln[\eta_i(a_w)] \quad (6.06)$$

Where m_{H_2O} is the mass fraction of water and x_i is the mole fraction of the i th component.

6.1.3 Aerosol Droplet Photochemical Reactions

Preliminary investigations of the relative humidity (i.e. viscosity) dependence of nitrate loss through photodegradation by UV light was explored in this work. Nitrate-laden aerosols are produced via the interaction of sea salt and mineral dust with nitric acid and nitrogen oxides in the atmosphere, alongside the release of anthropogenic NO_x resulting from the combustion of fossil fuels which are prevalent throughout the troposphere.^{328,329} K. Benedict observed nitrate photodegradation by light of $\lambda=302$ nm light in sodium nitrate droplets, with product yields dependent on droplet pH, nitrate concentration and the presence of a radical OH scavenger.³³⁰ The phototransformation of nitrate to its photoproducts influences the hygroscopic behaviour of particles, an important property in the growth of particles to form cloud droplets.^{331,332} The most stable photolysis products, nitrite (NO_2^-) and peroxyxynitrite ($ONOO^-$) shown in Figure 6-3, result in the formation of highly reactive oxidants, OH radicals and $O(^3P)$, both in gas phase photochemistry and environmentally relevant interfaces.^{333,334}

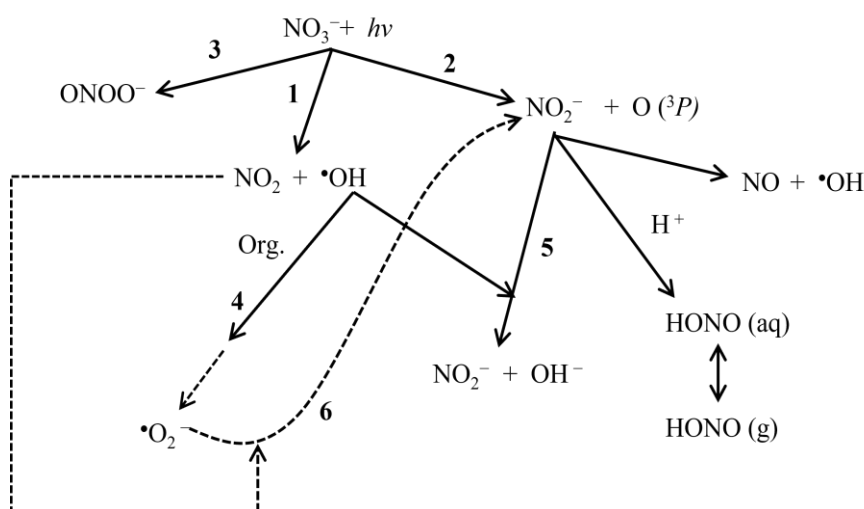


Figure 6-3: Relevant photochemical reactions of aqueous sodium nitrate which absorbs in the actinic wavelength $\lambda \sim 302$ nm, $\varepsilon = 6.2 \text{ M}^{-1} \text{ cm}^{-1}$.³³⁵ Pathway 1,2 and 4 denote photoproducts generated above $\lambda \sim 280$ nm and Pathway 3 denotes the photoproduct below $\lambda \sim 280$ nm in the bulk phase. Pathway 6 shows the secondary formation of nitrite via the reaction of NO_2 with $\bullet O_2^-$ indicated by the dashed lines. **This schematic is based on Figure 2 in K. Benedict et al, 2016.**³³⁶

Chapter 6- The Measurement of Viscosity and Photoinduced Size Change in Aerosol Droplets Under Different Humidity Conditions

The phase and reactivity of the nitrate ion has been found to be gas or particle phase dependent. Whereas in the gaseous phase, the structure of NO_3^- is planar and of D_{3h} symmetry, the lowering of its symmetry in the aqueous phase leads to absorbance at longer wavelengths due to the higher energy of the $\pi-\pi^*$ and $n-\pi^*$ transitions. It is proposed that diluted sodium nitrate solutions absorb at longer, more atmospherically relevant wavelengths ($\lambda > 290$ nm) leading to greater photoreactivity.^{329,332,333} Indeed, the phase of particles directly affects solar radiation absorption, light scattering and the activation of aerosol particles as cloud droplets.^{330,337}

A number of techniques have been employed to measure aerosol phase photochemical processes using contact free, wall-less techniques such as optical tweezers, electrodynamic balances³³⁸ and acoustic traps³³², each capable of isolating and levitating droplets over a range of sizes (< 30 μm). In previous studies, UV irradiation of nitrate droplets has been observed, for instance Seng et al.³³² used acoustic levitation to measure the impact of photo-irradiation on the deliquescence of nitrate particles. Using Raman spectroscopy to monitor the composition and size of the droplet over time revealed a higher than expected uptake of water by irradiated sodium nitrate particles in the atmosphere.³³² In this study, an EDB was used to monitor the size change of irradiated and non-irradiated sodium nitrate particles under different environment conditions.

6.2 Experimental

6.2.1 Holographic Optical tweezers (HOT)

To explore the viscosity of the water/sucrose/citric acid (CA) system (sucrose:CA= 60:40), aqueous droplets of diameter, D , $\sim 6\text{-}16$ μm were optically trapped using a holographic optical tweezers instrument (see Chapter 3). Droplets were generated with a medical nebuliser and then were captured in two optical traps, the relative positions of which were controllable. Air flow introduced into the custom-made stainless-steel trapping chamber contains a mixture of ultrapure dry and humidified (wet) nitrogen allowing the relative humidity within the trapping cell to be controlled and monitored using RH capacitance probes ($\text{RH} \pm 2$ %).³³⁹ Captured droplets were coalesced in a controllable manner by bringing one trapped droplet closer to the other. Upon coalescence, the image of the coalescing droplet was recorded by brightfield imaging with a high power LED.⁴⁰ The backscattered Raman light is imaged onto the slit of a spectrometer resulting in a Raman spectrum. The Raman spectrum consists of resonant structures known as whispering gallery modes superimposed onto an underlying Stokes band from which the radius and refractive index can be calculated to accuracies of ± 2 nm and ± 0.0005 , respectively.

In the underdamped regime, which tends to be at lower viscosities (high RH), when two droplets are trapped and coalesced, the composite droplet undergoes a series of oscillating shape distortions when resuming its spherical shape, i.e., tending to a droplet aspect ratio of 1, driven by the capillary forces minimising the surface energy. The coalesce process is usually monitored using the elastically backscattered light (EBL) directed to a photodiode connected to an oscilloscope. In the overdamped

Chapter 6- The Measurement of Viscosity and Photoinduced Size Change in Aerosol Droplets Under Different Humidity Conditions

regime, typically at higher viscosities (low RH), coalescence proceeds through a slow merging of two droplets from initially a dumbbell shape to a spherical droplet. This process occurs over longer timeframes (hundreds of milliseconds to hours) and is monitored using brightfield imaging¹⁶⁶. Summarised in Chapter 3, Section 3.1 and Section 3.2 but briefly explained here, in the underdamped region viscosity can be calculated using Eq. 6.07, whereas within the overdamped region viscosity is obtained using Eq. 6.08,

$$\tau_l = \frac{r^2 \rho}{(l-1)(2l+1)\eta} \quad (6.07)$$

$$\tau_l = \frac{2(2l^2 + 4l + 3) \eta r}{l(l+2)(2l+1) \sigma} \approx \frac{\eta r}{\sigma} \quad (6.08)$$

where l corresponds to the mode of deformation, a corresponds to the radius of the coalesced droplet, ρ is the density of the particle and η is the viscosity.

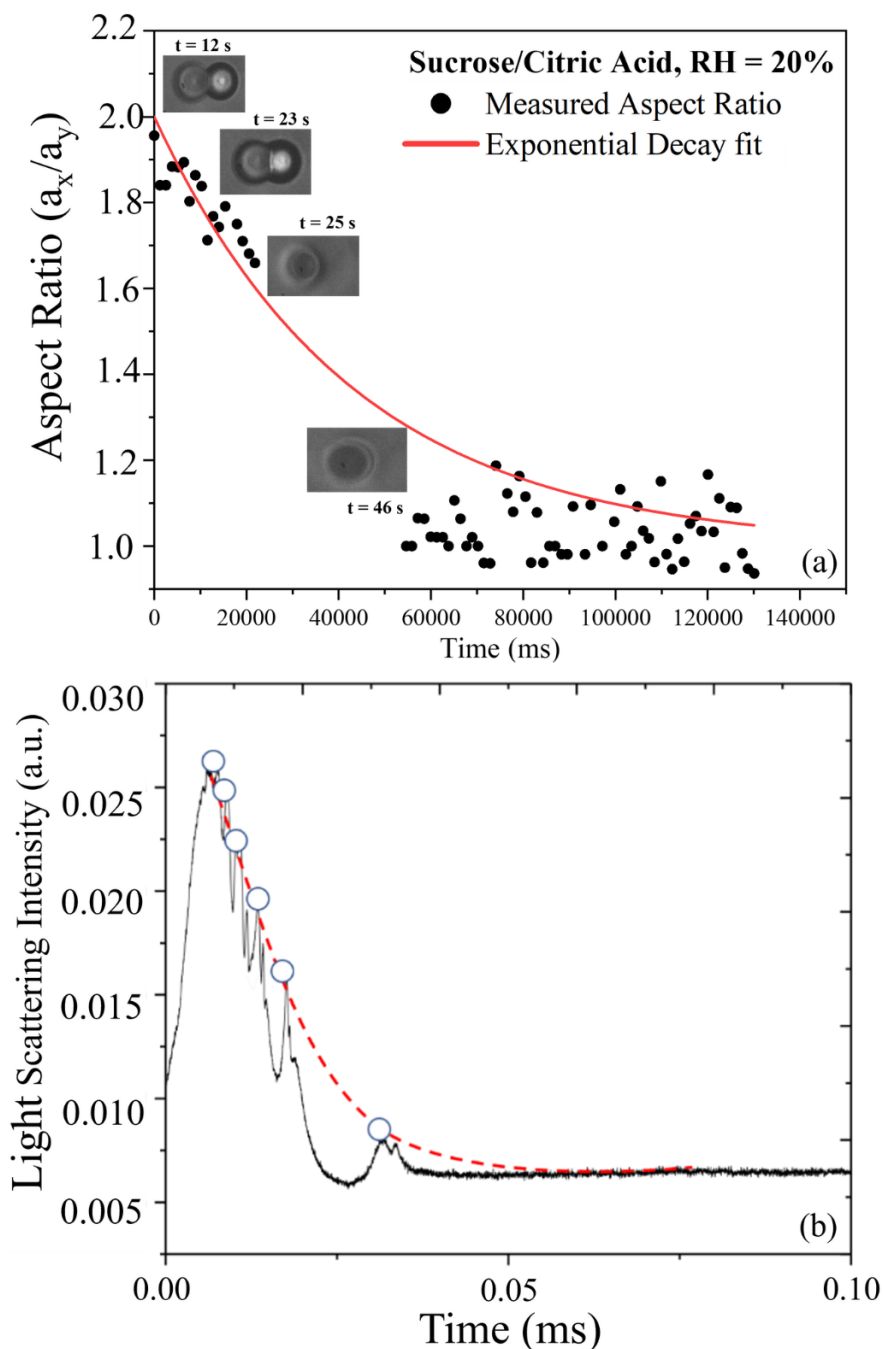


Figure 6-4: Calculation of viscosity using (a) aspect ratios corresponding to brightfield imaging of two coalescing droplets of sucrose: citric acid 60:40 wt% mixture at RH 20 %, and (b) the elastically backscattered light collected during the coalescence event of sucrose/ citric acid 60 60:40 wt% mixture at RH > 70 %.

6.2.2 Electrodynamic Balance

To collect preliminary photochemistry measurements, a modified electrodynamic balance (EDB) was used. This instrument, described in Chapter 3, allows trapping of charged droplets 5 – 30 μm radius in an electric field under controlled environmental conditions. The vertically positioned dual electrode configuration, grounded with copper, produces both an AC voltage between 0 and 1000 V and DC voltage with a maximum range of -80 to $+80$ V to stably confine droplets. Application of an AC voltage

Chapter 6- The Measurement of Viscosity and Photoinduced Size Change in Aerosol Droplets Under Different Humidity Conditions

across the concentric cylindrical electrodes creates an electric potential well within which a charged droplet is trapped. This voltage enables restorative forces to re-centre the confined droplet following lateral displacement. Additionally, the force of gravity can lead to a net downward displacement in which the DC voltage is able to counteract along the vertical axis of the trapped droplet.

The EDB allows highly reproducible measurements of droplet size from illumination by a laser of $\lambda=532$ nm laser and droplet mass from the DC offset adjustments. The particle phase state and radius are characterised by the laser elastic light scatter pattern and the geometric optics approach thus aerosol kinetics and nucleation can be studied.

The droplet is illuminated by a 532 nm continuous wave, green Laser Quantum Ventus CW diode laser operating at a maximum of 50 mW. Angularly resolved elastic scattering is collected in the near forward scattering direction by a CCD camera positioned in the trapping plane at a 45° angle to the levitated droplet to avoid back scattered light. The droplet's vertical position is monitored by a CCD camera positioned at 90° to the trapped droplet and collects light at a given angle. The droplet radius r is estimated from the angular separation, $\Delta\theta$, between the phase function fringes taken across a linear profile of the camera image using iterative fitting and Eq. 6.9:

$$r = \frac{\lambda}{\Delta\theta} \left(\cos\left(\frac{\theta}{2}\right) + \frac{n \sin\left(\frac{\theta}{2}\right)}{\sqrt{1 + n^2 - 2n \cos\left(\frac{\theta}{2}\right)}} \right) \quad (6.9)$$

where θ is the central viewing angle, n is the droplet refractive index and λ is the laser wavelength. The ability to estimate the radius in real-time using this approximation is advantageous. The accuracy of the approximated radius has previously been shown to be ± 100 nm.¹⁷⁵

For the photochemistry experiments, an aqueous sodium nitrate droplet was equilibrated to a selected relative humidity (80, 60, or 30 %) over seconds to hours. The equilibrated droplet was then irradiated continuously with light from a broadband UV Fibre Optic light source (with a wavelength range of 200 – 600 nm, Figure 6(c)) for 9 – 15 hrs hours to drive photochemistry, leading to changes in droplet size that were recorded over time. As a separate control experiment, equilibrated droplets were also held in the dark without illumination for the same period of time.

6.3 Results and Discussion

6.3.1 Measurement of Viscosity Under Different Environmental Conditions and Mass Ratios

Here the viscosity of aqueous- organic and -inorganic aerosol droplets were measured extending over an RH range from ~5 % to 90 %. A HOT was used to levitate two particles and manipulate their positions relative to one another to initiate droplet coalescence at 293 K. From the merging of these particles, the viscosity can be calculated under two regimes.

6.3.1.1 Comparison of inorganic-organic mixtures at different wt% ratios

Despite the abundance of inorganic species in the atmosphere, few studies have reported inorganic-organic mixed compounds covering a range of RH. The viscosities for aqueous sucrose/sodium nitrate droplets at the wt% ratios of 80/20 and 60/40 are reported in Figure 6-4. The viscosity data were binned into 15 % RH bins, and each average data point reports the average and standard deviation of 2-3 data points. The uncertainties present in the x- (RH) and y-axes (log viscosity) are the calculated standard deviations of each bin. The error observed in the viscosity in this study is an order of magnitude larger than those found in the literature for the same systems.³⁴⁰ A possible explanation for the increased uncertainty could be the small number of measurements per bin which in future studies will be increased.

As expected, lowering RH results, increases the viscosity of the droplet, with the values for mixtures sitting between those of binary aqueous sucrose and sodium nitrate, previously reported by Song et al. and Rovelli et al.^{166,324} Figure 6-5(a) compares the data collected in this study to previous data collected by Song et al. in 2016 and overall there is a very good agreement at both wt% ratios (< 1 order of magnitude difference). The viscosities obtained for the 60/40 wt% mixture was slightly lower than those for the 80/20 wt%, varying from 10^{-2} to 10^6 Pa s from ~86% to 31 % RH. The 80/20 wt% mixture particle varied from 10^{-2} to 10^5 Pa s. The semi-solid phase state ($\sim 10^2$ to $\sim 10^{12}$ Pa s) in 80/20 wt% ratio is reached at an RH 15% higher than in the 60/40 wt% ratio. This observed distinction can be attributed to a higher mass fraction of water which acts as a plasticiser in the mixture in the 60/40 wt% ratio than the 80/20 wt%, as shown in Figure 6-6 (RH and water activity are proportional).

Figure 6-5(b) shows the AIOMFAC and mixing binary models used to predict the mixture of sucrose/sodium nitrate. The difference observed between AIOMFAC model, and the measurement data can be attributed to inability to accurately represent sucrose within the model. As AIOMFAC does not feature sucrose as listed compound, sucrose had to be constructed using its subgroups (for example C(OH), CH₂(OH)) without the ability to include the ringed connectivity. The AIOMFAC binary sucrose was an order of magnitude lower than the measurement data which could explain the poor agreement between the mixture measurement data and the model. The mixing binary model shows excellent agreement between the model and measured data for both mass ratios and would be the more appropriate model to predict the viscosity of sucrose/sodium nitrate/H₂O mixtures.

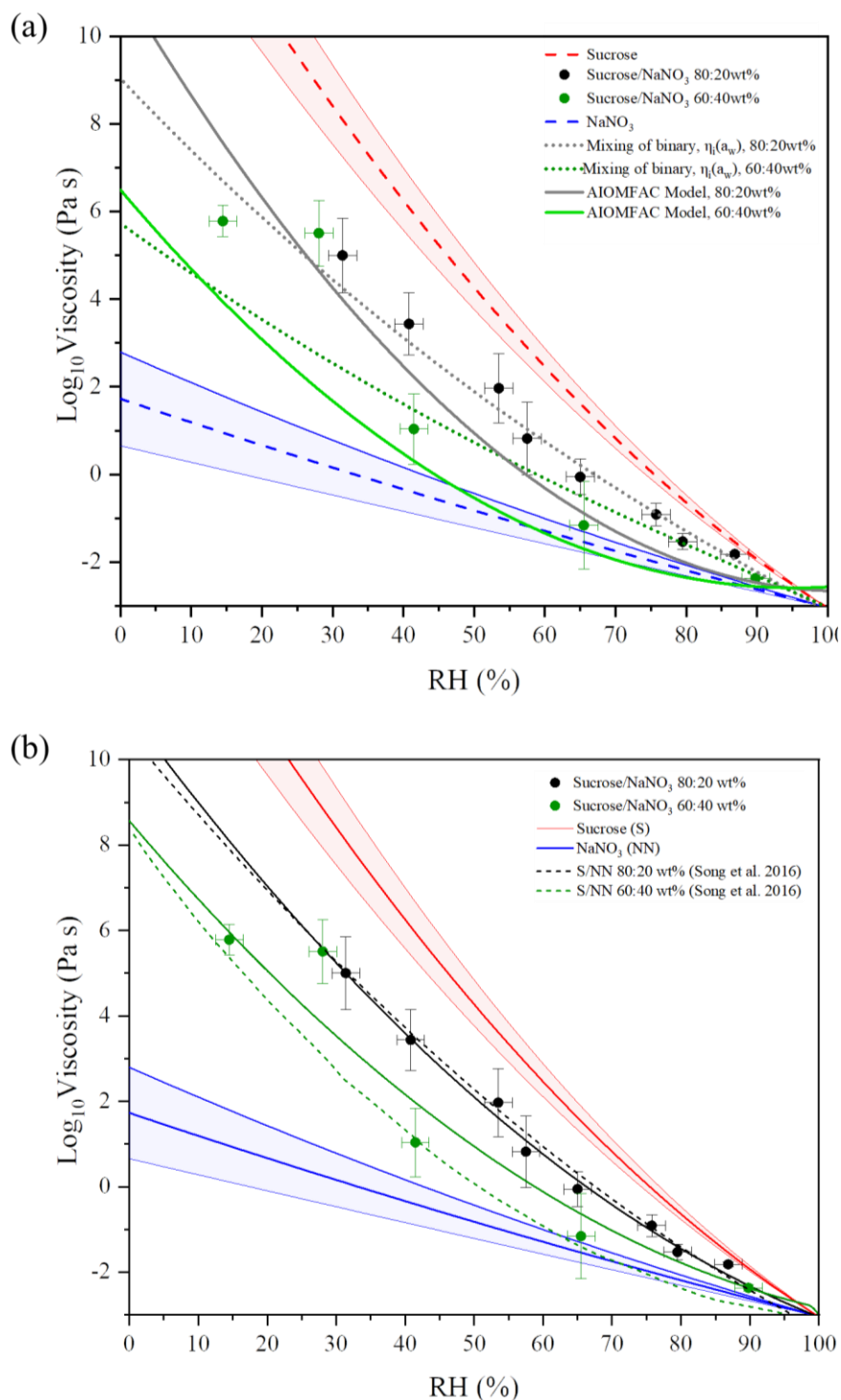


Figure 6-5: Measured and modelled relative humidity dependent viscosity of sucrose/sodium nitrate mixture shown (a) at 80/20 wt % (black symbols) fitted to a polynomial line (solid black line) and 60/40 wt %³²⁷ (solid green symbols) fitted to a polynomial line (green line), and literature data collected by Song et al shown by the dotted lines and (b) showing the AIOMFAC model fit (solid line) and the prediction of mixing binary viscosity value (dotted line) fitted using the sucrose/sodium nitrate mass ratios of 80/20 wt% and 60/40 wt%. Data for binary sucrose and sodium nitrate was collected from Song et al. polynomial fit.³⁴¹

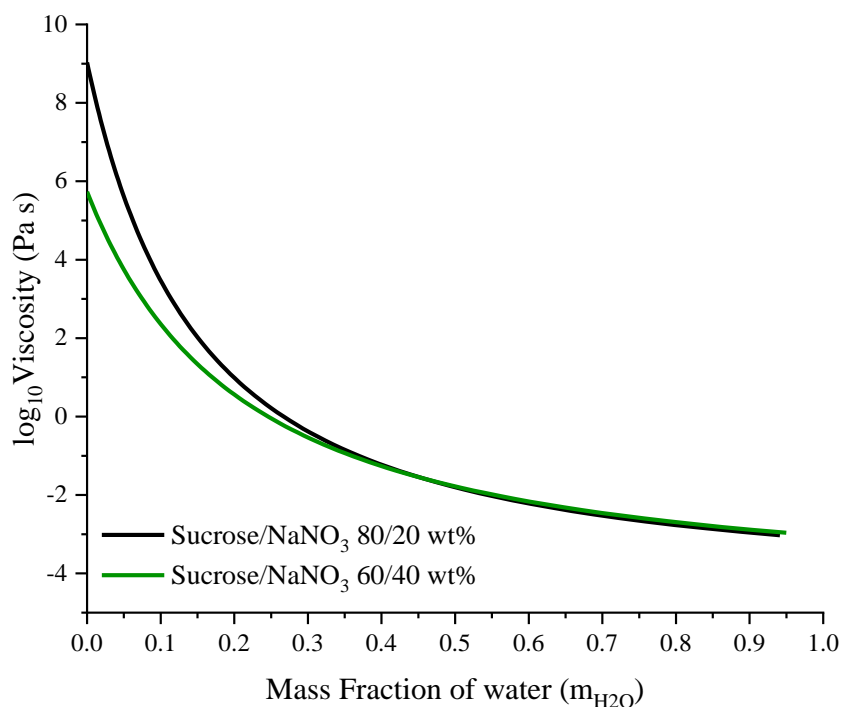


Figure 6-6: The $\log(\text{viscosity})$ plotted against the mass fraction of water and water activity for the ternary sucrose/sodium nitrate mixtures at 80/20 wt % and 60/40 wt%. As the mass fraction of water decreases the viscosity of solution increases.

6.3.1.2 Organic acid-organic compounds mixtures.

Figure 6-7(a) shows the viscosity of an atmospherically relevant organic system. The ternary mixture of sucrose/citric acid/water was investigated at a 60/40 wt% ratio. Lower uncertainties typically at ± 1 Pa s were observed in the viscosity data (c), which is more consistent with data from Rovelli et al.³²⁴ The viscosities of the mixture ranged from $\sim 10^{-1}$ to $\sim 10^9$ Pa s at $\sim 86\% < RH < 3\%$. At RH 3%, the coalescence monitored by brightfield imaging took place over 3 – 4 days before the droplet fell out of the trap hence the time point at which this happened was taken based on the limited coalescence that occurred during the long measurement time window. Droplets with viscosities between $\sim 10^{-3}$ to $\sim 10^2$ Pa s at $RH > \sim 50\%$ were in the liquid phase, viscosities in the range of $\sim 10^2$ to $\sim 10^{12}$ Pa s between $\sim 20\% < RH < 50\%$, droplets were in a semi solid state that shows a relationship between increasing citric acid content and the lowering of viscosity below that of sucrose. Not only does water act as a plasticizer, citric acid which is a lower viscosity component can also act as a plasticizer for the organic matrix.¹⁶⁶

Figure 6-7(b) shows poor agreement between the AIOMFAC model at low RH with a difference of 1 – 2 orders of magnitude however, at high RH better agreement can be observed. The mixing binary model shows a better fit than AIOMFAC to the sucrose/citric acid/H₂O mixture measurement however

there is an over prediction at low RH and under prediction at high RH. Overall, the mixing binary model appears to be the most appropriate model to use for ternary solutions as it represents the measurement data closely possibly accounting for solute-solvent interactions.

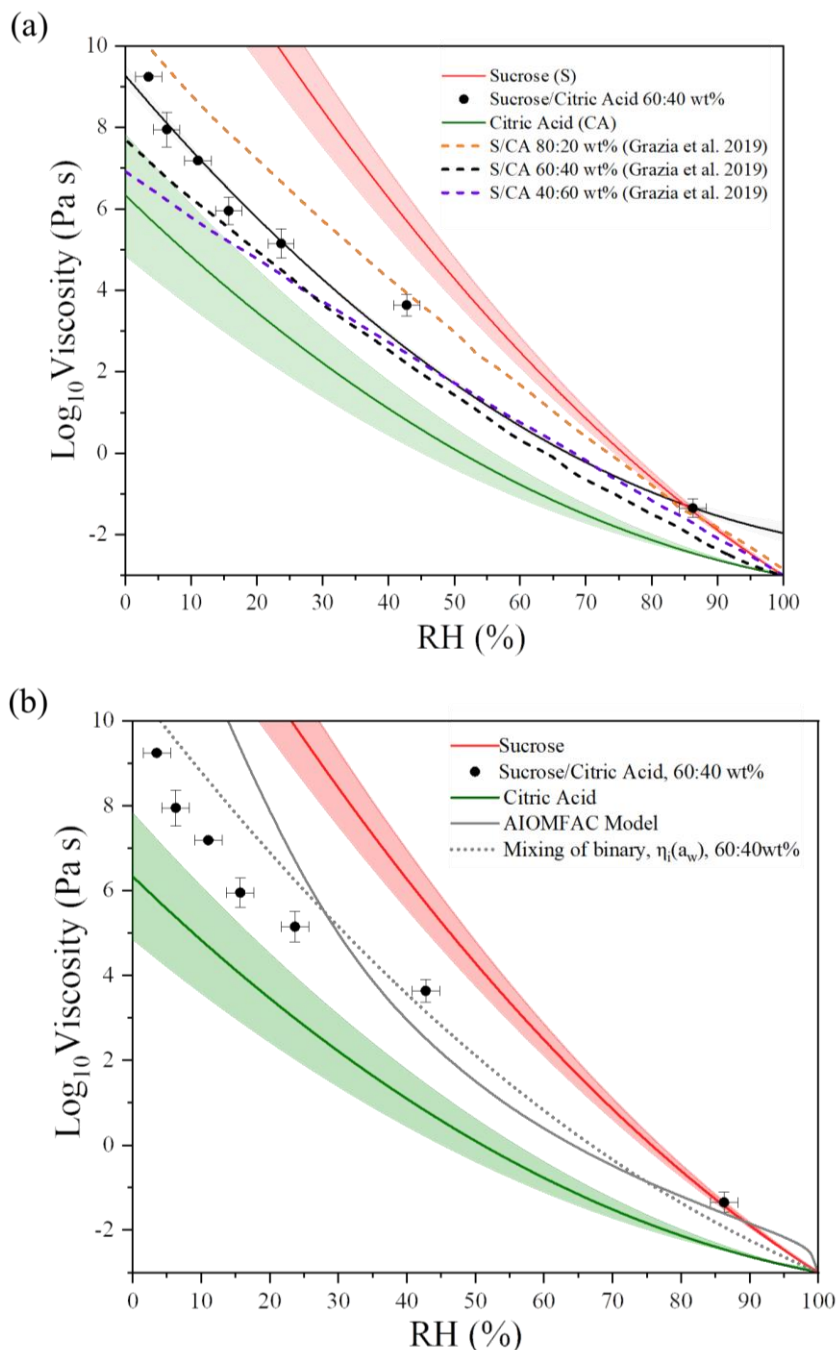


Figure 6-7: Measured and modelled relative humidity dependent viscosity of sucrose/citric acid mixtures shown (a) 60/40 wt % (black symbols) fitted to a polynomial line (black solid line), and literature data collected by Rovelli et al. shown by the dotted lines for mass ratios of 80/20, 60/40 and 40/60 wt% and (b) showing the AIOMFAC model fit (solid line) and the prediction of mixing binary viscosity value (dotted line) fitted using the sucrose/citric acid mass ratios of 60/40 wt%. Data for binary sucrose and citric acid was collected from Y.C. Song et al. and Rovelli et al. polynomial fitted data.^{324,325}

Viscosity is a property that plays a crucial role in determining the kinetics of chemical reactions taking place within it. In aerosol photochemistry, high viscosity leads to a reduction in the effective collision frequency of reactants and, thus, reaction rate is slowed. Additionally, the prolonged residence time of reactants in the droplet due to the high viscosity may cause a shift in the reaction pathway or equilibrium, leading to a different production and distribution of products. Therefore, the viscosity of an aerosol droplet acts as a critical determinant of the photochemical reaction kinetics.

6.3.2 Observations of Levitated Sodium Nitrate Droplet Size Changes Upon UV Illumination

To begin examining preliminary measurements of aerosol photochemistry, a series of sodium nitrate droplets were levitated and exposed to a UV light ($\lambda \sim 200 - 600$ nm) in the EDB at various RH values. Single droplets were equilibrated to one of three RH values, held within the trap (over time periods of 9 – 15 hours) and subsequently exposed to UV light or no UV light in order to ensure size change was a result of illumination. Within the EDB the droplet is constantly rotating upon its axes resulting in an even distribution of unidirectional UV light on the droplet even if the droplet is highly viscous. The droplets were equilibrated to the RH values of 80 %, 60 % and 30 %, corresponding to solute concentrations of 5.1, 10.9 and 15.6 M. The viscosity increased three orders of magnitude between 80 – 30 RH %, whereby at 80 % RH the droplet viscosity was close to that of water (10^{-3} Pa s) and at 30 % RH the droplet viscosity was close to that of honey (10^0 Pa s). Upon UV irradiation, Figure 6-3, shows nitrate is converted to nitrite which is converted into the highly volatile nitrous acid (HONO). In light of this reaction, a loss of HONO from the levitated aqueous sodium nitrate droplets is predicted along with a droplet size change. Within the EDB the droplet is constantly rotating upon its axes meaning continual stirring of the levitated droplet which could aid the removal of the gaseous products from the photolysis and result in the reduction in droplet radius observed in Figure 6-7.

The 30 % RH was used in this work therefore it is important to consider the efflorescence RH (ERH) and deliquescence RH (DRH) to ensure the droplet size is not a result of crystallisation. According to Gregson et al. the efflorescence RH (ERH) for sodium nitrate has been observed between 0.05 – 40%.³⁴² The ERH reported by Ghorai and Tavanki³⁴³ sits in between this range at RH 35 % measured by X-ray spectromicroscopy whereas the ERH was observed as a range by Lee et al. between 18 to 45 % RH with some droplets not appearing to undergo a crystallisation process at all.³⁴² The observed variability in the ERH values reported in the literature can be attributed to the fact that crystallisation of sodium nitrate particles is kinetically limited. It is the particle viscosity which hinders the formation of crystals in the inorganic salt. By measuring evaporation at 30 % RH, one might expect crystallisation to occur with and without the UV light, but this was not the case. From Figure 6-7(c), no crystallization is observed at RH 30 % with or without the UV light consistent with published studies on this system. If crystallisation were to occur the droplet would no longer be optically homogenous, the light and dark

Chapter 6- The Measurement of Viscosity and Photoinduced Size Change in Aerosol Droplets Under Different Humidity Conditions

fringes would become inconsistent and therefore the droplet size could not be calculated. At RH 30 %, the droplet has the highest nitrate concentration of all the measurements and the greatest change in droplet radius. Assuming density remains the same the radius change can be associated with a droplet mass loss. Roca et al.³³³ supports an increase in the initial nitrate concentration leads to an increase in nitrite concentration, whereas Benedict and co-workers an increase in nitrate concentration leads to a decrease in nitrite production.³³⁶ Additionally, a change in the droplet radius was also observed at 60 % RH in measurements taken with the UV light on compared to when the UV light source was off.

The impact of UV light and higher concentration on droplet size is noticeable at 30 % and 60 % RH. However, there is little to no change in droplet size is observed at 80 % RH. Further investigation is required to fully understand these observations. Compositional measurements using a Raman spectrometer incorporated into an EDB would need to be conducted in order to observe what loss from the droplet is driving the droplet size change it is possible nitrate could be lost itself. In their study, Dou et al.¹⁰⁶ reported observing a significant reduction in droplet mass following irradiation of iron (III) citrate complexes at similar timescales as those used in this study. To measure the extent of this mass loss an EDB was employed by Dou et al., and the results revealed an 80% reduction in particle mass due to photochemical degradation. Moreover, this reduction in mass and compositional change was found to be accelerated during the period of irradiation. Similarly, in this work at RH 30 %, smaller droplets (8 – 10 μ m) are irradiated compared to at a RH 80% (10 – 20 μ m), this may result in a different particle-light coupling and an acceleration in radial loss.

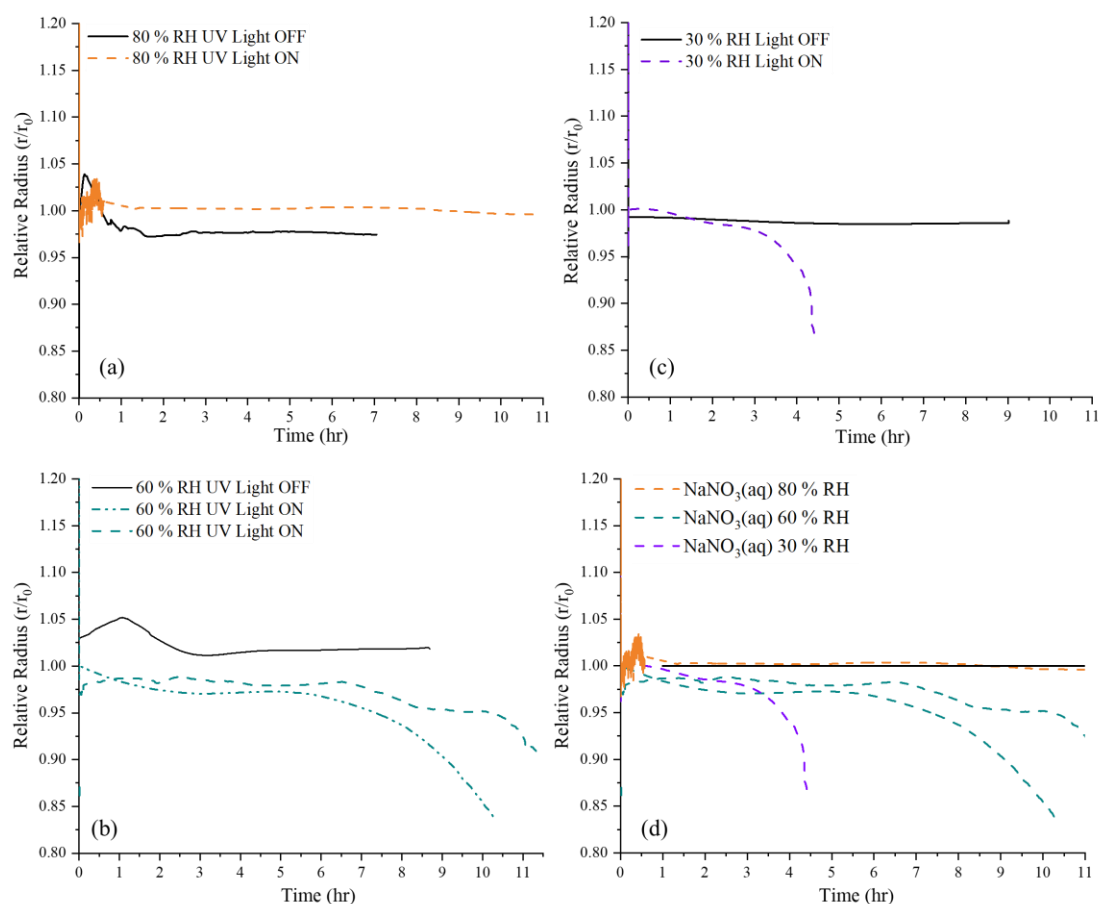


Figure 6-8: The evaporation of a droplet under the RH (a) 80%, $C=6.1$ M, $\eta\sim 10^{-2.19}$ (b) 60 %, $C=10.9$ M, $\eta\sim 10^{-1.29}$ (c) 30 % $C=16.5$ M, $\eta\sim 10^{0.16}$ with the UV-VIS light *on* and *off* shown as relative radius against time (d) comparison of the evaporation profiles under the different RH conditions. While the UV light was switched on the droplet radius appeared decrease substantially at RH 60 and 30%.

6.4 Conclusion and Future Work

To conclude, the viscosity of mixed component solutions was explored under different environmental conditions. Measurements of a two-particle coagulation event and the subsequent coalescence relaxation times were used to infer the viscosity of the ternary mixture sucrose/citric acid/H₂O and sucrose/sodium nitrate/H₂O under high and low RH. The results indicate that upon adding CA to sucrose, the viscosity of the droplet decreases by two orders of magnitude at 60/40 wt %. Moreover, the viscosity of sucrose is lowered in the presence of sodium nitrate across the span of RH values used in this work. Measured viscosities agreed closely with previous studies conducted by Y.C. Song et al., Marsh et al. and Rovelli et al. where viscosities were shown to span orders of magnitude 10^{-3} to 10^9 Pa s.^{166,327,324} The mixing of the binary water activity-dependent viscosities and the AIOMFAC model were used to predict the ternary mixed solutions in this work. Both were found to agree reasonably well with the measurement data, although the mixing of the binary water activity-dependent viscosities method was found to be more accurate than the AIOMFAC model.

Chapter 6- The Measurement of Viscosity and Photoinduced Size Change in Aerosol Droplets Under Different Humidity Conditions

In the future, there will be an expansion of the ternary mixtures measured, namely aqueous butanediol/sucrose and butanediol/citric acid systems over a range of different weight percentage ratios (80/20, 60/40, 40/60 and 20/80 wt %). Additionally, further work to compare the viscosities measured in laboratory using proxies with the viscosity of extracts collected during a field measurement would validate the use of compounds used in this study.

Nitrate containing aerosols are abundant in the atmosphere. The role played by nitrate is known within the atmospheric nitrogen cycle, but quantitative understandings about the role of aerosol photochemistry in the nitrogen cycle are poor due to the lack of detailed studies in aerosol phase. This work investigated the interaction of NaNO_3 droplets with a UV-Vis light source. The data collected here show a significant droplet radial decrease when exposed to UV light radiation at lower relative humidities, thus, as the concentration and viscosity of the droplet increases by two orders of magnitude from 80 to 30 % RH. For example, the diffusional mixing time in a 30 μm sodium nitrate droplet increases by two orders of magnitude and the viscosity is also increased by two orders magnitude. Understanding particle-light interactions and the properties that affect the production of products remains important to improving future climate modelling of the atmosphere. Further development to build upon the preliminary data collected is needed to gain additional compositional spectral information on the photochemical reaction in an aqueous nitrate droplet and beyond.

Further work would include resolving the size change during the photochemical reaction using an EDB where a Raman spectrometer is incorporated into the system. This will allow for a quantitative measurement of the evolving droplet composition during periods of illumination and for the reaction rate to be determined. Combining this with investigation into the effect of viscosity on sodium nitrate photolysis could provide valuable insight into the oxidant products that may be present in the atmosphere in different environmental conditions.³³⁶ To further expand this and to account for the role of the particle-air interface, surfactants could also be incorporated into the levitated aerosol droplets at increasing concentration below and above their CMC.

Chapter 7

Summary, Conclusions, and Future work

7.1 Summary of Findings

Aerosols have a direct and indirect effect on the Earth's radiative budget, but their impact remains one of the most significant uncertainties when accounting for the anthropogenic contribution to global climate change. This thesis is centred on enhancing our understanding of the indirect effect of aerosols by studying their microphysical properties, which influence their growth into cloud droplets. The body of work presented here encompasses various techniques and analytical methods that were employed to determine these crucial properties. A range of techniques, the droplet oscillation method, maximum bubble pressure tensiometer (MBT) and Wilhelmy plate, were presented in this work to measure the surface tension of atmospherically relevant mixtures over a range of time scales. This underpins future understanding and predictions of cloud droplet growth. To investigate the change in viscosity with relative humidity, a holographic optical tweezer method was used, and an electrodynamic balance was used to measure a change in droplet radius as a result of irradiation by UV light in different ambient conditions. Finally, discussion delved into methodologies for decolonising the curriculum and STEM environment, advocating for its essential integration into the EPSRC Centre for Doctoral Training in Aerosol Science program. This approach seeks to enhance the self-awareness and global consciousness of prospective PhD students improving their ability to conduct inclusive research. The objective is to equip early-career aerosol researchers with the skills to contextualise their scientific findings and reflect these findings in their thesis.

7.2 Conclusions

7.2.1 Addressing Aerosol Science research, Curriculum, and Culture

Chapter 2 proposes a novel approach to train university students to discuss and consider the socioeconomic, political, and social implications of a scientific research, with a specific focus on the field of aerosol science. Using a decolonial perspective, the chapter delves into the root causes of structural inequalities that exist within science and suggests ways to dismantle these structures by encouraging critical thinking among early researchers. The potential benefit of this approach is summarised below through the initiative founded based on the ideas stated in Chapter 2. These examples highlight the potential to cultivate a more inclusive and diverse aerosol science community not only in terms of the curriculum but also in the culture and environment fostered within the community.

7.2.1.1 The Creative Tuition Collective Initiative

Creative Tuition Collective (CTC) is a non-profit organisation based in Bristol that delivers tuition educational opportunities and life skills development for young people (ages of 13-18) from lower income backgrounds. CTC was established on a decolonial foundation, by seeking to dismantle the structural such as the accessibility of STEM and the lack of science capital that impedes individuals from marginalised backgrounds from attaining success in science, technology, engineering, and mathematics.

Two of the key outreach programs adopted by Creative Tuition; Learning Laboratory Skills (LLS) program, was adopted in 2022 to provide opportunities for 16-19-year-old college, Applied Sciences students to gain exposure to a university lab and conduct experiments using equipment they may not have had access to before. The program has been successful in providing a stimulating learning environment that encourages students to envision themselves as scientists and innovators within a university context. After each laboratory session, there is a lecture given to address the impacts of science on society and society on science. For example, in session one on the Extraction of Caffeine, the lecture focuses on the exploitation of land and deforestation caused by the coffee industry alongside the environmentally unfriendly process of caffeine extraction. Session 2 enables the students to do a DNA extraction experiment in the Biomedical teaching labs whereby they were able to use techniques such as gel electrophoresis, the proposed lecture following focused on the story of Henrietta Lacks and her stolen HeLa cells. The final session, session three, examines the structural integrity of buildings in an earthquake demonstration; the lecture subsequent to this laboratory experience focusses on decolonising engineering and the benefits of this action on creating a safer society.

The second initiative is the core school program where university students deliver science experiments and mental wellbeing sessions to young people from the ages of 11-16. As discussed in Chapter 2, the Inspirational Scientists Board project stemmed from the aspiration to introduce greater diversity into the university environment. This initiative was conceived on the premise that colonialism has systematically marginalised voices from various ethnic backgrounds within the field of scientific history.³⁴⁴ The core school program was inspired from the Inspirational Scientists Board project and the idea to increase representative figures students see who are within the STEM field.

Creative Tuition has since impacted over 3,000 school and university students and university academics working to centre decolonising knowledge and practices within the STEM space.

7.2.2 Surface tension measurements

In order to address the current limitations in our understanding of the impact of aerosols on the climate, an investigation into surface tension was conducted, utilizing both droplet and bulk aqueous phase measurements. Surface tension plays a crucial role in the ability of aerosol particles to uptake water and grow into cloud condensation nuclei, making it essential in the mechanism that impacts the indirect

effect. The composition of droplets is a critical factor in determining their surface tension, and therefore, this thesis examined various compositions to enhance our understanding and modelling of aerosols' impact on the climate.

Chapter 4 delved into a comprehensive study of the surface tension of inorganic and organic aqueous binary and ternary mixtures. To measure the surface tension of liquid particles, the droplet oscillation method was employed, where droplet oscillations were analysed over a user-controlled delay time, aided by brightfield imaging to capture droplet trajectory, and facilitate accurate measurement of droplet size and aspect ratio. The measured droplet data were then compared to bulk phase measurements obtained from the MBT to ensure the validity of the determined surface tension. Statistical thermodynamic and semi-empirical models were used to predict the degree of surface tension depression with an increase in solution concentration of binary and ternary inorganic and organic mixtures and compared to measurement data. The results showed good agreement, particularly for ternary mixtures of inorganic and organic mixtures, with some discrepancies that require further investigation.

A study of dynamic and equilibrium surface tension can be found in Chapter 5, where three different techniques were employed to investigate the properties of surfactant solutions. A novel analytical method enabled measurement of the dynamic surface tension of microscopic droplets on microscopic timescales, providing key information about the early stages of surfactant diffusion and adsorption to a fresh interface. Additionally, bulk measurements were used to determine the dynamic surface tension on millisecond timescales, enabling quantification of surfactant short-time and long-time diffusion coefficients. The Wilhelmy plate was also employed to determine key parameters of each surfactant such as maximum surface excess concentration, area per molecule, CMC, and the ratio of kinetic constants through application of the Langmuir and Frumkin isotherm to the data. This provided detail on their surface activity and ability to reduce surface tension at low concentrations. When compared to atmospheric aerosols some of the surfactants analysed in this study were shown to act as good proxies for future work.

7.2.3 Viscosity and Photochemistry Related measurements

Chapter 6 presents a study on the optical tweezing of inorganic-organic and organic-organic mixtures, examining the droplet viscosity under varying ambient conditions. The optical tweezers technique enabled controlled coalescence of two droplets to measure the droplet viscosity with relatively high precision. The results were compared with literature data and found to be in good agreement. Additionally, the chapter introduces a newly developed technique, to investigate the size change of irradiated sodium nitrate droplets, providing preliminary data for future exploration into the properties that limit droplet photochemical reactions.

7.3 Future Directions

Future work to expand aerosol science research taking a decolonial perspective and inclusive approach, sees the creation of multi-stage project involving key stakeholders such as school students, university academics and charitable organisations in the green sector.

7.3.1 CTC Aerosol Project Proposal with a Decolonial Approach

In order to foster global diversity in aerosol science, it is crucial for the aerosol community to invest in public engagement as the CDT curriculum recognises. However, there is still room within the CDT training program to improve opportunities for students from marginalized backgrounds to see themselves as aerosol scientists in a university setting, much like the LLS program. To showcase how adapt the public engagement training to include a more decolonial approach, a multi-year CTC research project has been designed as an example. The CTC research project would include school students from marginalised backgrounds, between 14 – 17 years old, in partnering schools in the UK and Ghana with the participation of postgraduates from the CDT aerosol program and teachers. The project would engage young people in aerosol science education, research and developing achievable, positive outcomes for reducing the indoor or outdoor air pollution in the schools. Jenkins et al. have also employed a similar project, as described in Section 2.4.1.

The CTC research project outline for year one includes:

1. Forming a research group in year 1 by pairing students from year 9 (13 – 14yo), year 12 (16 – 17yo), and CDT program students. Meetings will be conducted in person for UK students and online for Ghanian students.
2. To account for the impact of this work outside of the aerosol community such as in education and social sciences will be engaged.
3. Conducting training workshops led by the CDT student on aerosols and their impact on society, for school students.
4. Visiting university laboratories to observe advanced equipment and instruments.
5. Collaborating on designing a project to measure indoor or outdoor air quality and intended outcomes.
6. Employing a mobile PM 2.5 and PM 10 device, such as HabitatMap, for measurements in and around the school and university for comparison.
7. Analysing the data with the CDT students to identify the most effective way of disseminating knowledge gained from the project.
8. Discussing potential mitigations with the school based on the measurement results, to enable action-based consequences.
9. Creating infographics, presentations, and art to communicate the information learned throughout the process in the UK (with partnering Ghanian school).

The contributory citizen science project challenges the notion of who can contribute meaningful knowledge to the scientific community and includes unheard voices. Citizen science has increased greatly over recent years due to the use of the internet, smartphones and increased public interest. It is used as a tool to increase public knowledge and increase data collection in different areas. An example of where contributory citizen science has worked is the Dutch iSPEX Project.³⁴⁵ The project enabled the public to collect aerosol measurements, such as the spectrum and polarisation of scattered sunlight at their location using their smartphones and a small add-on to their camera.³⁴⁵ Together with a dedicated iSPEX app, volunteers were able to take single measurements on specific days in groups or individually with pictures submitted to the central database. One measurement provided low accuracy data, however a combination of measurements within the same area improved the accuracy of the data that could be used by researchers. This example shows that this form of study can be successful in engaging the public in aerosol scientific research and improving their knowledge of the science underpinning the research itself.³⁴⁵ Projects like these can serve as valuable lessons for the future of aerosol research and has informed the direction of future work leading on from this these.

The research presented in this thesis has the potential to expand future work in atmospheric aerosol chemistry. The original focus of this study was to develop an understanding of how aerosol photochemical reactions are affected by properties such as viscosity and surface tension. To further this research, future experiments could involve the development of a holographic optical tweezer with an embedded UV light source, allowing for the investigation of viscosity, surface tension, and temporal evolution of photochemical reactions in coalesced particles. Using photoactive compositions such as sucrose and sodium nitrate or sucrose and iron citrate, levitated droplets could be illuminated under different ambient conditions and monitored for compositional changes using Raman spectroscopy. This approach could reveal how photochemical reaction rates are limited by increasing viscosity in low RH conditions and decreased surface tension in the presence of surface-active molecules. Additionally, a modified electrodynamic balance with an integrated UV light source and Raman spectrometer could be used to monitor and measure photochemical reactions under different environmental conditions.

The aerosol droplets examined in this study lie within the coarse mode $> 1 \mu\text{m}$ which have a relatively short lifetime in the atmosphere. The accumulation mode where particles diameters range from $0.1 < D < 1 \mu\text{m}$ have the longest lifetimes in the atmosphere and therefore dominate atmospheric aerosol chemistry. Currently the experimental techniques used in this work are unable to measure particles of this size hence experimental development is needed to expand investigation into the accumulation mode. Hart and co-workers have developed a linear electrodynamic quadrupole device that enables the capture and levitation of particle sizes ranging from 0.5 to 30 μm with control of relative humidity and temperature.³⁴⁶ By adopting a similar development of an EDB with a Raman spectrometer, it may be possible to study hygroscopicity and photochemical reactions within accumulation mode droplets.

7.4 Final Remarks

The use of multiple techniques in this study has enabled the exploration of important properties that affect aerosol droplet growth and composition. The measurements obtained provide valuable information for models which are capable of predicting the behaviour of different systems and serve as powerful tools for understanding the impact of aerosols on the climate. As such, this work has significant implications for advancing our ability to rationally address the complex challenges associated with aerosol science.

References

- 1 F. Shain, Ü. K. Yıldız, V. Poku and B. Gokay, *Teach. High. Educ.*, 2021, **26**, 920–936.
- 2 A. A. Lushnikov, in *Aerosols: Science and technology*, ed. I. Agranonski, Wiley-CH, Weinham, 1st edn., 2010, 1–36.
- 3 B. J. Finlayson-Pitts and J. N. Pitts, *Chem. Up. Low. Atmos.*, 1999, 969.
- 4 X. Tang, S. Madronich, T. Wallington and D. Calamari, *J. Photochem. Photobiol. B Biol.*, 1998, **46**, 83–95.
- 5 C. Tomasi and A. Lupi, *Atmos. Aerosols*, 2016, 1–86.
- 6 H. Wang, J. Ding, J. Xu, J. Wen, J. Han, K. Wang, G. Shi, Y. Feng, C. E. Ivey, Y. Wang, A. Nenes, Q. Zhao and A. G. Russell, *Sci. Total Environ.*, 2019, **646**, 564–572.
- 7 UK, Particulate Matter in the United Kingdom, <https://uk-air.defra.gov.uk/assets/documents/reports/aeqg/ch2.pdf%0D>, (accessed 1 January 2018).
- 8 J. H. Seinfeld and S. N. Pandis, *Atmospheric Chemistry and Physics: From Air Pollution to Climate Change*, 2nd edn., 2006.
- 9 J. H. Seinfeld and S. N. Pandis, *Atmospheric Chemistry and Physics: From Air Pollution to Climate Change*, 1998, vol. 51.
- 10 S. E. Bauer, U. Im, K. Mezuman and C. Y. Gao, *J. Geophys. Res. Atmos.*, 2019, **124**, 4104–4120.
- 11 J. H. Kroll and J. H. Seinfeld, *Atmos. Environ.*, 2008, **42**, 3593–3624.
- 12 C. L. Heald, D. K. Henze, L. W. Horowitz, J. Feddema, J. F. Lamarque, A. Guenther, P. G. Hess, F. Vitt, J. H. Seinfeld, A. H. Godstein and I. Fung, *J. Geophys. Res. Atmos.*, 2008, **113**, D05211
- 13 J. Heintzenberg, *Tellus B*, 1989, **41B**, 149–160.
- 14 M. T. Parsons, D. A. Knopf and A. K. Bertram, *J. Phys. Chem. A*, 2004, **108**, 11600–11608.
- 15 J. L. Jimenez, M. R. Canagaratna, N. M. Donahue, A. S. H. Prevot, Q. Zhang, J. H. Kroll, P. F. DeCarlo, J. D. Allan, H. Coe, N. L. Ng, A. C. Aiken, K. S. Docherty, I. M. Ulbrich, A. P. Grieshop, A. L. Robinson, J. Duplissy, J. D. Smith, K. R. Wilson, V. A. Lanz, C. Hueglin, Y. L. Sun, J. Tian, A. Laaksonen, T. Raatikainen, J. Rautiainen, P. Vaattovaara, M. Ehn, M. Kulmala, J. M. Tomlinson, D. R. Collins, M. J. Cubison, E. J. Dunlea, J. A. Huffman, T. B. Onasch, M. R. Alfarra, P. I. Williams, K. Bower, Y. Kondo, J. Schneider, F. Drewnick, S. Borrmann, S. Weimer, K. Demerjian, D. Salcedo, L. Cottrell, R. Griffin, A. Takami, T. Miyoshi, S. Hatakeyama, A. Shimono, J. Y. Sun, Y. M. Zhang, K. Dzepina, J. R. Kimmel, D. Sueper, J. T. Jayne, S. C. Herndon, A. M. Trimborn, L. R. Williams, E. C. Wood, A. M. Middlebrook, C. E. Kolb, U. Baltensperger and D. R. Worsnop, *Science (80-.)*, 2009, **326**, 1525–1529.
- 16 S. Mahiuddin, B. Minofar, J. M. Borah, M. R. Das and P. Jungwirth, *Chem. Phys. Lett.*, 2008, **462**, 217–221.
- 17 J. P. D. Abbatt, K. Broekhuizen and P. Pradeep Kumar, *Atmos. Environ.*, 2005, **39**, 4767–4778.
- 18 L. Y. Hsieh, S. C. Kuo, C. L. Chen and Y. I. Tsai, *Atmos. Environ.*, 2007, **41**, 6648–6661.

References

- 19 2.4.4.2 Organic Carbon Aerosol from Fossil Fuels – AR4 WGI Chapter 2: Changes in Atmospheric Constituents and in Radiative Forcing, https://archive.ipcc.ch/publications_and_data/ar4/wg1/en/ch2s2-4-4-2.html, (accessed 12 September 2022).
- 20 C. Mohr, J. A. Huffman, M. J. Cubison, A. C. Aiken, K. S. Docherty, J. R. K. Kimmel, I. M. Ulbrich, M. Hannigan and J. L. Jimenez, *Environ. Sci. Technol.*, 2009, **43**, 2443–2449.
- 21 J. Li, G. Wang, C. Wu, C. Cao, Y. Ren, J. Wang, J. Li, J. Cao, L. Zeng and T. Zhu, *Sci. Rep.*, 2018, **8**, 535.
- 22 M. Hallquist, J. C. Wenger, U. Baltensperger, Y. Rudich, D. Simpson, M. Claeys, J. Dommen, N. M. Donahue, C. George, a. H. Goldstein, J. F. Hamilton, H. Herrmann, T. Hoffmann, Y. Iinuma, M. Jang, M. E. Jenkin, J. L. Jimenez, a. Kiendler-Scharr, W. Maenhaut, G. McFiggans, T. F. Mentel, a. Monod, a. S. H. Prévôt, J. H. Seinfeld, J. D. Surratt, R. Szmigielski and J. Wildt, *Atmos. Chem. Phys.*, 2009, **9**, 5155–5236.
- 23 A. G. Carlton, B. J. Turpin, H. Lim, K. E. Altieri and S. Seitzinger, *Geophys. Res. Lett.*, 2006, **33**, 2–5.
- 24 J. H. Kroll, N. L. Ng, S. M. Murphy, R. C. Flagan and J. H. Seinfeld, *Geophys. Res. Lett.*, 2005, **32**, 1–4.
- 25 S. L. Mkoma, G. O. da Rocha and J. B. de Andrade, *South African J. Chem.*, 2014, **67**, 0–0.
- 26 K. Kawamura and K. Ikushima, *Environ. Sci. Technol.*, 1993, **27**, 2227–2235.
- 27 K. Kawamura, H. Kasukabe, O. Yasui and L. A. Barrie, *Geophys. Res. Lett.*, 1995, **22**, 1253–1256.
- 28 A. Limbeck and H. Puxbaum, *Atmos. Environ.*, 1999, **33**, 1847–1852.
- 29 C. Neususs, M. Pelzing, A. Plewka and H. Herrmann, *J. Geophys. Res. Atmos.*, 2000, **105**, 4513–4527.
- 30 S. Myriokefalitakis, K. Tsigaridis, N. Mihalopoulos, J. Sciare, A. Nenes, K. Kawamura, A. Segers and M. Kanakidou, *Atmos. Chem. Phys.*, 2011, **11**, 5761–5782.
- 31 H. Adler and H. Sirén, *J. Anal. Methods Chem.*, 2014, **2014**, 1–10.
- 32 Z.-Q. Wang, Y.-R. Liu, C.-Y. Wang, S. Jiang, Y.-J. Feng, T. Huang and W. Huang, *Atmos. Environ.*, 2021, **267**, 118558.
- 33 K. Kawamura, E. Tachibana, K. Okuzawa, S. G. Aggarwal, Y. Kanaya and Z. F. Wang, *Atmos. Chem. Phys.*, 2013, **13**, 8285–8302.
- 34 H. Zhang, W. Wang, S. Pi, L. Liu, H. Li, Y. Chen, Y. Zhang, X. Zhang and Z. Li, *Chemosphere*, 2018, **212**, 504–512.
- 35 Y. Fu, Y. Zhang, F. Zhang, J. Chen, Z. Zhu and X.-Y. Yu, *Atmos. Environ.*, 2018, **191**, 36–45.
- 36 P. A. Leermakers and G. F. Vesley, *J. Am. Chem. Soc.*, 1963, **85**, 3776–3779.
- 37 K. J. Kappes, A. M. Deal, M. F. Jespersen, S. L. Blair, J. F. Doussin, M. Cazaunau, E. Pangui, B. N. Hopper, M. S. Johnson and V. Vaida, *J. Phys. Chem. A*, 2021, **125**, 1036–1049.
- 38 J. A. Conti Silva, L. M. Grilo, M. H. Vasconcelos and T. M. Lacerda, *Prod. Top 12 Biochem. Sel. by USDOE from Renew. Resour.*, 2022, 387–414.
- 39 B. J. Murray, *Environ. Res. Lett.*, 2008, **3**, 025008.
- 40 F. H. Marshall, T. Berkemeier, M. Shiraiwa, L. Nandy, P. B. Ohm, C. S. Dutcher and J. P. Reid,

References

- Phys. Chem. Chem. Phys.*, 2018, **20**, 15560–15573.
- 41 K. J. Kiland, A. M. MacLean, S. Kamal and A. K. Bertram, *J. Phys. Chem. Lett.*, 2019, **10**, 5902–5908.
- 42 M. yee Choi and C. K. Chan, *Environ. Sci. Technol.*, 2002, **36**, 2422–2428.
- 43 J. Y. Lee and L. M. Hildemann, *J. Aerosol Sci.*, 2013, **64**, 94–102.
- 44 L. Miñambres, E. Méndez, M. N. Sánchez, F. Castaño and F. J. Basterretxea, *Atmos. Environ.*, 2013, **70**, 108–116.
- 45 H. C. Boyer, B. R. Bzdek, J. P. Reid and C. S. Dutcher, *J. Phys. Chem. A*, 2017, **121**, 198–205.
- 46 M. Frosch, N. L. Prisle, M. Bilde, Z. Varga and G. Kiss, *Atmos. Chem. Phys.*, 2011, **11**, 3895–3911.
- 47 R. Tuckermann, *Atmos. Environ.*, 2007, **41**, 6265–6275.
- 48 C. N. Cruz and S. N. Pandis, *Environ. Sci. Technol.*, 2000, **34**, 4313–4319.
- 49 E. Andrews and S. M. Larson, *Environ. Sci. Technol.*, 1993, **27**, 857–865.
- 50 B. R. Bzdek, J. P. Reid, J. Malila and N. L. Prisle, *Proc. Natl. Acad. Sci.*, 2020, **117**, 8335–8343.
- 51 S. S. Petters and M. D. Petters, *J. Geophys. Res. Atmos.*, **121**, 1878–1895.
- 52 M. T. Latif and peter Brimblecombe, *Environ. Sci. Technol.*, 2004, **38**, 6501–6506.
- 53 V. Gérard, B. Nozière, C. Baduel, L. Fine, A. A. Frossard and R. C. Cohen, *Environ. Sci. Technol.*, 2016, **50**, 2974–2982.
- 54 M. C. Facchini, M. Mircea, S. Fuzzi and R. J. Charlson, *Nature*, 1999, **401**, 257–259.
- 55 N. L. Prisle, A. Asmi, D. Topping, A. I. Partanen, S. Romakkaniemi, M. Dal Maso, M. Kulmala, A. Laaksonen, K. E. J. Lehtinen, G. McFiggans and H. Kokkola, *Geophys. Res. Lett.*, 2012, **39**, 5802.
- 56 H. A. Razak, N. Bahiyah, A. Wahid, · Mohd and T. Latif, *Arch. Environ. Contam. Toxicol.*, 2019, **77**, 587–593.
- 57 K. V. Vejrurp and P. Wolkoff, *Sci. Total Environ.*, 2002, **300**, 51–58.
- 58 M. Feng, C. Böning, A. Biastoch, E. Behrens, E. Weller and Y. Masumoto, *Geophys. Res. Lett.*, 2011, **38**, L11604
- 59 Intergovernmental Panel on Climate Change, *Climate Change: The IPCC 1990 and 1992 Assessments*, 1992.
- 60 V. Ramaswamy, O. Boucher, J. Haigh, D. Hauglustaine, J. Haywood, G. Myhre, T. Nakajima, G. Shi, S. Betts, R. Charlson, C. Chuang, J. Daniel, A. Del Genio, R. van Dorland, J. Feichter, J. Fuglestedt, P. de Forster, S. Ghan, A. Jones, J. Kiehl, D. Koch, C. Land, J. Lean, U. Lohmann, K. Minschwaner, J. Penner, D. Roberts, H. Rodhe, G. Roelofs, L. Rotstayn, T. Schneider, U. Schumann, S. Schwartz, K. Shine, S. Smith, D. Stevenson, F. Stordal and I. Tegen, *Radiative Forcing of Climate Change 6*, 2001.
- 61 P. R. Shukla, J. Skea, R. Slade, A. Al Khourdajie, R. van Diemen, D. McCollum, M. Pathak, S. Some, P. Vyas, R. Fradera, M. Belkacemi, A. Hasija, G. Lisboa, S. Luz and J. Malley, *Mitigation of Climate Change. Working Group III Contribution to the IPCC Sixth Assessment Report*, Ne York, 2021.
- 62 P. Forster, K. Alterskjaer, C. Smith, R. Colman, H. Damon Matthews, V. Ramaswamy, T. Storelvmo, K. Armour, W. Collins, J. Dufresne, D. Frame, D. Lunt, T. Mauritsen, M. Watanabe,

References

- M. Wild, H. Zhang, A. Pirani, S. Connors, C. Péan, S. Berger, N. Caud, Y. Chen, L. Goldfarb, M. Gomis, M. Huang, K. Leitzell, E. Lonnoy, J. Matthews, T. Maycock, T. Waterfield, O. Yelekçi, R. Yu and B. Zhou, *The Earth's Energy Budget, Climate Feedbacks and Climate Sensitivity*, 2021.
- 63 C. J. Smith, R. J. Kramer, G. Myhre, K. Alterskjr, W. Collins, A. Sima, O. Boucher, J. L. Dufresne, P. Nabat, M. Michou, S. Yukimoto, J. Cole, D. Paynter, H. Shioyama, F. M. O'Connor, E. Robertson, A. Wiltshire, T. Andrews, C. Hannay, R. Miller, L. Nazarenko, A. Kirkevg, D. Olivi, S. Fiedler, A. Lewinschal, C. MacKallah, M. Dix, R. Pincus and P. M. Forster, *Atmos. Chem. Phys.*, 2020, **20**, 9591–9618.
- 64 In *Climate Change 2013 the Physical Science Basis: Working Group I Contribution to the Fifth Assessment Report of the Intergovernmental Panel on Climate Change*, 2013, vol. 9781107057, pp. 659–740.
- 65 R. Mueller, J. Trentmann, C. Träger-Chatterjee, R. Posselt and R. Stöckli, *Remote Sens.*, 2011, **3**, 2305–2320.
- 66 Cloud Radiative Effect, <https://www.gfdl.noaa.gov/cloud-radiative-effect/>, (accessed 12 October 2022).
- 67 J. Haywood and O. Boucher, *Rev. Geophys.*, 2000, **38**, 513–543.
- 68 S. K. Satheesh and K. Krishna Moorthy, *Atmos. Environ.*, 2005, **39**, 2089–2110.
- 69 G. Pitari, A. Ackerman, P. Adams, P. Austin, R. Boers, O. Boucher, M. Chin, C. Chuang, B. Collins, W. Cooke, P. Demott, Y. Feng, H. Fischer, I. Fung, S. Ghan, P. Ginoux, S. Gong, A. Guenther, M. Herzog, A. Higurashi, Y. Kaufman, A. Kettle, J. Kiehl, D. Koch, G. Lammel, C. Land, U. Lohmann, S. Madronich, E. Mancini, M. Mishchenko, T. Nakajima, P. Quinn, P. Rasch, D. L. Roberts, D. Savoie, S. Schwartz, J. Seinfeld, B. Soden, D. Tanré, K. Taylor, I. Tegen, X. Tie, G. Vali, R. Van Dingenen and M. Van Weele, *Clim. Chang. 2001 Sci. Basis. Contrib. Work. Gr. I to Third Assess. Rep. Intergov. Panel Clim. Chang.*
- 70 E. Pallé, P. R. Goode, V. Yurchyshyn, J. Qiu, J. Hickey, P. Montanés Rodríguez, M. C. Chu, E. Kolbe, C. T. Brown and S. E. Koonin, *J. Geophys. Res. Atmos.*, 2003, **108**, 4710
- 71 F. D. Pope, P. Braesicke, R. G. Grainger, M. Kalberer, I. M. Watson, P. J. Davidson and R. A. Cox, *Nat. Clim. Chang. 2012 210*, 2012, **2**, 713–719.
- 72 J. E. Penner, · C C Chuang, · K Grant, C. C. Chuang and) K Grant, *Clim. Dyn.*, 1998, **14**, 839–851.
- 73 O. Boucher and T. L. Anderson, *J. Geophys. Res.*, 1995, **100**, 26117–26134.
- 74 J. T. Kiehl, T. L. Schneider, P. J. Rasch, M. C. Barth and J. Wong, *J. Geophys. Res. Atmos.*, 2000, **105**, 1441–1457.
- 75 I. N. Sokolik and O. B. Toon, *Nature*, 1996, **381**, 681–683.
- 76 B. A. Albrecht, *Science*, 1989, **245**, 1227–1230.
- 77 R. Pincus and M. B. Baker, *Nature*, 1994, **372**, 250–252.
- 78 O. Alizadeh-Choobari, *Meteorol. Appl.*, 2018, **25**, 596–605.
- 79 S. Twomey, *J. Atmos. Sci.*, 1977, **34**, 1149–1152.
- 80 A. S. Ackerman, O. B. Toon, D. E. Stevens, A. J. Heymsfield, V. Ramanathan and E. J. Welton, *Science (80-)*, 2000, **288**, 1042–1047.
- 81 U. Lohmann and J. Feichter, *Geophys. Res. Lett.*, 2001, **28**, 159–161.

References

- 82 K. Wyser and J. Ström, *Geophys. Res. Lett.*, 1998, **25**, 1673–1676.
- 83 J. Ström and S. Ohlsson, *J. Geophys. Res. Atmos.*, 1998, **103**, 11355–11361.
- 84 Average Annual Relative Humidity – Atlas of the Biosphere | Center for Sustainability and the Global Environment (SAGE), <https://sage.nelson.wisc.edu/data-and-models/atlas-of-the-biosphere/mapping-the-biosphere/ecosystems/average-annual-relative-humidity/>, (accessed 14 September 2022).
- 85 G. Tian, P. W. Longest, X. Li and M. Hindle, *Aerosol Med. Pulm. drug Deliv.*, 2013, **26**, 1–25.
- 86 A. Marsh, R. E. H. Miles, G. Rovelli, A. G. Cowling, L. Nandy, C. S. Dutcher and J. P. Reid, *Atmos. Chem. Phys.*, 2017, **17**, 5583–5599.
- 87 J. Eastoe and J. S. Dalton, *Adv. Colloid Interface Sci.*, 2000, **85**, 103–144.
- 88 H. Manikantan and T. M. Squires, *J. Fluid Mech.*, 2020, **892**, 1.
- 89 X. Hua, J. Frechette and M. A. Bevan, *3818 | Soft Matter*, 2018, **14**, 3818.
- 90 A. Zdziennicka, K. Szymczyk, J. Krawczyk and B. Jańczuk, *Fluid Phase Equilib.*, 2012, **318**, 25–33.
- 91 V. B. Fainerman and E. H. Lucassen-Reynders, *Adv. Colloid Interface Sci.*, 2002, **96**, 295–323.
- 92 F. B. Sprow and J. M. Prausnitz, *Can. J. Chem. Eng.*, 1967, **45**, 25–28.
- 93 H. C. Boyer, B. R. Bzdek, J. P. Reid and C. S. Dutcher, *J. Phys. Chem. A*, 2017, **121**, 15.
- 94 J. J. Lin, J. Malila and N. L. Prisle, *Environ. Sci. Process. Impacts*, 2018, **20**, 1611–1629.
- 95 P. B. Petersen and R. J. Saykally, *Annu. Rev. Phys. Chem.*, 2006, **57**, 333–364.
- 96 N. J. Alvarez, L. M. Walker and S. L. Anna, *Soft Matter*, 2012, **8**, 8971–8925.
- 97 A. Bain, K. Ghosh, N. L. Prisle and B. R. Bzdek, *ACS Cent. Sci.*, 2023, **11**, 2076–2083
- 98 R. M. Power, University of Bristol, 2014.
- 99 P. Pokkunuri, P. Nissenon and D. Dabdub, *Atmos. Environ.*, 2010, **44**, 153–163.
- 100 J. F. Davies, R. E. H. Miles, A. E. Haddrell and J. P. Reid, *Proc. Natl. Acad. Sci. U. S. A.*, 2013, **110**, 8807–8812.
- 101 D. Hardy, University of Bristol, 2023.
- 102 M. Shiraiwa, M. Ammann, T. Koop and U. Pöschl, *Proc. Natl. Acad. Sci. U. S. A.*, 2011, **108**, 11003–11008.
- 103 M. Kuwata and S. T. Martin, *Proc. Natl. Acad. Sci. U. S. A.*, 2012, **109**, 17354–17359.
- 104 J. H. Seinfeld and S. N. Pandis, *Atmospheric Chemistry and Physics: From Air Pollution to Climate Change*, John Wiley & Sons, Ltd, 2016.
- 105 P. C. Arroyo, G. David, P. A. Alpert, E. A. Parmentier, M. Ammann and R. Signorell, *Science*, 2022, **376**, 293–296.
- 106 J. Dou, P. A. Alpert, P. Corral Arroyo, B. Luo, F. Schneider, J. Xto, T. Huthwelker, C. N. Borca, K. D. Henzler, J. Raabe, B. Watts, H. Herrmann, T. Peter, M. Ammann and U. K. Krieger, *Atmos. Chem. Phys.*, 2021, **21**, 315–338.
- 107 T. B. Nguyen, A. Laskin, J. Laskin and S. A. Nizkorodov, *Phys. Chem. Chem. Phys.*, 2012, **14**, 9702–9714.

References

- 108 A. L. Klodt, D. E. Romonosky, P. Lin, J. Laskin, A. Laskin and S. A. Nizkorodov, *ACS Earth Sp. Chem.*, 2019, **3**, 2736–2746.
- 109 V. Liweichao, Nitrous Pollutants, <https://commons.wikimedia.org/w/index.php?curid=74422940> (accessed September 2022).
- 110 R. R. Dickerson, S. Kondragunta, G. Stenchikov, K. L. Civerolo, B. G. Doddridge and B. N. Holben, *Science (80-.)*, 1997, **278**, 827–830.
- 111 T. E. Blackburn, S. T. Bairai and D. H. Stedman, *J. Geophys. Res.*, 1992, **97**, 10109–10117.
- 112 J. W. Cremer, K. M. Thaler, C. Haisch and R. Signorell, *Nat. Commun.*, 2016, **7**, 10941.
- 113 A. Hodzic, S. Madronich, P. S. Kasibhatla, G. Tyndall, B. Aumont, J. L. Jimenez, J. Lee-Taylor and J. Orlando, *Atmos. Chem. Phys.*, 2015, **15**, 9253–9269.
- 114 K. C. Neuman and S. M. Block, *Rev. Sci. Instrum.*, 2004, **75**, 2787–809.
- 115 P. Jing, J. Wu, G. W. Liu, E. G. Keeler, S. H. Pun and L. Y. Lin, *Sci. Rep.*, 2016, **6**, 19924.
- 116 J. E. Molloy and M. J. Padgett, *Contemp. Phys.*, 2002, **43**, 241–258.
- 117 K. Svoboda and S. M. Block, *Opt. Lett.*, 1994, **19**, 930–932.
- 118 K. Dholakia, G. Spalding and M. MacDonald, *Phys. World*, 2002, **15**, 31.
- 119 J. E. Curtis, B. A. Koss and D. G. Grier, *Opt. Commun.*, 2002, **207**, 169–175.
- 120 J. E. Molloy and M. J. Padgett, *Contemp. Phys.*, 2002, **43**, 241–258.
- 121 E. Fällman and O. Axner, *Appl. Opt. Vol. 42, Issue 19, pp. 3915-3926*, 2003, **42**, 3915–3926.
- 122 S. Ebnesajjad, *Handb. Adhes. Surf. Prep. Technol. Appl. Manuf.*, 2010, 21–30.
- 123 Pendant drop method — Optical determination of the surface/interfacial tension, <https://www.dataphysics-instruments.com/knowledge/understanding-interfaces/pendant-drop-method/>, (accessed 3 October 2022).
- 124 B. R. Bzdek, R. M. Power, S. H. Simpson, J. P. Reid and C. P. Royall, *Chem. Sci.*, 2016, **7**, 274–285.
- 125 H. J. J. Staat, A. van der Bos, M. van den Berg, H. Reinten, H. Wijshoff, M. Versluis and D. Lohse, *Exp. Fluids*, 2017, **58**, 1–8.
- 126 C. A. MacLeod and C. J. Radke, *J. Colloid Interface Sci.*, 1993, **160**, 435–448.
- 127 H. Lignell, M. L. Hinks and S. A. Nizkorodov, *Proc. Natl. Acad. Sci. U. S. A.*, 2014, **111**, 13780–13785.
- 128 J. P. Reid, A. K. Bertram, D. Topping, A. Laskin, S. T. Martin, M. D. Petters, F. D. Pope and G. Rovelli, *Nat. Commun.*, 2018, **9**, 1–14.
- 129 5 Ways to Measure Viscosity, [https://formulation.com/5-ways-to-measure-viscosity/#:~:text=Microfluidic rheometry is an innovative,by side with reference material.](https://formulation.com/5-ways-to-measure-viscosity/#:~:text=Microfluidic%20rheometry%20is%20an%20innovative,by%20side%20with%20reference%20material.), (accessed 4 October 2022).
- 130 M. Sellier, J. Taylor, A. K. Bertram and P. Mandin, *Aerosol Sci. Technol.*, 2019, **53**, 749–759.
- 131 B. J. Murray, *Atmos. Chem. Phys.*, 2008, **8**, 5423–5433.
- 132 L. Renbaum-Wolff, J. W. Grayson, A. P. Bateman, M. Kuwata, M. Sellier, B. J. Murray, J. E. Shilling, S. T. Martin and A. K. Bertram, *Proc. Natl. Acad. Sci. U. S. A.*, 2013, **110**, 8014–8019.
- 133 J. W. Grayson, M. Song, M. Sellier and A. K. Bertram, *Atmos. Meas. Tech.*, 2015, **8**, 2463–2472.

References

- 134 M. K. Kuimova, G. Yahiolu, J. A. Levitt and K. Suhling, *J. AM. CHEM. SOC.*, 2008, **130**, 19.
- 135 C. Fitzgerald, N. A. Hosny, H. Tong, P. C. Seville, P. J. Gallimore, N. M. Davidson, A. Athanasiadis, S. W. Botchway, A. D. Ward, M. Kalberer, M. K. Kuimova and F. D. Pope, *Phys. Chem. Chem. Phys.*, 2016, **18**, 21710–21719.
- 136 T. F. Kirkwood, *Soc. Stud.*, 2001, **92**, 10–15.
- 137 L. Hutfield, *Decolonising the SPAIS Curriculum*, 2021.
- 138 D. Murnane, A. Boies and J. P. Reid, *Building a UK pipeline of research, innovation and technology development for aerosol science*, 2018.
- 139 G. V. Research, *Aerosol Market Estimates & Trend Analysis By Application*, 2016.
- 140 Aerosol Science Search, <https://www.webofscience.com/wos/alldb/summary/28eddbfe-6769-42ff-9177-99558ed9bb5e-d0681b14/relevance/1> (accessed January 2024).
- 141 F. O. Abulude, S. D. Fagbayide, A. Akinnusotu, J. J. Elisha and O. E. Makinde, *Eng. Appl. Sci. Res.*, 2019, **46**, 151–169.
- 142 S. Bako, *Universities, Research and Development In Nigeria: Time for a paradigmatic shift*, 2005.
- 143 I. Overland, H. F. Sagbakken, A. Isataeva, N. P. Simpson, C. Trisos, P. Simpson and G. Kolodzinskaia, *Clim. Dev.*, 2022, **14**, 705–724.
- 144 J. K. Gani and J. Marshall, *Int. Aff.*, 2022, **8**, 5–22.
- 145 E. Polk and S. Diver, *Front. Commun.*, 2020, **5**, 1–10.
- 146 R. H. Cole, S. Y. Tang, C. A. Siltanen, P. Shahi, J. Q. Zhang, S. Poust, Z. J. Gartner and A. R. Abate, *Proc. Natl. Acad. Sci. U. S. A.*, 2017, **114**, 8728–8733.
- 147 B. S. Vaughn, P. J. Tracey and A. J. Trevitt, *RSC Adv.*, 2016, **6**, 60215–60222.
- 148 R. E. H. Miles, M. W. J. Glerum, H. C. Boyer, J. S. Walker, C. S. Dutcher and B. R. Bzdek, *J. Phys. Chem. A*, 2019, **123**, 3021–3029.
- 149 L. Rayleigh, *Proc. R. Soc. London*, 1879, **29**, 71–97.
- 150 C. A. Morrison, R. P. Leavitt and D. E. Wortman, *J. Fluid Mech.*, 2081, **104**, 295–309.
- 151 R. M. Power and J. P. Reid, *Rep. Prog. Phys.*, 2014, **77**, 074601.
- 152 N. Brosius, J. Livesay, Z. Karpinski, R. Singiser, M. SanSoucie, B. Phillips and R. Narayanan, *npj Microgravity*, 2023, **9**, 3.
- 153 X. Xiao, R. W. Hyers, R. K. Wunderlich, H.-J. Fecht and D. M. Matson, *Appl. Phys. Lett.*, 2018, **113**, 011903.
- 154 L. Hu, L. She, Y. Fang, R. Su and X. Fu, *AIP Adv.*, 2021, **11**, 045310.
- 155 B. S. Vaughn, P. J. Tracey and A. J. Trevitt, *RSC Adv.*, 2016, **6**, 60215–60222.
- 156 G. A. Ferron and S. C. Soderholm, *J. Aerosol Sci.*, 1990, **21**, 415–429.
- 157 I. M. Hauner, A. Deblais, J. K. Beattie, H. Kellay and D. Bonn, *J. Phys. Chem. Lett.*, 2017, **8**, 1599–1603.
- 158 J. K. Beattie, A. M. Djerdjiev, A. Gray-Weale, N. Kallay, J. Lützenkirchen, T. Preočanin and A. Selmani, *J. Colloid Interface Sci.*, 2014, **422**, 54–57.

References

- 159 Y. Fujimura and M. Iino, *J. Appl. Phys.*, 2008, **103**, 124903.
- 160 P. Dobriyal, A. Qureshi, R. Badola and S. A. Hussain, *J. Hydrol.*, 2012, **458–459**, 110–117.
- 161 How does capacitive level sensing work? » Gill Sensors & Controls – , <https://www.gillsc.com/newsitem/51/how-does-capacitive-level-sensing-work->, (accessed 23 August 2022).
- 162 T. R. Corle and G. S. Kino, *Confocal Scanning Opt. Microsc. Relat. Imaging Syst.*, 1996, 1–66.
- 163 D. R. Burnham and D. McGloin, *Opt. Express*, 2006, **14**, 4175.
- 164 J. S. Walker, PhD Thesis, University of Bristol, 2013.
- 165 B. R. Bzdek and J. S. Walker, *Spectroscopy*, 2019, **34**, 22–31.
- 166 Y. C. Song, A. E. Haddrell, B. R. Bzdek, J. P. Reid, T. Bannan, D. O. Topping, C. Percival and C. Cai, *J. Phys. Chem. A*, 2016, **120**, 8123–8137.
- 167 J. De Gouw and J. L. Jimenez, *Environ. Sci. Technol.*, 2009, **43**, 7614–7618.
- 168 R. M. Power, S. H. Simpson, J. P. Reid and A. J. Hudson, *Chem. Sci.*, 2013, **4**, 2597–2604.
- 169 R. M. Power, S. H. Simpson, J. P. Reid and A. J. Hudson, *Chem. Sci.*, 2013, **4**, 2597.
- 170 I. Roa, M. Renoult, J. César, B. De Motta, I. Roa, M. Renoult, J. César, B. De Motta, C. Dumouchel, I. Roa, M. Renoult, C. Dumouchel and C. Jorge, *Front. Phys.*, 2023, **11**, 1173521.
- 171 S. Chandrasekhar, *Proc. London Math. Soc.*, 1959, **s3-9**, 141–149.
- 172 C. Heinisch, J. B. Wills, J. P. Reid, T. Tschudi and C. Tropea, *Phys. Chem. Chem. Phys.*, 2009, **11**, 9720.
- 173 J. F. Davies, A. E. Haddrell, A. M. J. Rickards and J. P. Reid, *Anal. Chem.*, 2013, **85**, 17.
- 174 W. J. Glantschnig and S.-H. Chen, *Appl. Opt.*, 1981, **20**, 2499.
- 175 G. Rovelli, R. E. H. Miles, J. P. Reid and S. L. Clegg, *J. Phys. Chem. A*, 2016, **120**, 4376–4388.
- 176 J. J. Jankowski, D. J. Kieber and K. Mopper, *Photochem. Photobiol.*, 1999, **70**, 319–328.
- 177 K. B. Benedict, A. S. McFall and C. Anastasio, *Environ. Sci. Technol.*, 2017, **51**, 4387–4395
- 178 K. J. Mysels, *Langmuir*, 1986, **2**, 428–432.
- 179 V. . Fainerman and R. Miller, *Adv. Colloid Interface Sci.*, 2004, **108–109**, 287–301.
- 180 R. Miller, V. B. Fainerman, K. H. Schano, A. Hofmann and W. Heyer, *Tenside, Surfactants, Deterg.*, 1997, **34**, 357–363.
- 181 H. Liu and G. Cao, *Sci. Reports 2016 61*, 2016, **6**, 1–10.
- 182 L. M. Siqueland and S. M. Skjæveland, *Capillarity*, 2021, **4**, 23–30.
- 183 V. B. Fainerman, A. V Makievski and R. Miller, *Rev. Sci. Instrum.*, 2004, **75**, 213.
- 184 R. Miller and V. B. Fainerman, in *Handbook of Surfaces and Interfaces of Materials*, Elsevier, 2001, 383–421.
- 185 K. J. Mysels, *Langmuir*, 1986, **2**, 423–428.
- 186 C. K. Chua, C. H. Wong and W. Y. Yeong, *Stand. Qual. Control. Meas. Sci. 3D Print. Addit. Manuf.*, 2017, 1–250.
- 187 E. Ramé, *J. Colloid Interface Sci.*, 1997, **185**, 245–251.

References

- 188 X. Wang, Q. Min, Z. Zhang, Y. Duan, Y. Zhang and J. Zhai, *Colloids Surfaces A Physicochem. Eng. Asp.*, 2017, **527**, 115–122.
- 189 G. Buckton, P. Darcy and D. Mccarthy, *A Physicochem. Eng. Asp.*, 1995, **95**, 27–35.
- 190 P. Saxena, L. M. Hildemann, P. H. McMurry and J. H. Seinfeld, *J. Geophys. Res.*, 1995, **100**, 18755–18770.
- 191 K. H. Kim, S. H. Woo, S. B. Lee, G. N. Bae, K. Sekiguchi, R. Kobayashi and M. Kamiyama, *Aerosol Air Qual. Res.*, 2016, **16**, 361–372.
- 192 C. Alves, A. Carvalho and C. Pio, *J. Geophys. Res. Atmos.*, 2002, **107**, ICC 7-1-ICC 7-9.
- 193 S. H. Cadle and P. J. Groblicki, in *Particulate Carbon*, Springer US, Boston, MA, 1982, pp. 89–109.
- 194 S. Decesari, M. C. Facchini, S. Fuzzi and E. Tagliavini, *J. Geophys. Res. Atmos.*, 2000, **105**, 1481–1489.
- 195 H. Wex, F. Stratmann, D. Topping and G. McFiggans, *J. Atmos. Sci.*, 2008, **65**, 4004–4016.
- 196 G. Kiss, E. Tombácz and H. C. Hansson, *J. Atmos. Chem.*, 2005, **50**, 279–294.
- 197 M. C. Facchini, S. Decesari, M. Mircea, S. Fuzzi and G. Loglio, *Atmos. Environ.*, 2000, **34**, 4853–4857.
- 198 H. P. Meissner and A. S. Michaels, *Ind. & Eng. Chem.*, 2002, **41**, 2782–2787.
- 199 J. Y. Lee and L. M. Hildemann, *Atmos. Environ.*, 2014, **89**, 260–267.
- 200 C. N. Cruz and S. N. Pandis, *Atmos. Environ.*, 1997, **31**, 2205–2214.
- 201 P. T. Griffiths and R. A. Cox, *Atmos. Sci. Lett.*, 2009, **10**, 159–163.
- 202 F. J. Dentener and P. J. Crutzen, *J. Geophys. Res.*, 1993, **98**, 7149–7163.
- 203 R. M. Kirpes, Z. Lei, M. Fraund, M. J. Gunsch, N. W. May, T. E. Barrett, C. E. Moffett, A. J. Schauer, B. Alexander, L. M. Upchurch, S. China, P. K. Quinn, R. C. Moffet, A. Laskin, R. J. Sheesley, K. A. Pratt and A. P. Ault, *Proc. Natl. Acad. Sci. U. S. A.*, 2022, **119**, e2104496119.
- 204 K. W. Tu and G. M. Kanapilly, *Atmos. Environ.*, 1978, **12**, 1623–1629.
- 205 S. Gopalakrishnan, P. Jungwirth, D. J. Tobias and H. C. Allen, *J. Phys. Chem. B*, 2005, **109**, 8861–8872.
- 206 Y. You, L. Renbaum-Wolff and A. K. Bertram, *Atmos. Chem. Phys.*, 2013, **13**, 11723–11734.
- 207 M. L. Smith, A. K. Bertram and S. T. Martin, *Atmos. Chem. Phys.*, 2012, **12**, 9613–9628.
- 208 C. Xiong, B. Kuang, F. Zhang, X. Pei, Z. Xu and Z. Wang, *Atmos. Chem. Phys.*, 2023, **23**, 8979–8991.
- 209 J. Setschenow, *Zeitschrift für Phys. Chemie*, 1889, **4U**, 117–125.
- 210 M. Görgényi, J. Dewulf, H. Van Langenhove and K. Héberger, *Chemosphere*, 2006, **65**, 802–810.
- 211 S. Endo, A. Pfennigsdorff and K. U. Goss, *Environ. Sci. Technol.*, 2012, **46**, 1496–1503.
- 212 C. Wang, Y. D. Lei, S. Endo and F. Wania, *Environ. Sci. Technol.*, 2014, **48**, 28.
- 213 J. P. Reid, B. J. Dennis-Smith, N. O. A. Kwamena, R. E. H. Miles, K. L. Hanford and C. J. Homer, *Phys. Chem. Chem. Phys.*, 2011, **13**, 15559–15572.

References

- 214 B. E. Conway, J. E. D. Esnoyers and A. C. Smith, *Philos. Trans. R. Soc. London. Ser. A, Math. Phys. Sci.*, 1964, **256**, 389–437.
- 215 N. Sareen, E. M. Waxman, B. J. Turpin, R. Volkamer and A. G. Carlton, *Environ. Sci. Technol.*, 2017, **51**, 3327–3335.
- 216 W. F. Mcdevit and F. A. Long, *J. Am. Chem. Soc.*, 1952, **74**, 1773–1777.
- 217 W. H. Xie, W. Y. Shiu and D. Mackay, *Mar. Environ. Res.*, 1997, **44**, 429–444.
- 218 Y. F. Hu and H. Lee, *J. Colloid Interface Sci.*, 2004, **269**, 442–448.
- 219 Z. B. Li, Y. G. Li and J. F. Lu, *Ind. Eng. Chem. Res.*, 1999, **38**, 1133–1139.
- 220 H. C. Boyer and C. S. Dutcher, *J. Phys. Chem. A*, 2017, **121**, 4733–4742.
- 221 A. S. Wexler and C. S. Dutcher, *J. Phys. Chem. Lett.*, 2013, **4**, 1723–1726.
- 222 C. S. Dutcher, X. Ge, A. S. Wexler and S. L. Clegg, *J. Phys. Chem. C*, 2011, **115**, 16474–16487.
- 223 J. W. Gibbs, *Am. J. Sci.*, 1878, **s3-16**, 441–458.
- 224 I. Langmuir, *J. Am. Chem. Soc.*, 2002, **39**, 1848–1906.
- 225 M. Nakagaki and T. Handa, *Bull. Chem. Soc. Jpn.*, 2006, **48**, 630–635.
- 226 A. N. Schwier, G. A. Viglione, Z. Li and V. F. McNeill, *Atmos. Chem. Phys.*, 2013, **13**, 10721–10732.
- 227 H. C. Boyer and C. S. Dutcher, *J. Phys. Chem. A*, 2016, **120**, 4368–4375.
- 228 P. B. Ohm, C. Asato, A. S. Wexler and C. S. Dutcher, *J. Phys. Chem. A*, 2015, **119**, 3244–3252.
- 229 PubChem, <https://pubchem.ncbi.nlm.nih.gov/>, (accessed 20 April 2001).
- 230 A. J. García-Fernández, S. Espín, P. Gómez-Ramírez and E. Martínez-López, in *Encyclopedia of Toxicology*, Elsevier, 2014, pp. 730–734.
- 231 Levulinic acid,
https://www.chemicalbook.com/ChemicalProductProperty_EN_CB3213533.htm (accessed January 2022)
- 232 E. Aumann, L. M. Hildemann and A. Tabazadeh, *Atmos. Environ.*, 2010, **44**, 329–337.
- 233 A.-P. Hyvärinen, H. Lihavainen, A. Gaman, L. Vairila, H. Ojala, M. Kulmala and Y. Viisanen, *J. Chem. & Eng. Data*, 2005, **51**, 255–260.
- 234 B. Svenningsson, J. Rissler, E. Swietlicki, M. Mircea, M. Bilde, M. C. Facchini, S. Decesari, S. Fuzzi, J. Zhou, J. Mønster and T. Rosenørn, *Atmos. Chem. Phys.*, 2006, **6**, 1937–1952.
- 235 S. L. Clegg, P. Brimblecombe and A. S. Wexler, *J. Phys. Chem. A*, 1998, **102**, 2155–2171.
- 236 C. S. Dutcher, A. S. Wexler and S. L. Clegg, *J. Phys. Chem. A*, 2010, **114**, 12216–12230.
- 237 S. L. Clegg and J. H. Seinfeld, *Phys. Chem. Chem. Phys.*, 2006, **10**, 5692–5717.
- 238 A. N. Schwier, G. A. Viglione, Z. Li and V. F. McNeill, *Atmos. Chem. Phys.*, 2013, **13**, 10721–10732.
- 239 A. Schwier, D. Mitroo and V. F. McNeill, *Atmos. Environ.*, 2012, **54**, 490–495.
- 240 T. Katagi, *Rev. Environ. Contam. Toxicol.*, 2008, **194**, 71–177.
- 241 T. Wu and A. Firoozabadi, *Langmuir*, 2021, **37**, 4736–4743.

References

- 242 B. Singh Sekhon, *J. Pharm. Technol.*, 2013, **1**, 43–68.
- 243 T. Ishiwata and K. Sakai, *Appl. Phys. Express*, 2014, **7**, 077301.
- 244 M. S. Aston, *Chem. Soc. Rev.*, 1993, **22**, 67–71.
- 245 C. R. Ruehl, P. Y. Chuang and A. Nenes, *Atmos. Chem. Phys.*, 2010, **10**, 1329–1344.
- 246 J. F. Davies, A. Zuend and K. R. Wilson, *Atmos. Chem. Phys.*, 2019, **19**, 2933–2946.
- 247 M. D. Petters and S. M. Kreidenweis, *Atmos. Chem. Phys.*, 2007, **7**, 1961–1971.
- 248 A. Kroflič, S. Frka, M. Simmel, H. Wex and I. Grgić, *Environ. Sci. & Technol.*, 2018, **52**, 9179–9187.
- 249 I. M. Hauner, A. Deblais, J. K. Beattie, H. Kellay and D. Bonn, *J. Phys. Chem. Lett.*, 2017, **8**, 1599–1603.
- 250 S. R. Milner, *London, Edinburgh, Dublin Philos. Mag. J. Sci.*, 1907, **13**, 96–110.
- 251 A. F. H. Ward and L. Tordai, *J. Chem. Phys.*, 1946, **14**, 453–461.
- 252 G. Bleys and P. Joos, *J. Phys. Chem.*, 1985, **89**, 1027–1032.
- 253 V. B. Fainerman, A. V. Makievski and R. Miller, *Colloids Surfaces A Physicochem. Eng. Asp.*, 1994, **87**, 61–75.
- 254 J. Y. Park and R. C. Advincula, in *Nanocoatings and Ultra-Thin Films*, Elsevier, 2011, pp. 24–56.
- 255 A. Czajka, PhD Thesis, University of Bristol, 2018.
- 256 B. V. Zhmud, E. Poptoshev and R. J. Pugh, *Langmuir*, 1998, **14**, 3620–3624.
- 257 E. C. Wijaya, F. Separovic, C. J. Drummond and T. L. Greaves, *Phys. Chem. Chem. Phys.*, 2016, **18**, 24377.
- 258 C. D. Dushkin, I. B. Ivanov and P. A. Kralchevsky, *Colloids and Surfaces*, 1991, **60**, 235–261.
- 259 C. H. Chang and E. I. Franses, *Colloids Surfaces A Physicochem. Eng. Asp.*, 1995, **100**, 1–45.
- 260 L. Liggieri and F. Ravera, *Stud. Interface Sci.*, 1998, **6**, 239–278.
- 261 L. Liggieri, F. Ravera and A. Passerone, *Colloids Surfaces A Physicochem. Eng. Asp.*, 1996, **114**, 351–359.
- 262 J. Boos, W. Drenckhan and C. Stubenrauch, *Langmuir*, 2012, **28**, 9303–9310.
- 263 F. Jin, R. Balasubramaniam and K. J. Stebe, *J. Adhes.*, 2004, **80**, 773–796.
- 264 N. J. Alvarez, Carnegie Mellon University, 2011.
- 265 N. J. Alvarez, L. M. Walker and S. L. Anna, *Langmuir*, 2010, **26**, 13310–13319.
- 266 N. J. Alvarez, PhD Thesis, Carnegie Mellon University, 2011.
- 267 Y. Moroi, in *Micelles*, Springer, Boston, MA, 1992, pp. 7–8.
- 268 M. Talib Latif and P. Brimblecombe, *Environ. Sci. & Technol.*, 2004, **38**, 6501–6506.
- 269 S. Ekström, B. Nozière, M. Hultberg, T. Alsberg, J. Magnér, E. D. Nilsson and P. Artaxo, *Biogeosciences*, 2010, **7**, 387–394.
- 270 M. Ahmed, X. Guo and X. M. Zhao, *Atmos. Environ.*, 2016, **141**, 219–229.

References

- 271 E. Farsang, V. Gaál, O. Horváth, E. Bárdos and K. Horváth, *Mol.* 2019, Vol. 24, Page 1223, 2019, **24**, 1223.
- 272 D. Koley and A. J. Bard, *Proc. Natl. Acad. Sci. U. S. A.*, 2010, **107**, 16783–16787.
- 273 H. Akbaş, M. Boz and Ç. Batigöç, *Spectrochim. Acta Part A Mol. Biomol. Spectrosc.*, 2010, **75**, 671–677.
- 274 K. Lunkenheimer, W. Barzyk, R. Hirte and R. Rudert, *Langmuir*, 2003, **19**, 6140–6150.
- 275 D. Vollhardt, G. Czichocki and R. Rudert, *Colloids Surfaces A Physicochem. Eng. Asp.*, 1993, **76**, 217–225.
- 276 V. Fainerman, S. Lylyk, E. Aksenenko, J. Petkov, J. Yorke and R. Miller, *Colloids Surfaces A Physicochem. Eng. Asp.*, 2010, **354**, 8–15.
- 277 K. Szymczyk, M. Szaniawska and A. Taraba, *Colloids and Interfaces*, 2018, **2**, 34.
- 278 Q. Zhang, Y. Meng, H. Yang, X. Xiao and X. Li, *Rapid Commun. Mass Spectrom.*, 2013, **27**, 2777–2781.
- 279 A. Bąk and W. Podgórska, *Colloids Surfaces A Physicochem. Eng. Asp.*, 2016, **504**, 414–425.
- 280 J. Zhang and Y. Meng, *Tribol. Lett.*, 2014, **56**, 543–552.
- 281 Sigma-Aldrich, *Sigma*, 1999, 1–2.
- 282 G. Y. Wang, Y. Y. Wang and X. H. Wang, *J. Mol. Liq.*, 2017, **232**, 55–61.
- 283 A. Helenius, D. R. McCaslin, E. Fries and C. Tanford, *Methods Enzymol.*, 1979, **56**, 734–749.
- 284 Detergents for Protein Solubilization | Thermo Fisher Scientific – UK, [https://www.thermofisher.com/uk/en/home/life-science/protein-biology/protein-purification-isolation/cell-lysis-fractionation/detergents-protein-solubilization.html?gclid=Cj0KCQiA_P6dBhD1ARIsAAGI7HBcC0ZJuMif-w75Skd9qgTMMUZ6lq\\$qt-OsHFXqsq8RgwUMy-XtfIEaAnjtEALw_wcB&ef_id=Cj0KCQiA_P6dBhD1ARIsAAGI7HBcC0ZJuMif-w75Skd9qgTMMUZ6lq\\$qt-OsHFXqsq8RgwUMy-XtfIEaAnjtEALw_wcB:G:s&s_kwid=AL!3652!3!606658602389!e!!g!!np40!13368767895!123500397496&cid=bid_pca_ppf_r01_co_cp1359_pjt0000_bid00000_0se_gaw_nt_pur_con](https://www.thermofisher.com/uk/en/home/life-science/protein-biology/protein-purification-isolation/cell-lysis-fractionation/detergents-protein-solubilization.html?gclid=Cj0KCQiA_P6dBhD1ARIsAAGI7HBcC0ZJuMif-w75Skd9qgTMMUZ6lq$qt-OsHFXqsq8RgwUMy-XtfIEaAnjtEALw_wcB&ef_id=Cj0KCQiA_P6dBhD1ARIsAAGI7HBcC0ZJuMif-w75Skd9qgTMMUZ6lq$qt-OsHFXqsq8RgwUMy-XtfIEaAnjtEALw_wcB:G:s&s_kwid=AL!3652!3!606658602389!e!!g!!np40!13368767895!123500397496&cid=bid_pca_ppf_r01_co_cp1359_pjt0000_bid00000_0se_gaw_nt_pur_con), (accessed 12 January 2023).
- 285 C. A. MacLeod and C. J. Radke, *J. Colloid Interface Sci.*, 1993, **160**, 435.
- 286 A. V. Makievski, V. B. Fainerman and P. Joos, *J. Colloid Interface Sci.*, 1994, **166**, 6–13.
- 287 G. Geeraerts and P. Joos, *Colloids Surfaces A Physicochem. Eng. Asp.*, 1994, **90**, 149–154.
- 288 B. Nozière, C. Baduel and J.-L. Jaffrezo, *Nat. Commun.*, 2014, **5**, 3335.
- 289 R. M. Weinheimer, D. F. Evans and E. L. Cussler, *J. Colloid Interface Sci.*, 1981, **80**, 357–368.
- 290 M. Giglio and A. Vendramini, *Phys. Rev. Lett.*, 1997, **38**, 26.
- 291 D. Wu, G.Y. Xu, J. Liu and Y.-M. Li, *J. Dispers. Sci. Technol.*, 2006, **27**, 523–526.
- 292 G. Nilsson, *J. Phys. Chem.*, 1957, **61**, 1135–1142.
- 293 S. S. Petters and M. D. Petters, *J. Geophys. Res.*, 2016, **121**, 1878–1895.
- 294 N. J. Alvarez, L. M. Walker and S. L. Anna, *Phys. Rev. E. Stat. Nonlinear, Soft Matter Phys.*, 2010, **82**, 011604.

References

- 295 N. C. Christov, K. D. Danov, P. A. Kralchevsky, K. P. Ananthapadmanabhan and A. Lips, *Langmuir*, 2006, **22**, 7528–7542.
- 296 M. J. Qazi, S. J. Schlegel, E. H. G. Backus, M. Bonn, D. Bonn and N. Shahidzadeh, *Langmuir*, 2020, **36**, 7956–7964.
- 297 B. Nozière, C. Baduel and J. L. Jaffrezo, *Nat. Commun. 2014 51*, 2014, **5**, 1–7.
- 298 S. Tiwari, S. Namsani and J. K. Singh, *J. Mol. Liq.*, 2022, **360**, 119498.
- 299 H. O. T. Pye, A. Nenes, B. Alexander, A. P. Ault, M. C. Barth, S. L. Clegg, J. L. Collett, K. M. Fahey, C. J. Hennigan, H. Herrmann, M. Kanakidou, J. T. Kelly, I. T. Ku, V. Faye McNeill, N. Riemer, T. Schaefer, G. Shi, A. Tilgner, J. T. Walker, T. Wang, R. Weber, J. Xing, R. A. Zaveri and A. Zuend, *Atmos. Chem. Phys.*, 2020, **20**, 4809–4888.
- 300 F. Hernáinz and A. Caro, *Colloids Surfaces A Physicochem. Eng. Asp.*, 2002, **196**, 19–24.
- 301 A. G. Bykov, S. Y. Lin, G. Loglio, V. V. Lyadinskaya, R. Miller and B. A. Noskov, *Colloids Surfaces A Physicochem. Eng. Asp.*, 2010, **354**, 382–389.
- 302 B. Smit, A. G. Schlijper, L. A. M. Rupert and N. M. Van Ost, *J. Phys. Chem*, 1990, **94**, 6933–6935.
- 303 N. R. Smith, G. V Crescenzo, Y. Huang, A. P. S. Hettiyadura, K. Siemens, Y. Li, C. L. Faiola, A. Laskin, M. Shiraiwa, A. K. Bertram and S. A. Nizkorodov, *Environ. Sci. Atmos.*, 2021, **1**, 140–153.
- 304 B. Zobrist, C. Marcolli, D. A. Pedernera and T. Koop, *Atmos. Chem. Phys.*, 2008, **8**, 5221–5244.
- 305 Y.-K. Tong, Y. Liu, X. Meng, J. Wang, D. Zhao, Z. Wu and A. Ye, *Phys. Chem. Chem. Phys.*, 2022, **24**, 10514.
- 306 N. R. Gervasi, D. O. Topping and A. Zuend, *Atmos. Chem. Phys.*, 2020, **20**, 2987–3008.
- 307 F. H. Marshall, R. E. H. Miles, Y. C. Song, P. B. Ohm, R. M. Power, J. P. Reid and C. S. Dutcher, *Chem. Sci.*, [OI:10.1039/c5sc03223g](https://doi.org/10.1039/c5sc03223g).
- 308 I. Riipinen, T. Yli-Juuti, J. R. Pierce, T. Petäjä, D. R. Worsnop, M. Kulmala and N. M. Donahue, *Nat. Geosci. 2012 57*, 2012, **5**, 453–458.
- 309 M. Petters and S. Kasparoglu, *Sci. Reports 2020 101*, 2020, **10**, 1–10.
- 310 M. Shrivastava, C. D. Cappa, J. Fan, A. H. Goldstein, A. B. Guenther, J. L. Jimenez, C. Kuang, A. Laskin, S. T. Martin, N. L. Ng, T. Petaja, J. R. Pierce, P. J. Rasch, P. Roldin, J. H. Seinfeld, J. Shilling, J. N. Smith, J. A. Thornton, R. Volkamer, J. Wang, D. R. Worsnop, R. A. Zaveri, A. Zelenyuk and Q. Zhang, *Rev. Geophys.*, 2017, **55**, 509–559.
- 311 P. Liu, Y. J. Li, Y. Wang, A. P. Bateman, Y. Zhang, Z. Gong, A. K. Bertram and S. T. Martin, *ACS Cent. Sci.*, 2018, **4**, 207–215.
- 312 M. L. Hinks, M. V. Brady, H. Lignell, M. Song, J. W. Grayson, A. K. Bertram, P. Lin, A. Laskin, J. Laskin and S. A. Nizkorodov, *Phys. Chem. Chem. Phys.*, 2016, **18**, 8785–8793.
- 313 K. Ignatius, T. B. Kristensen, E. Järvinen, L. Nichman, C. Fuchs, H. Gordon, P. Herenz, C. R. Hoyle, J. Duplissy, S. Garimella, A. Dias, C. Frege, N. Höppel, J. Tröstl, R. Wagner, C. Yan, A. Amorim, U. Baltensperger, J. Curtius, N. M. Donahue, M. W. Gallagher, J. Kirkby, M. Kulmala, O. Möhler, H. Saathoff, M. Schnaiter, A. Tomé, A. Virtanen, D. Worsnop and F. Stratmann, *Atmos. Chem. Phys.*, 2016, **16**, 6495–6509.
- 314 A. M. Maclean, N. R. Smith, Y. Li, Y. Huang, A. P. S. Hettiyadura, G. V. Crescenzo, M. Shiraiwa, A. Laskin, S. A. Nizkorodov and A. K. Bertram, *ACS Earth Sp. Chem.*, 2021, **5**, 305–318.

References

- 315 M. Shiraiwa, A. Zuend, A. K. Bertram and J. H. Seinfeld, *Phys. Chem. Chem. Phys.*, 2013, **15**, 11441.
- 316 A. Zuend, C. Marcolli, A. M. Booth, D. M. Lienhard, V. Soonsin, U. K. Krieger, D. O. Topping, G. McFiggans, T. Peter and J. H. Seinfeld, *Atmos. Chem. Phys.*, 2011, **11**, 9155–9206.
- 317 A. Zuend, C. Marcolli, B. P. Luo and T. Peter, *Atmos. Chem. Phys.*, 2008, **8**, 4559–4593.
- 318 A. Zuend, C. Marcolli, T. Peter and J. H. Seinfeld, *Atmos. Chem. Phys.*, 2010, **10**, 7795–7820.
- 319 H. Yin, J. Dou, L. Klein, U. K. Krieger, A. Bain, B. J. Wallace, T. C. Preston and A. Zuend, *Atmos. Chem. Phys.*, 2022, **22**, 973–1013.
- 320 H. Ki Lam, R. Xu, J. Choczynski, J. F. Davies, D. Ham, M. Song, A. Zuend, W. Li, Y. L. Steve Tse and M. N. Chan, *Atmos. Chem. Phys.*, 2021, **21**, 2053–2066.
- 321 R. M. Power, S. H. Simpson, J. P. Reid and A. J. Hudson, *Chem. Sci.*, 2013, **4**, 2597.
- 322 R. Jeong, J. Lilek, A. Zuend, R. Xu, M. N. Chan, D. Kim, H. G. Moon and M. Song, *Atmos. Chem. Phys.*, 2022, **22**, 8805–8817.
- 323 A. P. Bateman, Z. Gong, T. H. Harder, S. S. De Sá, B. Wang, P. Castillo, S. China, Y. Liu, R. E. O'Brien, B. B. Palm, H. W. Shiu, G. G. Cirino, R. Thalman, K. Adachi, M. Elizabeth Alexander, P. Artaxo, A. K. Bertram, P. R. Buseck, M. K. Gilles, J. L. Jimenez, A. Laskin, A. O. Manzi, A. Sedlacek, R. A. F. Souza, J. Wang, R. Zaveri and S. T. Martin, *Atmos. Chem. Phys.*, 2017, **17**, 1759–1773.
- 324 G. Rovelli, Y.-C. Song, A. M. Maclean, D. O. Topping, A. K. Bertram and J. P. Reid, *Anal. Chem.*, 2019, **91**, 5074–5082.
- 325 Y. C. Song, J. Lilek, J. B. Lee, M. N. Chan, Z. Wu, A. Zuend and M. Song, *Atmos. Chem. Phys.*, 2021, **21**, 10215–10228.
- 326 A. Zünd, PhD Thesis, ETH Zurich, 2007.
- 327 A. Marsh, S. S. Petters, N. E. Rothfuss, G. Rovelli, Y. C. Song, J. P. Reid and M. D. Petters, *Phys. Chem. Chem. Phys.*, 2018, **20**, 15086–15097.
- 328 Y. Mamane and J. Gottlieb, *Atmos. Environ. Part A. Gen. Top.*, 1992, **26**, 1763–1769.
- 329 P. K. Hudson, J. Schwarz, J. Baltrusaitis, E. R. Gibson and V. H. Grassian, *J. Phys. Chem. A*, 2007, **111**, 545–48.
- 330 R. C. Hoffman, A. Laskin and B. J. Finlayson-Pitts, *J. Aerosol Sci.*, 2004, **35**, 869–887.
- 331 G. Mark, H.-G. Korth, H.-P. Schuchmann and C. von Sonntag, *J. Photochem. Photobiol. A Chem.*, 1996, **101**, 89–103.
- 332 S. Seng, F. Guo, Y. A. Tobon, T. Ishikawa, M. Moreau, S. Ishizaka and S. Sobanska, *Atmos. Environ.*, 2018, **183**, 33–39.
- 333 M. Roca, J. Zahardis, J. Bone, M. El-Maazawi and V. H. Grassian, *J. Phys. Chem. A*, 2008, **112**, 13275–13281.
- 334 S. Goldstein and J. Rabani, *J. Am. Chem. Soc.*, 2007, **129**, 10597–601.
- 335 J. Mack and J. R. Bolton, *J. Photochem. Photobiol. A Chem.*, 1999, **128**, 1–13.
- 336 K. B. Benedict, A. S. McFall and C. Anastasio, *Environ. Sci. Technol.*, 2017, **51**, 4387–4395.
- 337 I. N. Tang, *J. Geophys. Res. Atmos.*, 1996, **101**, 19245–19250.
- 338 I. N. Tang and H. R. Munkelwitz, *J. Geophys. Res.*, 1994, **99**, 18801.

References

- 339 S. Ingram, C. Cai, Y.-C. Song, D. R. Glowacki, D. O. Topping, S. O'Meara and J. P. Reid, *Phys. Chem. Chem. Phys.*, 2017, **19**, 31634–31646.
- 340 A. Marsh, G. Rovelli, R. E. H. Miles and J. P. Reid, *J. Phys. Chem. A*, 2019, **123**, 1648–1660.
- 341 Y. C. Song, A. E. Haddrell, B. R. Bzdek, J. P. Reid, T. Bannan, D. O. Topping, C. Percival and C. Cai, *J. Phys. Chem. A*, 2016, **120**, 8123–8137.
- 342 F. K. A. Gregson, J. F. Robinson, R. E. H. Miles, C. P. Royall and J. P. Reid, *J. Phys. Chem. B*, 2020, **124**, 6024–6036.
- 343 S. Ghorai and A. V. Tivanski, *Anal. Chem.*, 2010, **82**, 9289–9298.
- 344 M. Ideland, *Sci. Educ.*, 2018, **27**, 783–803.
- 345 A. M. Land-Zandstra, J. L. A. Devilee, F. Snik, F. Buurmeijer and J. M. Van Den Broek, *Public Underst. Sci.*, 2016, **25**, 45–60.
- 346 J. D. Eversole, L. J. Johnson, J. Czege, V. Sivaprakasam and M. B. Hart, *Appl. Opt.*, 2015, **54**, F174–F181.